



UNIVERSIDADE ESTADUAL DE CAMPINAS

Faculdade de Engenharia Mecânica

FELIPE DE CASTRO TEIXEIRA CARVALHO

**Modeling electrical submersible pump system
under multiphase flows using bond graphs**

**Modelagem do sistema de bombas centrífugas
submersas sob escoamento multifásico usando
bond graphs**

CAMPINAS

2024

FELIPE DE CASTRO TEIXEIRA CARVALHO

Modeling electrical submersible pump system under multiphase flows using bond graphs

Modelagem do sistema de bombas centrífugas submersas sob escoamento multifásico usando bond graphs

Thesis presented to the School of Mechanical Engineering of the University of Campinas in partial fulfillment of the requirements for the degree of Doctor in Mechanical Engineering, in the area of Solid Mechanics and Mechanical Project.

Tese apresentada à Faculdade de Engenharia Mecânica da Universidade Estadual de Campinas como parte dos requisitos exigidos para obtenção do título de Doutor em Engenharia Mecânica, na Área de Mecânica dos Sólidos e Projeto Mecânico.

Orientador: Prof. Dr. Alberto Luiz Serpa

ESTE EXEMPLAR CORRESPONDE À
VERSÃO FINAL DA TESE DEFENDIDA
PELO ALUNO FELIPE DE CASTRO TEIX-
EIRA CARVALHO, E ORIENTADO PELO
PROF. DR. ALBERTO LUIZ SERPA.

CAMPINAS

2024

Ficha catalográfica
Universidade Estadual de Campinas
Biblioteca da Área de Engenharia e Arquitetura
Rose Meire da Silva - CRB 8/5974

C253m Carvalho, Felipe de Castro Teixeira, 1993-
Modeling electrical submersible pump system under multiphase flows using bond graphs / Felipe de Castro Teixeira Carvalho. – Campinas, SP : [s.n.], 2024.

Orientador: Alberto Luiz Serpa.

Tese (doutorado) – Universidade Estadual de Campinas, Faculdade de Engenharia Mecânica.

1. Bombas centrífugas - Submersa. 2. Grafos de ligação. 3. Escoamento multifásico. 4. Problemas inversos (Equações diferenciais). 5. Redes neurais (computação). I. Serpa, Alberto Luiz, 1967-. II. Universidade Estadual de Campinas. Faculdade de Engenharia Mecânica. III. Título.

Informações Complementares

Título em outro idioma: Modelagem do sistema de bombas centrífugas submersas sob escoamento multifásico usando bond graphs

Palavras-chave em inglês:

Electrical submersible pumps

Bond graphs

Multiphase flows

Inverse problem

Neural networks

Área de concentração: Mecânica dos Sólidos e Projeto Mecânico

Títuloção: Doutor em Engenharia Mecânica

Banca examinadora:

Alberto Luiz Serpa [Orientador]

Ricardo Augusto Mazza

Alberto Costa Nogueira Junior

Luiz Carlos Sandoval Góes

Diego Eckhard

Data de defesa: 19-01-2024

Programa de Pós-Graduação: Engenharia Mecânica

Identificação e informações acadêmicas do(a) aluno(a)

- ORCID do autor: <https://orcid.org/0000-0002-0871-728X>

- Currículo Lattes do autor: <http://lattes.cnpq.br/9570604237754315>

**UNIVERSIDADE ESTADUAL DE CAMPINAS
FACULDADE DE ENGENHARIA MECÂNICA**

TESE DE DOUTORADO ACADÊMICO

**Modeling electrical submersible pump system
under multiphase flows using bond graphs**

**Modelagem do sistema de bombas centrífugas
submersas sob escoamento multifásico usando
bond graphs**

Autor: Felipe de Castro Teixeira Carvalho

Orientador: Prof. Dr. Alberto Luiz Serpa

A Banca Examinadora composta pelos membros abaixo aprovou esta Tese:

**Prof. Dr. Alberto Luiz Serpa, Presidente
DMC/FEM/UNICAMP**

**Prof. Dr. Ricardo Augusto Mazza
DE/FEM/UNICAMP**

**Dr. Alberto Costa Nogueira Junior
IBM Research**

**Prof. Dr. Luiz Carlos Sandoval Góes
DEMA/DP/ITA**

**Prof. Dr. Diego Eckhard
DPAM/IMA/UFRGS**

A Ata da defesa com as respectivas assinaturas dos membros encontra-se no SIGA/Sistema de Fluxo de Dissertação/Tese e na Secretaria do Programa da Unidade.

Campinas, 19 de Janeiro de 2024.

Dedication

This thesis is dedicated to my parents.

Acknowledgement

Foremost, I would like to express my profound gratitude to my advisor, Professor Dr. Alberto Luiz Serpa for their unwavering support, invaluable guidance, and insightful feedback throughout the course of this research. His expertise in and dedication to academic excellence have been instrumental in shaping my work and my growth as a researcher. I am profoundly grateful for the opportunity.

My sincere thanks also go to my thesis committee members for their constructive criticism and valuable suggestions that significantly improved the quality of this thesis.

I extend my sincere gratitude to Prof. Dr. George Em Karniadakis for graciously hosting me during my research internship. His invaluable guidance and the opportunity to work alongside him and his team have been pivotal in enhancing both the quality and scope of my thesis. This remarkable experience provided me with unique insights and exposure to cutting-edge research in physics-informed neural networks. For this, I am deeply thankful.

I am immensely grateful to the São Paulo Research Foundation (FAPESP) for their financial support under grant number 2019/14597-5, which was essential for the execution of this research. The provision of a scholarship, alongside the funding for necessary resources and tools, was critical in enabling this work.

I extend my appreciation to my colleagues and peers within the Computational Mechanics Department. Their camaraderie, engaging discussions, and the insights we shared have been invaluable to both my personal growth and professional development. Additionally, I am indebted to Kamaljyoti Nath for his steadfast support and friendship during my time in the CRUNCH group. His contributions through stimulating conversations and shared perspectives have been instrumental in enriching my research experience.

I express my profound appreciation to the Center for Energy and Petroleum Studies (CEPETRO) at the University of Campinas for providing the necessary facilities that have been fundamental to my research. My gratitude extends to the Artificial Lift and Flow Assurance research group for their support and invaluable contributions to the experimental aspects of my work. Additionally, I would like to extend my thanks to Equinor and the Brazilian National Agency of Petroleum, Natural Gas and Biofuels (ANP) for offering the research opportunity.

Special thanks are due to my parents and brother for their unwavering patience, encouragement, and support. Their presence has been a constant source of strength and motivation throughout my PhD journey and beyond. I am also deeply grateful to my friends who have provided invaluable support and companionship during this significant phase of my life.

Finally, I acknowledge the contributions of all the authors and researchers whose publications and works have informed and inspired this research. Their pioneering efforts have laid the groundwork for my study.

*Every ending in the quest for knowledge
opens a new chapter of endless curiosity,
weaving the infinite tapestry of our
eternal pursuit for understanding.*

Resumo

Bombas centrífugas submersas (ESPs) são amplamente utilizadas em setores industriais que necessitam de altas vazões e ganho de pressão. Na indústria de petróleo e gás, as ESPs frequentemente operam sob condições de escoamento multifásico, tais como emulsões de óleo-água. O comportamento não-Newtoniano das emulsões pode induzir um comportamento dinâmico e instável do sistema. Contudo, a literatura existente foca no comportamento em estado estacionário destes sistemas. O objetivo principal deste trabalho é desenvolver e validar um modelo dinâmico para ESPs utilizando *bond-graphs*, conduzir análises de identificabilidade e estimar parâmetros do sistema com um conjunto limitado de sensores. A metodologia adotada engloba a coleta de dados experimentais em condições estacionárias e dinâmicas, modelagem por meio de *bond-graphs* e o emprego de Redes Neurais Informadas por Física (PINNs). O modelo da ESP foi formulado utilizando uma biblioteca desenvolvida, neste trabalho, em Julia. Foram conduzidas análises de identificabilidade, tanto estrutural quanto prática do modelo. As PINNs foram empregadas para abordar o problema inverso e foram avaliadas em dados simulados e experimentais. A validação do modelo foi realizada através da comparação dos dados experimentais com simulações numéricas. A pesquisa resultou em um modelo dinâmico para ESPs baseado em *bond-graph* que incorpora os subsistemas mecânicos e hidráulicos, resultando em um conjunto de equações diferenciais ordinárias (ODEs). Em condições estacionárias, o modelo demonstrou um elevado coeficiente de determinação e um erro relativamente baixo. Para cenários dinâmicos, ajustes finos nos parâmetros resultaram em melhoria na precisão do modelo, especialmente em relação às pressões, embora algumas discrepâncias nos picos de pressão tenham sido observadas. A análise de identificabilidade estrutural local identificou 12 parâmetros que são determináveis, mas a identificabilidade prática foi alcançada apenas com oito. As PINNs mostraram eficácia na estimativa de parâmetros e estados, sobretudo em cenários de baixa fração de água, mas apresentaram limitações em altas frações de água e em presença de ruído nos dados. O modelo dinâmico, em conjunto com as PINNs, demonstra potencial para aplicações em controle, monitoramento, detecção de falhas e otimização. Embora o modelo capture a dinâmica do sistema, limitações surgem devido às hipóteses feitas quanto à viscosidade da emulsão e ao acoplamento bomba-tubo. Para trabalhos futuros é sugerido aprimorar na modelagem da propagação de ondas de pressão no sistema. Além disso, a adoção de algoritmos mais robustos para PINNs, que poderia melhorar a estimativa dos parâmetros desconhecidos. Este trabalho estabelece uma base para a modelagem de sistemas ESP mais complexos, com potencial de aplicação além do setor de petróleo e gás.

Palavras-chave: Sistema dinâmico; Bond graph; Problema inverso; Análise de identificabilidade; Redes Neurais Informadas por Física; Bomba centrífuga; Emulsão; Escoamentos multifásicos.

Abstract

Electrical Submersible Pumps (ESPs) are extensively utilized in industries requiring high flow rates and boosting pressures. In the oil and gas sector, ESPs frequently handle multiphase flows, including oil-water emulsions. The non-Newtonian behavior of the emulsions can lead to system instabilities, resulting in a dynamic behavior. However, existing research primarily targets the steady-state behavior of ESPs under emulsion conditions. The primary objective of this research is to develop and validate a dynamic model for ESPs using bond graph theory, to conduct identifiability analysis, and to estimate the system parameters with a limited number of sensors. The adopted methodology encompasses collecting experimental data under both stationary and dynamic conditions, modeling the ESP using bond graphs, and using Physics-Informed Neural Networks (PINNs). The ESP model equations were obtained using a library developed in this work in Julia. The identifiability analysis conducted on the model considered the structural and the practical. The PINNs were employed to address the inverse problem and evaluated using simulated and experimental data. The model was validated by comparing experimental data with numerical simulations. This study presents a bond graph-based dynamic model for ESPs that incorporates mechanical and hydraulic subsystems, resulting in a set of Ordinary Differential Equations (ODEs). In steady-state conditions, the model yielded a high coefficient of determination and relatively small error bounds, which attested to the model's reliability. In the dynamic scenario, the fine-tuning of parameters enhanced the model's capability in capturing pressure dynamics, although minor deviations in the pressure spike are observed. Through local structural identifiability analysis, twelve parameters were identified as uniquely determinable; however, practical identifiability was achieved with only eight. The application of PINNs demonstrated effectiveness in estimating parameters and states, particularly in low water cut conditions. The proposed method exhibited limitations in high water cut and noisy environments, being areas for future investigation. The model with the PINN can be used in control, condition monitoring, fault detection, and optimization, even in challenging scenarios of unknown fluid properties. While the model accurately captures system dynamics, limitations emerge due to assumptions on the viscosity and the pump-pipe coupling, requiring future work on better modeling the pressure wave velocity in the system. For the inverse problem, a robust PINN algorithm would enhance the unknown parameter estimation. The methodology lays a foundation for modeling more complex ESP systems with applications beyond the oil industry.

Keywords: Dynamic systems; Bond graph; Inverse problem; Identifiability analysis, Physics-Informed Neural Networks; Electrical Submersible Pump; Emulsion; Multiphase flows.

List of Figures

3.1	Bond graph obtained from the integration of the momentum equation.	54
3.2	C-element for pipelines.	55
3.3	Control volume (CV) and control surfaces of a centrifugal pump.	60
3.4	Entrance and discharge velocity triangle.	62
3.5	Centrifugal pump bond graph representation.	67
3.6	Shock component of peripheral velocity at entrance and discharge of the impeller.	70
3.7	Schematic of a typical control valve featuring a spring-diaphragm pneumatic actuator.	75
3.8	Bond graph representation of an ideal twin screw pump.	78
3.9	Bond graph representation of a screw pump, considering clearance and the mechanical components.	80
3.10	Twin-screw pump [130].	80
4.1	Schematic diagram of the experimental setup.	86
4.2	Steady-state experimental procedure flowchart.	93
4.3	Transient experimental procedure flowchart.	95
4.4	Steady-state experimental data of the ESP P100L for oil conditions.	97
4.5	Steady-state experimental data of the ESP P100L for water conditions.	98
4.6	Steady-state experimental data of the ESP P47 for oil conditions.	98
4.7	Steady-state experimental data of the ESP P47 for water conditions.	99
4.8	Duffing equation as a mass-spring-damper system and its bond graph representation.	100
4.9	Schematics representation of the physics-informed neural network for the ESP system.	108
5.1	Two tanks interconnected by a pipe problem.	117
5.2	Bond graph model for the two tanks interconnected by a pipe problem.	117
5.3	Bond graph and MoC comparison for inertial dynamics of the tank problem.	119
5.4	Bond graph and MoC comparison for pressure wave dynamics of the tank problem.	120
5.5	Bond graph model of the shaft and impeller subsystem.	123
5.6	Bond graph model for a shaft segment (\mathcal{S}^i).	124
5.7	Bond graph model for a pipe segment (\mathcal{P}^i).	124
5.8	Bond graph model for a centrifugal pump stage (\mathcal{C}^i).	125
5.9	Bond graph model the ESP system.	125
5.10	Simplified bond graph model for the ESP system.	130

5.11	Comparison of the numerical solution and the measured states for the ESP P100L in the first dynamic experimental investigation (Table 4.7, row 1).	134
5.12	Comparison of the numerical solution and the measured states for the ESP P100L in the second dynamic experimental investigation (Table 4.7, row 2).	135
5.13	Comparison of the numerical solution and the measured states for the ESP P47 in the third dynamic experimental investigation (Table 4.7, row 3).	136
5.14	Comparison of the numerical solution and the measured states for the ESP P47 in the fourth dynamic experimental investigation (Table 4.7, row 4).	137
5.15	Comparison of the numerical solution and the measured states for the ESP P47 in the fifth dynamic experimental investigation (Table 4.7, row 5).	138
5.16	Comparison of the numerical solution and the measured states for the ESP P47 in the sixth dynamic experimental investigation (Table 4.7, row 6).	139
5.17	Comparison of the numerical solution and the measured states for the ESP P100L in the first dynamic experimental investigation (Table 4.7, row 1), after to the fine-tuning of compliance elements in the bond graph model.	140
5.18	Comparison of the numerical solution and the measured states for the ESP P100L in the second dynamic experimental investigation (Table 4.7, row 2), after to the fine-tuning of compliance elements in the bond graph model.	141
5.19	Comparison of the numerical solution and the measured states for the ESP P47 in the third dynamic experimental investigation (Table 4.7, row 3), after to the fine-tuning of compliance elements in the bond graph model.	142
5.20	Comparison of the numerical solution and the measured states for the ESP P47 in the fourth dynamic experimental investigation (Table 4.7, row 4), after to the fine-tuning of compliance elements in the bond graph model.	143
5.21	Comparison of the numerical solution and the measured states for the ESP P47 in the fifth dynamic experimental investigation (Table 4.7, row 5), after to the fine-tuning of compliance elements in the bond graph model.	144
5.22	Comparison of the numerical solution and the measured states for the ESP P47 in the sixth dynamic experimental investigation (Table 4.7, row 6), after the fine-tuning of compliance elements in the bond graph model.	145
6.1	Correlation matrix of the ESP system model parameters.	147
6.2	Correlation matrix of the ESP system model parameters after the practical identifiability analysis.	148
7.1	Cases and scenarios evaluated.	150
7.2	Comparison of predicted and true states for simulated scenario of the first experimental investigation with unknown parameters.	153
7.3	Comparison of predicted and true states for the simulated case with noise of the first experimental investigation and unknown parameters.	156

7.4	Comparison of predicted and true states for the experimental case of the first experimental investigation with unknown parameters.	158
7.5	Box plot of the absolute percentage errors for Case 1.	160
7.6	Box plot of the absolute percentage errors for Case 2.	162
7.7	Box plot of the absolute percentage errors for Case 3.	165
A.1	The tetrahedron of state.	182
A.2	Representation of a bond graph power bond from subsystem 1 to subsystems 2.	182
A.3	Interpretation of the causal strokes in relation to the direction of power variables.	184
A.4	2-port element sign convention.	187
B.1	Oil viscosity plotted against temperature, ranging from 10 °C to 60 °C for the system with the ESP P100L.	189
B.2	Oil viscosity plotted against temperature, ranging from 10 °C to 60 °C for the system with the ESP P47.	190
C.1	Regression plot comparing measured and estimated values of pressure gain, ΔP , for the ESP system with the P100L.	192
C.2	Regression plot comparing measured and estimated values of pressure gain, ΔP , for the ESP system with the P47.	192
C.3	Regression plot comparing measured and estimated values of shaft torque for the ESP system with the P100L.	193
C.4	Regression plot comparing measured and estimated values of shaft torque for the ESP system with the P47.	194
C.5	Regression plot comparing estimated and measured values of P_1 for the first experimental dynamic investigation.	195
C.6	Regression plot comparing estimated and measured values of P_1 for the second experimental dynamic investigation.	196
C.7	Regression plot comparing estimated and measured values of P_0 for the twin-screw pump segment.	197
C.8	Regression plot comparing estimated and measured values of P_1 for the heat exchanger to ESP pump entrance segment.	198
C.9	Histogram of absolute percentage errors in P_0 for the twin-screw pump model.	199
C.10	Valve C_v as a function of the valve aperture a	201
C.11	Regression plot comparing calculated and estimated values of the valve C_v	201
C.12	Valve C_v as a function of valve aperture a	202
C.13	Regression plot comparing calculated and estimated values of valve C_v	203
C.14	Regression plot comparing estimated and measured values of P_r	204
D.1	Predicted states for the simulated and unknown flow parameters for the second experiment.	206

D.2	Predicted states for the simulated with noise and unknown flow parameters for the second investigation.	207
D.3	Predicted states for the experimental data and unknown flow parameters for the second investigation.	208

List of Tables

4.1	Specifications of components used in the experimental setup	87
4.2	Instrumentation specifications: range and uncertainty	89
4.3	Summary of experimental tests for evaluating ESP P100L performance for oil conditions.	96
4.4	Summary of experimental tests for evaluating ESP P100L performance for water conditions.	96
4.5	Summary of experimental tests for evaluating ESP P47 performance for oil conditions.	96
4.6	Summary of experimental tests for evaluating ESP P47 performance for water conditions.	97
4.7	Test matrix for assessing the dynamics of the ESP system in oil/water two-phase flows.	99
5.1	States of the ESP system bond graph model	128
5.2	Parameters for the ESP system bond graph model	129
5.3	Parameters for the twin-screw pump and pipeline.	131
5.4	Comparison of the MAPE and Pearson correlation coefficient between numerical solutions and experimental data. The units are percentages, and the parenthetical values correspond to the Pearson correlation coefficient, which is dimensionless.	133
5.5	Comparison of the MAPE and Pearson correlation coefficient between numerical solutions with tuned compliance element and experimental data. The units are percentages, and the parenthetical values correspond to the Pearson correlation coefficient, which is dimensionless.	139
6.1	Local structural identifiability results of the ESP system model, considering that the intake pressure (P_1) and discharge pressure (P_2) are known.	146
7.1	Transformations of the unknown parameters for each case evaluated.	151
7.2	Scaling constants for the unknown parameters.	151
7.3	MAPE for the simulated scenario.	152
7.4	MAPE for the simulated scenario with added noise.	154
7.5	MAPE for the experimental data scenario.	157
7.6	Mean of the absolute percentage error for Case 1.	159
7.7	Mean of the absolute percentage error for Case 2.	161
7.8	Mean absolute percentage error for Case 3.	164

A.1	Generalized variables for mechanical domain.	183
A.2	Generalized variables for mechanical rotation domain.	183
A.3	Generalized variables for hydraulic domain.	183
A.4	Generalized variables for electrical domain.	184
D.1	Mean absolute percentage error for the simulation case.	205
D.2	Mean absolute percentage error for the simulation with added noise case.	205
D.3	Mean absolute percentage error for the experimental case.	205
D.4	Estimation results of ESP system model parameters using PINN for Investigation 1.210	
D.5	Estimation results of ESP system model Parameters using PINN for Investigation 2211	
F.1	Adam training settings for neural network training in Case 1 (three unknown parameters).	214
F.2	Adam training settings for neural network training in Case 2 (seven unknown parameters).	215
F.3	Adam training settings for neural network training in Case 3 (eight unknown parameters).	215
F.4	Initial weights for the data, physics, and initial conditions (I.C.) losses.	216

Nomenclature

Acronyms/Abbreviations

AC Alternate current

CEPETRO Center for Energy and Petroleum Studies

DC Direct current

ESP Electrical submersible pump

LABPETRO Experimental Laboratory of Petroleum Kelsen Valente Serra

MoC Method of Characteristics

RTD Resistance temperature detector

RTT Reynolds Transport Theorem

SCADA Supervisory Control and Data Acquisition System

VSD Variable speed drive

Bond graph elements

0 0-junction (zero-junction)

1 1-junction (one-junction)

C Energy storage element associated with displacement

C_{eq} Equivalent compliance of a pipe segment, incorporating fluid compressibility and wall elasticity effects

C^i Centrifugal pump stage in the ESP generalized bond graph model

C_s Stiffness element of the shaft in bond graph notation, represented as $1/k_\theta$

GY Gyrator (2-port element)

I Energy storage element associated with inertia

I_{cf} Inertia of the fluid within the impeller

I_f Pipeline fluid inertia in the bond graph representation

I_s	Inertia of the shaft, calculated using the moment of inertia of a cylinder (Equation (5.4))
I_s^i	Moment of inertia for an individual segment of the shaft in a segmented representation
MGY	Modulated gyrator
MSe	Modulated effort-based source element
MSf	Modulated flow-based source element
MTF	Modulated transformer
\mathcal{P}^i	Pipe segment in the ESP generalized bond graph model
R	Dissipative element associated with power conversion to thermal energy
R_c	Pipeline resistance associated with dynamic pressure
R_{cf}	Friction loss represented in bond graph notation with grouped terms
R_{cf}	Friction loss represented in bond graph notation
R_{cl}	Leakage losses in the centrifugal pump; described in Section 3.5.4
R_{df}	Disk friction bond graph resistance element
R_f	Pipeline viscous friction term in the bond graph
R_{LS}	Bond graph resistance element for the twin-screw pump leakage simplified
R_L	Bond graph resistance element for the twin-screw pump leakage
R_{lcc}	Bond graph resistance element for the circumferential clearance of the twin-screw pump in laminar flows
R_{lrc}	Bond graph resistance element for the circumferential radius clearance of the twin-screw pump in laminar flows
R_m	Resistance element in bond graph notation representing local losses
R_{mc}	Bond graph element representing the combined local losses of the centrifugal pump
R_{mec}	Journal bearing and stuffing box bond graph resistance element
R_{sx}	Shock loss bond graph resistance element
R_{tcc}	Bond graph resistance element for the circumferential clearance of the twin-screw pump in turbulent flows

R_{trc}	Bond graph resistance element for the circumferential radius clearance of the twin-screw pump in turbulent flows
R_v	Bond graph valve resistance element
Se	Effort-based source element
Sf	Flow-based source element
S^i	Shaft segment in the ESP generalized bond graph model
TF	Transformer (2-port element)
\mathcal{T}	Twin-screw pump in the ESP generalized bond graph model
\mathcal{V}^i	Valve in the ESP generalized bond graph model

Dimensionless number

Re	Reynolds number
------	-----------------

Greek Symbols

α_t	Annular space portion between the root and the tip of the screw threads not occupied by the threads of the twin-screw pump
β	Centrifugal pump blade angle
Δc_{u1}	Difference in tangential velocity components at entrance
Δc_{u2}	Difference in tangential velocity components at discharge
δ_L	Factor to account for the relationship between Q_L and Q_{cc}
ΔP	Pressure drop in the pipe
Δx	Length of the pipe segment
ϵ_r	Surface roughness
η	Pipe wall thickness
Γ	Shear stress
γ	Expression for the bond graph gyrator element representing the centrifugal pump
$\mathbf{\Gamma}$	Stress tensor
Γ_{xy}	Shear stress component in the xy -plane

λ	Friction factor
λ_{cc}	Friction factor for the circumferential clearance
λ_{lam}	Laminar friction factor
μ	Fluid viscosity
ω	Angular velocity
ω_t	Angular velocity of the twin-screw
$\Phi_C(q)$	Constitutive relationship for C-elements
$\Phi_I(p)$	Constitutive relationship for I-elements
$\Phi_R(f)$	Constitutive relationship for R-elements
ψ	Set containing all the centrifugal pump local losses
ρ	Fluid density
ρ_0	Water density at 15 °C
ρ^*	Relative density of the fluid
ω_i	Electrical submersible pump initial angular velocity
ω_f	Electrical submersible pump final angular velocity
τ_{df}	Overall torque due to disk friction
τ	Torque
τ_{shaft}	Torque on the shaft
ξ	Angle of the conduit with respect to the ground
ζ_1	Term representing the influence of changes in impeller speed
ζ_2	Term representing the effect of flow rate changes
ζ_3	Coefficient representing $\rho (r_2^2 - r_1^2)$
ζ_4	Coefficient representing $\rho \left(\frac{\cot(\beta_2)}{2\pi h_2} - \frac{\cot(\beta_1)}{2\pi h_1} \right)$

Other symbols

\mathcal{SS} Steady state

\mathcal{U} Unsteady

Physics constants

ρ Density of fluid

Roman symbols

\mathbf{A} Area vector on the control surface, oriented normal to the surface

A Cross-sectional area of the pipe

a Velocity of the pressure wave in a conduit

A_{cc} Total circumferential clearance cross-sectional area

A_x Cross-sectional area of impeller vane

B Fluid bulk modulus

c Velocity of the flow entering or leaving the vanes

C_v Valve flow coefficient

c_m Normal velocity at the centrifugal pump

c_{mx}' Modified normal velocity

c_u Tangential component of the fluid velocity at the centrifugal pump

d Pipe diameter

d_{cc} Hydraulic diameter for the circumferential clearance

d_h Hydraulic diameter

d_s Tip diameter of the screw's root diameter

$d\mathbf{A}$ Differential area element

dV Differential volume element

dz Infinitesimal element along the axial coordinate z

E Energy at a multiport

e Generalized effort at a multiport

E_c Total energy within a control volume

e_c	Internal energy per unit mass
E_{ym}	Young's modulus of elasticity
f	Generalized flow at a multiport
F_d	Valve style modifier
F_L	The liquid pressure recovery factor for a control valve in the absence of any attached fittings
F_p	Valve pipe geometry factor
F_r	Valve Reynolds number factor
g	Gravitational acceleration
h	Height of the impeller
K_E	Constant describing conduit wall deformation due to pressure
k_i	Combined inertial loss constant
K_L	Loss coefficient representing flow losses in the circumferential clearance
k_{lam}	Laminar viscous friction coefficient
k'_{lam}	Grouped laminar viscous friction coefficient
K_{Lc}	Twin-screw pump local loss constant grouping geometrical parameters
K_{LL}	Twin-screw pump friction loss constant grouping geometrical parameters and constants
K_m	Local loss coefficient
K_{ma}	Local loss coefficient incorporating the cross-sectional area
k_{mec}	Journal bearing and stuffing box friction factor
k_{rd}	Ratio of the screw's root diameter to its tip diameter
K_{sr}	Roughness for the twin-screw pump
k_{turb}	Turbulent friction coefficient
k'_{turb}	Grouped turbulent friction coefficient
k_v	Combined viscous loss constant
k_i	Disk friction inertial loss constant

k_{mc}	Combined local loss coefficient in a single-stage centrifugal pump
k_{df}^s	Disk friction constant for geometry s
k_g^s	Inertial contribution constant for a given geometry s
k_{Re}^s	Viscous contribution constant for a given geometry s
k_{sx}	Shock loss constant
k_v	Disk friction viscous loss constant
L	Channel or pipe length
l	Pipeline segment length
L_{cc}	Equivalent length for the circumferential clearance
L_{cc}	Length of the circumferential clearance of the twin-screw pump
L_{ec}	Effective length of the radial clearance
L_{sc}	Active length of the flank clearance of the twin-screw pump
L_{sc}	Axial length of each pumping screw
L_{sd}	Chamber depth of the twin-screw pump
L_{sf}	Length of the flank clearance of the twin-screw pump
N_1	Valve numerical constant for unit conversion
N_2	Valve numerical constant for unit conversion
N_4	Valve numerical constant for unit conversion
n_L	Number of chambers of the twin-screw pump
n_l	Number of chambers created by the interlocking screws
n_s	Count of screw threads of a twin-screw pump
n_t	Exponent in turbulent friction term
n_v	Valve trim style constant
p	Generalized Momentum at a multiport
P	Fluid pressure

P_{wr}	Instantaneous power at a multiport
q	Generalized Displacement at a multiport
Q^*	Design flow rate
Q	Volumetric flow rate
Q_{cc}	Flow rate due to circumferential clearance
Q_{fc}	Flow rate due to flank clearance
Q_L	Leakage volumetric flow rate, representing internal leakage of a twin-screw pump
Q_{rc}	Flow rate due to radial clearance
Q_t	Theoretical volume displaced by a twin-screw pump
Q_s	Specific flow rate
\mathbf{r}	Position vector from the axis of rotation to a fluid element
r_t	Twin-screw pump transformer expression
r_x	Radius at specific point in impeller
t	Time
θ	Angular coordinate
u	Fluid velocity
u_x	Fluid tangential velocity at the centrifugal pump, where x is 1 or 2.
V	Average flow velocity
v	Absolute fluid velocity
V_D	Displacement volume, the theoretical volume of liquid displaced per rotor revolution
V_{i+1}	Volume at the exit of the i -th pipe segment
$V_i(t)$	Volume at the entrance of the i -th pipe segment
V_j	Difference in volume between the entrance and exit of the pipe segment
\mathbf{v}	Fluid flow velocity vector
w_{cc}	Width of the circumferential clearance of the twin-screw pump

w_{fc}	Width of the circumferential flank clearance of the twin-screw pump
w_{rc}	Width of the circumferential radius clearance of the twin-screw pump
w_{sp}	Width of the screw profile of the twin-screw pump
w_{ux}	Relative tangential component of velocity
z	Height as a function of x

Subscripts

1	Inlet condition
2	Outlet condition
cc	Circumferential clearance
CS	Control Surface
CV	Control Volume
fc	Flank clearance
rc	Radial clearance

Contents

List of Figures	10
List of Tables	14
Nomenclature	16
Contents	25
1 Introduction	29
1.1 Dynamic systems	29
1.2 Bond-graphs	29
1.3 Modeling and inverse problem	30
1.4 Multi-phase flows	31
1.5 Emulsions	32
1.6 Electrical submersible pumps	32
1.7 Objectives	33
1.8 Research contributions	34
2 Literature review	36
2.1 Two-phase flows	36
2.2 Emulsion	37
2.3 Electrical submersible pumps	40
2.4 Centrifugal pump transient	42
2.5 Bond graphs	44
2.6 Identifiability analysis	45
2.7 Inverse problems	46
3 Theoretical framework	48
3.1 Multiphase flow assumptions	48
3.2 Pipeline transient	50
3.2.1 Continuity equation	50
3.2.2 Momentum equation	52
3.2.3 Fluid dynamics with continuity and momentum equations	53
3.2.4 Bond graph	53
3.2.4.1 One-dimensional incompressible flow representation	53
3.2.4.2 Continuity equation representation	54

3.3	Viscous flow in ducts	56
3.3.1	Friction losses	57
3.3.2	Local losses	57
3.4	Centrifugal pumps	59
3.4.1	Power equation	59
3.4.2	Angular-momentum equation	60
3.4.3	Transient term analysis	62
3.4.4	Steady state term analysis	64
3.4.5	Bond graph representation	66
3.5	Centrifugal pump losses	67
3.5.1	Friction loss	67
3.5.2	Local losses	68
3.5.3	Shock loss	69
3.5.4	Leakage loss	71
3.5.5	Disk friction loss	71
3.5.6	Mechanical losses	74
3.6	Valves	75
3.6.1	Static model for turbulent flows in incompressible fluids	76
3.6.2	Static model for non-turbulent flows in incompressible fluids	76
3.6.3	Valve bond graph resistance model	77
3.7	Twin-screw pumps	78
3.7.1	Bond graph representation	78
3.7.2	Ideal displacement or swept volume flow rate	79
3.7.3	Liquid leakage in twin-screw pumps	81
3.7.4	Simplified liquid leakage in twin-screw pumps	83
3.8	Structural identifiability analysis	84
4	Materials and methods	85
4.1	Experimental study	85
4.1.1	Experimental assembly	85
4.1.2	Instrumentation and measured variables	88
4.1.3	Data acquisition system	90
4.1.4	Data collection	91
4.1.5	Experimental procedures	91
4.1.5.1	Steady state experiments	91
4.1.5.2	Dynamic experiments	93
4.1.6	Steady-state test matrix	96
4.1.7	Dynamic test matrix	97
4.2	Modeling using bond graphs	99

4.2.1	Initialization of 1-port elements	100
4.2.2	Custom 1-port elements	101
4.2.3	Connecting multiport elements	102
4.2.4	Equation Extraction	103
4.2.5	Analytical validation	104
4.2.6	Numerical simulation	105
4.3	Valve modeling	105
4.4	Practical identifiability analysis	106
4.5	Physics-informed neural networks	107
4.5.1	Neural network architecture	107
4.5.2	Physics-Informed loss function	108
4.5.3	Input and output transformations	110
4.6	Data generation	111
4.7	Parameter estimation and tuning	113
4.7.1	Steady-state parameter estimation	113
4.7.2	Dynamic model tuning	114
4.7.2.1	Dynamic model tuning ESP and pipeline	114
4.7.2.2	Dynamic model tuning C-element	114
5	Modeling results	116
5.1	Pipeline model	116
5.1.1	Problem definition	117
5.1.2	Validation inertial dynamics	118
5.1.3	Validation pressure wave dynamics	119
5.2	Shaft-pump bond graph model	121
5.3	General ESP system bond graph model	123
5.4	Single impeller approximation	126
5.5	Model validation	132
5.5.1	Pump and pipeline tuning	133
5.5.2	Compliance element tuning	138
6	Identifiability analysis results	146
6.1	Structural local identifiability	146
6.2	Practical identifiability	147
7	Inverse problem results	149
7.1	State estimation results	151
7.1.1	State estimation results for simulated data	152
7.1.2	State estimation results for simulated data with noise	154
7.1.3	State estimation results for experimental data	156

7.2	Parameter estimation results	159
7.2.1	Case 1: Three unknown parameters B , μ and ρ for different types of data	159
7.2.2	Case 2: Seven unknown parameters B , μ , ρ , k_u , k_d , k_{3p} and k_{4p} for different types of data	161
7.2.3	Case 3: Eight unknown parameters B , μ , ρ , k_u , k_d , k_{4p} , k_{1s} and k_{5s} for different types of data	163
8	Conclusions	166
	Bibliography	169
	Appendix A Bond graphs	180
A.1	Multiports	180
A.2	Ports and bonds	182
A.3	Causal stroke	184
A.4	Bond graph elements	185
A.4.1	Energy storage elements	185
A.4.2	Dissipative element	186
A.4.3	Source elements	186
A.4.4	Reversible transducer elements	186
A.4.5	Junction elements	188
	Appendix B Experimental setup	189
B.1	Fluid characterization	189
	Appendix C ESP system parameter estimation	191
C.1	ESP pump parameters	191
C.2	ESP shaft parameters	192
C.3	Upstream pipeline parameters	194
C.3.1	ESP system with P100L	194
C.3.2	ESP system with P47	196
C.4	Downstream pipeline parameters	199
C.4.1	ESP system with P100L	200
C.4.2	ESP System with P47	201
	Appendix D Additional PINN results	205
D.1	State estimation results	205
D.2	Estimated unknown parameters mean and standard deviation	209
	Appendix E Physics loss function for the PINN model for the ESP system detail	212
	Appendix F PINN training settings	214

1 Introduction

1.1 Dynamic systems

The term *dynamic* characterizes phenomena that undergo temporal evolution, where their attributes change over time. Thus, the term *dynamic* can be considered almost a synonym of *temporal evolution*, where the unfolding of a chain of events results in an ongoing evolutionary process [1, 2]. Many phenomena that we observe and study in daily life possess such dynamic traits. Conversely, a *system* is defined as an assembly of interrelated components that collectively form a cohesive whole. When combined, the notion of a *dynamic system* emerges, signifying that the state of such a system at any given time is influenced by its prior state. In essence, the study of *system dynamics* delves into understanding these temporal evolutions and the mathematical equations that describe them [3].

The exploration of dynamic systems is driven by two primary goals: prediction of system behavior and control. Climate forecasting, for instance, exemplifies the attempt to predict the dynamic system behavior of a vast dynamic system, while the thermostatic control of boilers for heating illustrates the control aspect [3]. The modeling approach depends on the intended purpose of the model. When emphasizing behavior prediction, it is prudent to utilize extensive relevant information. Conversely, model simplicity becomes paramount when the focus shifts to system control. This simplicity, driven by practical constraints like sensor availability, recognizes that an abundance of information does not always translate into enhanced control precision [3].

To achieve the goals mentioned above of prediction and control, it is necessary to develop a mathematical model that captures the system's behavior [3]. Most often, these models are represented by differential equations. As highlighted by Luenberger [1], the study of *dynamics* is deeply intertwined with the theory of differential equations. Through these equations, temporal relationships among various system variables can be established. While some systems can be described using linear differential equations, it is essential to acknowledge, as pointed out by Marinca and Herisanu [2], that the majority of natural phenomena inherently exhibit non-linear dynamics.

1.2 Bond-graphs

As highlighted by Damic and Montgomery [4], real engineering systems are inherently complex. Constructing a valid mathematical model that is simultaneously accurate and computationally feasible presents significant challenges. Recent advances in computing have enhanced the tractability of such problems, rendering the numerical solution of previously infeasible

problems now attainable. Given the multifaceted nature of engineering systems, which often span mechanical, electrical, hydraulic, and thermal domains, it becomes evident that domain-independent modeling techniques are invaluable. Such techniques, not only accommodate the diverse nature of these systems but also facilitate a seamless integration between the various domains.

In this context, the *bond-graphs* stand out as a notable tool for multidomain system modeling. Central to their approach is the principle of energy exchange among the system's constituent parts. This methodology allows for effects like friction and stiffness to be incorporated without necessitating a complete overhaul of the model [5]. The bond-graphs main characteristic is their modularity; modeling begins with basic elements and, step-by-step, evolves into a sophisticated mathematical representation suitable for computational analysis.

The foundational development of *bond-graphs* can be attributed to Paynter [6]. Subsequent refinements in their graphical representation and modeling methodologies were expanded by others, as highlighted by Borutzky [7]. The essence of this approach is the flow of energy between the ports of system components. These ports serve as conduits, ensuring the transmission of energy from one component to another, its storage within a component, or its transformation, all in accordance with established physical laws [8].

In the preliminary stages of bond-graph modeling, the focus is on a qualitative assessment of the physical effects and interactions within the system. As the process unfolds, these qualitative observations are incrementally supplemented with detailed specifics, yielding a refined mathematical model. A noteworthy aspect, as mentioned by Borutzky [7], is that a correctly implemented bond-graph model is inherently consistent with the first law of thermodynamics. This agreement eliminates the need for additional adjustments, presenting a unified modeling methodology applicable across diverse physical domains [8].

1.3 Modeling and inverse problem

The task of generating a mathematical representation of a physical system inherently involves some abstraction. Any model is a simplification of reality capturing mainly crucial features. It is a challenging endeavour to encapsulate the whole complexity of a given system [3]. When modeling, the main challenge is to balance the model's complexity and its accuracy. As the model's complexity increases, often by incorporating additional physics, parameters, or structural elements, it may offer improved accuracy but at the cost of increased computational burden and the need for more information about the system. Information which may be unknown or difficult to obtain in real conditions. Conversely, simpler and more parsimonious models may suffer from accuracy loss due to idealizations or inaccurate parameter estimation.

In the mathematical modeling process of a physical system, the problems can be categorized into direct and inverse types. The direct problem involves constructing a model that takes known causes as inputs and predicts the resultant effects. However, real-world applications

often necessitate the reverse: determining the underlying causes or system properties based on observed effects. Such problems are termed inverse problems [9, 10]. Unlike direct problems, where solutions' existence, uniqueness, and stability are often assumed, inverse problems are less forgiving. These key attributes may be absent, introducing considerable challenges in finding viable solutions [10].

The challenges inherent to inverse problems extend beyond the identification of mathematically consistent solutions [11]. Once it may exist, several parameters may satisfactorily fit the available data. Hence, it is crucial to assess the physical plausibility of these solutions. They must not only fit the data well but also align with other known constraints and exhibit predictive capability. In cases where multiple models fit the available data, additional information or constraints must be introduced to restrict the search space to a unique, physically meaningful solution. Among all challenges, stability, or the lack of it, is the most critical. Without stability, any attempt to solve the problem becomes unproductive, as minor errors in measurement or computation can lead to remarkably inaccurate solutions [12].

Inverse problems find applications in various disciplines, from biomedical imaging and geophysical exploration to groundwater flow dynamics [13]. The shared objective among various applications is to accurately estimate attributes that may not be directly observed or are unobserved. While parameter estimation is a typical goal, inverse problems also offer a pathway to discover missing physics by identifying functions or relations that complete the direct model. However, these problems are often ill-posed where slight inaccuracies in measurement data can drastically change the missing physics model.

1.4 Multi-phase flows

According to Falcone [14], a general definition of multiphase flow encompasses the simultaneous flow of a stream composed of two or more phases in a specific system. This multiphase flow scenario is ubiquitous, ranging from biological systems like blood flow in the human body to industrial applications involving oil-water-gas-sand mixtures in offshore pipelines [14, 15]. A more straightforward category within multiphase flow is two-phase flow, which occurs when a single pure substance is present in two different phases, such as steam-water, or when different chemical substances co-exist, such as oil-water flow [14].

While the hydrodynamics of single-phase flow are well understood, Shoham [16] highlight that the addition of even one more phase drastically increases the complexity, resulting in challenges otherwise non-existent in single-phase systems. One of the notable aspects is the drastic increase in the number of variables required for its characterization when compared to single-phase flows. The increase in complexity is even more noteworthy for liquid-gas flows, where the effect of gas compressibility is significant. Shoham [16] mentions that the exact solution for two-phase flow is often impractical or exceedingly challenging.

A distinctive attribute of two-phase flows, setting them apart from their single-phase counter-

parts, is the emergence of *flow patterns* or *flow regimes* [16]. These patterns emerge due to the interaction between the phases and are a result of competing forces or mechanisms occurring simultaneously within the flow [14]. As a result, the phases can rearrange in distinct ways that can result in flows with considerably different characteristics, such as phase velocity and phase percentage in a specific region. Importantly, identifying these flow patterns is critical, as the process variables and literature models heavily rely on them [16].

In engineering applications, two-phase flow phenomena are indispensable across several sectors. These range from petroleum, chemical, and nuclear industries to space and geothermal applications [15]. In the context of the petroleum industry, for instance, understanding two-phase flows is paramount during the conveyance of oil and gas across pipelines with varied orientations.

1.5 Emulsions

Two-phase flows involving immiscible liquid can provide the conditions necessary for formation of emulsions. According to the IUPAC definition, an emulsion is characterized as a dispersion when droplets of one liquid are dispersed in another immiscible liquid [17]. There are primarily three types of dispersions pertinent to this context: gas foams in liquids, solid suspensions in liquids, and emulsions formed by one liquid dispersed in another in the form of droplets [18]. According to Perazzo *et al.* [19], the emulsions are typically formed by an organic phase and an aqueous phase, for example, oil and water mixtures. In certain scenarios, the phases are continually interpenetrated one in the other, being impossible to distinguish between the dispersed phase and the continuous phase.

Emulsions, in their native state, are thermodynamically unstable and tend to phase separation in pursuit of thermodynamic equilibrium. However, due to the characteristics of the constituting fluids, emulsions can often exist in a metastable state. The relative thermodynamic stability of emulsions presents challenges in numerous industries, especially when phase separation is desired [19]. Several processes lead to the separation of phases, such as sedimentation, due to specific mass differences and flocculation, when droplets tend to aggregate. Nevertheless, there exists a category of emulsions called microemulsions. They are characterized by oil droplets with nanometric diameters, and they are considered to be thermodynamically stable [19, 20].

1.6 Electrical submersible pumps

Multistage centrifugal pumps, play a vital role in diverse industrial applications such as oil and gas extraction, water supply, chemical processes, power generation, and pulp transportation. Introduced to the oil and gas sector in 1927, Electrical Submersible Pumps (ESP) have become the second most widely utilized form of artificial lifting equipment [21]. Comprising a multistage centrifugal pump driven by a submerged electric motor, ESP are commonly employed in high-pressure boosting applications where significant flow rates are required [22, 23, 24].

Typically installed at the end of the production column within an oil well, the ESP is powered by an electric motor connected to an external power source through an electric cable [25, 26, 27, 28]. To enhance performance, some ESP configurations incorporate a gas separator for the extraction of minor gas fractions present in the fluid flow. Further, to ensure operational integrity, ESP are designed with components that insulate the motor from the reservoir fluids [25, 26, 27, 28].

Within the petroleum industry, ESP often encounter two-phase liquid-liquid flows, commonly consisting of oil and water mixtures [29, 30]. These flows frequently give rise to colloidal dispersions such as emulsions due to the inherent chemical characteristics of the liquids involved. Emulsions are particularly noteworthy because they manifest non-Newtonian behavior, which could cause instabilities in ESP operations [31].

1.7 Objectives

The overall objective of this research is to develop a bond graph-based model for electrical submersible pump systems, conduct an identifiability analysis of the resulting model, and propose a methodology for parameter estimation using a limited set of known measurements. The validation of the model and estimation technique will be carried out in experimental multiphase flow scenarios.

To realize the aforementioned research aim, the following specific objectives are outlined:

1. To formulate a bond graph-based model encapsulating the pumps' mechanical and hydraulic domains.
2. To deduce the fundamental bond graph elements constituting the system from fundamental model equations and ESP literature.
3. To validate the model against experimental data and existing literature, focusing on varying multiphase flow conditions.
4. To carry out identifiability analysis on the established model for assessing structural, practical identifiability, and parameter sensitivity.
5. To employ Physical-Informed Neural Networks (PINN) as an inverse problem-solving technique for estimating unknown parameters and unmeasured states.

This work aims to develop a lumped system model for electrical submersible pumps (ESPs), particularly for applications in the oil and gas industry. The model balances computational efficiency with the complexity needed for practical industrial applications. By employing a bond graph approach, the model simplifies the dynamics of fluid behavior in emulsions and multiphase flows, which are critical for understanding the interactions within ESP systems. Although the model abstracts detailed phase separation and droplet interactions to improve computational

tractability, it retains the essential dynamics relevant for monitoring, fault diagnosis, and control applications.

The model's fidelity to fluid dynamics is balanced with computational feasibility, validated against experimental data to ensure reliability for practical applications. Acknowledging the model's simplified nature, it is designed to capture crucial operational dynamics while recognizing its limitations in representing complex multiphase flow phenomena under untested conditions.

Furthermore, the modular nature of bond graph modeling facilitates the model's expansion to accommodate more complex systems, such as those involving multiple pumps or valves. This adaptability ensures the model's relevance and scalability for practical applications, allowing for the integration of well-validated subsystems into larger system models.

Thus, this work employs a combination of analytical, numerical, and machine learning techniques to develop a comprehensive framework for ESP systems. Initially, the bond graph method is utilized to develop a foundational model that captures the main dynamics of the ESP system. Subsequently, Physics-Informed Neural Networks (PINNs), which leverage the physics delineated by the bond graph model, are employed for state and parameter estimation. By incorporating real-time measurements, PINNs facilitate relatively accurate monitoring and adaptive adjustments in response to operational changes, such as water fraction variation and wax deposition. This integration enables effective control and predictive capabilities, ensuring the model's accuracy and relevance under the evolving conditions of oil field operations.

1.8 Research contributions

This section presents the research contributions in the mechanical engineering domain, specifically focusing on the modeling, analysis, and simulation of electrical submersible pumps (ESP). Existing literature predominantly focuses on ESP under steady-state conditions, thus limiting the scope for dynamic operational understanding. Further challenges arise in applications such as oil exploration due to changes in fluid properties attributable to the well conditions and temporal variations in pipeline characteristics attributable to phenomena like wax deposition. Such variations require inverse problem-solving methodologies to enhance the reliability and applicability of existing and developed models in this work.

Considering these aspects, the present research employed a multifaceted approach, leveraging a variety of methodologies and tools to address distinct aspects of the ESP problem. The contributions are detailed below.

Contribution 1 **Development of a bond graph model for electrical submersible pumps:**

This study advances the field by introducing a bond graph model that comprehends ESP systems' hydraulic and mechanical subsystems. Different from existing bond graph models for centrifugal pumps, the proposed model incorporates the dynamic behavior of upstream

and downstream pipelines, which was crucial to the considered experimental setup. The bond graph elements of the pump model are derived from established literature, thereby ensuring direct comparison with existing models. Thus, further advances in this area can be seamlessly integrated into the model. Moreover, the model includes a formulation for capturing pipeline transients with bond graphs derived from the continuity equation. For the emulsion non-Newtonian behavior, the model uses literature effective viscosity model.

Contribution 2 Identifiability analysis of electrical submersible pump parameters:

The study provides an identifiability analysis of the model of the ESP system, encompassing both local structural and practical identifiability. This analytical approach enables effective parameter estimation and addresses a lacuna in the existing ESP literature. Consequently, the analysis provides a foundational basis for developing more robust parameter estimation techniques in future investigations by delineating the parameters that can be estimated reliably.

Contribution 3 Application of physics-informed neural networks for state and parameter estimation in electrical submersible pumps:

This work also employs Physics-Informed Neural Networks (PINN) for addressing the inverse problems of parameter and state identification in ESP models. The PINN implementation is designed to estimate key properties of the system from a restricted set of available information, such as intake and discharge pressures. Notably, the method is capable of obtaining reasonable accuracy even in noisy and experimental measurements. Moreover, it does not require computing the numerical derivatives, offering an advantage over traditional methods, like direct non-linear least squares, where accurate derivative estimation is often challenging due to noise.

Contribution 4 Development of a software library in Julia for bond graph models:

Furthermore, the study introduces a software library, developed in the Julia programming language, for the automated generation of bond graph equations and the derivation of corresponding model governing equations. This software library is a significant contribution as it streamlines the modeling process and introduces greater flexibility in dealing with bond graph elements and equation manipulation. While devised in the context of mechanical engineering, the applicability of this software library extends to other disciplines, thereby broadening the impact of this contribution.

2 Literature review

2.1 Two-phase flows

According to Angeli and Hewitt [30], liquid-liquid flow is present in several industrial processes, particularly in the oil industry, where oil and water are produced and transported together in long pipelines. The knowledge of the flow pattern in these processes is crucial in these industries since the optimization of production, artificial lifting system design, and system modelling are directly related to the flow pattern [32, 33].

The first studies on horizontal two-phase liquid-liquid flow were made by Russell *et al.* [34]. The authors observed, by images and varying the water and oil ratio, three patterns of distinct flows called bubbles, stratified, and mixture. Russell *et al.* [34] also showed the pressure loss as a function of the water's superficial velocity. Then, Charles *et al.* [35] observed the same flow patterns with the addition of the intermittent and concentric flow patterns. The authors found that the flow pattern is independent of the oil viscosity.

Subsequently, Hasson *et al.* [36] observed flow patterns similar to that observed by Charles *et al.* [35], but they classified the pattern called concentric by Charles *et al.* [35] as annular. Thus, after Hasson *et al.* [36], several other authors have proposed several distinct flow patterns for liquid-liquid flows until Bannwart *et al.* [37] proposed simplifying the number of flow patterns for both vertical and horizontal flows. According to the Bannwart *et al.* [37] classification, the horizontal flows were restricted to stratified, bubbles, dispersed bubbles, and annular. The flow patterns for vertical flows were defined as bubbles, dispersed bubbles, intermittent, and annular.

Abood *et al.* [38] mention that the flow patterns are heavily dependent on the specific mass of the fluids. In addition to the specific mass, the surface tension, the pipe geometry, and the pipe roughness are relevant [39, 40]. Angeli and Hewitt [30] mention that another critical factor in the flow pattern is tube wettability and how the phases are inserted in the pipe.

The main interest in studying liquid oil-water flows is mainly due to the low-pressure losses and the energetic advantage of the annular flow pattern [41, 39, 37]. In this case, according to Cavicchio *et al.* [42], the pressure loss of the annular flow is considerably smaller than the single-phase oil flow. According to Rodriguez and Bannwart [43], Charles *et al.* [35] was the first to observe a significant drop in the pressure loss in the annular and intermittent flow patterns. In Charles *et al.* [35] work, such a decrease in the pressure loss was more significant with the oil viscosity increase.

Thus, the development of the *Core-Annular Flow* (CAF) technique is made to maintain the oil flow in the center of the pipe and the water flow on the periphery of the pipe by adding small amounts of water to the flow [37, 41]. In this way, the water serves as a continuous lubricant layer

along the pipe, which reduces the pressure loss [43]. Such a technique is particularly attractive in transporting lubricants and for the oil industry, which often face highly viscous oil [37].

2.2 Emulsion

In oil production, emulsions are present in the various stages of transport and production. One of the properties that the formation of emulsion influences significantly and has been studied is the viscosity [20]. In the petroleum industry, crude oil's viscosity directly influences transportation and processing. In addition, the formation of emulsion is often inevitable since it is often produced water with oil or the water is injected into the reservoirs to increase production, or the water is used to reduce energy in production, *core-annular flow*. Goodarzi and Zendehboudi [20] comments that emulsion formation in the oil industry is a problem that generates unexpected thermodynamic and rheological behaviors in the fluids produced. Moreover, water emulsions and crude oil are also considered a problem in the oil industry by causing inefficient separation of phases, operational problems, and corrosion [20].

Jahanzad *et al.* [18] mention that despite the properties of the liquids that form the emulsion can be established accurately, the final properties of the emulsion are not easily predictable and depend heavily on the emulsification process used. Another emulsion feature is phase inversion, obtained when there is an exchange between the dispersed and continuous phases. Such a process is often desired in the industry because it is possible to obtain a more stable emulsion [44, 19]. Jahanzad *et al.* [18] and Perazzo *et al.* [19] mention that the process of phase inversion phases is fast, and in this process, the emulsion properties also vary at the same rate. In this sense, the phase inversion process has been described as catastrophic or transitional.

Emulsions tend to separate the liquid phases due to oil-water or water-oil immiscibility. The separation time may vary from a scale of minutes or hours and can extend to days, months, and even years according to the stability of the emulsion. The droplet size distribution, chemical properties of the liquid phases, and the presence of surfactants determine the stability and type of emulsion (water-in-oil or oil-in-water) [45]. Furthermore, there is the transition from one emulsion type to another, commonly called phase inversion [46, 19, 47]. Emulsion in the ESP system may be caused by turbulence and shear stress caused by the ESP, pipe system, and valve Bulgarelli *et al.* [48].

The study by Pal [49] observed the impact of droplet size on the rheological characteristics of water-in-oil (W/O) and oil-in-water (O/W) emulsions. The author found that fine emulsions exhibit significantly higher viscosities than coarse emulsions. Moreover, fine emulsions demonstrate a shear-thinning effect on non-Newtonian behavior. Later [50] introduced a model to correlate the effective viscosity of emulsions. The model considers factors such as shear rate, droplet size and distribution, and the viscosity of the continuous and dispersed phases. The author correlation was validated using experimental data from mineral oil-in-water and kerosene-in-water emulsions. Pal [50] correlation establishes that the relative viscosity of the

emulsion is functionally dependent on the Reynolds number, the volume fraction of the dispersed phase, the maximum packing concentration of the dispersed phase, and the continuous phase viscosity.

Derkach [51] provides a comprehensive review of the rheological properties of emulsions, varying from dilute to highly concentrated systems. For dilute emulsions, Derkach [51] presents parallels and contrasts with the properties of suspensions. The author examined various rheological behaviors in concentrated emulsions, such as non-Newtonian flow curves. It also presented different effective viscosities models. The review also elaborates on the shear stability of droplets and the crucial role of surfactants in the stability of emulsions over time.

Plasencia *et al.* [52] conducted a comparative study on the pipe flow of water-in-crude-oil emulsions with six different types of crude oil. The authors observed that the point of phase inversion varies and is fluid-dependent and that the effective viscosity was relatively insensitive to mixture velocities but was highly sensitive to water cut, significantly beyond 30%. Higher shear rates led to the formation of smaller droplets, while larger droplets appeared as the amount of dispersed water approached the inversion point.

Perazzo *et al.* [19] provides a comprehensive review of the phenomenon of phase inversion in emulsions, detailing two primary methods: phase inversion composition (PIC) and phase inversion temperature (PIT). The review illuminates how phase inversion is not an equilibrium process, significantly influenced by factors such as the addition rate of one phase into another and the dynamics of droplet breakup and coalescence. Mechanisms underlying phase inversion are primarily attributed to changes in interfacial curvature, influenced by temperature or compositional changes affecting surfactant affinity. The review highlights the challenges in quantitative modeling of phase inversion, particularly at high addition rates, where the system deviates significantly from equilibrium.

The Ariffin *et al.* [53] work conducted an investigation into the rheological behavior of light crude oil emulsions, mainly focusing on their viscosity characteristics. They observed that these emulsions exhibited non-Newtonian shear-thinning behavior at low shear rates, transitioning to approximately Newtonian behavior at high shear rates for the light crude oil emulsions. Additionally, in accordance with the literature, they observed the phase inversion phenomena and the effective viscosity dependence on the water fraction.

Liu *et al.* [54] conducted systemic experiments focusing on the effect of droplet sizes on the rheological properties of W/O emulsions. Their results reveal that the emulsions transition from Newtonian to non-Newtonian flow behavior with increasing shear rates. In the Newtonian regime, smaller droplets corresponded to higher viscosities, particularly at high dispersed phase volume fractions. In agreement with other studies, they observed a shear-thinning behavior in the non-Newtonian regime, which was well-described by the power law model. The authors concluded that shear-thinning mainly arises from a reduction in cluster sizes and that more compact and smaller clusters are formed at higher dispersed phase volume fractions.

Goodarzi and Zendehboudi [20] provides an exhaustive review of the formation and stability

of W/O emulsions, particularly their behavior in physical systems like pipeline networks and porous media. It emphasizes the inadequacy of current models to comprehensively link emulsion stability to crucial parameters such as temperature, water-to-oil ratio, and salinity. Advanced computational methods like Molecular Dynamics (MD) and Computational Fluid Dynamics (CFD) are recommended for understanding thermodynamic properties and transport phenomena behaviors in porous media despite the computational overhead involved. Goodarzi and Zendejboudi [20] recommends adopting comprehensive modeling strategies and experimental works at both macro and micro-scales to better understand emulsion behaviors.

Vita *et al.* [55] employed numerical simulations to investigate the rheological properties of emulsions under shear flow in dilute and moderate concentration regimes. They utilized Navier-Stokes equations with the Volume of Fluid (VoF) technique for tracking the fluid interface, allowing the study of droplet coalescence. They developed an Eulerian collision model to isolate coalescence's effects on emulsions' rheological behavior. Thus, the authors observed that the coalescence led to an effective viscosity reduction attributed to reduced interfacial tension stress. On the other hand, when inhibiting coalescence, the authors observed that the emulsions behave more like suspensions of deformable particles.

Additionally, Vita *et al.* [55] observed the presence of large droplets migrating toward the channel center when coalescence is allowed, as well as a variable droplet size dependent on volume fraction and viscosity ratio. The study suggests that realistic emulsion behaviors likely lie between the two extremes of complete coalescence and no coalescence.

Yi *et al.* [56] investigated the dynamics of oil droplets dispersed in an ethanol-water solution in turbulent shear flow without surfactants. They find that droplet sizes' probability density function (PDF) adheres to a log-normal distribution, indicating a fragmentation-driven droplet generation process. By employing the Hinze theory for comparison, the study identified a scaling dependence of droplet size on Reynolds number.

Yi *et al.* [56] observed that the effective viscosity increased with the oil volume fraction but at a less pronounced rate than solid particle suspensions. The authors attributed this behavior to the inherent characteristics of the dispersed phase, such as deformability and size distribution. They observed that the emulsion exhibits a shear-thinning behavior as the shear rate increases, which can be quantitatively modeled using the classical Herschel-Bulkley equation, with a dependency on the volume fraction for the flow index.

More recently, Yi *et al.* [57] has focused on understanding the hydrodynamics of emulsions in turbulent shear flow across varying oil volume fractions. The authors found that the average droplet size in O/W and W/O emulsions is relatively insensitive to the oil volume fraction. The authors concluded that droplet fragmentation is governed by dynamic pressure within the boundary layer rather than energy dissipation rates, as indicated by the Weber number.

Yi *et al.* [57] observed that the effective viscosity follows an increasing trend as the dispersed phase volume fraction increases, with O/W emulsions showing higher effective viscosities than W/O under similar Reynolds numbers. However, this asymmetry in the effective viscosity, and

also observed in droplet size, was attributed to the presence of surface-active contaminants, primarily originating from the wall of the containment. By introducing an oil-soluble surfactant, the authors were able to recover the symmetry in both droplet size and effective viscosity for O/W and W/O emulsions.

2.3 Electrical submersible pumps

Dutra Leite Do Amaral [58] developed a model for evaluating the performance of ESP and conventional centrifugal pumps in handling oils with medium to high viscosities. The author used experimental data, collected from tests involving fluids with wide variety of viscosities, to refine and validate the proposed model. The proposed model were benchmarked against the experimental data and existing literature.

Vieira *et al.* [59] work serves as a comprehensive parametric study, contrasting various correlations from existing literature against experimental data to address hydraulic losses in ESP, specifically in the context of viscous fluid flow. The study distinguishes itself by its meticulous analysis aimed at identifying the most accurate closure relationships for different hydraulic losses, including impeller friction, disk friction, and diffuser losses.

Vieira *et al.* [59] provided an invaluable review of the available models and correlations and compared which combination is the most appropriate for accurately modeling the hydraulic losses in ESP. The authors quantified the predictive accuracy of diverse theoretical models and combinations using Root Mean Square Error (RMSE) values, which revealed that the most precise correlations vary depending on the specific conditions under study. However, the study also uncovers limitations in the existing parameterizations. While some models excel in case-specific settings, they may lack general applicability across different operational conditions. This is especially true when accounting for fluid viscosity and rotational speed effects, indicating that further research is warranted to extend the model's adaptability.

Paternost *et al.* [60] proposes a correlation to estimate the pressure gain of ESP operating under viscous and gas-liquid two-phase flows. The correlation is based on Euler's equation and theoretical losses inside the pump and was validated experimentally. The correlation allows the prediction of pump performance across a wide range of viscosities and rotational speeds. The authors observed that large bubbles at the pump intake, resulting from coalescence, negatively impact pump performance, leading to surging conditions. The paper also identifies that higher liquid viscosities exacerbate this problem due to low turbulence and fewer bubble breakups.

Biazussi [61] developed and experimentally evaluated a drift flux model for the ESP operating under gas-liquid two-phase flows. The experimental tests were performed on three different ESP configurations to determine characteristic curves under variable flow rates, inlet pressures, and rotational speeds. In the single-phase water flow tests, the author used the correlation model based on Paternost *et al.* [60] to describe the ESP head. In the case of two-phase (water-air) flows, the developed model, when fitted with experimental data, demonstrated high accuracy in

capturing the main trends of the ESP behavior. The authors observed that the centripetal and Coriolis fields affect the velocity and phase distribution. Furthermore, the drift parameter in the model was notably significant only for pumps with the smallest capacity, suggesting that gas bubble drift becomes negligible at high liquid flow rates.

Ofuchi *et al.* [62] employed dimensional analysis and CFD simulations to study head and flow rate degradation in ESP when dealing with highly viscous fluids. The dimensional analysis revealed that while normalized rotational Reynolds numbers could generalize viscosity effects for a given ESP, they were insufficient for correlating data across different pumps. However, a trend was observed where head degradation occurred along curves of constant normalized specific speeds, regardless of the pump geometry. Moreover, the author presented a model based on Stepanoff [63] to correlate head and flow rate correction factors. It agreed well with the numerical results for ESP and the experimental data for radial-type pumps.

Morrison *et al.* [64] investigated the flow behavior in a mixed-flow type pump with varying fluid viscosities using CFD. The primary aim was to modify the conventional pump affinity laws to incorporate the effects of viscosity. By simulating various fluids under different operating conditions, the authors assessed how fluid viscosity influences the impeller and diffuser's performance. Dimensionless parameters like flow coefficient, head coefficient, and rotational Reynolds number were utilized to characterize the changes in pump performance with respect to fluid viscosity.

The study validated its CFD-derived modified affinity laws with empirical data from various pump designs with different specific speeds and fluid viscosities. The modified laws produced a common performance curve irrespective of operating conditions and viscosities for each specific pump design. The results also indicated that the pump's performance is more adversely affected by high-viscosity fluids at higher flow rates. Furthermore, the study demonstrated that maximum efficiency is lowered, and the flow rate at the best efficiency point decreases as the fluid viscosity increases.

Patil and Morrison [65] aimed to provide a simplified methodology for predicting centrifugal pump performance changes due to variations in fluid viscosity. The authors introduced an approach that blends the Modified Affinity Law for viscosity with friction loss modeling. The head coefficient, flow coefficient, and rotational Reynolds number were found to be key parameters for characterizing pump performance across different fluid viscosities. A dimensionless parameter termed the Morrison number, was proposed as a function of the rotational Reynolds number to delineate the impact of operational conditions like fluid viscosities and rotational speeds.

Zhu *et al.* [66] proposed a mechanistic model to estimate the pressure gain in ESP operating under viscous-fluid flow conditions. The proposed model is based on Euler equations for centrifugal pumps and introduces the concept of a best-match flow rate, which occurs when the flow direction of the impeller outlet matches the intended flow direction. The mismatch of velocity triangles, resulting from velocities different from the best efficient point, is to determine recirculation losses. The proposed model also considers additional head losses due to flow-

direction change, friction, and leakage. The authors argue that once the best-match flow rate is determined, the hydraulic head under conditions of viscous fluid flow can be reliably calculated. They validated the model with a large dataset and argued that the model could be calibrated against catalog curves provided by manufacturers.

More recently Ofuchi *et al.* [67] proposed a novel, geometry-independent model to estimate head and flow rate degradation across a broad spectrum of Reynolds numbers, incorporating high fluid viscosities and low rotating speeds, differently from the other methods for adjusting the performance of centrifugal pumps with viscous fluids which are either pump-specific or rely on hard-to-obtain geometric parameters. The authors' proposed model utilizes readily available design parameters and the water baseline curve for its calculations. They validated the model with experimental data from two mixed-flow and one radial type of ESP. However, further validation with a more diverse set of pumps and extensions is still required to accommodate gas-liquid flow effects.

Zhu *et al.* [68] proposed a model based on the Brinkman [69] to estimate the effective viscosity of emulsion inside the ESP. Their experiments showed that the model yields results within an error band of 10 % error for oil-water emulsions when predicting the ESP pressure gain.

Bulgarelli *et al.* [48] proposes model to predict the relative viscosity of stable emulsions in ESP. The model takes into account the properties of the continuous phase and operational parameters of the ESP. The authors also carried out experiments to understand ESP performance under the emulsions condition. The experimental results showed the impact of surfactants on effective viscosity, the influence of demulsifiers on relative viscosity, and a correlation between ESP rotational speed and relative viscosity.

Bulgarelli *et al.* [47] focuses on the characterization of rheological behavior of stable and unstable W/O emulsions in the context of ESP. The authors introduce a criterion based on the slip ratio between the dispersed and continuous phases to understand the flow behavior of emulsions in centrifugal pumps. The study identified a linear relationship between the Sauter mean diameter and maximum droplet diameter, which may be directly associated with the ESP's geometrical properties and the number of stages. The study also noted that stable emulsions exhibited a slip ratio of one in the impeller, indicating a homogeneous flow. Conversely, unstable w/o emulsions exhibited drag reduction, likely due to slip between phases. The authors further introduce a dimensionless parameter termed the Slip Relevance number to differentiate between stable and unstable emulsion behaviors.

2.4 Centrifugal pump transient

The Dazin *et al.* [70] study presents a model based on angular momentum and energy equations to predict various internal parameters, including torque, power, and impeller head, for turbomachinery under transient conditions. The model is validated by comparing its predictions

with experimental data from a single-stage, single-volute radial flow pump during fast startup periods. The model exhibited good agreement with experimental results. The authors identified two distinct phases in the startup phase: an initial stage where the transient pressure significantly exceeds the steady-state value due to substantial angular acceleration and a subsequent phase dominated by flow acceleration where the pressure drops below the steady-state value. Furthermore, the authors observed that the behavior of a pump impeller depends not only on the acceleration and flow rates but also on the velocity profiles and their evolution. Dazin *et al.* [70] suggest that future refinements to the model would include a more detailed evaluation of flow losses, velocity profiles, and equivalent pipe lengths.

Chalghoum *et al.* [71] conducted a theoretical and numerical analysis to investigate the transient flow characteristics inside a centrifugal pump during its starting period. The authors considered a one-dimensional equation flow approximation. The authors considered that the system is governed by a set of partial differential equations (PDE), taking into account the motion and continuity. This set of PDE was solved numerically using the method of characteristics (MoC). The pump impeller was modeled as a series of straight conduits connected in parallel. The study performed numerical simulations under varying discharge valve openings and compared the outcomes with existing experimental data, revealing a satisfactory match.

Chalghoum *et al.* [71] observed that the pressure increase within the pump is notably significant in scenarios involving short startup periods and large pipeline water mass. The study also explored the impact of impeller geometric properties such as diameter and number of blades on pressure evolution. It was observed that the valve opening percentages and the starting time significantly affect the pressure evolution during the startup period but have no substantial influence on the steady-state pump characteristic curve. On the other hand, the impeller's radius and blade height were found not to affect the transient characteristic of the system.

Zhang *et al.* [72] employed CFD using a three-dimensional model of a single-stage centrifugal pump with a dynamic mesh method. The study aimed to simulate the pump's unsteady, three-dimensional, incompressible viscous flow during its startup phase. The authors found that rotor-stator interactions introduce minor fluctuations in the flow rate, even under stable operating conditions. Importantly, they highlighted that the quasi-steady assumption is inadequate for fully capturing the transient behavior, especially during the initial stages of startup.

The study by Kullick and Hackl [73] introduced a detailed state-space model for ESP in the context of deep geothermal energy systems. This model is comprehensive, encompassing electrical, mechanical, and hydraulic subsystems. However, it considers the pipeline dynamics with the dynamic Bernoulli equation, which neglects the pressure transients. The authors considered a simulation scenario where a Megawatt ESP system situated 950 m below the surface, which handles geothermal fluid at a temperature of 140 °C and a flow rate of $0.145 \text{ m}^3 \text{ s}^{-1}$. Notably, the simulations captured electrical frequency changes from 0 Hz to 60 Hz and voltage amplitude adjustments from 0 V to 5750 V during the system's startup phase. Moreover, the study investigated the role of motor self-excitation and its effects on system dynamics. While the mechanical

two-mass system showed low-pass characteristics, cable effects were minimal at studied frequencies. The work's primary contributions include identifying key system components, abstraction and rigorous simplification of governing physics, and a comprehensive and detailed state-space modeling framework. However, the paper also notes that it lacks experimental validation.

Tanaka and Takatsu [74] performed both experimental and CFD analyses to study the transient behaviors of centrifugal pumps during rapid startup. The authors measured instantaneous pressure and flow rate at the pump's suction and discharge ports while capturing the rotational speed. The transient behaviors during the startup were found to deviate considerably from quasi-steady changes, particularly at the early stages, similar to the observations of Zhang *et al.* [72]. The authors attributed the deviation to the inability of the flow field to fully develop at high flow rate changes, as compared to quasi-steady changes.

Li *et al.* [75] also utilized CFD but leveraged the Detached Eddy Simulation (DES) model to investigate fast pump startups. Their simulations were validated against experimental data and focused on identifying the most suitable startup time. The results revealed that optimal performance is attainable when the startup time is equal to the difference between the time constants of the pump and the downstream valve.

Similarly to the work of Chalghoum *et al.* [71], Omri *et al.* [76] analyzed rapid startup conditions in pumps by solving a set of PDE accounting for continuity and motion. These equations were solved using the MoC, and the results were experimentally validated. The study found that faster startups were associated with increased torque oscillations and more significant head impact. A positive correlation was also observed between transient head fluctuation and the final pump flow rate.

2.5 Bond graphs

Given the possibility of easily using the *bond-graphs* in systems that have various physical domains, this technique has been widely used in mechatronics, where several books such as Damic and Montgomery [4], Merzouki *et al.* [5] and Das [77] used the bond-graphs to model systems that depend on the electrical, hydraulic and mechanical domains. In addition, it is of particular interest in this discipline because it enables easy modelling of sensors, valves, and other components.

In addition to the mechatronics, the *bond-graphs* has been used for the modelling of biomolecular systems such as in Gawthrop and Crampin [78], also in the organs modelling as in Moin *et al.* [79] and in cardiovascular system modelling as in Le Rolle *et al.* [80]. In engineering, the *bond-graphs* have been used to develop more robust diagnostic techniques as in Abdallah *et al.* [81], Touati *et al.* [82] and Benmoussa *et al.* [83].

In fluid dynamic systems, there is some development, such as in the Karnopp [84], which is one of the first works in this area, where incompressible and compressible unidimensional flow are modelled considering the flow inertial effects. In addition, Baliño *et al.* [85] used the

bond-graphs as an approach to solve CFD (*Computational Fluid Dynamics*), for single-phase and compressible flows. Moreover, Li *et al.* [86] used the *bond-graphs* to model a power regeneration system that includes positive displacement pumps, emulsions, and valves.

In the context of centrifugal pumps, one of the efforts to employ bond graph modeling is presented by Paynter [87]. The authors introduce the concept of an Eulerian Turbomachine (ETM), which refers to turbines and centrifugal pumps. The authors generically model the ideal ETM as a modulated gyrator port. In addition to the modulated port, the authors propose two additional loss terms: one capturing the mechanical dissipation related to the shaft and the other accounting for hydraulic losses due to whirl and shock losses. Furthermore, the author presents various case studies to validate the proposed dynamic models for ETM, focusing on pump startup and control simulations.

Later, Tanaka *et al.* [88] extended the modeling of centrifugal pumps using bond graphs, incorporating the mechanical domain by accounting for the rotational inertia of the pump shaft. The energy conversion between the mechanical and hydraulic domains and the system loss relationships were derived from the steady-state characteristics of each pump component. This model was validated against experimental data, exhibiting high accuracy in capturing dynamic characteristics, even in rapid transient states. The authors argue that the bond graphs proved robust enough to make predictions based solely on steady-state parameters. Furthermore, the authors introduce a new bond graph model for a torque converter based on the centrifugal pump model. This new model was found to share its basic structure with existing models, further attesting to the versatility of bond graphs in modeling complex fluid mechanical systems.

Higo *et al.* [89] investigate the reliability of utilizing bond graph lumped parameter models for capturing the dynamic behavior of pipelines, critical components in hydraulic systems. The proposed bond graph models are validated through comparative analysis against the Method of Characteristics (MoC) and experimental results. The study reveals that bond graph models yield predictions with similar precision to those obtained via MoC when an appropriate number of lumped elements are incorporated into the pipe model. The authors assert that bond graph methods offer a robust framework for the design and analysis of hydraulic circuits.

2.6 Identifiability analysis

The problem of estimating unknown properties based on measurements indirectly related to these parameters is referred to as the inverse problem. It is a common challenge shared with various fields, such as biomedical and geophysical imaging and groundwater flow modeling [13]. However, solving inverse problems can be challenging due to non-guaranteed existence, non-uniqueness, and stability issues. Additionally, multiple parameters may potentially provide satisfactory fits to a given data [10, 9, 11, 90].

In this context, the identifiability analysis aims to determine if a specific system parameter (or a set of parameters) can be accurately estimated uniquely (globally or locally) based on the

available input and output states. The structural identifiability analysis assumes an ideal scenario where the observed states are noise-free, and the model itself is error-free [91, 90, 92]. This analysis, also known as prior identifiability, can be performed without actual experimental data. However, as noted by Tuncer and Le [92], while structural identifiability is necessary, it alone is insufficient to identify model parameters accurately in noisy real-world data.

Various methods have been developed to analyze a system's local and global structural identifiability. Chis *et al.* [93] and Raue *et al.* [94] conducted comparative studies of these methods found in the literature, focusing on biological systems. Castro and Boer [95] introduced a simple scaling method, which exploits the invariance of the equations under parameter scaling transformations. More recently, Dong *et al.* [96] proposed a method based on differential elimination. It is important to note that structural identifiability alone does not account for the quantity and quality of available data or the numerical optimization algorithm employed [97, 92]. Therefore, practical parameter estimation in real-world data necessitates practical identifiability as a prerequisite, with structural identifiability serving as a necessary condition [96, 97].

2.7 Inverse problems

According to Karniadakis *et al.* [98], the inverse problems are ill-posed, and solve them is frequently prohibitively expensive computationally requiring complicated formulations, novel algorithms, and complex computer codes. Also, the standard techniques are still incapable of solving real-life physical problems involving missing, gappy, or noisy boundary conditions.

The solution of an inverse problem is tightly connected with the data, information, available which comes with an uncertainty that may vary according to the information source. The noisy data will affect the inverse problem solution by adding uncorrelated information to the true model. The only way to overcome this difficulty is by using more observational data [12]. However, as stated by Karniadakis *et al.* [98], even with the prospect influx of multi-fidelity data of different sources being collected or generated, in many real cases, such data cannot yet be seamlessly integrated into current physical models.

Several methods have been developed to estimate unknown parameters of ordinary differential equations (ODE). The Nonlinear Least Squares (NLS) method is widely adopted due to its versatility and applicability to various ODE systems. However, it is computationally intensive, and the inaccuracy in numerical approximations of derivatives may pose challenges, particularly for stiff systems [99, 100, 101]. In addition to NLS, other methods, such as collocation methods [99], Gaussian process-based approaches [102], Bayesian methods [103], and the recently proposed two-stage approach using Neural ODE [101], are a few alternative techniques for parameter estimation. The physics-informed neural network is one of the recent neural network-based methods for parameter estimation for ODE/PDE.

In this context, the neural network has recently gained attention on inverse problems due to its ability to handle complex and ill-posed problems. Raissi *et al.* [104] proposed the Physics-

informed neural networks (PINN) to solve forward and inverse problems in the context of differential equations. It trains the neural networks differently from the standard approach. The method takes into account the physics of the problem while formulating the loss function. The physics of the problem is introduced in the loss function by minimizing the residue of the differential equations of the problem at some collocation points. Generally, the derivatives of the predicted unknown are calculated using automatic differentiation [105].

The neural network and deep learning success in handling complex problems of interest, not only on inverse ill-posed problems, derives from its capability to decompose the original complex problem into several simpler representations and tasks. Thus, deep-learning enables a computer to construct complex concepts from simpler ones [106, 107]. Deep learning approaches, according to Karniadakis *et al.* [98], are capable of extracting features from vast amounts of multi-fidelity observational data. Therefore, they can explore large design spaces, find multi-dimensional correlations, and handle ill-posed problems.

Despite being capable of dealing with complex problems without any additional procedures, the deep learning techniques that rely solely on data may present physically inconsistent or implausible predictions resulting in poor generalization performance. In this context, the PINN are a subset of deep learning algorithms that combine data with abstract mathematical operators, such as PDE with or without missing physics. They yield more interpretable machine learning methods robust to imperfect data and able to deliver accurate and physically consistent extrapolation predictions. [98]. However, as mentioned by Jagtap *et al.* [108], the PINN have limitations. One is the inaccuracy associated with solving high-dimensional non-convex optimization problems that may result in local minima. The other limitation is the high computational cost of training deep neural networks and the long-time integration of the governing PDE.

The PINN was further developed to different variants like conservative PINN (cPINN) [109], extended PINN (XPINN) [110], hp-VPINN [111], Parareal PINN (PPINN) [112], Separable PINN [113] etc. Furthermore, McClenny and Braga-Neto [114] proposed a self-adaptive weights technique that automatically tuned the weights for different loss functions in a multi-loss function problem in PINN problem. In the present study, we consider self-adaptive weights for calculating the total loss. PINN and its variants were considered in inverse problems like unsaturated groundwater flow [115], diesel engine [116], supersonic flows [117] to name just a few.

3 Theoretical framework

This chapter presents a brief overview of the theory, the development of the bond graph elements used in this study and the structural identifiability analysis, structured into eight sections. The first section introduces the assumptions regarding multiphase flow that underpin this research. The second section delineates the bond graph representation of pipelines, grounded in the assumptions detailed in Section 3.1. The subsequent section offers a succinct review of flow losses within pipelines. The fourth section delves into the modeling of centrifugal pumps using bond graph techniques. The fifth section is dedicated to discussing losses associated with centrifugal pumps. The sixth section provides an overview of valve dynamics. The seventh section discusses the characteristics and modeling of twin-screw pumps. Lastly, the eighth section presents the concept of structural identifiability analysis. Readers seeking a foundational understanding of bond graph theory are referred to Chapter A.

The primary objective of this chapter is to elucidate the bond graph modeling of each subsystem within an ESP system, encompassing pipelines, valves, centrifugal pumps, and twin-screw pumps. It details the dynamics of pipelines in Sections 3.2 and 3.3, valve dynamics in Section 3.6, the dynamics of centrifugal pumps in Sections 3.4 and 3.5, and the behavior of twin-screw pumps in Section 3.7.

3.1 Multiphase flow assumptions

Given the complexity inherent in multiphase flow, particularly in systems involving emulsions, a simplifying assumption is often adopted where the emulsion is considered a dispersed flow and treated as a pseudo-fluid (Assumption 3.1.1). Thus, the homogeneous model is used for the pseudo-fluid density and the viscosity is considered the effective viscosity from emulsion literature. Consequently, the emulsion's non-Newtonian behavior hinges on the selected model for effective viscosity.

These assumptions simplifies the mathematical and computational modeling by considering the emulsion as a homogeneous mixture with uniform properties. It enables us to simplify the complex interfacial dynamics between the immiscible liquids constituting the emulsion. However, it is important to acknowledge that this approach may only partially capture the distinct flow characteristics and phase interactions, especially under conditions where phase separation is pronounced.

Assumption 3.1.1. *Emulsions are treated as pseudo-fluids with a dispersed flow.*

The applicability of this assumption is most justifiable under conditions where the emulsion is well-mixed and exhibits stable characteristics, with minimal phase separation (Assumption 3.1.2)

within the time interval analyzed. Furthermore, it is particularly valid when the relative velocities between the phases are low.

Assumption 3.1.2. *Stable emulsion conditions within the time interval studied.*

Furthermore, the pseudo-fluid assumption assumes that the temperature, pressure, and shear rate do not significantly alter the stability and rheology of the emulsion (Assumption 3.1.3). While these factors can indeed influence the properties of emulsions, their impact is considered negligible for the initial development of the model.

Assumption 3.1.3. *Negligible impact of temperature, pressure, and shear rate on emulsion properties.*

It is important to highlight that in experimental setups and real-world applications, emulsion properties are not static but vary due to several factors. These include turbulence and shear forces generated by the ESP, valves, and other inline devices. These interactions can significantly alter the properties of the emulsion as it moves through the system. Additionally, the fluid's chemical properties, the emulsion's inherent stability, and the presence or addition of emulsifiers and surfactants further complicate the emulsion characterization. Furthermore, temperature gradients along the pipeline introduce another layer of complexity by significantly affecting emulsion properties.

In the specific context of the ESP system analyzed in this study, several operational characteristics justify the pseudo-fluid assumption. The system's closed-loop nature provides a controlled environment where the fluid's properties, particularly temperature, can be regulated effectively through a heat exchanger. This control reduces the variations in the emulsion's rheological properties that would otherwise arise from temperature fluctuations.

Moreover, the operational parameters of the ESP system, such as the volume of the emulsion compartment, the operating volumetric flow rate, and the duration of transient experiments, support the assumption of emulsion stability. Under these conditions, it is reasonable to infer that the emulsion remains relatively homogeneous and stable throughout the duration of a dynamic experimental run. This stability implies that the emulsion's properties, including viscosity, do not exhibit significant temporal variations, thus aligning with the pseudo-fluid model assumption. The experimental details will be further discussed in Section 4.1.

This assumption of emulsion stability and uniformity allows for a considerable reduction in the complexity of the modeling process. While it introduces a certain level of abstraction from the intricacies of actual multiphase flow behavior, this simplification is deemed acceptable within the scope of this study. It strikes a balance between the need for a manageable computational model and the desire to capture the essential dynamics of the ESP system. Future work could extend this model to incorporate more complex rheological characteristics of emulsions, particularly in cases where the stability assumption may not hold or where the effects of external factors like emulsifiers become significant.

In the subsequent development of the bond graph model for the ESP system, the pseudo-fluid assumption is employed with an understanding of these limitations. The implications of this simplification on the model's accuracy and applicability are further examined with the validation with experimental data.

3.2 Pipeline transient

In the context of the ESP system dynamic analysis and modeling, it is fundamental to consider the dynamics of the pipeline downstream and upstream of the ESP. In this section, it is presented the dynamic equations that govern fluid dynamics in pipes, the continuity (Section 3.2.1) and the momentum (Section 3.2.2) equations. Then, in Section 3.2.4 the bond graph elements are obtained from these equations, which can be used to couple to the other elements of the ESP system.

3.2.1 Continuity equation

The analysis of transient behaviors in pipeline systems is often initiated with the general continuity equation for three-dimensional fluid flows. For the scope of this work, a less rigorous but conceptually insightful approach is adopted, with a more exhaustive derivation available in Chaudhry [118]. The differential form of the continuity equation is given by

$$\frac{\partial \rho}{\partial t} + \nabla \cdot (\rho \mathbf{v}) = 0, \quad (3.1)$$

where ρ denotes the fluid density and \mathbf{v} represents the flow velocity vector. Equation (3.1) states that the rate at which mass enters the system is equal to the rate at which it exits, as indicated by the divergence term $\nabla \cdot (\rho \mathbf{v})$. Concurrently, the term $\partial \rho / \partial t$ accounts for the accumulation or depletion of mass within the system.

In practical applications involving ducts, Equation (3.1) can often be simplified to a one-dimensional form by assuming a two-dimensional flow, and negligible flow in the vertical direction when compared to the axial flow. The one-dimensional continuity equation is then expressed as:

$$\frac{\partial(\rho A)}{\partial t} + \frac{\partial(\rho u A)}{\partial x} = 0, \quad (3.2)$$

where u is the axial fluid velocity and A is the cross-sectional area of the pipe. By expanding the terms of Equation (3.2), the equation becomes:

$$A \frac{\partial \rho}{\partial t} + \rho \frac{\partial A}{\partial t} + u A \frac{\partial \rho}{\partial x} + \rho A \frac{\partial u}{\partial x} + u \rho \frac{\partial A}{\partial x} = 0. \quad (3.3)$$

Isolating ρA as a common factor, we rewrite the equation as:

$$\rho A \left(\frac{1}{\rho} \frac{\partial \rho}{\partial t} + \frac{1}{A} \frac{\partial A}{\partial t} + \frac{u}{\rho} \frac{\partial \rho}{\partial x} + \frac{u}{A} \frac{\partial A}{\partial x} + \frac{\partial u}{\partial x} \right) = 0. \quad (3.4)$$

By examination, we identify that specific terms within the parentheses can be rewritten as components of total derivatives:

$$\frac{d\rho}{dt} = \frac{\partial \rho}{\partial t} + u \frac{\partial \rho}{\partial x}, \quad (3.5)$$

$$\frac{dA}{dt} = \frac{\partial A}{\partial t} + u \frac{\partial A}{\partial x}. \quad (3.6)$$

Incorporating these total derivatives into the equation, we obtain:

$$\rho A \left(\frac{1}{\rho} \frac{d\rho}{dt} + \frac{1}{A} \frac{dA}{dt} + \frac{\partial u}{\partial x} \right) = 0. \quad (3.7)$$

Dividing the equation by ρA , we arrive at the following form:

$$\frac{1}{\rho} \frac{d\rho}{dt} + \frac{1}{A} \frac{dA}{dt} + \frac{\partial u}{\partial x} = 0. \quad (3.8)$$

The density variation with pressure can be expressed in terms of the fluid bulk modulus B as follows:

$$B = \rho \frac{dP}{d\rho} \therefore \frac{d\rho}{dt} = \frac{\rho}{B} \frac{dP}{dt}, \quad (3.9)$$

where P is absolute the pressure. Additionally, for conduits with elastic walls, the cross-sectional can vary according to the pressure variation. Thus, more generally, we have that

$$\frac{1}{A} \frac{dA}{dt} = \frac{1}{K_E} \frac{dP}{dt}, \quad (3.10)$$

where K_E is a constant that describes the conduit wall deformation due to pressure. For conduit walls with linearly elastic walls, Chaudhry [118] deduced that it is given by:

$$\frac{1}{K_E} = \frac{1}{\frac{\eta E_{ym}}{d} - \frac{P}{2}}, \quad (3.11)$$

where d is the pipe diameter, η is the pipe wall thickness, and E_{ym} is Young's modulus of elasticity. For $P/2 \ll \eta E_{ym}/d$, the K_E equation simplifies to

$$\frac{1}{K_E} = \frac{1}{\frac{\eta E_{ym}}{d}}. \quad (3.12)$$

Replacing these parameters in Equation (3.8) we have:

$$\left(\frac{1}{B} + \frac{1}{K_E}\right) \frac{dP}{dt} + \frac{\partial u}{\partial x} = 0. \quad (3.13)$$

Then, expanding the total derivatives and rearranging, we have:

$$\frac{\partial P}{\partial t} + u \frac{\partial P}{\partial x} + \rho a^2 \frac{\partial u}{\partial x} = 0, \quad (3.14)$$

where a is defined as:

$$a^2 = \frac{BK_E}{\rho(K_E + B)}, \quad (3.15)$$

where a represents the velocity of the pressure wave in a conduit filled with a slightly compressible fluid, as mentioned by Chaudhry [118].

3.2.2 Momentum equation

The fluid dynamics can be comprehensively described by the Navier-Stokes equations. In their three-dimensional form, these equations are given as:

$$\rho \frac{d\mathbf{v}}{dt} = \rho \mathbf{g} - \nabla P + \nabla \cdot \mathbf{\Gamma}, \quad (3.16)$$

where \mathbf{v} denotes the fluid velocity vector, ∇P represents the pressure gradient, ρ is the fluid density, \mathbf{g} accounts for body force acceleration, and $\mathbf{\Gamma}$ is the stress tensor.

Analogous to the simplifications discussed in Section 3.2.1, Equation (3.16) can be reduced to a one-dimensional form for practical applications involving ducts. This reduction is justified by assuming a two-dimensional flow in the xy -plane, thereby neglecting variations in the z -direction. The one-dimensional momentum equation is then given by:

$$\rho \left(\frac{\partial u}{\partial t} + u \frac{\partial u}{\partial x} \right) = -\rho g \sin(\xi) - \frac{\partial P}{\partial x} + \frac{\partial \Gamma_{xy}}{\partial y}, \quad (3.17)$$

where ξ is the angle of the conduit with respect to the ground, and Γ_{xy} is the shear stress component in the xy -plane.

Assuming a Newtonian fluid, the shear stress Γ_{xy} is proportional to the velocity gradient in the y -direction, as expressed by:

$$\Gamma_{xy} = \mu \frac{\partial u}{\partial y}, \quad (3.18)$$

where μ is the fluid viscosity. Substituting this into Equation (3.17), we obtain:

$$\rho \left(\frac{\partial u}{\partial t} + u \frac{\partial u}{\partial x} \right) = -\rho g \sin(\xi) - \frac{\partial P}{\partial x} + \mu \frac{\partial^2 u}{\partial y^2}, \quad (3.19)$$

assuming the viscosity is constant along y -direction. The term $\mu \partial^2 u / \partial y^2$ will be further discussed

in Section 3.3.

3.2.3 Fluid dynamics with continuity and momentum equations

Solving the coupled Navier-Stokes (Section 3.2.2) and continuity equations (Section 3.2.1) analytically is often intractable due to the inherent complexity of fluid dynamics. This complexity frequently necessitates the use of numerical methods for solutions. Among these, the Method of Characteristics (MoC) is commonly employed. The MoC is particularly effective as it transforms the partial differential equations into ordinary differential equations along the characteristic lines, thereby simplifying the computational requirements. Furthermore, the boundary conditions definition is a critical aspect that must be carefully selected based on the specific engineering application under consideration.

3.2.4 Bond graph

In this section, the focus is on deriving the essential elements for representing one-dimensional fluid flow in pipelines through bond graph modeling. The derivation is based on the one-dimensional incompressible Navier-Stokes and the continuity equations.

3.2.4.1 One-dimensional incompressible flow representation

Starting from the Equation (3.19), we have that the one-dimensional Navier-Stokes equation is given by

$$\rho \left(\frac{\partial u}{\partial t} + u \frac{\partial u}{\partial x} \right) = -\rho g \sin(\xi) - \frac{\partial P}{\partial x} + \mu \frac{\partial^2 u}{\partial y^2}.$$

The bond graph framework represents the flow variable by the volumetric flow rate, denoted as Q . Thus, considering an incompressible flow, the velocity u can be expressed in terms of Q as $Q = A(x)u$. Substituting this into Equation (3.19), and considering the height (z) as a function of x , we obtain

$$\frac{\rho}{A(x)} \frac{\partial Q}{\partial t} + \frac{\rho Q^2}{A(x)} \frac{\partial 1/A(x)}{\partial x} = -\rho g \frac{dz}{dx} - \frac{\partial P}{\partial x} + \frac{\mu}{A(x)} \frac{\partial^2 Q}{\partial y^2}. \quad (3.20)$$

The terms in Equation (3.20) have the following physical interpretations:

$$\underbrace{\frac{\rho}{A(x)} \frac{\partial Q}{\partial t}}_{\text{Inertia}} + \underbrace{\frac{\rho Q^2}{A(x)} \frac{\partial 1/A(x)}{\partial x}}_{\text{Convective}} = \underbrace{-\rho g \frac{dz}{dx}}_{\text{Gravity}} - \underbrace{\frac{\partial P}{\partial x}}_{\text{Pressure}} + \underbrace{\frac{\mu}{A(x)} \frac{\partial^2 Q}{\partial y^2}}_{\text{Viscous}}. \quad (3.21)$$

The viscous friction term, denoted as R_f , will be discussed in detail in Section 3.3.1. For the current analysis, we consider R_f as a constant.

In the bond graph framework, systems are described using lumped elements. To account for

this, we integrate Equation (3.20) over x from 0 to l :

$$I_f \frac{\partial Q}{\partial t} + R_c Q - (x_l - x_0) R_f Q + \rho g(z_l - z_0) + (P_l - P_0) = 0, \quad (3.22)$$

where

$$I_f = \int_0^l \frac{\rho}{A(x)} dx, \quad (3.23a)$$

$$R_c = \rho Q \int_0^l \frac{\partial(1/A(x))}{\partial x} dx = \frac{\rho Q}{2} \left(\frac{1}{A_l} - \frac{1}{A_0} \right). \quad (3.23b)$$

From Equation (3.22), the system can be represented by a 1-junction bond graph connected to inertia (I_f), resistance (R_c and R_f), and source of effort elements, as illustrated in Figure 3.1.

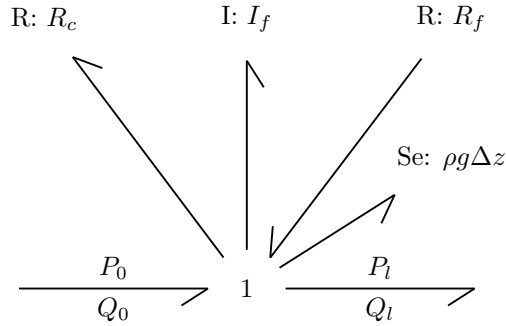


Figure 3.1: Bond graph obtained from the integration of the momentum equation.

It is important to note that in Figure 3.1 the $\Delta z = z_l - z_0$. Moreover, if we consider a pipeline segment with constant cross-sectional area, the Equation (3.23) can be written as:

$$I_f = \frac{\rho l}{A}, \quad (3.24a)$$

$$R_c = 0. \quad (3.24b)$$

where l is the pipeline segment length. Notably, the term R_c is associated with the dynamic pressure of the fluid, which becomes significant only when there is a variation in the pipeline's cross-sectional area.

3.2.4.2 Continuity equation representation

In this section, the objective is to incorporate the effects of fluid compressibility and conduit wall deformation into the bond graph representation. Starting from Equation (3.13), the continuity equation is given by:

$$\left(\frac{1}{B} + \frac{1}{K_E} \right) \frac{dP}{dt} + \frac{\partial u}{\partial x} = 0.$$

In the bond graph framework, the flow variable is represented by the volumetric flow rate, denoted as Q . The velocity u can be expressed in terms of Q as $Q = A(x)u$. Differentiating with respect to x and assuming a constant cross-sectional area ($\partial A/\partial x = 0$), we obtain:

$$\frac{\partial u}{\partial x} = \frac{1}{A} \frac{\partial Q}{\partial x}. \quad (3.25)$$

In the bond graph, the systems are described using lumped elements. Therefore, for a finite pipe segment with Δx length, the spatial derivative can be approximated as:

$$\frac{\partial Q}{\partial x} = \frac{Q_{i+1} - Q_i}{\Delta x} \implies \frac{\partial u}{\partial x} = \frac{1}{A} \frac{Q_{i+1} - Q_i}{\Delta x}, \quad (3.26)$$

where Q_i and Q_{i+1} are the flow rate entering and leaving the i -th pipe segment, respectively. Substituting Equation (3.26) into Equation (3.13), we arrive at:

$$\left(\frac{1}{B} + \frac{1}{K_E} \right) \frac{dP}{dt} = -\frac{1}{A\Delta x} (Q_{i+1} - Q_i), \quad (3.27a)$$

$$\Delta x A \left(\frac{1}{B} + \frac{1}{K_E} \right) \frac{dP}{dt} = Q_i - Q_{i+1}. \quad (3.27b)$$

From the tetrahedron of state, we can observe that this equation essentially describes the relationship between effort ($e(t)$) and displacement ($q(t)$) but derived in time. The Equation (3.27b) can be represented by the following bond graph, shown in Figure 3.2.

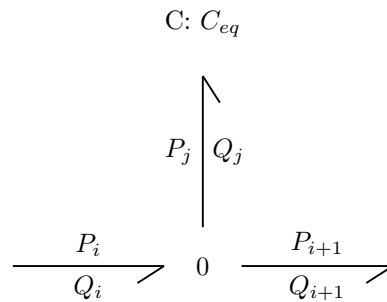


Figure 3.2: C-element for pipelines.

The equivalent compliance C_{eq} is defined as:

$$C_{eq} = \Delta x A \left(\frac{1}{B} + \frac{1}{K_E} \right). \quad (3.28)$$

It is important to note that Equation (3.28) accounts for the compliance effects due to both fluid compressibility and wall elasticity. The equation allows for separating these two contributions, enabling the derivation of a distinct C-element for each.

For completeness, to establish a standard relationship between effort $e(t)$ and displacement

$q(t)$, we integrate Equation (3.27b) over time. We commence by isolating $\frac{dP}{dt}$ in Equation (3.29):

$$\frac{dP}{dt} = \frac{1}{\Delta x A \left(\frac{1}{B} + \frac{1}{K_E} \right)} (Q_i - Q_{i+1}). \quad (3.29)$$

Integrating both sides of Equation (3.29) with respect to t yields:

$$\int_{P_0}^{P(t)} dP = \frac{1}{\Delta x A \left(\frac{1}{B} + \frac{1}{K_E} \right)} \int_{t_0}^t (Q_i - Q_{i+1}) dt \quad (3.30)$$

Upon integration, we obtain:

$$P(t) - P_0 = \frac{1}{\Delta x A \left(\frac{1}{B} + \frac{1}{K_E} \right)} ((V_i(t) - V_i(t_0)) - (V_{i+1}(t) - V_{i+1}(t_0))), \quad (3.31)$$

where P_0 denotes the initial pressure, $V_i(t)$ and $V_{i+1}(t)$ represent the volumes corresponding with Q_i and Q_{i+1} at time t and t_0 , the initial time instant.

Although P_0 , $V_i(t_0)$, and $V_{i+1}(t_0)$ are essential for an absolute representation of these variables, they are often omitted in bond graph modeling. This omission is motivated by focusing on dynamic behavior rather than absolute states. Consequently, P_0 , $V_i(t_0)$, and $V_{i+1}(t_0)$ serve to define the system's equilibrium state but do not affect its intrinsic dynamics. This practice is analogous to the frequent omission of the spring's undeformed length when modeling mass-spring systems, focusing instead on the deformation to capture the dynamics. Therefore, we can omit these variables in Equation (3.31), and we obtain the following form:

$$V_i(t) - V_{i+1}(t) = \Delta x A \left(\frac{1}{B} + \frac{1}{K_E} \right) P(t), \quad (3.32)$$

It is important to note that the energy stored in the fluid compressibility and wall deformation is represented by the difference in volume between the pipe segment entrance and exit. Thus, we define $V_j(t) = V_i(t) - V_{i+1}(t)$. This leads to a more compact form:

$$V_j(t) = \Delta x A \left(\frac{1}{B} + \frac{1}{K_E} \right) P(t). \quad (3.33)$$

3.3 Viscous flow in ducts

This section presents a brief overview of viscous flow in ducts. The objective is to introduce the friction and local losses of a flow inside a duct, which can be a pipe, or the centrifugal pump channel for instance.

3.3.1 Friction losses

According to White [119], Weisbach proposed an empirical correlation to model pressure losses in ducts, which accounts for the friction losses, and it is expressed as:

$$\Delta P = \lambda \frac{\rho L V^2}{d_h 2}, \quad (3.34)$$

where λ is the dimensionless friction coefficient, L denotes the length of the duct, d_h represents the hydraulic diameter, and V is the fluid average velocity within the duct.

The concept of frictional losses in ducts is fundamentally linked to the fluid's shear stress, denoted by Γ . This stress arises due to the presence of a velocity gradient in the fluid flow. Specifically, for Newtonian fluids, the shear stress is proportional to the velocity gradient, $\partial u / \partial y$, as expressed by:

$$\Gamma = \mu \frac{\partial u}{\partial y}. \quad (3.35)$$

Given this relationship, it is necessary to know the velocity profile across the duct's cross-sectional area to quantify the frictional losses attributable to shear stresses. In the case of laminar flows, deriving this profile is relatively straightforward, as illustrated by the classical Hagen–Poiseuille flow, where the friction factor for laminar flow is determined by:

$$\lambda_{\text{lam}} = \frac{64}{Re}, \quad (3.36)$$

where Re is the Reynolds number. However, characterizing this profile becomes considerably more complex in turbulent flow conditions. In this study, due to the viscosity of the oil and the emulsion, the flow is presumed to be laminar, as indicated by the Reynolds number in the pipeline, which is below 2000.

In the context of bond graph notation, the friction loss as defined by Equation (3.34) can be represented using a resistance element. From the tetrahedron of state and considering $V = Q/A$, the friction losses in bond graph notation can be expressed as:

$$R_f = \lambda \frac{\rho L}{d_h} \frac{Q}{2A^2}, \quad (3.37)$$

where A is the cross-sectional area.

3.3.2 Local losses

According to White [119] and Fox *et al.* [120], there are local or minor losses in a pipe system besides the friction losses that occur along the duct length. Such losses arise from various system factors like pipe entrances and exits, abrupt dimensional transitions from expansions or contractions, and specific fittings such as bends, elbows, and tees. Additionally, the valves' operational state, whether in a fully open or partially closed state, is a significant source of such

losses. Therefore, these local losses are not always negligible. For instance, a partially opened valve can induce a pressure drop comparable to or surpass the loss in a long pipeline.

As highlighted by White [119], the flow complexity within pipeline devices is notably high, making the derivation of a generalized formulation quite challenging. Crane Co [121] elaborates that local losses within these devices arise from various causes. These include alterations in the fluid flow direction, the presence of obstructions in the flow trajectory, changes in the cross-sectional area, and friction. It is important to note that friction is intrinsically affected by factors such as the roughness of the internal surfaces, the piping's inner diameter, and fluid attributes like velocity, density, and viscosity. As a result of these intricacies, these losses are predominantly obtained experimentally and then associated with the respective pipe flow parameters.

The local loss, denoted as K_m , is commonly expressed by grouping the Darcy friction factor with the pipe geometrical parameters L and d of the Weisbach equation. Thus, the K_m expression is given by:

$$\Delta P = \lambda \frac{L}{d} \frac{\rho}{2} V^2, \quad (3.38)$$

$$\Delta P = K_m \frac{\rho}{2} V^2,$$

$$K_m = \frac{2 \Delta P}{\rho V^2}. \quad (3.39)$$

As noted by White [119], while K_m is dimensionless, it is frequently associated more closely with the raw size of the pipe in the literature than with parameters such as the Reynolds number or the roughness ratio.

According to Crane Co [121], for the majority of valves and fittings operating in the complete turbulence zone, losses from flow path length due to friction are considerably smaller when compared to losses from directional changes, obstructions, and cross-sectional changes. As a result, in turbulent conditions, the local loss K_m can be considered approximately constant and independent of the Reynolds number. This suggests that for any given obstruction, the K_m remains constant under fully turbulent flows. However, Crane Co [121] argues that in non-turbulent flow regimes, the frictional effects tend to become more dominant compared to other losses. This is especially true when the friction factor increases as the Reynolds number decreases in both transition and laminar regimes. As a result, the resistance coefficient increases.

Crane Co [121] details that while resistance coefficients for various valves and fittings have been derived from multiple investigations and works, obtaining this data for every specific size and variant is challenging due to the time-intensive and expensive nature of the required tests. Consequently, Crane Co [121] recommends using the manufacturer data or actual test data for a system when available.

In the context of bond graph notation, the local loss as defined in Equation (3.39) can be depicted using a resistance element. From the tetrahedron of state and considering $V = Q/A$,

the local losses in bond graph notation can be expressed as:

$$R_m = \frac{\rho K_m Q}{2 A^2}. \quad (3.40)$$

While K_m is typically determined experimentally, as mentioned before, the cross-sectional area A can present its own set of challenges for determination. To address this, we can incorporate it with K_m and determine experimentally. This simplifies Equation (3.40) to:

$$R_m = \frac{\rho K_{ma} Q}{2} \quad (3.41)$$

with $K_{ma} = K_m/A^2$.

3.4 Centrifugal pumps

3.4.1 Power equation

The dynamics of a centrifugal pump can be modeled by analyzing the energy within a control volume (CV) that encompasses the pump. The CV approach allows for a comprehensive analysis of fluid behavior within the pump system. In such systems, the total energy is typically composed of internal, kinetic, and potential energies. Accordingly, the total energy within a given CV can be expressed as

$$E_c = \int_{CV} \rho \left(e_c + \frac{v^2}{2} + gz \right) dV, \quad (3.42)$$

where ρ represents the fluid density and e_c denotes the internal energy per unit mass. The term $v^2/2$ is the kinetic energy per unit mass, where v is the absolute fluid velocity. The gz represents the potential energy per unit mass, where g is the acceleration due to gravity and z is the elevation.

Although Equation (3.42) provides a model for the pump, it is primarily focused on the steady-state condition and does not encompass the dynamic aspects, which are crucial for this study. The dynamic behavior of the pump, particularly under varying operational conditions, necessitates an approach that more comprehensively incorporates pump dynamics.

To capture the power dynamics and by extension the pump dynamics, we can view the power dynamics as the rate of change of energy over time within the control volume (CV). Consequently, the dynamic model can be derived by differentiating the total energy E_c (as defined in Equation (3.42)) with respect to time t . This differentiation yields:

$$\frac{dE_c}{dt} = \frac{d}{dt} \int_{CV} \rho \left(e_c + \frac{v^2}{2} + gz \right) dV. \quad (3.43)$$

Applying the Reynolds Transport Theorem (RTT) to Equation (3.43) allows us to connect the temporal rate of change of energy within the CV to the energy flux across the control surface

(CS), leading to:

$$\frac{dE_c}{dt} = \frac{\partial}{\partial t} \int_{CV} \left(\rho \left(e_c + \frac{v^2}{2} + gz \right) \right) dV + \int_{CS} \rho \left(e_c + \frac{v^2}{2} + gz \right) \mathbf{v} \cdot d\mathbf{A}. \quad (3.44)$$

In Equation (3.44), \mathbf{v} denotes the velocity vector of the fluid, and $d\mathbf{A}$ is the differential area vector on the CS, oriented normal to the surface. The first term represents the rate of change of energy within the CV. The second term accounts for the net energy flow across the CS. The CV and CS of the centrifugal pump are illustrated in Figure 3.3.

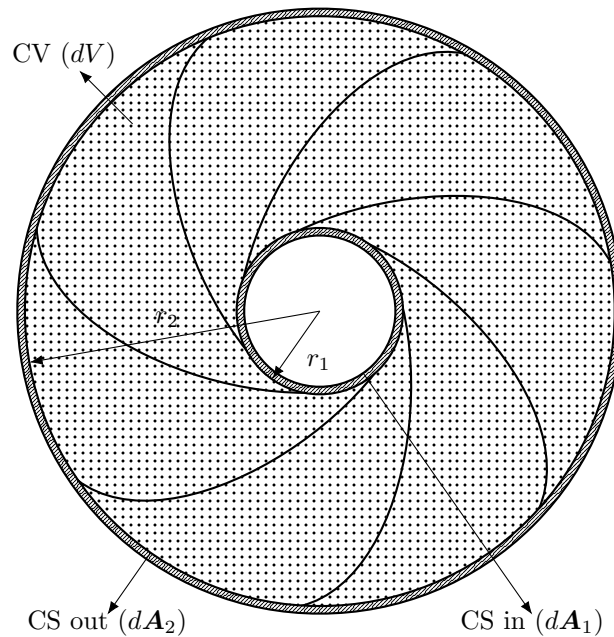


Figure 3.3: Control volume (CV) and control surfaces of a centrifugal pump.

3.4.2 Angular-momentum equation

Although the model presented in Equation (3.44) incorporates various aspects of the centrifugal pump and has a small number of assumptions its analytical tractability is challenging. For instance, it is required to know the velocity profile inside the control volume. Thus, another approach for modeling the centrifugal pump involves applying the angular momentum conservation principle to the same control volume (CV) presented in Figure 3.3. This approach yields the following equation:

$$\tau_{\text{shaft}} = \frac{d}{dt} \int_{CV} \mathbf{r} \times \mathbf{v} \rho dV. \quad (3.45)$$

In this equation, \mathbf{r} represents the position vector from the axis of rotation to a fluid element, and \mathbf{v} is the fluid element's velocity vector. The fixed coordinate system is chosen with the z-axis aligned with the axis of rotation of the centrifugal pump. This alignment simplifies the calculation of the cross-product $\mathbf{r} \times \mathbf{v}$. The Equation (3.45) states that the torque applied to or

produced by the shaft results in a change of the fluid's angular momentum within the CV [122].

Similar to the application of the RTT on the energy equation, we apply RTT to the angular momentum equation (Equation (3.45)), resulting in:

$$\tau_{\text{shaft}} = \frac{\partial}{\partial t} \int_{CV} \mathbf{r} \times \mathbf{v} \rho dV + \int_{CS} \mathbf{r} \times \mathbf{v} \rho \mathbf{v} \cdot d\mathbf{A}. \quad (3.46)$$

We can relate Equation (3.46) to the power equation using the angular velocity (ω). Thus, we obtain the following power expression for the shaft:

$$\tau\omega = \underbrace{\omega \frac{\partial}{\partial t} \int_{CV} \mathbf{r} \times \mathbf{v} \rho dV}_{\text{Unsteady}(U)} + \underbrace{\omega \int_{CS} \mathbf{r} \times \mathbf{v} \rho \mathbf{v} \cdot d\mathbf{A}}_{\text{Steady state}(SS)}. \quad (3.47)$$

In modeling the centrifugal pump using the conservation of angular momentum, the aim is to improve analytical tractability and facilitate the development of a parsimonious bond graph representation. This approach, however, introduces several assumptions, each crucial for simplifying the model without significantly compromising its accuracy.

Firstly, it is assumed inviscid flow (Assumption 3.4.1). Although real fluids exhibit viscosity, for the initial development of the model, the effects of viscosity are neglected. The impact of viscous losses will be addressed in subsequent sections, allowing us to initially focus on the primary dynamics of the fluid flow.

Assumption 3.4.1. *Inviscid flow.*

Additionally, given the symmetry within the pump, it is assumed that gravitational and other body forces do not significantly affect the flow (Assumption 3.4.2). This assumption is based on the understanding that, within the context of the pump's operation, these forces do not significantly influence the flow dynamics.

Assumption 3.4.2. *Neglected body forces.*

To further simplify our model, it is assumed uniform flow across the inlet and outlet of the impeller (Assumption 3.4.3). This assumption reduces the complexity associated with varying velocity profiles that are inherently dependent on the impeller's geometry and operational conditions.

Assumption 3.4.3. *Uniform flow.*

Furthermore, it is omitted considerations of leakage or secondary flows (Assumption 3.4.4). While the intricate geometry of centrifugal pumps can lead to such complexities, their effects will be addressed using simplified models based on literature in subsequent thesis sections.

Assumption 3.4.4. *No leakage or secondary flows.*

Finally, the fluid being pumped is assumed to be incompressible (Assumption 3.4.5). This simplification, treating the fluid density as constant across the control volume and over time, is a reasonable approximation for liquids at moderate pressures and temperatures. It streamlines the analysis, although it is important to note that this assumption may not be applicable for gases or under conditions of significant pressure variations.

Assumption 3.4.5. *Incompressible flow.*

3.4.3 Transient term analysis

In this section, we focus on developing the transient term (\mathcal{U}) of Equation (3.67), while the steady-state term (\mathcal{SS}) will be further developed in Section 3.4.4, for clarity. The development will consider the assumptions made in Section 3.4.2 with the angular-momentum equation (Section 3.4.2). Thus, we have

$$\mathcal{U} = \omega \frac{\partial}{\partial t} \int_{CV} \mathbf{r} \times \mathbf{v} \rho dV. \quad (3.48)$$

The velocity of the liquid within the impeller of a centrifugal pump can be decomposed into various components, each representing different aspects of the flow dynamics. These components are conveniently represented in a triangle of velocities, as illustrated in Figure 3.4, for both the entrance and discharge regions of the pump impeller. The decomposition of the velocity vector into radial, axial, and tangential components allows us to isolate the component that primarily contributes to the angular momentum under the pump's specific design and operational conditions.

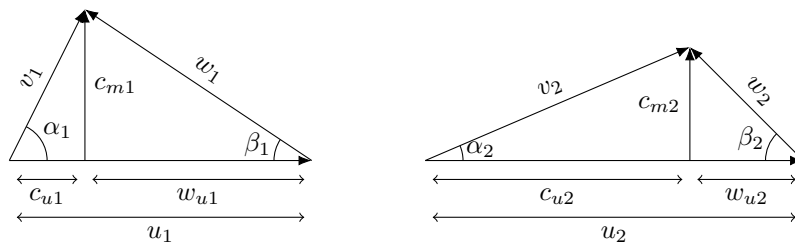


Figure 3.4: Entrance and discharge velocity triangle.

Given the fixed coordinate system defined in Section 3.4.2 and considering the triangle of velocities presented in Figure 3.4, the cross-product $\mathbf{r} \times \mathbf{v}$ in Equation (3.67) can be expressed as rc_u . This simplification is justified by the fact that, within the impeller, the tangential component of the fluid velocity, c_u , is predominantly responsible for imparting angular momentum to the fluid. Therefore, the Equation (3.48) can be rewritten as:

$$\mathcal{U} = \omega \frac{\partial}{\partial t} \int_{CV} rc_u \rho dV. \quad (3.49)$$

Referring to Figure 3.4, we have that c_u can be expressed as:

$$c_u = u_x - w_u, \quad (3.50a)$$

$$= u_x - \frac{c_m}{\tan(\beta(r))}, \quad (3.50b)$$

$$= u_x - c_m \cot(\beta(r)), \quad (3.50c)$$

where $u_x = \omega r$ represents the tangential velocity, being r the radius in polar coordinate system. Substituting this into Equation (3.50c), we obtain:

$$c_u = \omega r - c_m \cot(\beta(r)). \quad (3.51)$$

Additionally, by the assumption of uniform flow (Assumption 3.4.3) we have that the normal velocity (c_m) relates to the volumetric flow rate by:

$$Q = 2\pi r h c_m \therefore c_m = \frac{Q}{2\pi r h}, \quad (3.52)$$

where h is the height of the impeller. Substituting, Equation (3.52) into Equation (3.51) we have:

$$c_u = \omega r - \frac{Q \cot(\beta(r))}{2\pi r h}. \quad (3.53)$$

Substituting Equation (3.53) into Equation (3.49), and writing the control volume (CV) in cylindrical coordinate, $dV = r dr d\theta dz$, we obtain:

$$\mathcal{U} = \omega \frac{\partial}{\partial t} \int_{CV} r \left(\omega r - \frac{Q \cot(\beta(r))}{2\pi r h} \rho \right) dV, \quad (3.54a)$$

$$= \omega \frac{\partial}{\partial t} \int_{CV} \omega r^2 \rho dV - \omega \frac{\partial}{\partial t} \int_{CV} \frac{Q \cot(\beta(r))}{2\pi h} \rho dV. \quad (3.54b)$$

$$= \omega \frac{\partial}{\partial t} \iiint \omega r^3 \rho dr d\theta dz - \omega \frac{\partial}{\partial t} \iiint \frac{Q \cot(\beta(r))}{2\pi h} \rho r dr d\theta dz. \quad (3.54c)$$

Considering the impeller height h in Equation (3.54c), we can integrate z from 0 to h . Similarly, we can integrate and the angle (θ) from 0 to 2π to consider the whole impeller. Moreover, with the incompressible flow assumption we have move the density out of the integral. Thus, we have that Equation (3.54c) yields

$$\mathcal{U} = \omega \frac{\partial}{\partial t} \iiint \omega r^3 \rho dr d\theta dz - \omega \frac{\partial}{\partial t} \iiint \frac{Q \cot(\beta(r))}{2\pi h} \rho r dr, \quad (3.55a)$$

$$= \omega \frac{\partial}{\partial t} \left(\omega \rho 2\pi h \int r^3 dr \right) - \omega \frac{\partial}{\partial t} \left(Q \rho \int r \cot(\beta(r)) dr \right). \quad (3.55b)$$

Assuming that the density and the impeller geometrical characteristics do not change with time,

the Equation (3.55b) can be rewritten as:

$$\mathcal{U} = \omega\rho 2\pi h \int r^3 dr \frac{\partial\omega}{\partial t} - \omega\rho \int r \cot(\beta(r)) dr \frac{\partial Q}{\partial t}. \quad (3.56)$$

Rewriting Equation (3.56) in a more compact form, we obtain:

$$\mathcal{U} = \omega\zeta_1 \frac{\partial\omega}{\partial t} + \omega\zeta_2 \frac{\partial Q}{\partial t}, \quad (3.57)$$

where the terms ζ_1 and ζ_2 are defined as:

$$\zeta_1 = \rho 2\pi h \int r^3 dr, \quad (3.58a)$$

$$\zeta_2 = -\rho \int r \cot(\beta(r)) dr. \quad (3.58b)$$

In Equation (3.57), the first term represents the influence of changes in impeller speed on the fluid's momentum, reflecting how alterations in angular velocity (ω) impact the fluid within the impeller. The second term accounts for the effect of flow rate (Q) changes on the tangential velocity of the fluid. It highlights the relationship between flow rate variations and the transient component of the shaft torque.

3.4.4 Steady state term analysis

In this section, we focus on developing the transient term (\mathcal{SS}) of Equation (3.67). The development will consider the assumptions made in Section 3.4.2 with the angular-momentum equation (Section 3.4.2). Thus, we have

$$\mathcal{SS} = \omega \int_{CS} \mathbf{r} \times \mathbf{v} \rho \mathbf{v} \cdot d\mathbf{A}. \quad (3.59)$$

Given the coordinate system and the triangle of velocities presented in Figure 3.4, we can express the dot product $\mathbf{v} \cdot d\mathbf{A}$ in Equation (3.59) as $c_m dA$. From the Figure 3.3 we have that the control surface (CS) is composed by two surfaces, one defining the pump inlet and the other defining the pump outlet. Considering, these two areas the Equation (3.59) can be rewritten as

$$\mathcal{SS} = \omega \int_{CS} \mathbf{r} \times \mathbf{v} \rho c_{m2} dA_2 - \omega \int_{CS} \mathbf{r} \times \mathbf{v} \rho c_{m1} dA_1. \quad (3.60)$$

Similarly to the discussed in Section 3.4.3 we can express the cross-product $\mathbf{r} \times \mathbf{v}$ in Equation (3.60) as rc_u . Additionally, the c_u can be further developed to Equation (3.53). Thus,

we can rewrite the Equation (3.60) as:

$$\mathcal{S}\mathcal{S} = \omega \int_{CS} r_2 \rho \left(\omega r_2 - \frac{Q \cot(\beta_2)}{2\pi r_2 h_2} \right) c_{m2} dA_2 - \omega \int_{CS} r_1 \rho \left(\omega r_1 - \frac{Q \cot(\beta_1)}{2\pi r_1 h_1} \right) c_{m1} dA_1. \quad (3.61)$$

Exploiting the cylindrical symmetry of the control surface, where $dA = r d\theta dz$, equation (3.61) becomes:

$$\mathcal{S}\mathcal{S} = \omega \iint r_2 \rho \left(\omega r_2 - \frac{Q \cot(\beta_2)}{2\pi r_2 h_2} \right) c_{m2} r_2 d\theta dz - \omega \iint r_1 \rho \left(\omega r_1 - \frac{Q \cot(\beta_1)}{2\pi r_1 h_1} \right) c_{m1} r_1 d\theta dz. \quad (3.62)$$

Integrating equation (3.62) with respect to θ and z , we obtain:

$$\mathcal{S}\mathcal{S} = \omega r_2 \rho \left(\omega r_2 - \frac{Q \cot(\beta_2)}{2\pi r_2 h_2} \right) \iint c_{m2} r_2 d\theta dz - \omega r_1 \rho \left(\omega r_1 - \frac{Q \cot(\beta_1)}{2\pi r_1 h_1} \right) \iint c_{m1} r_1 d\theta dz, \quad (3.63a)$$

$$= \omega r_2 \rho \left(\omega r_2 - \frac{Q \cot(\beta_2)}{2\pi r_2 h_2} \right) (2\pi r_2 h_2 c_{m2}) - \omega r_1 \rho \left(\omega r_1 - \frac{Q \cot(\beta_1)}{2\pi r_1 h_1} \right) (2\pi r_1 h_1 c_{m1}). \quad (3.63b)$$

Recognizing that $2\pi r h c_m$ is the volumetric flow rate Q from Equation (3.52), we can simplify Equation (3.63b) to:

$$\mathcal{S}\mathcal{S} = \omega r_2 \rho \left(\omega r_2 - \frac{Q \cot(\beta_2)}{2\pi r_2 h_2} \right) Q - \omega r_1 \rho \left(\omega r_1 - \frac{Q \cot(\beta_1)}{2\pi r_1 h_1} \right) Q, \quad (3.64a)$$

$$= \omega Q \rho \left(\omega r_2^2 - \frac{Q \cot(\beta_2)}{2\pi h_2} \right) - \omega Q \rho \left(\omega r_1^2 - \frac{Q \cot(\beta_1)}{2\pi h_1} \right), \quad (3.64b)$$

$$= \omega \left[\rho \omega Q (r_2^2 - r_1^2) - \rho Q^2 \left(\frac{\cot(\beta_2)}{2\pi h_2} - \frac{\cot(\beta_1)}{2\pi h_1} \right) \right]. \quad (3.64c)$$

Finally, we can express Equation (3.64c) in a more compact form as:

$$\mathcal{S}\mathcal{S} = \omega (\zeta_3 \omega Q - \zeta_4 Q^2), \quad (3.65)$$

where the coefficients ζ_3 and ζ_4 are defined as:

$$\zeta_3 = \rho (r_2^2 - r_1^2), \quad (3.66a)$$

$$\zeta_4 = \rho \left(\frac{\cot(\beta_2)}{2\pi h_2} - \frac{\cot(\beta_1)}{2\pi h_1} \right). \quad (3.66b)$$

3.4.5 Bond graph representation

Given the development of the unsteady \mathcal{U} and steady state \mathcal{SS} terms of the Equation (3.67) equation in the Sections 3.4.3 and 3.4.4 we can rewrite Equation (3.67) as:

$$\tau\omega = \omega\zeta_1 \frac{\partial\omega}{\partial t} + \omega\zeta_2 \frac{\partial Q}{\partial t} + \omega(\zeta_3\omega Q - \zeta_4 Q^2). \quad (3.67)$$

To represent Equation (3.67) in bond graph notation, we rewrite it into the angular mechanical domain by dividing both sides by ω , yielding:

$$\tau = \zeta_1 \frac{\partial\omega}{\partial t} + \zeta_2 \frac{\partial Q}{\partial t} + (\zeta_3\omega Q - \zeta_4 Q^2). \quad (3.68)$$

Reorganizing Equation (3.69), we have:

$$\underbrace{\tau}_{\text{Source}} - \underbrace{\zeta_1 \frac{\partial\omega}{\partial t}}_{\text{Inertia}} - \underbrace{\zeta_2 \frac{\partial Q}{\partial t}}_{\text{Q effects}} = \underbrace{\zeta_3\omega Q - \zeta_4 Q^2}_{\text{Coupling}}. \quad (3.69)$$

The left-hand side of Equation (3.69) can be represented by a bond graph 1-junction and the right-hand side by a two-port bond graph element, as described in Section A.4. However, the term $\zeta_2 \partial Q / \partial t$ representation in bond graph notation is not straightforward. Furthermore, the $\zeta_2 \partial Q / \partial t$ can be neglected based on the assumption that the angular mechanical domain dynamics are significantly faster than the hydraulic domain dynamics. This assumption is similar to the Kallesøe [123] and Kullick and Hackl [73] approach while simplifying similar models in their work.

Assumption 3.4.6. *The dynamics of the hydraulic domain are such that*

$$\zeta_2 \frac{\partial Q}{\partial t} \ll \zeta_3\omega Q - \zeta_4 Q^2 - \tau, \quad (3.70)$$

holds at all times.

In the coupling term of Equation (3.69), there is a notable relationship between the effort variable in the angular mechanical domain (torque τ) and the flow variable in the hydraulic domain (flow rate Q). According to Section A.4, this relationship is characteristic of the two-port element known as a gyrator. Therefore, in this context, the gyrator has the following expression:

$$\gamma = \zeta_3\omega - \zeta_4 Q. \quad (3.71)$$

Subsequently, the bond graph representation of Equation (3.69), excluding the $\zeta_2 \partial Q / \partial t$ term, is illustrated in Figure 3.1.

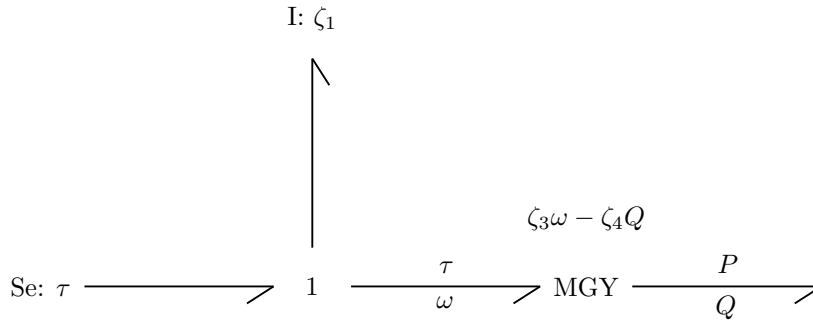


Figure 3.5: Centrifugal pump bond graph representation.

3.5 Centrifugal pump losses

Not all the torque applied to the shaft of a centrifugal pump is effectively converted into hydraulic energy due to various operational losses. These losses, both hydraulic and mechanical, significantly influence the pump's overall performance and efficiency. This section aims to characterize these losses, which include friction, local, shock, disk friction, and mechanical losses, and to derive corresponding bond graph resistance elements for each.

3.5.1 Friction loss

In the Darcy equation, as delineated in Section 3.3.1, the frictional loss within a generic channel is expressed as:

$$\Delta P = \lambda \frac{\rho L V^2}{d_h 2}. \quad (3.72)$$

According to Stepanoff [63], the Equation (3.72) can be employed for various pump components, including the suction nozzle, impeller channel, volute, and discharge nozzle. However, the practical measurement of both L and the hydraulic diameter d_h can pose challenges in numerous scenarios. As a solution, Stepanoff [63] proposed grouping all frictional losses under a single term. In contrast, Paternost *et al.* [60] distinguished between local and viscous frictional losses. They assumed that the friction factor within a generic channel is the sum of a viscous term, which dominates at reduced flow rates, and a turbulent component that becomes significant at high flow rates. As such, the friction factor within the pump's channel can be expressed as:

$$\lambda = \frac{k_{\text{lam}}}{Re} + k_{\text{turb}} Re^{n_t}, \quad (3.73)$$

where k_{lam} , k_{turb} , and n_t are constants determined empirically.

Substituting Equation (3.73) into Equation (3.72) and taking into account that $V = Q/A$, we

obtain:

$$\begin{aligned}
\Delta P &= \left(\frac{k_{\text{lam}}}{Re} + k_{\text{turb}} Re^{n_t} \right) \frac{\rho L}{d_h} \frac{Q^2}{2A^2}, \\
&= \left(\frac{k_{\text{lam}} \mu A}{\rho Q d_h} + k_{\text{turb}} \left(\frac{\rho Q d_h}{\mu A} \right)^{n_t} \right) \frac{\rho L}{d_h} \frac{Q^2}{2A^2}, \\
&= \frac{k_{\text{lam}} \mu L Q}{2d_h^2 A} + k_{\text{turb}} \left(\frac{\rho Q d_h}{\mu A} \right)^{n_t} \frac{\rho L}{d_h} \frac{Q^2}{2A^2}.
\end{aligned} \tag{3.74}$$

Incorporating the friction losses using bond graph notation, by considering the tetrahedron of states, Equation (3.74) can be rewritten as:

$$R_{cf} = \frac{k_{\text{lam}} \mu L}{2d_h^2 A} + k_{\text{turb}} \left(\frac{\rho Q d_h}{\mu A} \right)^{n_t} \frac{\rho L}{d_h} \frac{Q}{2A^2}. \tag{3.75}$$

Grouping the geometrical terms as constants, for simplification, we can express Equation (3.75) as:

$$R_{cfg} = k'_{\text{lam}} \mu + k'_{\text{turb}} \rho \left(\frac{\rho Q}{\mu} \right)^{n_t} Q, \tag{3.76}$$

where k'_{lam} and k'_{turb} are the grouped terms for the laminar and turbulent coefficients.

3.5.2 Local losses

As discussed in Section 3.3.2, obtaining an analytical expression to calculate losses in components like valves and fittings presents a considerable challenge due to the intricate nature of the flow. Similarly, Stepanoff [63] argues that under the specific flow conditions encountered within pumps, deriving an analytical solution for friction loss is also complex. In this context, Stepanoff [63] suggests an approach that aligns with the methodology outlined in Section 3.3.2 for evaluating the equivalent local losses in valves and pipe fittings. In the context of a single-stage centrifugal pump, these local losses encompass those originating from components such as the suction nozzle, diffuser, discharge nozzle, and volute. It can be expressed as:

$$k_{mc} = \sum_{i \in \psi} K_m^i, \tag{3.77}$$

where ψ is the set containing all the centrifugal pump local losses. In practice, however, it is challenging to obtain the local loss for each component individually and then sum them. Usually, the local losses are combined into one, k_{mc} , and obtained experimentally. For the bond graph element to represent this combined loss, we can use the expression presented in Equation (3.41), which yields.

$$R_{mc} = \frac{\rho k_{mc} Q}{2}. \tag{3.78}$$

3.5.3 Shock loss

Considering an impeller design where at a flow rate Q_s , the flow direction aligns with the vane angles at both entrance and exit of the impeller, there will be no additional losses in these points. However, for flow rates other than Q_s , there will be sudden changes in flow velocity direction and magnitude that will induce losses [63]. These losses can be expressed as:

$$\Delta P_{s1} = \rho k_{s1} \Delta c_{u1}^2, \quad (3.79)$$

for the entrance, and

$$\Delta P_{s2} = \rho k_{s2} \Delta c_{u2}^2, \quad (3.80)$$

for the exit of the impeller, where k_{sx} is a constant.

In Figure 3.6, when the flow rate is at Q_s , the normal velocity at the entrance of the impeller is denoted as c_{m1} . In this condition, the flow approaches the impeller at an angle of α_1 with a tangential component of the absolute velocity, represented as c_{u1} . If there is a reduction in flow rate such that $c_{m1}' < c_{m1}$, the liquid is then expected to have a tangential component c_{u1}' , such the liquid keeps entering the vanes at an angle β_1 . The difference between these tangential components can be calculated as:

$$\Delta c_{u1} = c_{u1}' - c_{u1}. \quad (3.81)$$

Similarly, at the pump discharge, as depicted in Figure 3.6, for the flow rate Q_s , the normal velocity is denoted as c_{m2} , and the tangential component of the absolute velocity is given by c_{u2} . If the flow rate is reduced, the tangential component will increase to c_{u2}' . Consequently, the increment in the tangential component is computed as:

$$\Delta c_{u2} = c_{u2}' - c_{u2}. \quad (3.82)$$

For flow rates exceeding Q_s , the values of both Δc_{u1} and Δc_{u2} turn negative.

Considering Figure 3.6 and a scenario wherein a flow rate, Q^* , the flow either enters or exits perpendicular to the impeller:

$$\alpha_x = 90^\circ \implies c_{ux} = 0 \therefore \Delta c_{ux} = c_{ux}'. \quad (3.83)$$

From the velocity triangle illustrated in Figure 3.4, c_{ux}' can be represented as:

$$c_{ux}' = u_x - w_{ux}, \quad (3.84a)$$

$$= u_x - \frac{c_{mx}'}{\tan \beta_x}. \quad (3.84b)$$

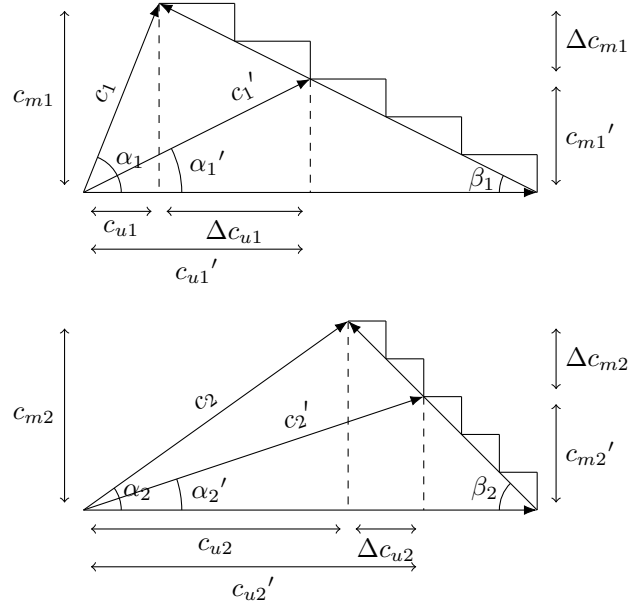


Figure 3.6: Shock component of peripheral velocity at entrance and discharge of the impeller.

Furthermore, the volumetric flow from all the impeller vanes can be expressed as:

$$Q = c_{mx}' A_x \therefore c_{mx}' = \frac{Q}{A_x}. \quad (3.85)$$

Given that $u_x = \omega r_x$, and by substituting Equations (3.84b) and (3.85) into Equation (3.83) we obtain:

$$\Delta c_{ux} = u_x - \frac{c_{mx}'}{\tan \beta_x}, \quad (3.86a)$$

$$= \omega r_x - \frac{c_{mx}'}{\tan \beta_x}, \quad (3.86b)$$

$$= \omega r_x - \frac{Q}{A_x \tan \beta_x}. \quad (3.86c)$$

Then, by substituting Equation (3.86c) into Equation (3.79) and Equation (3.80) we obtain:

$$\Delta P_{s1} = \rho k_{s1} \Delta c_{u1}^2, \quad (3.87a)$$

$$= \rho k_{s1} \left(\omega r_1 - \frac{Q}{A_1 \tan \beta_1} \right)^2, \quad (3.87b)$$

$$= k_{s1} r_1^2 \rho \omega^2 - \frac{2k_{s1} r_1 \rho \omega Q}{A_1 \tan \beta_1} + \frac{k_{s1} \rho Q^2}{A_1^2 \tan^2 \beta_1}. \quad (3.87c)$$

Similarly, for the impeller's exit, we have:

$$\Delta P_{s2} = k_{s2} r_2^2 \rho \omega^2 - \frac{2k_{s2} r_2 \rho \omega Q}{A_2 \tan \beta_2} + \frac{k_{s2} \rho Q^2}{A_2^2 \tan^2 \beta_2}. \quad (3.88)$$

To represent this in bond graph notation, considering the tetrahedron of states, we can rewrite

Equations (3.87c) and (3.88) as:

$$R_{sx} = k_{sx} \left(\frac{r_x^2 \rho \omega^2}{Q} - \frac{2r_x \rho \omega}{A_x \tan \beta_x} + \frac{\rho Q}{A_x^2 \tan^2 \beta_x} \right), \quad (3.89)$$

where the subscript x can represent either 1 or 2, referring to the impeller's inlet and outlet respectively.

3.5.4 Leakage loss

According to Takács [124], the primary sources of leakage losses in pumps are the clearances between stationary and rotating components, specifically in regions like the impeller eye and balancing holes. Furthermore, the leakage losses tend to reduce as the liquid flow rate increases. Additionally, Gülich [125] mentions that the annular seal significantly contributes to these losses. They degrade the pump efficiency by transforming the kinetic energy from the impeller into heat, which could have been converted into pressure instead.

As highlighted by Gülich [125], the friction estimation for turbulent flow due to these leakages is primarily experimental. Obtaining these friction coefficients of annular seals across a broad spectrum of Reynolds numbers is challenging. Since they require high-pressure differences and due to measurement accuracy problems in these conditions, it is often necessary to extrapolate from the available test data to analyze higher Reynolds numbers conditions.

Gülich [125] provides an expression for the friction coefficient that considers variations on the seal surface, including potential grooves and isotropic patterns. However, as Gülich [125] mentions, these coefficients and the related corrections are approximations. The effective resistance coefficients are highly susceptible to the specificities of the surface structure. Due to the various factors affecting leakages and the scarcity of pertinent test data, Gülich [125] acknowledges that leakage calculations can carry uncertainties up to $\pm 30\%$. Such uncertainties can arise from turbulence, roughness structures, pressure variations across the seal, manufacturing-related clearance variations, and considerations like stator deformations under operational stresses. Notably, seemingly inconsequential deviations such as minor rounding or chamfering might lead to substantial variations, often resulting in diminished loss coefficients.

3.5.5 Disk friction loss

When a circular disk or a cylinder is immersed and rotates within a static fluid, a velocity gradient can be observed. This gradient induces shear stresses, denoted as Γ , in the fluid. These stresses are directly proportional to the velocity gradient, $\partial u / \partial y$, as shown in:

$$\Gamma \propto \frac{\partial u}{\partial y}. \quad (3.90)$$

In practical applications, directly deriving Equation (3.90) can be challenging. Instead, it is often represented using a coefficient $f_d(Re, \epsilon_r/L)$ [125]. Therefore, for a disk rotating in a stationary fluid (without the influence of a casing), the shear stress can be expressed as:

$$\Gamma = \frac{f_d(Re, \frac{\epsilon}{L})\rho v^2}{2}, \quad (3.91)$$

where in case u is the fluid velocity. The frictional force acting on a surface element, defined by:

$$dA = 2\pi r dr, \quad (3.92)$$

can be expressed in terms of shear stress as:

$$dF = \Gamma dA \implies dF = \Gamma 2\pi r dr. \quad (3.93)$$

This frictional force dF exerts a moment due to its position relative to the disk's radius. This torque due to friction is given by:

$$d\tau = r dF. \quad (3.94)$$

By substituting Equations (3.91) and (3.93) into Equation (3.94), we obtain:

$$d\tau = \pi \rho f_d \left(Re, \frac{\epsilon}{L} \right) v^2 r^2 dr. \quad (3.95)$$

Using $u = \omega r$, the expression becomes:

$$d\tau = \pi \rho f_d \left(Re, \frac{\epsilon}{L} \right) \omega^2 r^4 dr. \quad (3.96)$$

When computing the overall torque τ_d due to disk friction, it is essential to account for the contributions of all surfaces rotating within the fluid. These surfaces encompass the impeller's front and rear shrouds, cylindrical faces, and annular seals. Thus, we need to integrate Equation (3.96) over the surfaces of these components. Consider ψ_n a parameter that describes the geometry of each component. The integral limits for the geometry n are given by ψ_n^1 and ψ_n^2 . Then we define a set ϕ containing these settings:

$$\phi = \{\psi_0 \ \psi_1 \ \psi_2 \ \dots\}. \quad (3.97)$$

Using the set ϕ , the overall torque τ_{df} can be obtained by integrating over all elements of set ϕ and summing up the contributions from all components:

$$\tau_{df} = \sum_{s \in \phi} \int_{s^1}^{s^2} \pi \rho f_d^s \left(Re_s, \frac{\epsilon}{L_s} \right) \omega^2 r^4 dr. \quad (3.98)$$

The superscript or subscript s denotes applicability to the geometry ψ_n . In the specific scenario

where we focus on one of the impeller's faces (treated as a disk), the torque can be computed by integrating Equation (3.96) between the impeller's inner radius (r_1) and outer radius (r_2):

$$\tau_{df}^i = \int_{r_1}^{r_2} \pi \rho f_d^i \left(Re, \frac{\epsilon}{L} \right) \omega^2 r^4 dr, \quad (3.99a)$$

$$\tau_{df}^i = \frac{\pi}{5} \rho f_d^i \left(Re, \frac{\epsilon}{L} \right) \omega^2 r_2^5 \left(1 - \frac{r_1^5}{r_2^5} \right). \quad (3.99b)$$

However, obtaining an analytical solution for the integral becomes complex for other geometries due to their distinctive characteristics. Notably, the resulting expressions from these integrals mainly depend on the specific geometry, allowing us to represent them with a constant k_{df}^s where $s \in \phi$, we can group with others constants and geometrical parameters. Thus, Equation (3.98) can be simplified as:

$$\tau_{df} = \sum_{s \in \phi} k_{df}^s \rho f_d^s \left(Re_s, \frac{\epsilon}{L_s} \right) \omega^2. \quad (3.100)$$

Nonetheless, we still have to define the friction coefficient function. It is worth noting that, despite the various correlations for the disk friction coefficient ($f_d(Re, \epsilon/L)$), and friction contributions of the complex geometries beyond the impeller's face. The friction coefficient and geometrical parameters are often grouped and obtained experimentally. Following the approach by Biazussi [61], we consider two distinct contributions: a viscous component dependent on the reciprocal of Reynolds number and an inertial one reliant solely on geometry. Thus, Equation (3.100) can be expressed as:

$$\tau_{df} = \sum_{s \in \phi} k_{df}^s \rho \omega^2 \left(\frac{k_{Re}^s}{Re} + k_g^s \right), \quad (3.101a)$$

$$= \sum_{s \in \phi} k_{df}^s \rho \omega^2 \left(\frac{k_{Re}^s \mu}{\rho \omega r} + k_g^s \right), \quad (3.101b)$$

$$= \sum_{s \in \phi} \frac{k_{Re}^s \mu k_{df}^s \omega}{r} + k_g^s k_{df}^s \rho \omega^2, \quad (3.101c)$$

where k_{Re}^s is a constant for viscous contribution and k_g^s the constant for inertial contribution. Then, we can further combine constants across all components into just two terms, k_v and k_i , resulting in:

$$\tau_{df} = k_v \mu \omega + k_i \rho \omega^2 \quad (3.102)$$

Furthermore, Gülich [125] states that when a body revolves within a casing, as is common in pumps, the velocity distribution between the casing and the rotating body is influenced by the distance between the impeller and the casing wall. This distribution is also affected by the boundary layers forming on both stationary and rotating surfaces. Consequently, a core flow of $u = 1/2\omega r$ is typically established, suggesting that $u = \omega r$ might not always hold. Thus, as

mentioned by Gülich [125], for a disk within a casing, the power absorbed can be half that for a free disk in a stationary fluid. However, when obtained experimentally, the grouped constants of Equation (3.102) will inherently account for the aforementioned disparities.

In the bond graph notation, to represent this loss using a resistance element, as illustrated by the tetrahedron of states, we have to divide Equation (3.102) by ω . Thus, the disk friction resistance is given by:

$$R_{df} = k_v \mu + k_i \rho \omega. \quad (3.103)$$

3.5.6 Mechanical losses

The mechanical losses associated with bearings and stuffing boxes have been extensively researched, as evidenced by a vast literature. One key empirical phenomenon that emerges in the context of journal bearings is the Stribeck effect, which describes the relationship between friction, angular velocity, and contact forces. This effect typically considers three lubrication regimes: boundary, mixed, and hydrodynamic.

In the boundary lubrication regime, surface roughness plays a pivotal role, mainly in dry or semi-lubricated bearings. This state of lubrication is most pronounced during the start, stop, and low-speed operations of machinery. Conversely, hydrodynamic lubrication is characterized by a separating fluid film being drawn into a converging, wedge-shaped zone. Both the frictional power loss and pressure within this film are determined by the lubricant's viscosity, in conjunction with the geometry and shear rate dictated by the bearing's operational conditions. The mixed lubrication is an intermediate condition between the boundary and hydrodynamic regimes. In this condition, the load imposed on the system is shared between the fluid and the tips of the asperities [126, 127].

In the context of centrifugal pumps, Stepanoff [63] states that friction loss in bearings and stuffing boxes is of secondary importance. It is also worth noting that although the friction loss in journal bearings has been standardized, discrepancies arise due to manufacturer-specific variations. Furthermore, these losses are typically marginal and necessitate specialized instrumentation to measure.

Given the scope of this study, the mechanical friction analysis was simplified by excluding the boundary and mixed lubrication regimes. Instead, it was opted for a constant as an approximation of the hydrodynamic regime. This work focuses primarily on evaluating the dynamics stemming from varying operational points and the impact of emulsions rather than delving into pump startups and stops. Accordingly, the frictional components from the bearing and stuffing box can be succinctly represented as:

$$\begin{aligned} \tau_m &= k_{\text{bearing}} \omega + k_{\text{seal}} \omega, \\ &= k_{\text{mec}} \omega. \end{aligned} \quad (3.104)$$

where k_m is an empirically derived constant encapsulating the friction factors from both the bearings and the stuffing box. In the context of bond graph notation, this loss can be represented using a resistance element, as delineated by the tetrahedron of states. Taking Equation (3.104) and dividing by ω , we can then define the mechanical of bearings and stuffing boxes as friction resistance as:

$$R_{\text{mec}} = k_{\text{mec}}. \quad (3.105)$$

3.6 Valves

A typical type of valve utilized in the process industry is the valve equipped with a spring-diaphragm pneumatic actuator, as illustrated in Figure 3.7. This valve operates by injecting pressurized air into a chamber, which contains a diaphragm. Variations in the air pressure cause the diaphragm to actuate the valve stem, consequently modulating the valve's position. The regulation of this air pressure enables precise control over the valve's position. Moreover, the valve is designed with an integrated spring mechanism. This ensures the valve reverts to a predetermined safe state (fully open or closed) during air pressure loss.

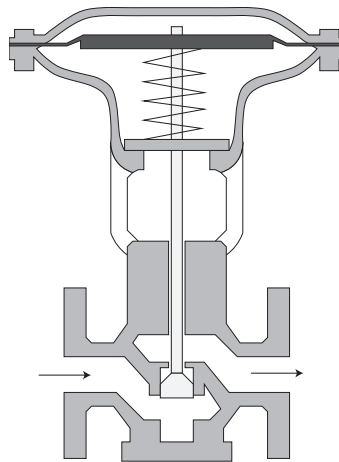


Figure 3.7: Schematic of a typical control valve featuring a spring-diaphragm pneumatic actuator.

This section provides an overview of the valve within the context of the ESP system under study. It commences with the presentation of static models for turbulent and laminar flow regimes in incompressible fluids (Sections 3.6.1 and 3.6.2). Following this, a bond-graph resistance model pertinent to the valve is formulated in Section 3.6.3. Notwithstanding the inherent dynamic nature of the valve, this study will not explore its dynamic characteristics. For the purpose of the experimental investigations, the valve's position will be assumed as fixed.

Assumption 3.6.1. *The valve is considered to exhibit static behavior, with no dynamic changes in position during the experiments.*

3.6.1 Static model for turbulent flows in incompressible fluids

According to ISA75.01.01 [128], the valve fundamental equation for turbulent flow in incompressible fluids can be expressed as:

$$Q = C_v N_1 F_p \sqrt{\frac{\Delta P}{\rho^*}}, \quad (3.106)$$

where C_v is the flow coefficient, N_1 is a numerical constant for unit conversion. The term ρ^* is the relative density of the fluid in respect to the water density at 15 °C (ρ_0). The F_p denotes the pipe geometry factor, which accounts for variations in diameters between valves and pipes.

As mentioned by ISA75.01.01 [128], the relationship described in Equation (3.106), can be used to obtain either the flow coefficient, the flow rate, or the pressure differential, given any two of these variables. However, it is crucial to note the application limitations of this model. As emphasized by ISA75.01.01 [128], this equation strictly applies to single-component, single-phase fluids. Nevertheless, it is possible to cautiously extend its applicability to multi-component liquid mixtures, provided certain conditions are met, such as the fluid mixture is homogeneous. The mixture should be in chemical and thermodynamic equilibrium, and the throttling process should predominantly occur outside the multiphase region.

In some scenarios, non-turbulent flow conditions might occur in the control valve due to reduced flow rates and high fluid viscosities. In such conditions, a separate model becomes necessary. According to ISA75.01.01 [128], the Equation (3.106) is applicable when the Reynolds number of the valve, denoted as Re_v , is greater or equal than 10 000. This Reynolds number can be computed using:

$$Re_v = \frac{\rho N_4 F_d Q}{\mu \sqrt{C_v F_L}} \left(\frac{F_L^2 C_v^2}{N_2 d^4} + 1 \right)^{1/4}, \quad (3.107)$$

where N_2 and N_4 are a numerical constant for unit conversion. The term F_d denotes the valve style modifier, and F_L is the liquid pressure recovery factor for a control valve without any attached fittings.

3.6.2 Static model for non-turbulent flows in incompressible fluids

It is crucial to consider the scope and applicability of the valve models and coefficients found in the literature before using them. In this context, according to ISA75.01.01 [128], for $Re_v \leq 10\,000$, the equation Equation (3.106) is non-longer valid and appropriate equations for non-turbulent flow should be applied. The ISA75.01.01 [128] states that the valve fundamental

flow model for non-turbulent incompressible flow can be expressed as:

$$Q = C_v N_1 F_r (Re_v) \sqrt{\frac{\Delta P}{\rho^*}}, \quad (3.108)$$

where F_r is the Reynolds number factor. This factor, when $Re_v \geq 10$, is described as:

$$F_r = \min \begin{cases} 1 + \frac{0.33 \sqrt{F_l}}{n_v^{0.25}} \log_{10} (ReV/10000), \\ \frac{0.026}{F_L} \sqrt{n_v Re_v}, \\ 1.0. \end{cases} \quad (3.109)$$

The trim style of the valve is described by the constant n_v , obtained as:

$$n_v = \frac{N_2}{(C_v/d^2)^2}. \quad (3.110)$$

Noteworthy, this is strictly pertinent to valves with “full size” trim.

As stated by ISA75.01.01 [128], the Equations (3.108) and (3.109) are valid for fluids exhibiting Newtonian rheology and non-vaporizing fluids. They argue that non-Newtonian fluids require a different treatment due to their characteristic change in viscosity as a function of shear rate (which is proportional to flow rate).

3.6.3 Valve bond graph resistance model

The valve models given by Equations (3.106) and (3.108), as discussed in Sections 3.6.1 and 3.6.2 respectively, are similar. Their main difference is the valve factor. The turbulent flows use a valve pipe geometry factor (F_p), while the non-turbulent flows use the Reynolds number factor (F_r). The latter, as indicated in Section 3.6.2, depends on the Reynolds number and has the model restrictions. Therefore, considering a single expression for the valve in both flow regimes, we introduce F^* as:

$$F^* = \begin{cases} F_p, & Re_v > 10000, \\ F_r(Re_v), & Re_v \leq 10000. \end{cases} \quad (3.111)$$

As mentioned in Section 3.6.1, the relationship described in Equation (3.106), can also be used to obtain the pressure difference. Thus, considering the valve factor F^* and rearranging the

Equation (3.106) we have:

$$Q = C_v N_1 F^* \sqrt{\frac{\Delta P}{\rho^*}}, \quad (3.112a)$$

$$Q^2 = (C_v N_1 F^*)^2 \frac{\Delta P}{\rho^*}, \quad (3.112b)$$

$$\Delta P = \frac{\rho^* Q^2}{(C_v N_1 F^*)^2}. \quad (3.112c)$$

From the bond graph tetrahedron of states, we have that $\Delta P = R_v Q$. Considering the relationship in Equation (3.112c) we have that the R_v can be expressed as:

$$R_v = \frac{\rho^* Q}{(C_v N_1 F^*)^2}. \quad (3.113)$$

If we consider the valve actuation we can rewrite Equation (3.113) as:

$$R_v(a) = \frac{\rho^* Q}{(C_v(a) N_1 F^*)^2}, \quad (3.114)$$

where a is the valve opening.

3.7 Twin-screw pumps

3.7.1 Bond graph representation

According to Karassik [129], screw pumps are positive displacement devices that deliver a specific volume of liquid at each rotor revolution. This volume is denoted as the displacement volume, V_D . It represents the theoretical volume of liquid displaced per rotor revolution and depends solely on the rotors' physical dimensions. In an ideal scenario, without internal clearances, the actual net flow rate Q matches with the theoretical flow rate. Thus, we can model this ideal relationship of rotor rotation with displaced volume using the transformer port of bond graphs as shown in Figure 3.8.

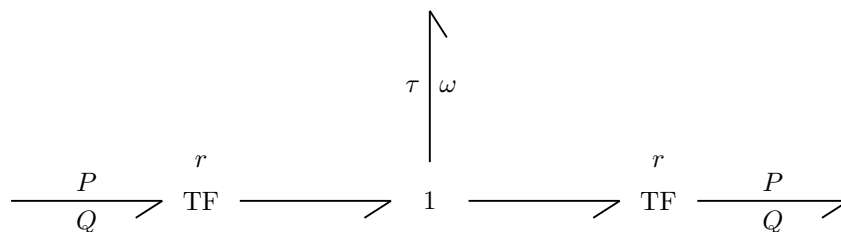


Figure 3.8: Bond graph representation of an ideal twin screw pump.

In Figure 3.8, the bond graph provides a schematic representation of the screw pump, omitting other significant elements. The series arrangement of the two transformers reflects the screw pump's series placement within the flow line, emphasizing the continuous flow passing through it. In this arrangement regarding power flow, we have that the hydraulic power is first converted to mechanical power and then reconverted to hydraulic power. Within the mechanical domain, elements such as the rotor's inertia and stiffness of the screw pump and mechanical frictional losses can be modeled and considered.

However, in real-world conditions, there are internal clearances in the screw pumps. Consequently, a pressure difference leads to internal leakage from the outlet to the inlet. This phenomenon, termed "slip", varies based on factors like the pump model, clearance amount, the liquid's viscosity during pumping, and the pressure difference. Notably, for any given set of these conditions, the slip remains largely unaffected by the pump's speed [129]. Therefore, the actual screw pump flow rate is given by:

$$Q = Q_t - Q_L(\Delta P, \mu), \quad (3.115)$$

where Q_t denotes the theoretical flow rate, and Q_L represents the slip flow rate. In scenarios where the pressure difference between the pump's inlet and outlet is minimal, the influence of slip can be disregarded, resulting in $Q \approx Q_t$. Although the slip can be computed from literature correlations, it is usually obtained from experimental data.

Thus, we can further develop the bond graph model presented in Figure 3.8. We can incorporate the inertia of the pump's shaft and screw and account for losses from mechanical friction from bearings and the interaction between the screw and the fluid, for instance. These aspects can be directly incorporated into the bond graph's mechanical domain. Further, based on Equation (3.115), the internal leakage due to clearances can be modeled by introducing a resistance element connecting the input and output of the screw pump with a 0-junction. Consequently, the pump's output Q will be the theoretical flow rate (Q_t) minus and the leakage flow rate (Q_L). Considering these aspects, a simplified bond graph representation of the screw pump is illustrated in Figure 3.9.

As discussed by Karassik [129], the inertia effects within twin-screw pumps are minimal. The inertia of the shaft, the screw, and the liquid dynamics inside the pump are argued to have negligible impact on the overall system dynamics. It allows us not to consider the effects of the inertia elements shown in Figure 3.9.

3.7.2 Ideal displacement or swept volume flow rate

In Section 3.7.1, it was introduced the bond graph model for a general screw-type pump. However, the transformer port's expression and leakage resistance values still need to be addressed. In this section, we present the formulation to obtain the expression relating to the transformer port, particularly for a twin-screw pump, as illustrated in Figure 3.10.

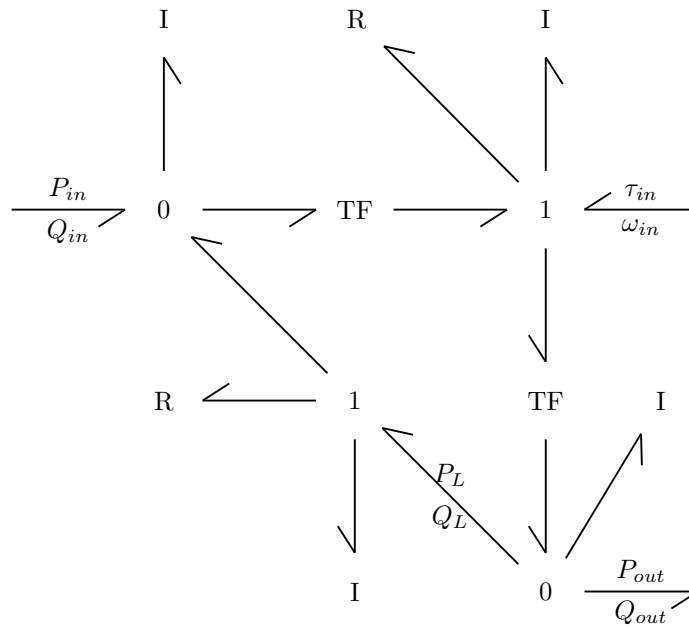


Figure 3.9: Bond graph representation of a screw pump, considering clearance and the mechanical components.

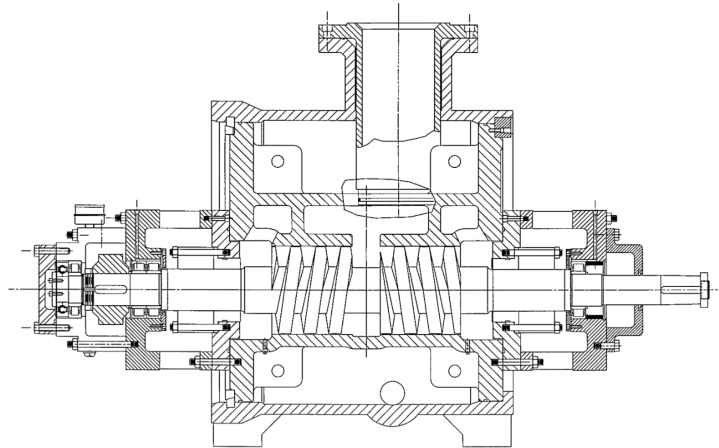


Figure 3.10: Twin-screw pump [130].

According to Prang and Cooper [130], the theoretical volume displaced by a twin-screw pump can be described as:

$$Q_t = n_s \omega_t \frac{d_s^3}{2(n_l + 1)} \frac{L_{sc}}{d_s} \alpha_t (1 - k_{rd}^2). \quad (3.116)$$

In this formulation, the angular velocity of the twin-screw (ω_t) is in radians per second. The fraction α_t signifies the annular space portion between the root and the tip of the screw threads not occupied by the threads. The ratio of the screw's root diameter to its tip diameter (d_s) is expressed as k_{rd} . The term L_{sc} stands for the axial length of each pumping screw. n_l indicates the number of chambers created by the interlocking screws, and n_s is the count of screw threads.

Examining the Equation (3.116), we note that a transformer port characterizes the relationship between the rotational mechanical and hydraulic domains. Where the hydraulic domain's flow variable, Q_t , corresponds to the mechanical domain's flow variable, ω_t . Consequently, the transformer expression for the twin-screw pump can be given as:

$$r_t = n_s \frac{d_s^3}{2(n_l + 1)} \frac{L_{sc}}{d_s} \alpha_t (1 - k_{rd}^2). \quad (3.117)$$

It is important to note that, as the parameters in Equation (3.117) are all constant and geometrical parameters, we can group them into a single constant coefficient.

3.7.3 Liquid leakage in twin-screw pumps

In Section 3.7.1 it was introduced the general bond graph model for screw-type pumps. However, the resistance due to leakage was not detailed. This section focuses on formulating this resistance. According to Vetter [131], the primary leakage sources in twin-screw pumps arise from the circumferential clearance between the screw's peripheral diameter and the housing, the radial clearance between the screw profile's internal and external diameters, and the flank clearances between the screw profile's flanks.

Factors such as machining tolerances, screw stiffness, and housing compliance due to pressure directly relate to these clearances. Consequently, the total clearance flow rate is a summation of all individual leakages:

$$Q_L = Q_{cc} + Q_{rc} + Q_{fc}, \quad (3.118)$$

where Q_{cc} , Q_{rc} , and Q_{fc} represent the flow rates due to circumferential, radial, and flank clearances, respectively. Vetter [131] emphasized that the circumferential clearance, given its larger cross-section, often dominates when compared to the others.

Vetter [131] provided formulations for both laminar and turbulent flows to calculate the leakage flow rate for each clearance. These can be expressed in the bond graph framework as resistance elements. For the circumferential clearance in laminar flow:

$$R_{lcc} = \frac{12 w_{sp} \mu}{L_{cc} w_{cc}^3}, \quad (3.119)$$

where w_{sp} is the width of the screw profile, w_{cc} denotes the width of the circumferential clearance, and L_{cc} represents the length of the circumferential clearance. For turbulent flow:

$$R_{tcc} = \frac{\rho w_{sp} Q}{4 w_{cc} \left(2 L_{cc} w_{cc} \log \left(\frac{2 w_{cc}}{K_{sr}} + 0.97 \right) \right)^2}, \quad (3.120)$$

where K_{sr} is roughness factor for the twin-screw pump. For the radial clearance under laminar

flow, it can be expressed as:

$$R_{lrc} = \frac{12\mu}{w_{sp}} \int_0^{L_{ec}} \frac{1}{w_{rc}(x)} dx, \quad (3.121)$$

where w_{rc} is the width of the radial clearance, and L_{ec} represents the effective length of the radial clearance. For turbulent flow:

$$R_{trc} = \frac{\rho Q}{w_{sp}} \int_0^{L_{ec}} \frac{1}{(2 \log(2 w_{rc}(x)/K_{sr} + 0.97))^2 w_{rc}(x)^3} dx. \quad (3.122)$$

For the flank clearance under laminar flow, we have:

$$R_{lfc} = \frac{24 L_{sf} \mu}{L_{sd} w_{fc}^3}, \quad (3.123)$$

where w_{fc} is the width of the flank clearance, L_{sf} represents the length of the flank clearance, and L_{sd} denotes the chamber depth. For turbulent flow is given as:

$$R_{tfc} = \frac{\rho L_{sc} Q}{w_{fc} \left(2 L_{sd} w_{fc} \log \left(\frac{2 w_{cc}}{K_{sr}} + 0.97 \right) \right)^2}, \quad (3.124)$$

where L_{sc} is the active length of the flank clearance.

The bond graph resistance elements derived from Vetter [131] rely heavily on knowledge of the twin-screw pump geometry. However, obtaining precise geometry parameters in practice can be challenging. Prang and Cooper [130] provides a simplified approach for calculating the total leakage flow rate, Q_L . They observed experimentally that Q_{cc} approximates to 80 % of Q_L , a value that varies with the Reynolds number. A higher Reynolds number results in higher values. As a result, they excluded Q_{fc} and Q_{rc} from their considerations, focusing only on Q_{cc} and introducing a factor δ_L to account for the 80 %. It allows for a simplified bond graph resistance element for the twin-screw pump leakage with experimentally determined constants.

Given this, the pressure difference between the chambers, ΔP_L , can be expressed as:

$$\Delta P_L = n_L \frac{\rho}{2} \left(\frac{Q_{cc}}{A_{cc} \delta_L} \right)^2 \left(\frac{\lambda_{cc} L_{cc}}{d_{cc}} + K_L \right), \quad (3.125)$$

where, A_{cc} refers to the total circumferential clearance cross-sectional area. The friction factor for the circumferential clearance is given by λ_{cc} . The variables L_{cc} and d_{cc} correspond to the equivalent length and hydraulic diameter for the circumferential clearance, respectively. K_L is the loss coefficient representing flow losses as it enters the gap between the screw and the housing, while n_L denotes the number of chambers. We can rearrange Equation (3.125) to solve

for the flow rate:

$$Q_{cc} = \delta_L A_{cc} \sqrt{\frac{2 \Delta P_L}{n_L \rho \left(\frac{\lambda_{cc} L_{cc}}{d_{cc}} + K_L \right)}}. \quad (3.126)$$

In bond graph modeling, the resistance element is usually more easily characterized by the effort variable, in this case, ΔP_L . For laminar flows in pipelines, the friction factor is $64/Re$. Assuming only laminar flow through the clearances, we obtain:

$$\Delta P_L = n_L \frac{\rho}{2} \left(\frac{Q_{cc}}{A_{cc} \delta_L} \right)^2 \left(\frac{64 \mu}{\rho Q_{cc} d_{cc}} \frac{L_{cc}}{d_{cc}} + K_L \right), \quad (3.127a)$$

$$= \frac{32 \mu n_L L_{cc} Q_{cc}^2}{d_{cc}^2 \delta_L^2 A_{cc}^2} + \frac{\rho K_L Q_{cc}^2}{2 A_{cc}^2 \delta_L^2}. \quad (3.127b)$$

From the bond graph's tetrahedron of states and Equation (3.127b), the resistance element for leakage is given by:

$$R_L = \frac{32 \mu n_L L_{cc}}{d_{cc}^2 \delta_L^2 A_{cc}^2} + \frac{\rho K_L Q_{cc}}{2 A_{cc}^2 \delta_L^2}. \quad (3.128)$$

Grouping the terms, constants, and loss coefficient from Equation (3.128), we define K_{LL} for friction losses and K_{Lc} for local losses, we have:

$$R_L = K_{LL} \mu + K_{Lc} \rho Q_{cc}. \quad (3.129)$$

3.7.4 Simplified liquid leakage in twin-screw pumps

In Section 3.7.1, it was presented a bond graph model for screw-type pumps, including leakage as a connection between inlet and outlet. In this configuration the bond graph model could result in a Differential-Algebraic Equation (DAE) system. To simplify, it is possible to model leakage as a resistance at the twin-screw pump's outlet, which results into an Ordinary Differential Equation (ODE) format. This change streamlines the model by eliminating implicit variables, facilitating the analysis while maintaining essential dynamics.

In Section 3.7.3, the leakage volumetric flow rate (Q_L) was approximated by the circumferential clearance flow rate (Q_{cc}), and the leakage-induced pressure drop could be described by Equation (3.127b). By disregarding the minor loss K_L , attributable to flow entering the gap between the screw and the housing, and assuming predominant friction losses, we simplify Equation (3.127b) to:

$$\Delta P_L = \frac{32 \mu n_L L_{cc} Q_{cc}}{d_{cc}^2 \delta_L^2 A_{cc}^2}. \quad (3.130)$$

Aggregating geometrical and constant parameters from Equation (3.130) results in:

$$Q_{cc} = \frac{\Delta P_L}{K_{LL} \mu}. \quad (3.131)$$

Following Equation (3.115), the actual flow rate (Q) is:

$$Q = Q_t - Q_{cc}. \quad (3.132)$$

Substituting from Equation (3.131), the modified expression for the twin-screw pump is:

$$Q = r_t \omega - \frac{\Delta P_L}{K_{LL} \mu}. \quad (3.133)$$

The term $r_t \omega$ corresponds to a modulated transformer element as discussed in Section 3.7.2, while $\frac{\Delta P_L}{K_{LL} \mu}$ is as a resistance bond graph element, similar to Equation (3.129), thus:

$$R_{LS} = K_{LL} \mu. \quad (3.134)$$

3.8 Structural identifiability analysis

Given a set of ODE that describes a system dynamics, it contains a set of parameters and state variables. Thus, before trying to estimate the unknown parameters of a given dynamic system using an inverse problem-solving method, it is important to assess whether or not the parameters can be uniquely determined from a given set of data.

Consider a dynamical system in the following format

$$\dot{\mathbf{x}}(t) = \mathbf{f}(\mathbf{x}(t), \mathbf{u}(t), \Theta), \quad (3.135)$$

$$\mathbf{y}(t) = \mathbf{h}(\mathbf{x}(t), \mathbf{u}(t), \Theta), \quad (3.136)$$

where $\mathbf{x}(t)$ is an m -dimensional state vector, $\mathbf{u}(t)$ is an n -dimensional input signal, $\mathbf{y}(t)$ is an r -dimensional output signal or the measurable output, and Θ is k -dimensional vector of parameters. A parameter set Θ is said to be structurally globally identifiable if the following property holds:

$$\mathbf{h}(\mathbf{x}(t), \mathbf{u}(t), \Theta) = \mathbf{h}(\mathbf{x}(t), \mathbf{u}(t), \theta) \implies \Theta = \theta, \quad (3.137)$$

where θ is a k -dimensional vector of parameters. Furthermore, if the property in Equation (3.137) holds within a neighborhood of Θ , it is referred to as structurally locally identifiable.

Thus, the identifiability property serves as a prerequisite for practical parameter estimation. Additionally, as stated by Daneker *et al.* [132], if a parameter is locally identifiable, it implies that the search range for that parameter should be limited before attempting its estimation. On the other hand, for globally identifiable parameters, there is no need to define a search range.

4 Materials and methods

4.1 Experimental study

This chapter presents the experimental investigation carried out to validate the dynamic model and obtain the parameters of the Electrical Submersible Pump (ESP) system. The chapter is organized as follows: Sections 4.1.1 and 4.1.2 provide an in-depth description of the experimental setup, detailing the equipment and materials used. Sections 4.1.3 and 4.1.4 describes the data acquisition system employed for sampling instrument readings and the post-processing applied in the signals. Section 4.1.5 elaborates on the development of the experimental procedure, designed to ensure both safety and accurate data collection. Finally, Sections 4.1.6 and 4.1.7 outlines the experimental test matrix, specifying the various combinations of variables and conditions examined in this study.

4.1.1 Experimental assembly

The experimental setup is situated in the Experimental Laboratory of Petroleum Kelsen Valente Serra (LABPETRO) at the Center for Energy and Petroleum Studies (CEPETRO) of the University of Campinas. It was designed to investigate the behavior of Electrical Submersible Pumps (ESP) under various flow conditions. The setup accommodates both single-phase and two-phase (water/oil) flows. It serves multiple purposes, including pump performance evaluation under varying emulsion conditions, pump parameter identification, control technique validation, and dynamic model verification. The schematic representation of the experimental assembly is provided in Figure 4.1.

The experimental setup consists of four distinct flow lines: an oil flow line, a water flow line, a two-phase flow line dedicated to the oil-water mixture, and a closed-loop water line associated with the heat exchanger (HE). The oil and water flow lines start from a separation tank and converge at a T -joint, initiating the two-phase flow line forming the emulsion. Subsequently, the emulsion is directed into the ESP and returns to the separation tank. Each flow line has a specific instrumentation and devices mounted on it. The detailed explanation and the purpose of each flow line is presented as follows:

- **Oil flow line:** It conveys the oil phase from the separation tank to the mixing point. Along the oil flow line, a twin-screw pump is mounted to pressurize the line, and a shell and tube heat exchanger for temperature control of the oil. This flow line has a water-cut meter and a Coriolis meter used to measure the water fraction and the mass flow rate, respectively.

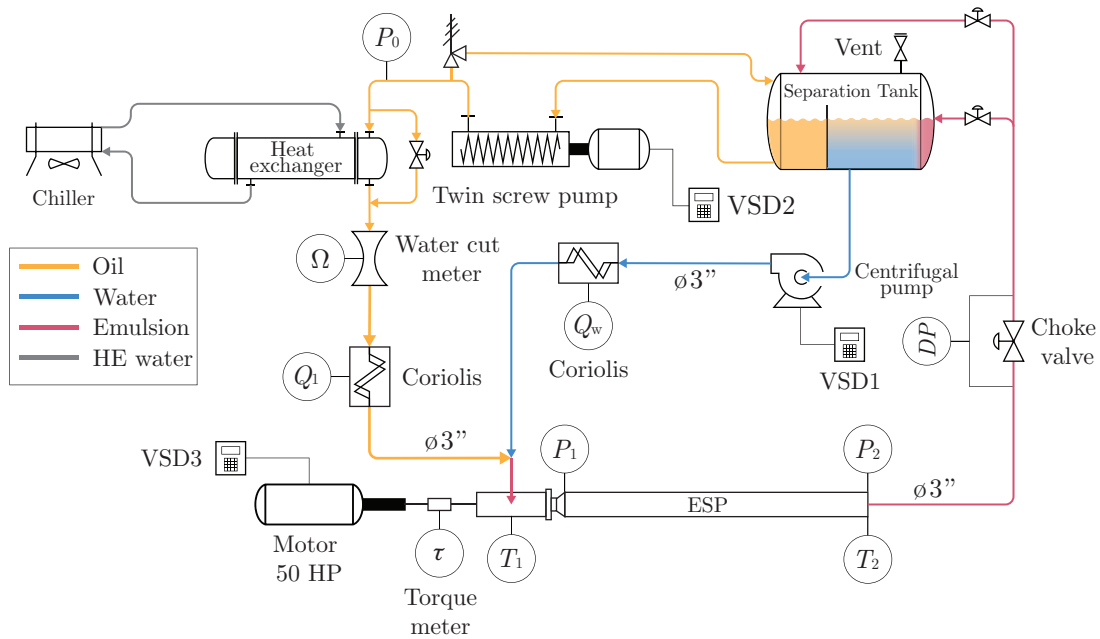


Figure 4.1: Schematic diagram of the experimental setup.

The primary purpose of this line is to provide a controlled oil flow for the two-phase experiments;

- **Water flow line:** Similar to the oil flow line, this line conveys the water phase from the separation tank to the mixing point. A centrifugal pump pressurizes the water line to enable the flow into the two-phase flow line. Additionally, the water line has a Coriolis meter for measuring mass flow rate and a remotely controlled valve to regulate the line's open or closed state. The primary purpose of this line is to provide a controlled water flow to obtain the desired emulsion condition;
- **Two-phase flow line:** This line conveys the oil-water mixture from the mixing point (in the T -joint) back to the separation tank. The ESP, which is the primary subject of this study, is mounted in this flow line. After being pumped by the ESP, the emulsion flows through a remotely controlled valve, which controls the ESP pressure gain and the flow rate. The main objective of this line is to enable the study of ESP performance under two-phase flow conditions;
- **Heat exchanger loop:** This heat exchanger water loop allows the operation of the shell and tube heat exchanger while regulating the oil flow line's temperature. The heat exchanger is equipped with a chiller, a heater, and a water tank, allowing for both cooling and heating of the fluid to adjust the temperature.

The primary equipment of the experimental setup comprises two models of Electrical Submersible Pumps (ESP) from Baker Hughes[®]: the eight-stage model P100L 538 series and the nine-stage model P47 538 series. These pumps are positioned downstream of the oil-water

mixing point, facilitating the study of pump behavior under various flow conditions. The P100L model features impellers with mixed flow geometry, each having an outer diameter of 108 mm and 7 blades. In contrast, the P47 model is a radial impeller of 108 mm in diameter and 7 blades.

The ESP is driven by a three-phase AC induction motor controlled by a variable speed driver (VSD). The VSD is programmed to change the pump speed in accordance with the desired angular velocity. The instrumentation for the ESP includes pressure transmitters at each pump stage, including the pump inlet and outlet, and temperature transmitters at the inlet and outlet. Thus, it is possible to measure the suction and discharge pressures at each stage and the suction and discharge temperatures. These measurements are crucial for real-time monitoring and proper experimental data acquisition.

The equipments specifications are presented in Table 4.1, and the instrumentation characteristics will be discussed in Section 4.1.2.

Table 4.1: Specifications of components used in the experimental setup

Line	Device	Manufacturer	Model/Specification
Oil	Pump	NETZSCH	Two-screw pump
	Motor	WEG	45 kW; 1775 RPM
	SY-101	WEG	CFW 700 Vectrue inverter; input signal 4 mA to 20 mA
Water	Pump	IMBIL	65160
	Motor	WEG	22 kW; 3535 RPM
	SY-102	WEG	CFW 700 Vectrue inverter; input signal 4 mA to 20 mA
Emulsion	Pump	Baker Hughes	P100L 538 series
	Motor	WEG	37 kW; 3555 RPM
	SY-103	WEG	CFW 09 Vectrue inverter; input signal 4 mA to 20 mA
	Tank	Intelfibra	Capacity 12 000 L
Heat control	Heat exchanger	FYTERM	T3480 shell and tube
	Heater	Mecalor	TMR-M-18-380/C
	Chiller	Mecalor	MSA-60-CA-380/C
Valve	Globe valve	Fisher	657; input signal 4 mA to 20 mA

The experimental setup employs two different fluids: water and a blend of mineral oil. These fluids are selected to obtain a two-phase liquid-liquid flow, forming a suitable emulsion for evaluating the ESP dynamics in this condition. The water used in the experiments has no

additional conditioning. The mineral oil blend was selected primarily for obtaining higher viscosity fluids, approximating real-field conditions. The viscosity of the mineral oil blend was characterized using a HAAKE MARS III rotational rheometer, as detailed in Appendix B.1. This characterization is essential for determining the fluid's viscosity while operating at different temperatures.

The temperature control in the experiments is crucial as the oil viscosity strongly depends on the temperature. Thus, the experiments can be conducted under different viscosity conditions using the same oil by regulating the temperature. Additionally, as the system operates in a closed loop, the temperature tends to rise over time, which leads to a constant temperature increase in the fluid temperature. Such change could result in misleading measurements and analysis, given that fluid viscosity directly influences the pump performance. Therefore, the temperature control allows fluid viscosity adjustment and stabilizes the fluid temperature during experiments. The temperatures at the inlet and outlet of the ESP are monitored, and the temperature control considers the temperature at the pump's inlet.

4.1.2 Instrumentation and measured variables

In Section 4.1.1, four distinct lines and their instrumentation were introduced as part of the experimental setup. While their purpose was mentioned, the specific instrumentation was not described. This section provides more detail on the variables that the experimental assembly can measure and the instrumentation specifications. An overview of the types of variables that are measured in this experimental setup is provided below.

- **Pressure and temperature:** The intake and discharge pressures of the ESP are monitored using capacitive-type pressure transmitters. Temperature transmitters are installed at approximately the same locations to measure the fluid temperature, which is crucial for viscosity calculations. The pressure is also measured and monitored at each ESP stage using the same pressure transmitter model. In configurations equipped with the ESP P47 model, the experimental assembly incorporates further pressure monitoring instrumentation: a pressure measurement at the heat exchanger intake and a differential pressure measurement across the valve.
- **Flow parameters:** The water and oil mass flow rates are measured using Coriolis meters. The water cut, or the water fraction in the oil phase, is determined using the water-cut meter.
- **Fluid properties:** The oil viscosity was characterized using a rotational rheometer, and this data is used in conjunction with temperature measurements to estimate the oil viscosity. The oil and water densities are measured using the Coriolis meters. Additionally, as the emulsion flows in the oil flow line, its density is measured by the Coriolis flow meter.

- **Mechanical parameters:** The torque and the ESP shaft angular velocity are measured by a torque meter.
- **Electrical Parameters:** The VSDs of each pump motor supply the three-phase induction motors. Additionally, the VSD of the ESP electrical motor provides the motor voltage and current measurements.

The pressure is measured using capacitive pressure transmitters of the 2088 series manufactured by Emerson RosemountTM. A temperature transmitter equipped with a PT100 resistance temperature detector (RTD) is employed for temperature monitoring, with a four-wire configuration and 1/10 DIN accuracy. The torque and angular velocity of the pump shaft are measured using the T21WN torque meter from HBM[®]. The water fraction in the oil phase is measured with the water cut meter model Nemko 05 ATEX 112, manufactured by Roxar[®]. Additionally, the Coriolis meter model F300S355 from Micro Motion[®] is utilized to measure the density and mass flow rates in the oil and water flow lines. The operational ranges and uncertainties associated with these instruments are provided in Table 4.2.

Table 4.2: Instrumentation specifications: range and uncertainty

Tag	Instrument	Model	Range	Uncertainty
FT-10X [‡]	Flow meters	Micro Motion [®] F300S355	0 to 100 m ³ h ⁻¹	0.2 % O.V.*
TT-10X [‡]	Temperature sensors	ECIL [®] PT100	0 to 100 °C	1/10 DIN
PT-10X [‡]	Pressure transducers	Emerson Rosemount 2088	0 to 2 MPa	0.065 % F.S. [†]
PDT-101 [‡]	Pressure transducers	Emerson Rosemount 2051	-0.1 to 2 MPa	0.065 % F.S. [†]
WCM-101	Water cut meter	Roxar Nemko 05 ATEX 112	0 to 100 %	1 % F.S. [†]
TTQ-101	Torque transmitter	HBM T21WN	0 to 100 N m	0.1 % F.S. [†]
TE-101	Encoder	Minipa MDT-2238A	0 to 166 Hz	0.05 % F.S. [†]

* O.V. : of value;

[†] F.S. : of full scale;

[‡] The X means that the specifications are also valid for the other instruments.

The sensors PT-10X, FT-10X, and WCM-101 produce output signals within the range of 4 mA to 20 mA, whereas the TTQ-101 and TE-101 sensors generates signals in the voltage range of -10 V to 10 V. Notably, the TT-10X sensor utilizes a 4-wire resistance measurement scheme for accurate signal acquisition.

4.1.3 Data acquisition system

As presented in Sections 4.1.1 and 4.1.2, the instrumentation and actuators integrated into the experimental apparatus exhibit different operational requirements. Specifically, the pressure, water cut, and Coriolis meters generate DC signals, while the torque and angular velocity meters produce DC voltage signals. The temperature transmitters employ a 4-wire scheme for resistance measurements. In contrast, the variable-frequency drives (*SY-101*, *SY-102*, *SY-103*) and the flow control valves (*FCV-101*, *FCV-102*, *FCV-103*) requires input signals within the range of 4 mA to 20 mA. Additionally, the temperature control system operates based on the Modbus protocol.

The experimental measurements are conducted through a data acquisition system model *cDAQ-9188 (DAQ-101)* from the manufacturer *National Instruments*. For the pressure, Coriolis, and water cut meters, which necessitate a 4 mA to 20 mA analog signal, an acquisition module model *NI-9203* from the same manufacturer is employed. This module comprises eight channels, each with a 16-bit resolution, an operational range of ± 20 mA, and a maximum sampling rate of 200 kHz. In the case of the torque and encoder meters, the acquisition is managed by a *NI-9201* module, which supports a voltage range of ± 10 V, a maximum sampling rate of 500 kHz, and has a 12-bit resolution. The temperature signals are captured using a *NI-9215* module, designed to accommodate a voltage range of ± 10 V, a sampling rate of 100 kHz per channel, and a 16-bit resolution. All modules used are integrated into the *DAQ-101*.

All the signal acquisition, generation, and control routines for the *SY-101*, *SY-102*, *SY-103*, *FCV-101*, *FCV-102*, and *FCV-103* were implemented in a Supervisory Control and Data Acquisition (SCADA) system using the LabVIEW™ software from *National Instruments*. The signal generation is managed by a *NI-9265* module integrated into the *DAQ-101*. It supports generating a signal in the range of 0 mA to 20 mA with a 16-bit resolution. In addition to the data collection and actuation routines, the SCADA development included designing and implementing two independent fuzzy logic controllers.

The first controller actuates on the *FCV-101* and the set-point of the temperature control system, with the specific objective of achieving and maintaining the ESP intake temperature (*TT-101*) within a range of a given set-point. The *FCV-101* influences the fluid temperature by controlling the volumetric flow rate that passes through the heat exchanger in the oil flow line.

The second controller actuates on the *FCV-103* and *SY-101* to obtain a desired volumetric flow rate in the oil line (*FT-101*). Concurrently, the controller monitors the ESP intake pressure (*PT-102*) to prevent low and high pressure. For the purposes of the experimental tests, a pressure below 100 kPa is considered low, whereas a pressure above 600 kPa is considered high for the intake pressure (*PT-102*). These limits can be adjusted in the SCADA code. The main objective of this controller is to safely reach the targeted volumetric flow rate within the experimental setup.

The SCADA program was developed using a multi-threading paradigm, incorporating producer-consumer loops, state machines, and control loops. This architecture allowed for

independent storage of measured signals from the instruments, real-time display on the user interface, and execution of control routines. For the user interface, the SCADA system computes a moving average of the instrument measurements over the most recent 5 s. In addition to the directly measured variables, the SCADA system also estimates and displays the current viscosity in the user interface, serving for reference and monitoring purposes.

Furthermore, the experimental procedures, that will be described in Sections 4.1.5.1 and 4.1.5.2, were automated in the SCADA developed. This ensures that the points measured will rigorously follow the same experimental procedure and timing. Also, several safety protocols were implemented and integrated into the SCADA. It includes critical pressure checks for *PT-102* and *PT-103*, as well as the computer RAM availability checks. These protocols ensure the safe and reliable operation of the experimental apparatus.

4.1.4 Data collection

The instrumentation described in Section 4.1.2 was collected at a sampling rate of 250 Hz. For steady-state analysis, the signals from each experimental point were averaged over the entire acquisition time. On the other hand, for transient analysis, the collected signals were post-processed in a separate computer, where they were downsampled to 10 Hz. This downsampling rate was selected to adhere to the Nyquist-Shannon sampling theorem based on the maximum frequency specifications provided by the pressure transmitter manufacturer. In order to ensure accurate signal representation and remove high-frequency noise, an 8th-order Butterworth low-pass filter was employed with a cut-off frequency of 10 Hz.

4.1.5 Experimental procedures

4.1.5.1 Steady state experiments

In this section, the experimental procedure designed to investigate the steady-state behavior of the ESP system is delineated. It focuses on obtaining the ESP pressure difference between the intake and discharge under different ESP shaft angular velocities and volumetric flow rates for single-phase and two-phase oil and water flows. For clarity, any reference to ESP rotation pertains to the angular velocity of the ESP shaft.

The experimental procedure is divided into two discrete phases. The first phase, denoted as the *start-up step*, aims to reach a volumetric flow rate and a stable water cut for the two-phase experiments. The second step, referred to as the *steady-state acquisition step*, outlines the approach for an appropriate data collection, ensuring a relatively stable temperature and that all pressures and volumetric flow rates are stable. The flow chart illustrating the experimental procedure is presented in Figure 4.2 and detailed further below:

Step 1: Start-up:

- (a) Begin by slowly starting the oil pump and water pump (for two-phase flow experiments) at a low rotational speed (e.g., 62 rad s^{-1}) to ensure system stability and prevent sudden pressure surges.
- (b) Incrementally adjust the ESP angular velocity (SY-103) to a pre-determined target speed while ensuring that the suction pressure remains above 100 kPa to prevent cavitation in the ESP first stages.
- (c) In the context of a two-phase flow experiment, monitor the water cut using the water cut meter (WCM-101) and adjust the water pump angular velocity (SY-102) as necessary until the pre-defined water cut is obtained.
- (d) Stop the water pump operation after confirming the stabilization of the desired water cut.
- (e) Check the volumetric flow rate (FT-101). Fine-tune the twin-screw pump angular velocity (SY-101) and the valve position downstream the ESP (FCV-103) until the pre-defined volumetric flow rate is achieved.

Step 2: Steady-state acquisition:

- (a) Allow sufficient time for the suction, discharge pressure, and volumetric flow rate to stabilize. This stabilization period allows capturing only the steady state condition of the ESP.
- (b) Ascertain that the intake temperature of the ESP (TT-101) is within $\pm 0.25 \text{ }^\circ\text{C}$ of the targeted temperature.
- (c) Initiate data acquisition.
- (d) Collect data for a pre-defined duration of 15 s.
- (e) Conclude data acquisition.
- (f) Validate the stability of all monitored variables. Remove the data and return to the stabilization step if any variables are outside the pre-defined tolerances or criteria (**Step 2:a**).
- (g) For new experimental point return to the step **Step 1:c**.

A variable is considered stable if the coefficient of variation (CV) computed over the last 20 s of measurements is less than 0.8%. This criterion is the same as described by de Castro Teixeira Carvalho *et al.* [133]. The time window was chosen based on preliminary system tests. The coefficient of variation CV is defined as:

$$CV = \frac{\sigma_x}{\bar{x}}, \quad (4.1)$$

where σ_x is the standard deviation and \bar{x} is the mean of the last 20 s of measurements for a variable x . It is worth noting that steps **Step 1:e** to **Step 2:g** were automated in the SCADA system.

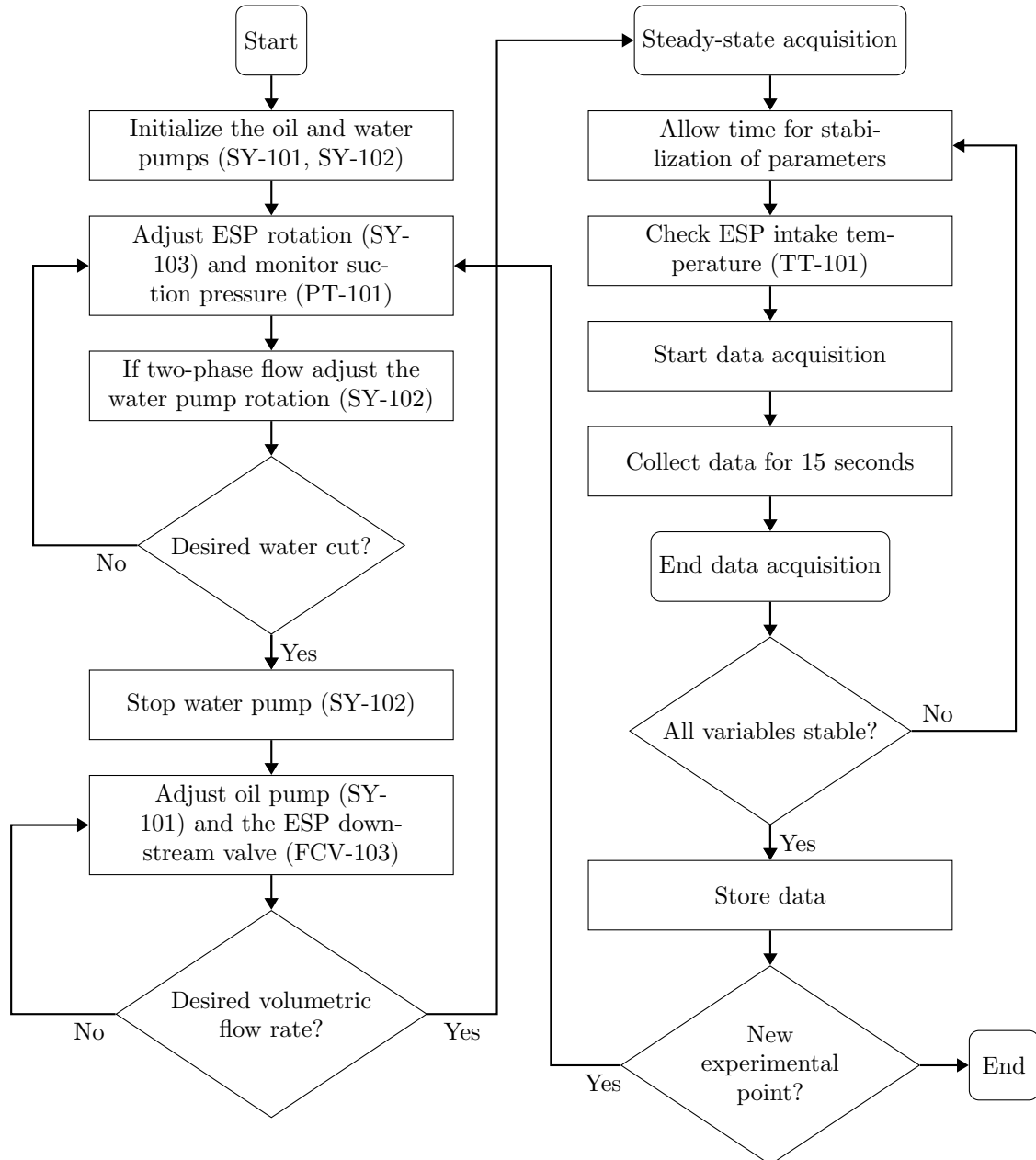


Figure 4.2: Steady-state experimental procedure flowchart.

4.1.5.2 Dynamic experiments

In this section, the developed experimental procedure employed to assess the dynamic behavior of the ESP system is presented. It focuses on variations in the ESP shaft's angular velocity during operation under single-phase and two-phase flows. For clarity, any reference to ESP rotation refers to the angular velocity of the ESP shaft.

The experimental procedure is partitioned into two distinct steps. The first step, denoted as *start-up step*, aims to obtain a stable water cut for the dynamic experiment. The second step, referred to as *transient acquisition step*, presents the procedure to obtain the ESP transient and data collection safely. The experimental procedure flow chart is presented in Figure 4.3, and it is detailed below:

Step 1: Start-up:

- (a) Begin by slowly starting the oil pump and water pump at a low speed (e.g., 62 rad s^{-1}) to ensure system stability and prevent sudden pressure surges.
- (b) Gradually increase the rotation speed of the ESP while monitoring the suction pressure. Maintain the ESP angular velocity below 105 rad s^{-1} and ensure the suction pressure remains above 100 kPa to prevent cavitation in the ESP first stages.
- (c) Check the measured water cut and adjust the water pump angular velocity if necessary. Repeat this step until the desired water cut is achieved.
- (d) Stop the water pump operation after confirming the stabilization of the desired water cut.

Step 2: Transient acquisition:

- (a) Increase the ESP angular velocity to the desired initial value.
- (b) Increase the oil pump angular velocity while closing the ESP downstream valve to maintain the suction pressure within the range of 100 kPa to 600 kPa. The upstream pressure of the ESP should not exceed 600 kPa for a safe operation.
- (c) Gradually increase the ESP angular velocity to reach the desired final value.
- (d) Increase the oil pump angular velocity while closing the downstream valve to maintain the suction pressure within the range of 100 kPa to 600 kPa.
- (e) Return the ESP angular velocity to the desired initial speed.
- (f) Allow sufficient time for the suction, discharge pressure, and volumetric flow rate to stabilize. This stabilization period allows capturing only the dynamics of the ESP angular velocity change.
- (g) Start data acquisition.
- (h) Wait 5 s.
- (i) Adjust the ESP angular velocity on the VSD to the final desired value.
- (j) Allow another stabilization period for the suction, discharge pressure, and volumetric flow rate. This period allows the capture of the complete dynamic system response to the rotation change.
- (k) End data acquisition.

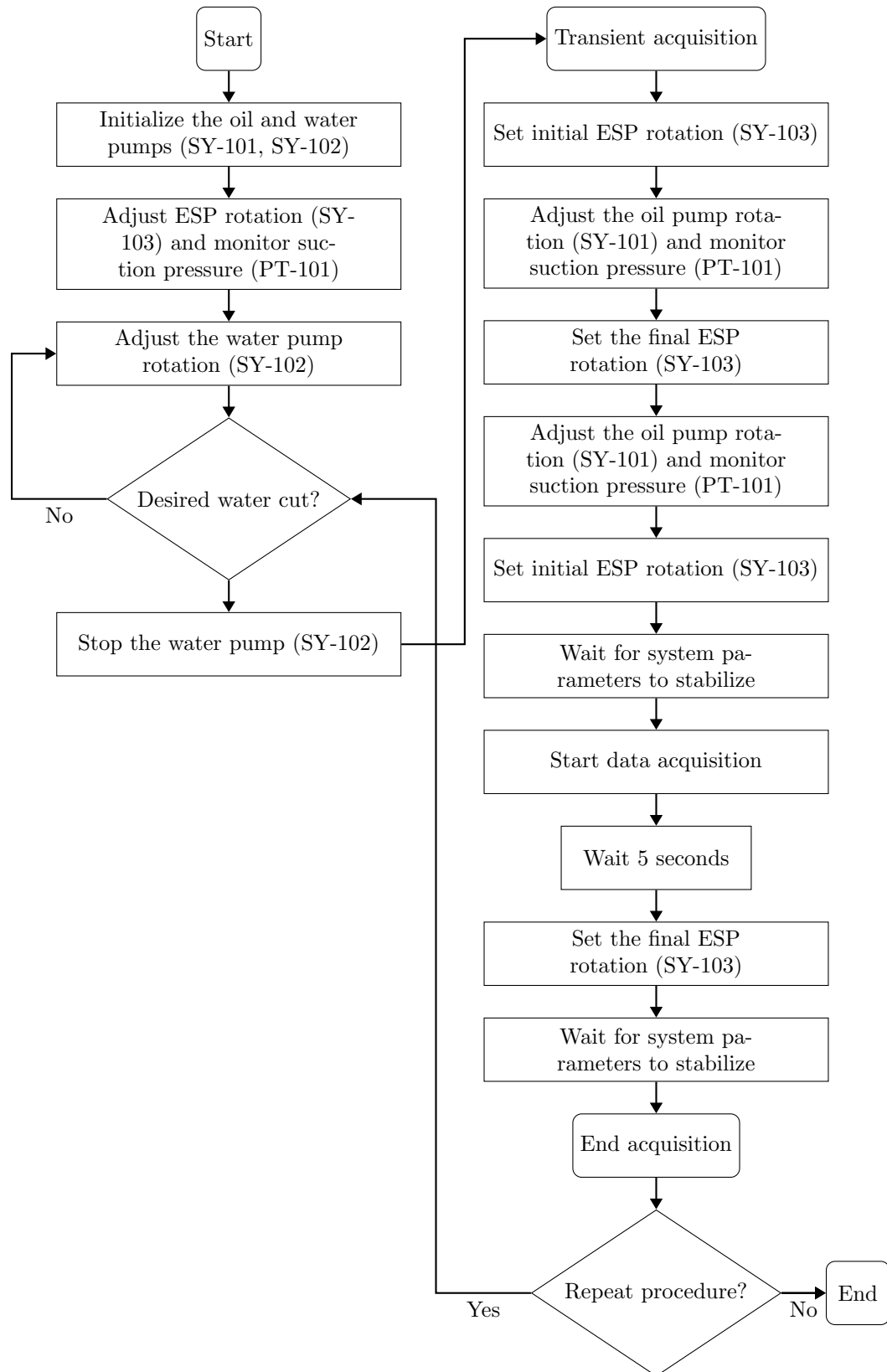


Figure 4.3: Transient experimental procedure flowchart.

(l) Return to the **Step 1:c**

The criteria for system stabilization in the dynamic experiments were the same as those spec-

ified in Section 4.1.5.1. Similar to the automation implemented in the steady-state experimental procedure, the SCADA system autonomously monitors for system stabilization. Once stabilized, it executes the steps automatically from **Step 2:f** to **Step 2:k**.

4.1.6 Steady-state test matrix

The steady-state experimental investigations focused on single-phase experiments examining oil and water conditions for both ESP (P100L and P47). The Tables 4.3 and 4.4 summarize the test parameters employed to assess ESP P100L performance for oil and water, respectively. For the ESP P45, the test parameters used to assess its performance are summarized in the Tables 4.5 and 4.6. Each row in these tables represents a distinct parameter or factor that was varied during the tests, with each parameter having multiple levels.

Table 4.3: Summary of experimental tests for evaluating ESP P100L performance for oil conditions.

Parameter	Levels	Description
Temperature	3	20, 25 and 30°C
ESP rotation	4	188, 251, 314 and 366rad s ⁻¹
Flow rate	Varying	0 to open flow, $\Delta = 0.5 \text{ m}^3 \text{ h}^{-1}$

Table 4.4: Summary of experimental tests for evaluating ESP P100L performance for water conditions.

Parameter	Levels	Description
Temperature	3	30, 35 and 40°C
ESP rotation	4	188, 251, 314 and 366rad s ⁻¹
Flow rate	Varying	0 to open flow, $\Delta = 1.5 \text{ m}^3 \text{ h}^{-1}$

Table 4.5: Summary of experimental tests for evaluating ESP P47 performance for oil conditions.

Parameter	Levels	Description
Temperature	3	22, 33 and 50°C
ESP rotation	4	208, 259, 312 and 363rad s ⁻¹
Flow rate	Varying	0 to open flow, $\Delta \approx 0.25 \text{ m}^3 \text{ h}^{-1}$ *

* The flow rate increment was subjected to adjustments based on the specific experimental conditions and the system's capacity to maintain a stable temperature within the parameters set.

The data points collected from the experimental setup, following the test summaries previously described, are displayed in separate figures for the ESP P100L and ESP P45 models. For the ESP P100L, data under oil and water conditions can be found in Figures 4.4 and 4.5, respectively.

Table 4.6: Summary of experimental tests for evaluating ESP P47 performance for water conditions.

Parameter	Levels	Description
Temperature	3	23, 25 and 28°C
ESP rotation	4	208, 259, 312 and 363 rad s ⁻¹
Flow rate	Varying	0 to open flow, $\Delta \approx 0.25 \text{ m}^3 \text{ h}^{-1}$

* The flow rate increment was subjected to adjustments based on the specific experimental conditions.

Correspondingly, for the ESP P45, the Figures 4.6 and 4.7 present the data for oil and water conditions.

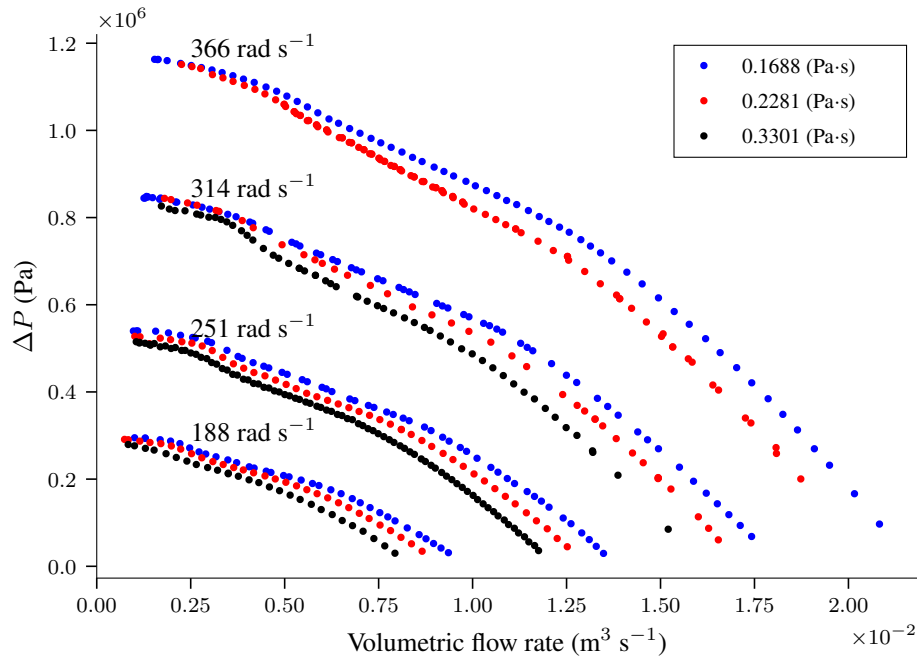


Figure 4.4: Steady-state experimental data of the ESP P100L for oil conditions.

4.1.7 Dynamic test matrix

To evaluate the dynamic performance of the ESP system modeled through bond graphs, it is essential to consider varying operational conditions. In this work, it was focused on two distinct water-in-oil emulsion conditions to account for two-phase flows. The parameters selected for variation included the water fraction, temperature, and angular velocity step size. These parameters significantly influence the system's dynamic behavior. Moreover, the fluid properties, such as density and viscosity, are subjected to change based on well conditions. Furthermore, the variation in angular velocity is designed to simulate shifts in operational conditions.

The test matrix, detailed in Table 4.7, includes several experimental parameters: initial angular

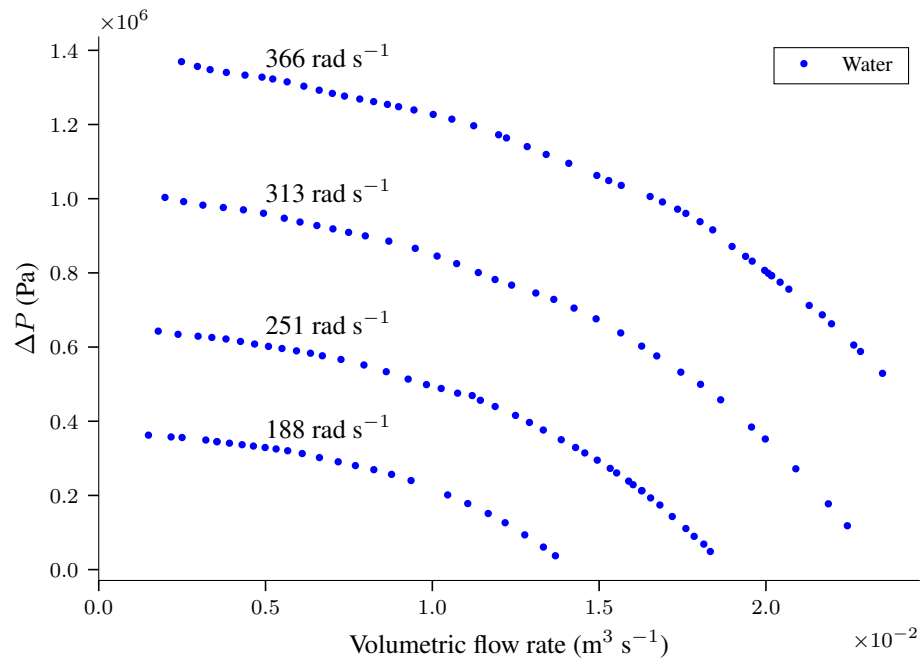


Figure 4.5: Steady-state experimental data of the ESP P100L for water conditions.

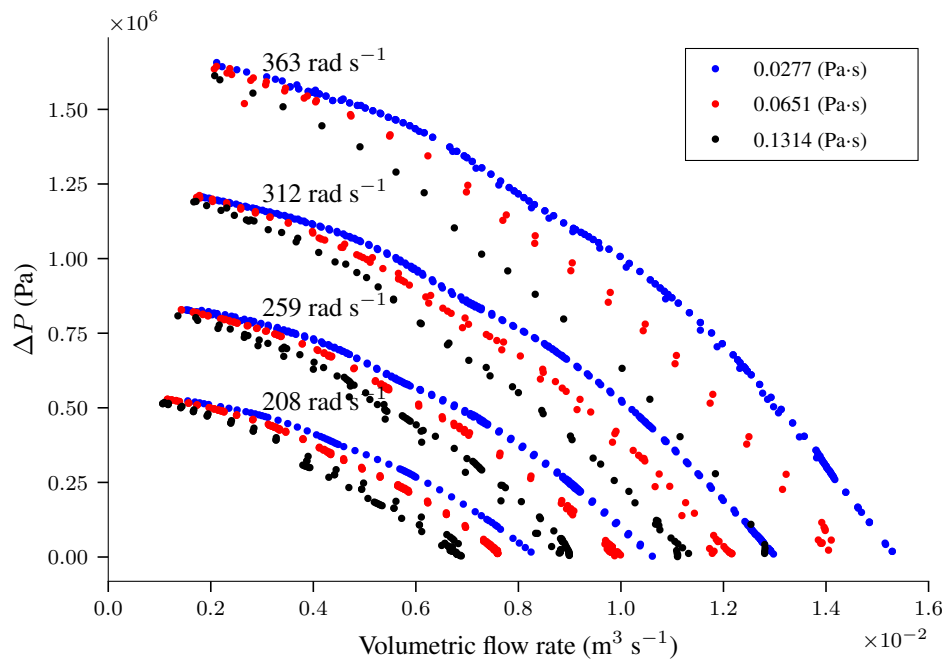


Figure 4.6: Steady-state experimental data of the ESP P47 for oil conditions.

velocity (ω_i), final angular velocity (ω_f), water cut, temperature, and twin-screw pump rotation (ω_t). Thus, the objective is to analyze the system's dynamic behavior across different density and viscosity conditions. Moreover, this approach enables the evaluation of the model's accuracy in capturing the performance of the ESP system, especially when influenced by emulsion formation.

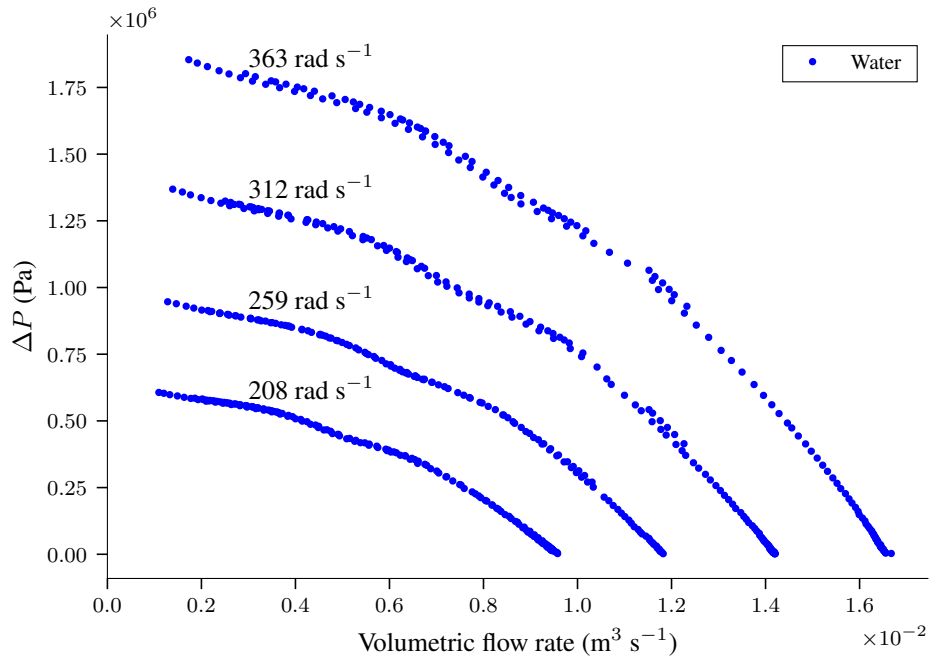


Figure 4.7: Steady-state experimental data of the ESP P47 for water conditions.

Table 4.7: Test matrix for assessing the dynamics of the ESP system in oil/water two-phase flows.

Inv. (#)	Pump	ω_i (rad s $^{-1}$)	ω_f (rad s $^{-1}$)	Ω (%)	Temp. (°C)	ω_t (RPM)
1	P100L	272.3	314.2	14.0	33.5	1280.0
2	P100L	251.3	314.2	5.0	26.0	1160.0
3	P47	167.6	230.4	4.0	30.5	200.0
4	P47	219.9	282.7	4.0	35.5	400.0
5	P47	219.9	282.7	10.0	38.5	400.0
6	P47	125.7	178.0	15.0	33.0	200.0

4.2 Modeling using bond graphs

In this work, bond graph modeling serves as a cornerstone for analyzing and simulating the ESP system. The theoretical foundations and mathematical derivations associated with bond graph elements are elaborated in Chapter 3. This section is dedicated to the methodology for constructing bond graph models, extracting the associated equations, and solving these equations numerically. To facilitate these tasks, a specialized Julia library, *BondGraphToolkit.jl*, has been developed. This library is built upon the *ModelingToolkit.jl* framework [134], which offers a robust platform for defining acausal subsystems, establishing interconnections, and deriving equations.

The primary objective of this section is to elucidate the process of bond graph modeling via the developed library. For illustrative purposes, we consider a single-degree-of-freedom mass-spring-damper system augmented with a nonlinear cubic spring term. This leads to the well-known Duffing equation, given as

$$m_{\text{duff}} \frac{d^2 x}{dt^2} + c_{\text{duff}} \frac{dx}{dt} + k_{\text{lin}} x + k_{\text{nl}} x^3 = F(t). \quad (4.2)$$

where m_{duff} , c_{duff} , k_{lin} , k_{nl} are system parameters, and $F(t)$ is the forcing function. A schematic representation of the system and its bond graph are depicted in Figure 4.8. It should be noted that

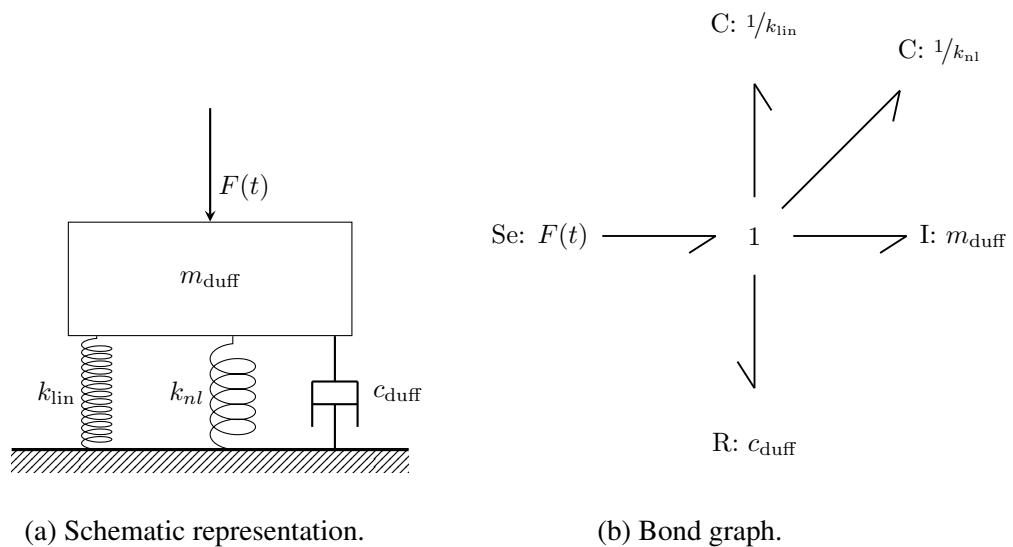


Figure 4.8: Duffing equation as a mass-spring-damper system and its bond graph representation.

the methodologies described herein are generalizable, offering applicability to various systems beyond the mass-spring-damper. The bond graph causalities are automatically assigned by the *ModelingToolkit.jl* framework.

4.2.1 Initialization of 1-port elements

Prior to system definition, it is required to initialize the 1-port elements, which are fundamental elements in bond-graph modeling, and then interact with 2-port elements, 0-junctions, or 1-junctions (described in Chapter A). For the purpose of this demonstration, the bond-graph 1-port elements were mapped to a longitudinal mechanical power system representation, a choice motivated by its ubiquity in mechanical systems. Thus, the inertance is characterized using the `Mass()` function, damping is represented through the `Damper()` function, and compliance is defined via the `Spring()` function.

The `Mass()` function accepts two arguments: the inertia element value or expression and the initial velocity. The `Damper()` function requires only the damping coefficient or an expression. Similarly, the `Spring()` function necessitates the stiffness value or expression and the initial

position as arguments. The expression refers to an algebraic mathematical expression. These elements can be initialized as demonstrated in the following code.

```

1  @named m = Mass(m=1.); # Mass element
2  @named spring = Spring(k=5., x=1.); # Linear spring element
3  @named damper = Damper(c=0.2); # Damper element

```

The external forcing term, denoted by $F(t)$ in Figure 4.8, can be defined either as an algebraic expression or as a Julia function. The specific form of $F(t)$ can be defined prior to solving the resulting ordinary differential equations (ODE).

```

1  @parameters F(t) # Definition of the forcing term
2  @named f = Se(F) # Initialization of the 1-port source effort
   ↪ element

```

4.2.2 Custom 1-port elements

The library provides a framework for defining custom 1-port elements, thereby enabling the representation of non-linear or complex physical phenomena beyond the standard linear elements. The custom elements necessitate the formulation of their constitutive relationship in terms of power variables, specifically generalized effort (e) and generalized flow (f). This formulation ensures compatibility with the bond-graph framework developed, facilitating the integration of custom elements into more complex models.

The code snippet below presents the definition of a cubic spring element, denoted as `Spring3`:

```

1  @oneport function Spring3(; name, k = 1.0, x = 0.0)
2      # Arguments
3      # name -> multiport name
4      # k -> spring constant
5      # x -> initial position
6
7      # Initialize the state variable for displacement
8      @variables q(t) = x
9      # Define the spring constant parameter
10     @parameters C = 1 / k
11
12     # Constitutive equations for the Spring3 element
13     [

```

```

14         power.e ~ q^3 / C, # Cubic non-linearity
15         D(q) ~ power.f # Flow as the derivative of displacement
16     ]
17 end

```

After executing the code above, the custom element can be initialized similarly to the standard 1-port elements, facilitating its integration into larger systems.

```

1 # Initialize cubic spring element
2 @named spring3 = Spring3(k=5., x=1.);

```

4.2.3 Connecting multiport elements

The process of interconnecting multiport elements constitutes a fundamental step in bond graph modeling. Within the utilized library, both 1-junction and 0-junction elements are encapsulated by the `Junction1` and `Junction0` functions, respectively. These functions mandate as arguments the elements intended for interconnection, with the sole requirement that each element or subsystem should encapsulate a variable named `power`, initialized as `@named power = Power()`.

To exemplify, consider the bond graph model depicted in Figure 4.8b. The following code snippet demonstrates the usage of `Junction1` for interconnecting its components:

```

1 @named mdl = Junction1([-1, m], [-1, d], [-1, s], [-1, s3], f)

```

The structure generically defined as `[-1, component]` is used to define the direction of the bond graph connection of the component. The `-1` serves as an indication that the *half arrow* is leaving the 1-junction. In cases involving complex networks of interconnected elements, an alternative method is the `connect()` function. This function accepts two arguments, representing the multiport elements in which the power flows. In this framework, the convention is that power flows from the first argument to the second. The subsequent code snippet performs the same operations as the preceding one but employs the `connect()` function.

```

1 @named j1 = Junction1() # Initialize an empty 1-junction
   ↪ element
2
3 # Manually specify the connections
4 cons = [
5     connect(j1.power, m.power),
6     connect(j1.power, d.power),

```

```

7     connect(j1.power, s.power),
8     connect(j1.power, s3.power),
9     connect(f.power, j1.power),
10 ]
11
12 # Define the overall system using the connections
13 @named mdl = ODESystem(cons, t)
14 # Integrate the elements into the model
15 mdl = compose(mdl, j1, m, d, s, s3)

```

4.2.4 Equation Extraction

This subsection elucidates the methodology for extracting the governing equations of the bond graph model, denoted as `mdl`, and their subsequent rendering into \LaTeX code for documentation. The function `equations(expand_connections())` enables the extraction of these equations, while `latexify()` serves to convert them into \LaTeX code. The resultant equations are presented below:

$$\frac{dm_{+power+f}(t)}{dt} = \frac{m_{+power+e}(t)}{m_{+I}} \quad (4.3a)$$

$$d_{+power+e}(t) = d_{+R}d_{+power+f}(t) \quad (4.3b)$$

$$s_{+power+e}(t) = \frac{s_{+q}(t)}{s_{+C}} \quad (4.3c)$$

$$\frac{ds_{+q}(t)}{dt} = s_{+power+f}(t) \quad (4.3d)$$

$$s3_{+power+e}(t) = \frac{(s3_{+q}(t))^3}{s3_{+C}} \quad (4.3e)$$

$$\frac{ds3_{+q}(t)}{dt} = s3_{+power+f}(t) \quad (4.3f)$$

$$f_{+power+e}(t) = f_{+F}(t) \quad (4.3g)$$

$$s_{+power+f}(t) = d_{+power+f}(t) \quad (4.3h)$$

$$s_{+power+f}(t) = m_{+power+f}(t) \quad (4.3i)$$

$$s_{+power+f}(t) = s3_{+power+f}(t) \quad (4.3j)$$

$$s_{+power+f}(t) = f_{+power+f}(t) \quad (4.3k)$$

$$\begin{aligned} 0 = & -m_{+power+e}(t) + f_{+power+e}(t) \\ & -d_{+power+e}(t) - s_{+power+e}(t) \\ & -s3_{+power+e}(t), \end{aligned} \quad (4.3l)$$

where $e(t)$ and $f(t)$ represent the power variables, while $q(t)$ is the generalized displacement. The system parameters are denoted as mass m_{+I} , the linear and cubic spring stiffness s_{+C} and

s_3C , and the damping coefficient d_+R .

It should be noted that the *ModelingToolkit.jl* library automatically appends each element's name along with a $_+$ suffix to each parameter in the equation. For instance, a 1-port resistance element named d with a damping coefficient represented by R in the model would appear as d_+R in the equations and \LaTeX rendering. This nomenclature is intentional, as it serves to uniquely identify parameters in cases where similar elements are present in the system.

As shown in Equation (4.3), these equations are in the form of DAE. For subsequent computational analysis, especially employing the `solve` function from the *DifferentialEquations.jl* library, these equations must be simplified, in this case to ODE. This simplification is achieved using a custom function `simplifysys()`, which utilizes functionalities from the *ModelingToolkit.jl* library. The resultant equations are presented as follows.

$$\frac{dm_+power_+f(t)}{dt} = \frac{\frac{-(s_3q(t))^3}{s_3C} + \frac{-s_+q(t)}{s_+C} - d_+Rm_+power_+f(t) + f_+F(t)}{m_+I} \quad (4.4a)$$

$$\frac{ds_+q(t)}{dt} = m_+power_+f(t) \quad (4.4b)$$

$$\frac{ds_3q(t)}{dt} = m_+power_+f(t) \quad (4.4c)$$

4.2.5 Analytical validation

It is fundamental to verify the correctness of the equations presented in Equation (4.4). We can analytically rearrange and simplify the equations, obtaining:

$$\frac{dm_+power_+f(t)}{dt} = \frac{\frac{-(s_3q(t))^3}{s_3C} + \frac{-s_+q(t)}{s_+C} - d_+Rm_+power_+f(t) + f_+F(t)}{m_+I}, \quad (4.5a)$$

$$\frac{ds_+q(t)}{dt} = \frac{ds_3q(t)}{dt} = m_+power_+f(t), \quad (4.5b)$$

Considering the states variables as only the displacement $q(t)$, we derive:

$$m_+I \frac{d^2s_+q(t)}{dt^2} = \frac{-(s_+q(t))^3}{s_3C} + \frac{-s_+q(t)}{s_+C} - d_+R \frac{ds_+q(t)}{dt} + f_+F(t), \quad (4.6)$$

$$m_+I \frac{d^2s_+q(t)}{dt^2} + \frac{(s_+q(t))^3}{s_3C} + \frac{s_+q(t)}{s_+C} + d_+R \frac{ds_+q(t)}{dt} = f_+F(t). \quad (4.7)$$

As can be seen, the Equation (4.7) can be directly compared to the Duffing equation in Equation (4.2), where the parameters map as $m_{\text{duff}} = m_+I$, $x = s_+q(t)$, $k_{\text{lin}} = 1/s_+C$, $k_{\text{nl}} = 1/s_3C$, $c_{\text{duff}} = d_+R$, and $F(t) = f_+F(t)$. This analytical validation confirms the accuracy of the library in deriving the correct bond graph model.

4.2.6 Numerical simulation

The system equations in Equation (4.4) can be solved using `solve`. However, we still need to define the forcing term $F(t)$. In this example, we considered an unforced system where $F(t) = 0$. Then, we define the force function on the system, the simulation time range, the initial conditions, and finally solve the system. The code snippet below shows the simulation steps:

```

1  # Set the forcing term to zero
2  sys = substitute(sys, Dict{f.F => 0.0})
3
4  # Specify the simulation time range
5  tspan = (0, 10)
6
7  # Define the ODE problem with initial conditions
8  prob = ODEProblem(sys_unforced, [m.power.f => 0.0, s.q => 1.0, s3.q
   ↪ => 1.0], tspan)
9
10 # Perform the numerical simulation
11 sol = solve(prob)

```

4.3 Valve modeling

As discussed in Section 3.6.3, the fundamental valve equations for turbulent and non-turbulent flow in incompressible fluids are similar. The main difference arises when the valve Reynolds number, Re_v , is lower than 10 000. In this regime, the factor multiplying the model changes from a constant in the turbulent model, F_p , obtained from the ISA75.01.01 [128] table to a Reynolds-dependent factor, F_r , whose expression is given by Equation (3.109).

As mentioned in Section 3.6.2, the F_r expression is particularly developed for fluids that exhibit Newtonian rheology and non-vaporizing fluids. When dealing with non-Newtonian fluids, the elevated shear rates experienced as the fluid passes through the valve can lead to significant viscosity variations. These changes can influence the energy loss within the valve, thereby impacting the standard model's accuracy, which does not consider these variations. Despite emulsions being non-Newtonian, the ISA75.01.01 [128] restriction regarding the model applicability in turbulent conditions is related to mixture homogeneity and whether the multiphase mixture is in chemical and thermodynamic equilibrium. In the context of emulsions, the multiphase flow is expected to be homogeneous. However, the emulsions are not in thermodynamic equilibrium. Therefore, for instance, as the fluid flows through the valve, the temperature change could lead to separate the phases.

Due to the high viscosity of the oil and previously discussed challenges, the ISA75.01.01

[128] approach becomes less feasible for scenarios involving multiphase flows, laminar flows, and non-Newtonian fluids. Instead of using the ISA75.01.01 [128] expressions for F_p or F_r , it is recommended to derive these values experimentally. It should be noted, as indicated by Equation (3.109), that the F_r factors is dependent on the Reynolds number, and by extension, on fluid viscosity and density. Therefore, the applicability of the experimentally derived values may be confined to a specific range of viscosity and density conditions.

Given the equation Equation (3.112c), we can combine terms C_v , N_1 , and F^* . Thus, Equation (3.112c) can be reformulated as:

$$\Delta P = \frac{\rho^* Q^2}{C_v^{*2}}, \quad (4.8)$$

where C_v^* is a term that accounts for C_v , N_1 , and F^* . Therefore, the bond graph resistance element described by Equation (3.114) can be expressed as:

$$R_v(a) = \frac{\rho Q}{(C_v^*(a))^2}. \quad (4.9)$$

4.4 Practical identifiability analysis

The practical identifiability can be assessed using either Monte Carlo simulations or sensitivity analysis. The Monte Carlo approach rigorously determines the practical identifiability of the model but comes with a high computational cost due to the requirement of multiple model fits. On the other hand, sensitivity analysis offers a faster computation method and provides information about the correlation structure among the parameters. This correlation structure can guide the fixing of parameters when practical identifiability is not achieved [92, 135].

In the sensitivity approach to practical identifiability, it was used the Fisher information matrix (FIM) to compute the correlation matrix of all parameters to determine their practical identifiability. The sensitivities of the ESP system model with respect to the parameters were estimated with the Julia package DiffEqSensitivity.jl. For the sensitivity analysis, it was considered the simulated case, and similarly to Daneker *et al.* [132], it was considered a noise level of the measurements of 1 %.

Then, to obtain the correlation matrix, we first estimate the covariance matrix (C), which can be approximately obtained from the FIM by

$$C = FIM^{-1}. \quad (4.10)$$

We then estimate the correlation matrix from (C) with

$$\begin{cases} r_{ij} = \frac{C_{ij}}{\sqrt{C_{ii} C_{jj}}}, & \text{if } i \neq j, \\ r_{ij} = 1, & \text{if } i = j. \end{cases} \quad (4.11)$$

When $|r_{ij}|$ is close to 1, the parameters i and j are strongly correlated and cannot be individually estimated. Therefore, the parameters are practically unidentifiable [92, 135].

4.5 Physics-informed neural networks

4.5.1 Neural network architecture

The Physics-Informed Neural Network (PINN) comprises two key elements: a Neural Network (NN) used to approximate the solution of a specific differential equation and an auxiliary component that incorporates this differential equation into the optimization process of the network parameters. The embedding of the differential equation within the loss function of the NN is facilitated by automatic differentiation [105]. In this work, the primary focus is on employing a fully connected, feed-forward Deep Neural Network (DNN) for approximating the state variables of the ESP system, the details of which will be elaborated in Sections 5.3 and 5.4. For illustrative purposes, it is considered the set of state variables denoted as Φ^1 corresponding to the model states delineated in Section 5.4.

$$\Phi^1 = \{Q_p, \omega, Q_1, Q_2, P_1, P_2\}. \quad (4.12)$$

It is pertinent to note that the methodology described herein is equally applicable to alternative sets of state variables, denoted generically as Φ .

The architecture of the DNN is composed of one input layer, h hidden layers, and one linear output layer. It can be formally represented as:

$$\mathbf{y}_0 = t, \quad (\text{Input layer}) \quad (4.13a)$$

$$\mathbf{y}_i = \sigma(\mathbf{W}_i \mathbf{y}_{i-1} + \mathbf{b}_i), \quad (\text{Hidden layers}), \forall 1 \leq i \leq h - 1 \quad (4.13b)$$

$$\hat{\mathbf{y}} = \mathbf{y}_h = \mathbf{W}_h \mathbf{y}_{h-1} + \mathbf{b}_{h-1}, \quad (\text{Output layer}) \quad (4.13c)$$

where $\mathbf{W} \in \mathbb{R}^{m \times n}$ and $\mathbf{b} \in \mathbb{R}^m$ are the weight matrix and bias vector of the NN, respectively. The terms n and m refer to the size of the previous and current layers. The function $\sigma(\cdot)$ represents the NN activation function, which in this work was chosen to be $\tanh(\cdot)$. For the remainder of this work, the weights and biases are referred collectively to as the parameters of the neural network, denoted as $\theta = \{\mathbf{W}, \mathbf{b}\}$. They were initialized randomly using the Xavier initialization method [136].

The schematic diagram of the PINN used in this study is shown in Figure 4.9. In this work, one DNN is employed to approximate the set of state variables Φ^1 . This strategy yielded satisfactory results while reducing the computational cost compared to training individual DNNs for each state variable of Φ^1 , as will be discussed in Chapter 7.

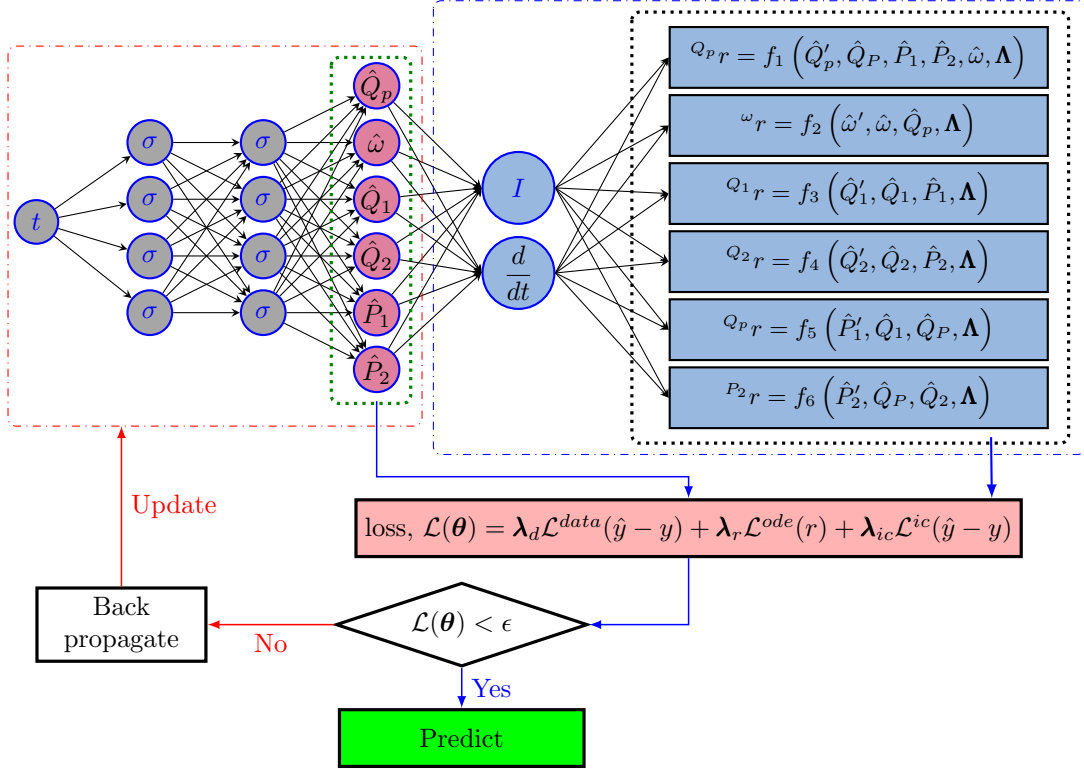


Figure 4.9: Schematics representation of the physics-informed neural network for the ESP system.

The architecture of the DNN is illustrated in the red dashed-dotted rectangle on the left side of Figure 4.9. The DNN takes time, t , as its input and yields the state variables in Φ^1 as its output, highlighted in the green dotted rectangle of the figure. The DNN is evaluated at N^{ODE} collocation points, each associated with a residual term corresponding to the ESP system's differential equations. These residuals are indicated in the black-dotted region on the right side of Figure 4.9. The time derivatives of the state variables are computed via automatic differentiation. In the DNN architecture, the activation function is denoted by σ .

The architecture of the DNN considered in this study is denoted as $[1, 20, 20, 20, 6]$. This indicates that the input layer consists of a single neuron corresponding to time t , followed by three hidden layers each containing 20 neurons, and an output layer with 6 outputs corresponding to the elements of Φ^1 .

4.5.2 Physics-Informed loss function

The NN loss function is denoted as $\mathcal{L}(\theta, \Lambda, \lambda_d, \lambda_r, \lambda_{ic})$, and it is defined as

$$\mathcal{L}(\theta, \Lambda, \lambda_d, \lambda_r, \lambda_{ic}) = \mathcal{L}^{ode}(\theta, \Lambda, \lambda_r) + \mathcal{L}^{data}(\theta, \lambda_d) + \mathcal{L}^{ic}(\theta, \lambda_{ic}). \quad (4.14)$$

It is a composition of three distinct losses: the data loss $\mathcal{L}^{data}(\theta, \lambda_d)$ which compares the NN adjustment regarding the data, the physics (ODE) loss $\mathcal{L}^{ode}(\theta, \Lambda, \lambda_r)$ corresponding to the

residues at collocation points, and the initial condition loss $\mathcal{L}^{ic}(\boldsymbol{\theta}, \boldsymbol{\lambda}_{ic})$ which compares the DNN output at $t = 0$ to the given initial conditions. The weights $\boldsymbol{\lambda}_d$, $\boldsymbol{\lambda}_r$, and $\boldsymbol{\lambda}_{ic}$ are assigned to each of these loss components and may be either fixed or adapted during the optimization process and $\boldsymbol{\Lambda}$ denotes the unknown parameters within the ODE system.

The physics-informed loss function, $\mathcal{L}^{ode}(\boldsymbol{\theta}, \boldsymbol{\Lambda}, \boldsymbol{\lambda}_r)$, was defined as a weighted (self-adaptive weights) sum of individual physics losses corresponding to each differential equation in the system. This sum is expressed as:

$$\mathcal{L}^{ode}(\boldsymbol{\theta}, \boldsymbol{\Lambda}, \boldsymbol{\lambda}_r) = \sum_{s \in \Phi} m(\lambda_r^s) \mathcal{L}_s^{ode}, \quad (4.15a)$$

$$= \sum_{s \in \Phi} m(\lambda_r^s) \left[\frac{1}{sN^{ode}} \sum_{i=1}^{sN^{ode}} ({}^s r_i)^2 \right], \quad (4.15b)$$

$$= \sum_{s \in \Phi} m(\lambda_r^s) \left[\frac{1}{sN^{ode}} \sum_{i=1}^{sN^{ode}} \left(\left. \frac{d\hat{y}_s}{dt} \right|_{t_i} - f_s(\hat{y}(t_i; \boldsymbol{\theta}), \tau(t_i); \boldsymbol{\Lambda}) \right)^2 \right], \quad (4.15c)$$

where s is an element of the set Φ^1 ($s \in \Phi^1$), representing each state variable in the system. The \mathcal{L}_s^{ode} represents the physics-informed loss associated with the s state differential equation of the system. The term sN^{ode} denotes the number of collocation points for the equation of the s state. The λ_r^s is the self-adaptive weight associated with the state s equation of the physics loss. In this work, $m(\cdot)$ serves as a mask function and is specifically chosen to be the softplus function $S_p(\cdot)$, defined as:

$$S_p(x) = \ln(1 + e^x). \quad (4.16)$$

The variable ${}^s r_i$ stands for the residual at the i -th collocation point for the s state differential equation. It should be noted that, in this study, it was considered that all state variables use the same set of collocation points, implying that all sN^{ode} are identical. The detailed elaboration of the calculation for these residuals for each state s differential is available in Appendix E for the ESP system model evaluated.

The data loss, $\mathcal{L}^{data}(\boldsymbol{\theta}, \boldsymbol{\lambda}_d)$, is calculated as a weighted sum, defined by self-adaptive weights of individual data losses corresponding to a state variable in the set ϕ of known states. The data loss is given by:

$$\mathcal{L}^{data}(\boldsymbol{\theta}, \boldsymbol{\lambda}_d) = \sum_{s \in \phi} m(\lambda_d^s) \mathcal{L}_s^{data}, \quad (4.17a)$$

$$= \sum_{s \in \phi} m(\lambda_d^s) \left[\frac{1}{sN^{data}} \sum_{i=1}^{sN^{data}} [y_s(t_i) - \hat{y}_s(t_i; \boldsymbol{\theta})]^2 \right], \quad (4.17b)$$

where s is an element of the known state set ϕ , and the sN^{data} are the number of data points available for each state variable s . The term $y_s(t_i)$ refers to the actual value of the measured state

variable s at time t_i , and $\hat{y}_s(t_i; \boldsymbol{\theta})$ is its corresponding neural network approximation. Similar to the physics loss, λ_d^s is the self-adaptive weight assigned to each data loss component, and $m(\cdot)$ is a mask function chosen to be $S_p(\cdot)$ in this study.

The initial condition loss, $\mathcal{L}^{ic}(\boldsymbol{\theta}, \boldsymbol{\lambda}_{ic})$, is calculated as a weighted sum, determined by self-adaptive weights, of individual initial condition losses corresponding to a state variable s in the set Φ^1 . The initial condition loss is given by:

$$\mathcal{L}^{ic}(\boldsymbol{\theta}, \boldsymbol{\lambda}_{ic}) = \sum_{s \in \Phi} m(\lambda_{ic}^s) \mathcal{L}_s^{ic}, \quad (4.18a)$$

$$= \sum_{s \in \Phi} m(\lambda_{ic}^s) [(y_s(t_0) - \hat{y}_c(t_0; \boldsymbol{\theta}))^2], \quad (4.18b)$$

where $y_s(t_0)$ is the known value of the s state variable at $t = 0$, and the NN approximation is $\hat{y}_s(t_0; \boldsymbol{\theta})$. Similarly to the other losses, the mask function $m(\cdot)$ was chosen to be $S_p(\cdot)$ in this study.

The set of adjustable parameters, comprising $\boldsymbol{\theta}$, $\boldsymbol{\Lambda}$, $\boldsymbol{\lambda}_d$, $\boldsymbol{\lambda}_r$, and $\boldsymbol{\lambda}_{ic}$, is optimized using the Adam optimizer [137]. The automatic differentiation required for evaluating the derivatives of the outputs with respect to input, the loss with respect to the NN parameters, and the loss with respect to the self-adaptive weights are evaluated using the Python library JAX [138]. At the same time, the optimization process employs the Optax library [139]. Thus, in order to handle the adjustment of these parameters, distinct optimizers were defined for each of them: one for the neural network parameters (i.e., weights and biases), another for the unknown physical parameters, and another for the self-adaptive weights. The training epochs and the learning rate scheduling details were elaborated in Appendix F for each case under consideration that will be discussed in Chapter 7.

4.5.3 Input and output transformations

As previously defined, NN takes the time variable t as its input. Before proceeding to the first hidden layer, the time input is scaled to the interval $[-1, 1]$. The scaling transformation is expressed as follows:

$$h_0^{sc}(\mathbf{y}_0) = 2 \frac{\mathbf{y}_0 - \min(\mathbf{y}_0)}{\max(\mathbf{y}_0) - \min(\mathbf{y}_0)} - 1, \quad (4.19)$$

where \mathbf{y}_0 denotes the initial time vector, as discussed in Equation (4.13a).

Subsequent to the NN output layer, the outputs undergoes an additional transformation to map them back to the physical domain. This transformation is represented as:

$$h_h^{sc}(x) = \frac{(x + 1)(x_{\max} - x_{\min})}{2} + x_{\min}, \quad (4.20)$$

where $h_h^{sc}(x)$ denotes the state variable in the physical domain, while x indicates the NN's output corresponding to that specific state.

For known states, such as the intake and discharge pressures of the ESP represented by P_1 and P_2 , the bounds x_{\min} and x_{\max} correspond to the minimum and maximum measured values, respectively. However, for the non-measured or unknown states, the x_{\min} and x_{\max} are estimated by solving a system of equations at two specific time points t_1 and t_2 . This system of equations is derived from simplifications of the model that will be described in Section 5.4 and can be expressed as follows:

$$\begin{cases} k_{1p} \rho \omega(t_i) Q_p(t_i) + k_{2p} \rho \omega(t_i)^2 + k_{4p} \rho Q_p(t_i)^2 - (P_2(t_i) - P_1(t_i)) = 0, \\ k_{1s} \rho Q_p(t_i)^2 - k_{2s} \rho \omega(t_i) Q_p(t_i) + \tau(t_i) = 0, \quad t_i \in \{t_1, t_2\} \end{cases} \quad (4.21)$$

where k_{1p} , k_{2p} , k_{4p} , k_{1s} , and k_{2s} are the ESP system parameters, ρ represents the fluid density, and t_i denotes the time instant for the state variables (ω , Q_p , P_1 , P_2) and system input (τ).

Furthermore, the time points t_1 and t_2 are determined based on the pressure difference between $P_2(t)$ and $P_1(t)$ as follows:

$$t_1 = \arg \min_t (P_2(t) - P_1(t)), \quad t_2 = \arg \max_t (P_2(t) - P_1(t)), \quad (4.22)$$

Solving Equation (4.21) at t_1 yields an estimation for x_{\min} , and at t_2 for x_{\max} . However, in order to solve it, the ESP system parameters k_{1p} , k_{2p} , k_{4p} , k_{1s} , and k_{2s} and the fluid density ρ must be defined. Thus, for the sake of solving these equations, as an initial guess the fluid density is considered to have a corresponding value to a water fraction of 50 % (e.g. $\rho = 931.51 \text{ kg m}^{-3}$). All the other ESP system parameters are assumed to be 15 % of their true values in this work. Furthermore, the estimated values obtained for the volumetric flow rate Q_p , are used for the other volumetric flow rates state. The state ω is the state corresponding to the ESP shaft angular velocity.

It is noteworthy that the state variables exhibit significant difference in their scale (magnitude). To address these differences, the transformation described by Equation (4.20) was employed. It aimed to obtain a more uniform magnitude for the state variables being approximated by the NN. Therefore, this transformation can have different forms which will depend on the specific requirements of the problem under analysis. The details of the transformations used in this work will be elucidated in Chapter 7, as they varied according to the case being analyzed. Furthermore, when considering the intake and discharge pressures (P_1 and P_2) as known quantities, for instance, the bounds for x_{\min} and x_{\max} will vary across the different experimental investigations.

4.6 Data generation

This section elaborates on the methodology used for simulating the bond graph model of the ESP system. The simulated data will serve two purposes. Firstly, the simulated data is used to obtain the system response for validation with the experimental data. Secondly, the simulated

data serves as a synthetic testbed for assessing the performance and reliability of PINN in inverse problem-solving.

The mathematical formulation resulting from the bond graph model can be either a set of ODE or Differential Algebraic Equations (DAE). Each set of equations necessitates the employment of a distinct numerical solver. In this work, the equations derived from the bond graph model resulted in a set of ODE. Consequently, the Tsitouras 5/4 Runge-Kutta method was utilized, setting both relative and absolute tolerances to 1×10^{-8} . The solver operates with a variable time step, which was subsequently resampled to a fixed time step. A time step of $\Delta t = 0.0001$ s was established, selected to adequately capture the system's dynamics while ensuring compatibility with the sampling rate utilized in experimental tests.

In this work, as previously mentioned, the ESP system model focuses exclusively on the mechanical and hydraulic domains. Thus, the model did not consider the electrical motors that drive each pump described in Section 4.1. Instead, torque, an experimentally measured quantity from instrumentation outlined in Section 4.1.2, serves as the system input. Despite undergoing post-processing according to the methodology described in Section 4.1.3, the torque signal retained relatively high-frequency components, which are unrealistic as a direct input for the ESP system. Therefore, in addition to the procedure described in Section 4.1.3, a Butterworth low-pass filter with a cut-off frequency of 2 Hz was applied to the torque signal to obtain a more representative input. This filtered signal was subsequently employed as input for the simulations.

Regarding the fluid properties required for system simulation, a single viscosity and density value was assumed for the entire system under consideration. The viscosity was estimated by first calculating the average temperature and water cut based on measurements taken at the experimental investigation point of interest. These average values were then input into the Brinkman [69] model to compute the emulsion viscosity. As for the fluid density, it was determined as the average of readings obtained from the Coriolis meter (FT-101) during the corresponding experimental investigation. For the states of the model, the initial values were considered as the mean over the first 5 s of measurements before changing the ESP angular velocity.

During the tuning phase of the dynamic model, parameter values are adjusted to align the model's output closely with real-world observations. Despite this calibration effort, discrepancies between model predictions and measured data are inevitable. These discrepancies can originate from uncertainties inherent in the collected data and the model's inability to capture all the nuances of the physical system it represents due to its assumptions and simplifications to improve the problem tractability. In the context of inverse problems, it should be noted that even minor variations or inaccuracies in the adjusted parameters can significantly influence the estimated parameters of interest.

In the context of employing PINN for solving inverse problems to assess their capability in accommodating measurement uncertainties while isolating the influences of either missing physics or tuning steps, Gaussian noise was introduced into the simulated states considered

as known quantities. The magnitudes of this noise were determined in accordance with the manufacturer's specifications for the uncertainties associated with the pressure transmitters, as elaborated in Table 4.2.

4.7 Parameter estimation and tuning

This section aims to present the techniques employed for parameter estimation and tuning within the context of the ESP system. Both steady-state and dynamic scenarios are considered.

4.7.1 Steady-state parameter estimation

In steady-state conditions, the time derivatives of a dynamic system vanish, converting the dynamic system equations into a set of algebraic equations. Consequently, there is no need to estimate the state derivatives. To identify the unknown system parameters denoted by ψ , an optimization problem can be formulated using the steady-state data. The general form of this problem is:

$$\min_{\psi} \mathcal{L}^{ps}(A\psi, \mathbf{a}), \quad (4.23)$$

where $\mathcal{L}^{ps}(\cdot, \cdot)$ represents a loss function measuring the difference between the predicted and observed outputs. In this work, the L_2 -norm is employed as the loss function:

$$\min_{\psi} \|A\psi - \mathbf{a}\|_2^2, \quad (4.24)$$

where A is the matrix composed of steady-state experimental data and the system's model equations. The columns of A represent the terms of the algebraic equations whose parameters are being estimated. The vector ψ represents the parameters to be estimated, and \mathbf{a} denotes the observed output vector, in this case, the sum of the system's coupling and forcing terms.

The optimization problem in Equation (4.24) can be solved analytically by finding the point where the gradient of the loss function with respect to ψ is zero. If $A^T A$ is invertible, the parameter $\hat{\psi}$ minimizing Equation (4.24) can be found using the Moore-Penrose pseudo-inverse A^+ :

$$\hat{\psi} = A^+ \mathbf{a}, \quad (4.25)$$

where the pseudo-inverse A^+ is defined as:

$$A^+ = (A^T A)^{-1} A^T. \quad (4.26)$$

Furthermore, the efficacy of the model resultant from the parameters adjustment can be

quantified through the coefficient of determination (R^2), which is defined as:

$$R^2 = 1 - \frac{\sum_{i=1}^n (y_i - \hat{y}_i)^2}{\sum_{i=1}^n (y_i - \bar{y})^2} \quad (4.27)$$

where y_i and \hat{y}_i are the measured and predicted values, respectively, and \bar{y} is the mean of the measured values.

4.7.2 Dynamic model tuning

The ESP system model underwent fine-tuning to enhance its predictive capability with respect to experimental observations. Initial parameter estimates were obtained from steady-state analysis, detailed in Section 4.7.1. The process of obtaining these initial estimates as a basis for further refinement in a dynamic setting is elaborated in Appendix C. The tuning procedure consists of two sequential steps: the first focuses on the ESP and pipeline model parameters, and the second on the tuning of the pipeline C-elements. These stages are presented in the subsequent sections.

4.7.2.1 Dynamic model tuning ESP and pipeline

The tuning strategy employed a manual iterative technique wherein one parameter was adjusted at a time, holding others constant. Significant changes in model predictions were primarily attributed to the equivalent resistance terms in the pump and pipeline models. These terms will be discussed in further sections.

The model's performance was evaluated using the Mean Absolute Percentage Error (MAPE) calculated from the first and last 5 s of the dynamic pressure data at both the ESP intake and discharge points. The MAPE is formulated as:

$$\text{MAPE}_{\text{dyn}} = \frac{1}{n_{5s}} \sum_{i=1}^{n_{5s}} \left| \frac{P_x^i - \hat{P}_x^i}{P_x^i} \right|, \quad (4.28)$$

where n_{5s} denotes the number of samples in a 5 s interval, P_x^i and \hat{P}_x^i represent the measured and model-estimated pressures at time instant i , respectively. The subscript x can be 1 or 2 to refer to the intake or discharge pressure, respectively. The MAPE metric was chosen to minimize the impact of varying magnitudes among the variables when fine-tuning the model. The model was considered tuned when $\text{MAPE}_{\text{dyn}} < 1\%$.

4.7.2.2 Dynamic model tuning C-element

In contrast to the procedures delineated in Section 4.7.2.1, tuning the C-elements within the pipelines required a more elaborated methodology, which is outlined as follows:

- **Offset removal:** The initial step focused on eliminating any potential offset or vertical translation between the simulated and experimental data. This process considered the difference between the means during the first 5 s of measurements and simulations.
- **Initial grid search:** A preliminary parameter search was performed over the range $[1, 1000]$ with 20 discrete points for each variable.
- **Error metric:** The optimal parameter set was determined by minimizing the function O defined in Equation (4.29).
- **Refinement:** After identifying a promising parameter set, the search space is then halved for each subsequent iteration.
- **Convergence:** The algorithm converges when the difference between successive minimum objective function values is smaller than a pre-defined tolerance, $\epsilon = 1 \times 10^{-8}$.

The error metric O is defined as:

$$O = \frac{\text{NRMSE}_1 + \text{NRMSE}_2}{2}, \quad \text{where} \quad \text{NRMSE}_x = \frac{\sqrt{\frac{1}{n_{\text{meas}}} \sum_{i=1}^{n_{\text{meas}}} (P_x^i - \hat{P}_x^i)^2}}{\frac{1}{n_{\text{meas}}} \sum_{i=1}^{n_{\text{meas}}} P_x^i}, \quad (4.29)$$

where n_{meas} denotes the number of experimental data points, and P_x^i and \hat{P}_x^i represent the measured and model-estimated pressures at time instant i , respectively. The subscript x takes values 1 or 2 to denote intake and discharge pressures. The pseudo-code for this methodology is presented below.

Algorithm 1 Dynamic model tuning for C-elements

- 1: **Initialize:** Set initial parameter bounds $[1, 1000]$
 - 2: **Define:** Tolerance $\epsilon = 1 \times 10^{-8}$
 - 3: **Compute:** Calculate mean offset for the first 5 s of data
 - 4: **while** $|\text{last_min_val} - \text{min_val}| \geq \epsilon$ **do**
 - 5: Conduct grid search within parameter bounds
 - 6: Evaluate the error for each grid point using Equation (4.29)
 - 7: Update last_min_val to min_val
 - 8: Set min_val to minimum error found
 - 9: Halve the parameter bounds around the new min_val
 - 10: **end while**
 - 11: **Output:** Optimized C-element parameters
-

5 Modeling results

5.1 Pipeline model

In Section 3.2 it was discussed the pipeline dynamic governing equations, and from them, several bond graph 1-port elements with junction elements were derived. However, despite the similarity to the models proposed by Karnopp *et al.* [140] and Higo *et al.* [89], it is still required to validate whether the obtained model produces accurate results. Due to experimental constraints of the experimental setup described in Section 4.1, it was not possible to conduct pressure transient analysis on it. Therefore, instead of validating the model with experimental data. It was opted to validate the model against the continuity and momentum equations solved using the method of characteristics (MoC), as mentioned in Section 3.2.3.

From the momentum equation delineated in Section 3.2, specifically equation (Equation (3.19)), it can be simplified by incorporating the viscous friction term from the Darcy equation as discussed in Section 3.3. Consequently, the following equations can be derived:

$$\frac{\partial P}{\partial t} + u \frac{\partial P}{\partial x} + \rho a^2 \frac{\partial u}{\partial x} = 0, \quad (5.1a)$$

$$\frac{\partial u}{\partial t} + u \frac{\partial u}{\partial x} + \frac{1}{\rho} \frac{\partial P}{\partial x} - g \sin(\theta) - \lambda \frac{u|u|}{2d_h} - \frac{J_u}{\rho} = 0, \quad (5.1b)$$

where the term J_u represents an additional term incorporated to capture unsteady flow viscous friction.

As shown in previous works Chaudhry [118] and Vítkovský *et al.* [141], the steady-state friction modeled by the Darcy equation does not adequately capture the dynamics observed experimentally in unsteady flow conditions. This study employs the one coefficient Instantaneous Acceleration-Based (IAB) method to address this limitation. The IAB model assumes that unsteady friction arises from instantaneous local and convective accelerations. The general expression for this model is given as:

$$J_u = \rho K_{ju} \left(\frac{\partial u}{\partial t} + \text{sign}(u) a \left| \frac{\partial u}{\partial x} \right| \right), \quad (5.2)$$

where K_{ju} is an experimentally determined coefficient, which, as mentioned by Chaudhry [118], ranges from 0.015 to 0.016.

5.1.1 Problem definition

The current work aims to compare the bond graph model with the model described in Equation (5.1). For this purpose, it was considered a system comprising two large tanks initially filled with a liquid at different heights and interconnected by a pipe of constant diameter, as depicted in Figure 5.1. The tanks are sufficiently large that the liquid level remains approximately constant during the evaluation period, ensuring that the pressures at the pipe's entrance and exit remain nearly constant. The valve is assumed to open instantaneously and have a negligible impact on the flow. Thus, the boundary conditions for the problem are constant pressures on both ends of the pipe. Additional assumptions include a rigid pipe wall, excluding wall deformations from the analysis.

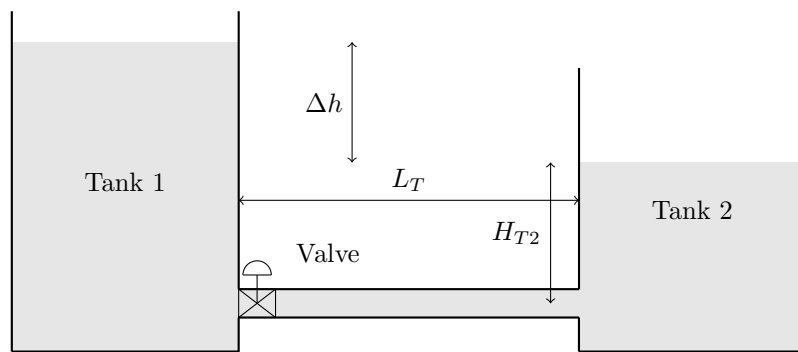


Figure 5.1: Two tanks interconnected by a pipe problem.

The system was modeled utilizing 1-port elements as deduced in Section 3.2.4. Due to the pipe's horizontal alignment and constant diameter, the convective term and hydrostatic pressure contributions can be neglected, thereby simplifying the model to the bond graph shown in Figure 5.2.

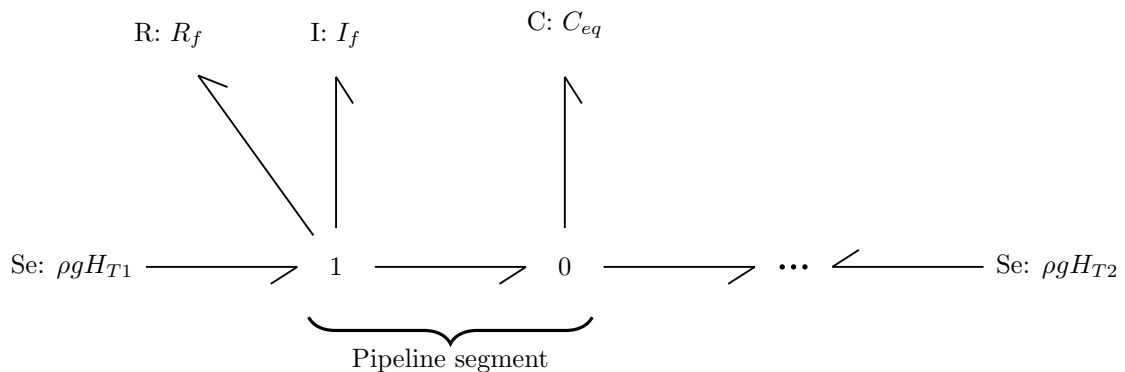


Figure 5.2: Bond graph model for the two tanks interconnected by a pipe problem.

In Figure 5.2, H_{T1} represents the height of liquid in Tank 1, expressed as $H_{T1} = \Delta h + H_{T2}$. For the compliance element C_{eq} in the pipeline, only the liquid's compressibility is considered, consistent with the assumption of a rigid pipe wall. The ellipsis in Figure 5.2 signifies that the number of pipeline segments representing the interconnecting pipe can vary.

In the Figure 5.2 bond graph model, two key dynamic behaviors are considered: inertial dynamics and pressure wave dynamics. The inertial dynamics are governed by the inertance element I_f , which primarily accounts for the fluid's mass inertia. On the other hand, pressure wave dynamics are characterized by the fluid's compressibility and the pipe wall's elasticity. Thus, a single pipeline segment in the bond graph model can be considered sufficient to accurately capture the inertial dynamics in the Figure 5.1. However, the representation of pressure wave dynamics may require additional pipeline segments to capture wave propagation effects accurately, as suggested by Higo *et al.* [89].

Thus, to assess the bond-graph model approximation accuracy in modeling both inertial and pressure wave dynamics, specific dimensions and fluid properties were selected for the two-tank system. The choice of these properties and parameters aimed to ensure laminar flow conditions throughout the simulation, thereby avoiding the complexities in determining the friction factor in the laminar-turbulent transition.

For the tanks, the dimensions are defined as $H_{T2} = 0.25$ m, $\Delta h = 0.75$ m, and $L_T = 1$ m. The fluid considered in this problem was the oil SAE 30W White [119]. At 20 °C and a pressure of 101.325 kPa, the oil's viscosity 0.29 Pa s, the density is 891 kg m^{-3} , and the bulk modulus is 1.31×10^9 Pa. The results for the inertial dynamics are presented in Section 5.1.2 while for the pressure wave in Section 5.1.3.

5.1.2 Validation inertial dynamics

To evaluate the inertial dynamics, simulations were conducted over a time range of 0 s to 5 s, chosen to allow the system to reach the steady-state condition. For the bond graph discretization of the pipeline, only one pipeline segment was considered to represent the entire pipeline, while for the MoC, it was considered a length discretization of 0.1 m. The results for the simulation using the MoC with IAB and bond graph model using one pipeline segment are shown in Figure 5.3.

It is noticeable in Figure 5.3 that the bond graph model with a single pipeline segment resulted in a relatively accurate approximation of the inertial dynamics, as substantiated by the mean absolute error of $1.563 \times 10^{-2} \text{ m s}^{-1}$ for the entire simulation duration. As can be seen, the bond graph approximation closely follows the MoC solution. In Figure 5.3, it is presented a zoom in the region of 0.8 s to 1.25 s to highlight a region with a high absolute error.

The time interval 0.8 s to 1.25 s in Figure 5.3 indicates that the bond graph model converges to the steady-state condition marginally faster than the MoC model. This observation persisted even when multiple pipeline segments were incorporated into the bond graph model, suggesting that the source of this discrepancy could be attributed to the damping effect induced by unsteady friction.

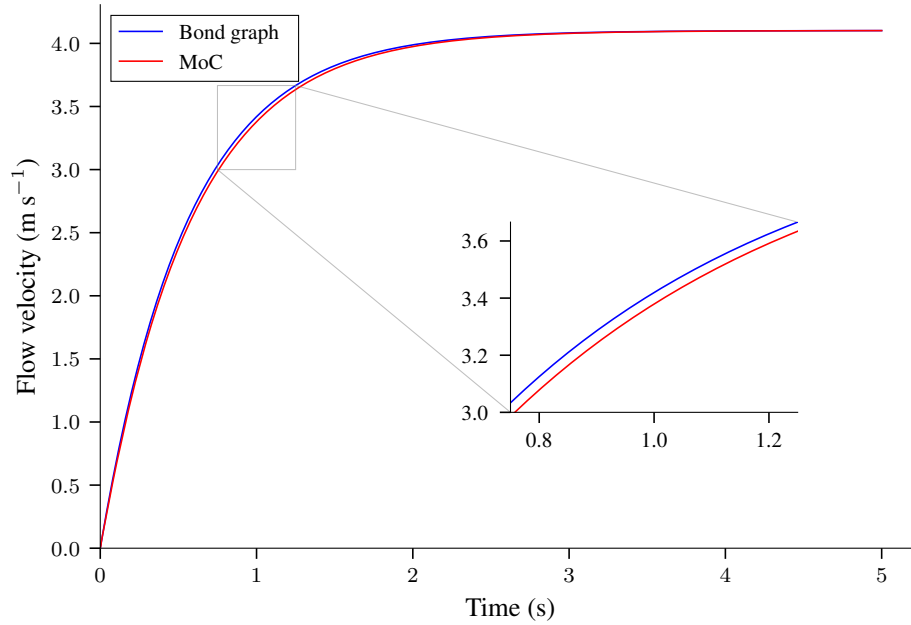


Figure 5.3: Bond graph and MoC comparison for inertial dynamics of the tank problem.

5.1.3 Validation pressure wave dynamics

In this section, the analysis is extended to the pressure wave dynamics. The simulations were conducted over a time frame of 0 s to 5 s, consistent with Section 5.1.2, to ensure steady-state conditions. For the bond graph model, the pipeline was discretized into 164 segments. This discretization was selected based on a relative error criterion defined as

$$\frac{\|\kappa^{i+1} - \kappa^i\|_2}{\|\kappa^{i+1}\|_2} < 10^{-2} \quad (5.3)$$

where κ represents the discretization with i segments. For the MoC, the same length discretization as in Section 5.1.2 was adopted. The comparative results between the MoC with IAB and the bond graph model using 164 segments are depicted in Figure 5.4.

Figure 5.4 reveals that the bond graph model with 164 segments offers a reasonably accurate approximation of the pressure wave dynamics, evidenced by a mean absolute error of $1.829 \times 10^{-3} \text{ m s}^{-1}$ over the simulation duration presented in Figure 5.4. The bond graph model approximates the MoC solution closely up to $3 \times 10^{-3} \text{ s}$. Beyond it, the bond graph approximation slowly deviates from the MoC solution. This behavior is consistent with observations from Section 5.1.2.

Additionally, it is observable oscillations around each step in the flow velocity, as indicated in Figure 5.4. These oscillations are similar to those reported by Chaudhry [118] for finite-difference methods. Chaudhry [118] mentions these oscillations are numerical artifacts and not representative of the true system dynamics. In the context of the bond graph model, the oscillations are likely attributable to the finite representation of the pipeline segments. An

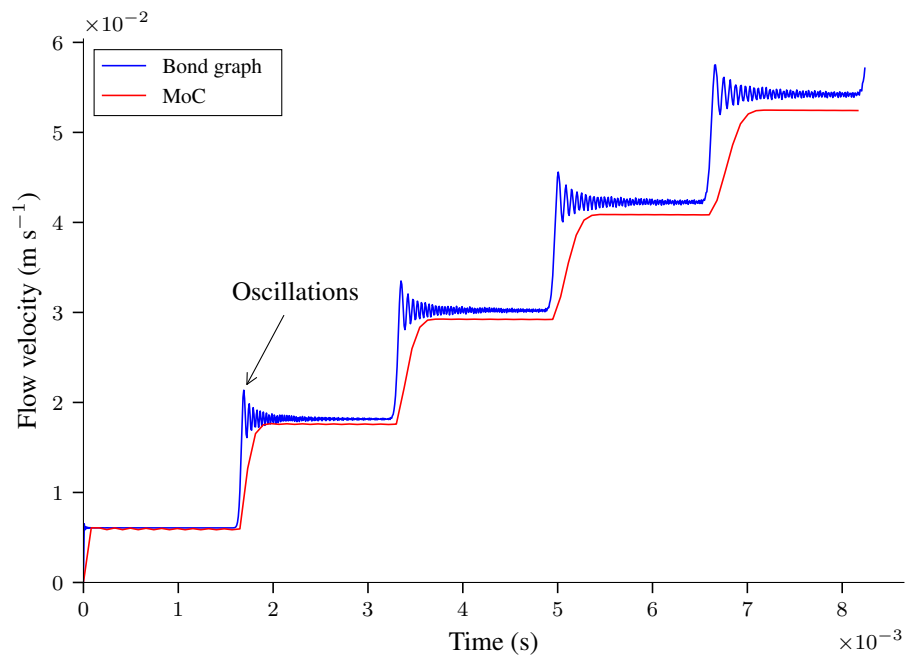


Figure 5.4: Bond graph and MoC comparison for pressure wave dynamics of the tank problem.

increase in the number of segments was found to alleviate these oscillations.

5.2 Shaft-pump bond graph model

In Sections 3.4 and 3.5, the bond graph elements for the centrifugal pump were derived by analyzing the physical principles governing the pump system and reviewing existing literature on centrifugal pumps. As an initial step in modeling the ESP system using bond graphs, the shaft-pump subsystem with a single impeller is considered. The bond graph methodology enables the straightforward integration of additional impellers, the validated pipeline model, and the twin-screw pump to form a comprehensive model of the ESP system.

The most critical element within the bond graph of the shaft-pump model is the gyrator, as defined in Section 3.4.5. This 2-port element establishes the relationship between the angular velocity ω of the centrifugal pump shaft mechanical domain and the volumetric flow rate Q in the hydraulic domain. This relationship is quantitatively represented by Equation (3.71), reproduced below for clarity.

$$\gamma = \zeta_3\omega - \zeta_4Q, \text{ where } \zeta_3 = \rho(r_2^2 - r_1^2) \text{ and } \zeta_4 = \rho\left(\frac{\cot(\beta_2)}{2\pi h_2} - \frac{\cot(\beta_1)}{2\pi h_1}\right).$$

The other elements essential to the bond graph representation of the pump subsystem include the following resistance components:

- R_{cf} : Addresses friction loss within the impeller and is defined in Section 3.5.1.
- R_{mc} : Represents local losses in the centrifugal pump, as elaborated in Section 3.5.2.
- R_{sx} : Accounts for shock losses in the centrifugal pump, detailed in Section 3.5.3.
- R_{cl} : Models the leakage losses; it is described in Section 3.5.4.

For the bond graph of the shaft subsystem, the resistance elements are as follows:

- R_{df} : Accounts for disk friction losses in the pump shaft, as defined in Section 3.5.5.
- R_m : Represents the friction from the journal bearing and stuffing box, detailed in Section 3.5.6.

In addition to the frictional losses, it is necessary to account for the inertia of both the fluid within the impeller, I_{cf} , and the shaft, I_s . For the shaft, the inertia can be straightforwardly calculated using the moment of inertia of a cylinder with respect to its central axis, as expressed by:

$$I_s = \frac{m_s r_s^2}{2}, \quad (5.4)$$

where m_s is the mass of the shaft and r_s is its radius. The shaft can be conceptualized as comprising multiple segments, akin to the discretization applied to the pipeline in Section 5.1. In this segmented representation, I_s^i would denote the moment of inertia for an individual segment i .

In contrast, estimating the fluid inertia within the impeller, I_f , poses a greater challenge. Derived from the momentum equation, Equation (3.23) presents an expression for the inertia within a duct I_f as:

$$I_f = \int_0^l \frac{\rho}{A(x)} dx. \quad (5.5)$$

The equation accounts for unidimensional flow through a generic duct. If the impeller channel is approximated as such a duct, the fluid inertia can be estimated. However, determining an accurate cross-sectional area expression along the radius of the impeller is not trivial. As an alternative, from Biazussi [61] measurements for the impeller of the pump used in this study, we can estimate the cross-sectional areas at the entrance and exit of the impeller.

As a simplification, the cross-sectional area of the impeller channel is assumed to vary linearly from the entrance to the exit along the radius, and the mean cross-sectional area is considered. For this equivalent duct, the axial length is approximated as the radial difference between the inner and outer radii of the impeller. Consequently, the inertia for this equivalent duct is given by the following adapted equation from Equation (3.24a), rather than Equation (3.23):

$$I_{cf} = \frac{n_b \rho (r_2 - r_1)}{A_{cm}}, \quad (5.6)$$

where n_b is the number of blades and A_{cm} is the mean cross-sectional area.

It is pertinent to acknowledge that the assumptions and simplifications made to estimate the fluid inertia within the impeller constitute a limitation of this study. Although more accurate estimates could be obtained with detailed geometric characterizations of the impeller, the inertia of the liquid within the pump is considerably less significant than that of the pipeline fluid, given that for this study, the pipeline inertia is 1.345×10^3 greater than the impeller. Therefore, the errors introduced by these assumptions are not expected to substantially affect the behavior of the entire system.

Furthermore, it is necessary to incorporate the stiffness of the shaft due to torsional deformations. The estimation of this parameter is straightforward and is expressed as:

$$k_\theta = \frac{GJ}{L_s}, \quad \text{where} \quad J = \frac{\pi r_s^4}{2}. \quad (5.7)$$

The term G represents the shear modulus of the shaft material, L_s denotes the length of the shaft, and J is the polar moment of inertia. Analogous to the approach for inertia, the shaft may be viewed as a composite of multiple segments in bond graph modeling. In this discretized model, k_θ^i would represent the stiffness associated with individual segment i . In the bond graph notation, the stiffness is represented by a C-type element where $C_s = 1/k_\theta$.

By integrating the shaft and impeller elements, we obtain the bond graph model for the shaft-impeller subsystem, which is illustrated in Figure 5.5. This model consists of two subsystems: the shaft and a single impeller, which are connected via a gyrator port. In Figure 5.5, these

subsystems are demarcated by dashed black rectangles. The ellipsis within the figure signifies points of connection to other subsystems, which may include additional impellers or the upstream and downstream pipelines.

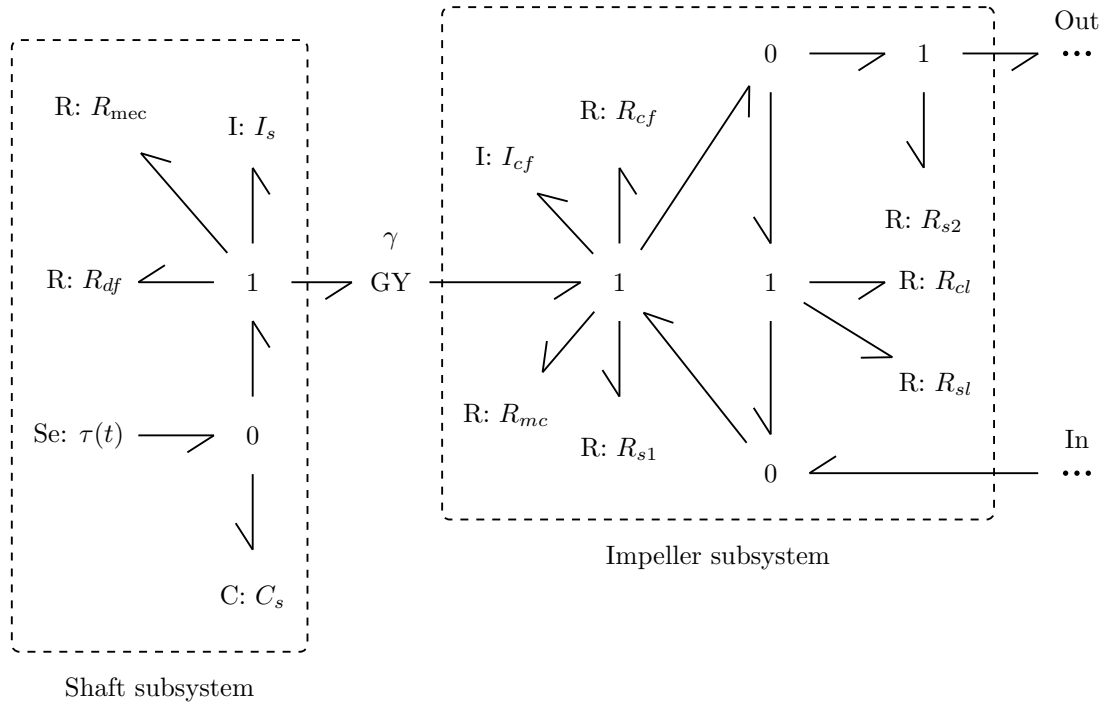


Figure 5.5: Bond graph model of the shaft and impeller subsystem.

5.3 General ESP system bond graph model

The objective of this section is to delineate a comprehensive bond graph model for an ESP system. This model incorporates an arbitrary number of pump stages, shaft segments, and pipeline segments, which were previously discussed. Additionally, the model includes the valve and twin-screw pump bond graph models outlined in Section 3.6.3 and Section 3.7.1, respectively. Due to the model's complexity, custom port names are employed to represent individual subsystems.

To simplify connections among custom subsystems, the direction of *half arrows* is utilized to indicate input or output ports. Specifically, *half arrows* originating from a subsystem denote outputs, while those entering denote the inputs. The shaft segment is denoted as \mathcal{S}^i where i represents the segment index; its bond graph model is presented in Figure 5.6. This model accepts one input and provides multiple outputs. Importantly, the disk-friction loss term R_{df}^i is only relevant for shaft segments immersed in a fluid.

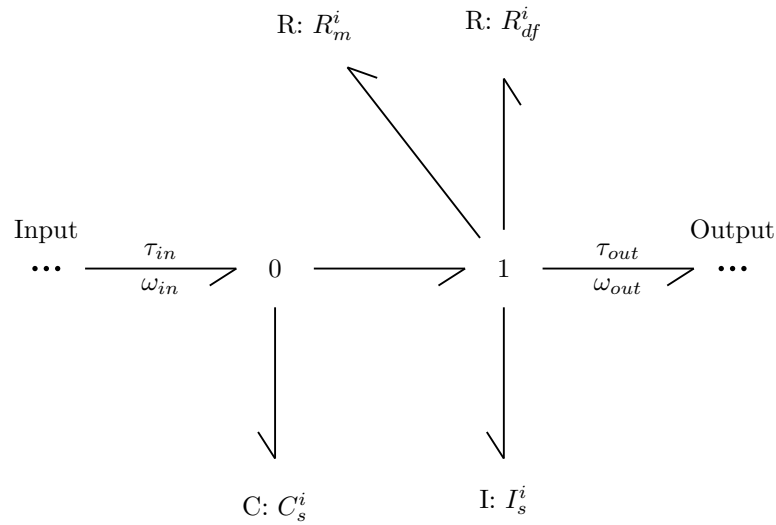


Figure 5.6: Bond graph model for a shaft segment (\mathcal{S}^i).

Similarly, the pipe segment is denoted as \mathcal{P}^i , its bond graph model is shown in Figure 5.7. It integrates the bond models discussed in Section 3.2.4 and validated in Section 5.1. It has multiple inputs and outputs.

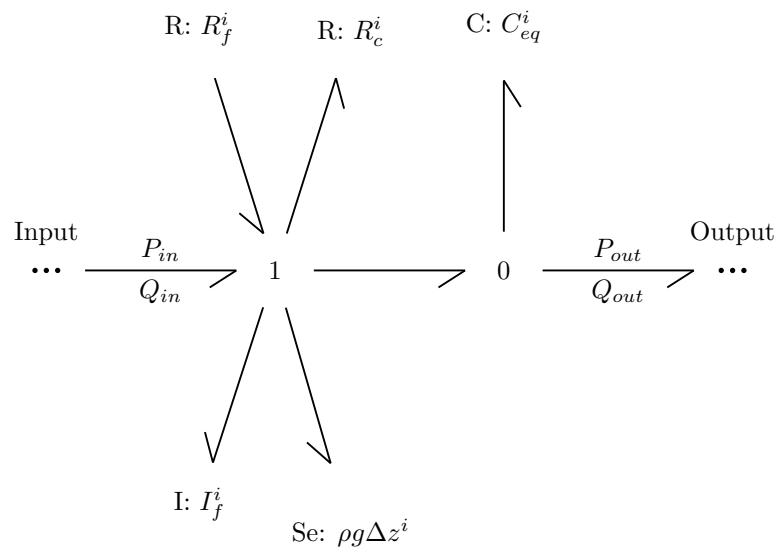


Figure 5.7: Bond graph model for a pipe segment (\mathcal{P}^i).

The centrifugal pump stage is represented as \mathcal{C}^i , with its bond graph model specified in Figure 5.8. It accepts two inputs, incoming torque and flow, and provides one output representing the outgoing flow.

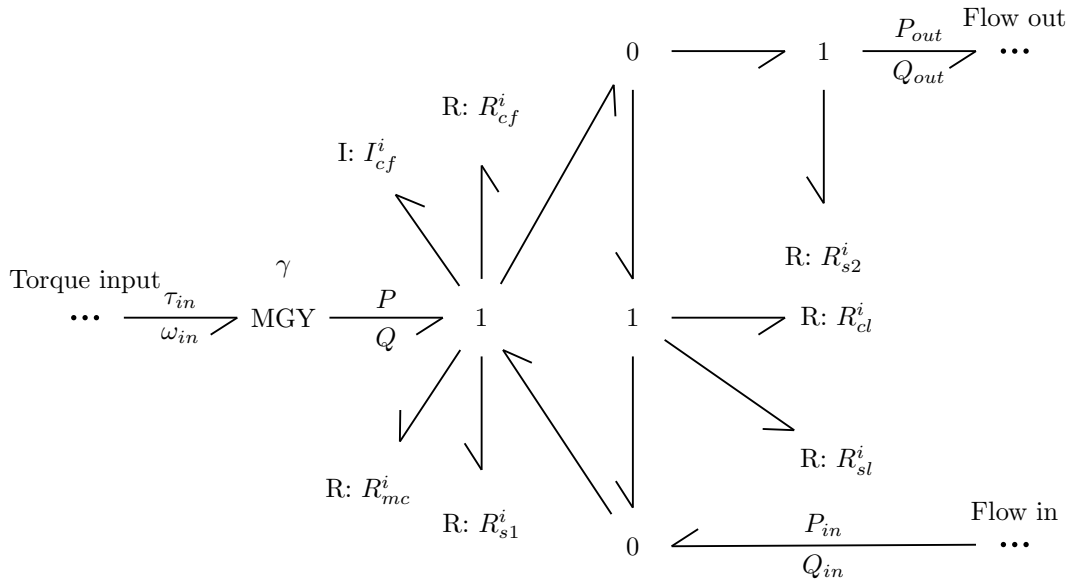


Figure 5.8: Bond graph model for a centrifugal pump stage (C^i).

Additionally, the valve, discussed in Section 3.6, is denoted as \mathcal{V}^i , where i serves as the valve identifier. As for the twin-screw pump, its model has been previously detailed in Figure 3.9 and is denoted by \mathcal{T} . This model is characterized by two inputs: the angular velocity of the twin-screw pump, ω_t , and the pressure at the pump’s intake, P_{in} . It yields a single output, which is the flow exiting the twin-screw pump.

By integrating these subsystems, a comprehensive bond graph model of the ESP system is assembled as follows:

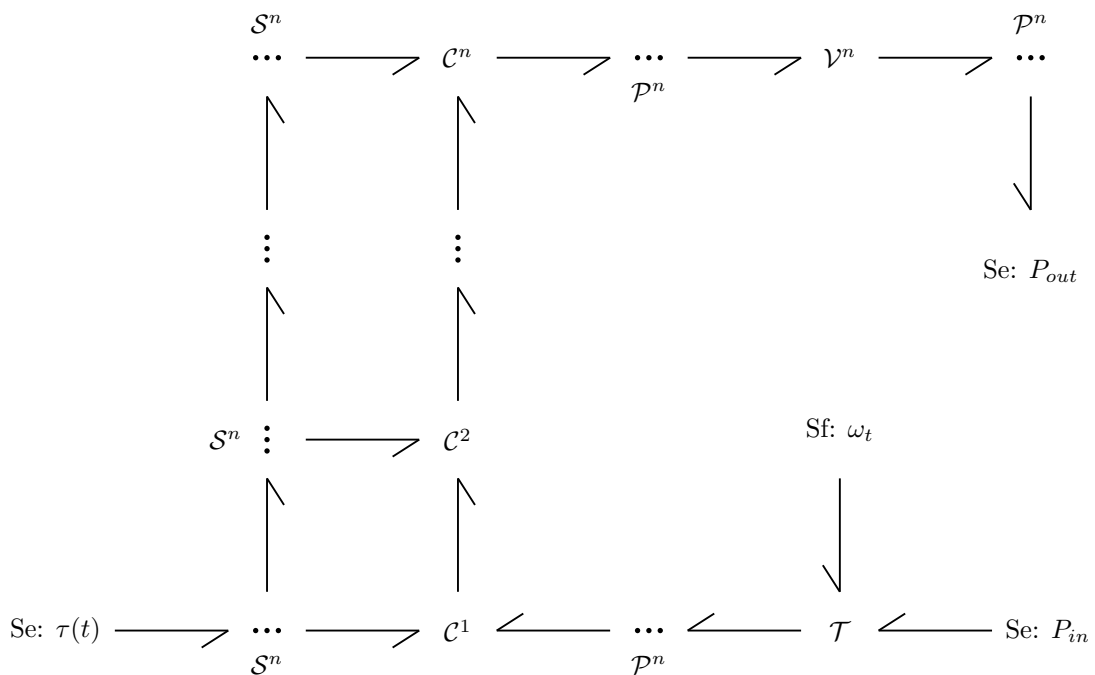


Figure 5.9: Bond graph model the ESP system.

In Figure 5.9, the subsystems accompanied by an ellipsis symbolize the capability to include

multiple instances of that particular subsystem in the model.

It is worth noting that the presented bond graph model, although constructed with a focus on a single multistage ESP and a twin-screw pump denoted by \mathcal{T} , possesses inherent modularity that allows for extensions to more complex ESP configurations. Specifically, the twin-screw pump model can be substituted with a well-characterized well model. Additionally, further ESP can be connected in parallel within the downstream pipeline. Consequently, the model's architecture is amenable to the incorporation of additional subsystems. The model equations are generated in an automated fashion and are solvable using both ODE and DAE numerical solvers, thereby facilitating both modifications and simulations of the ESP system.

5.4 Single impeller approximation

The ESP system bond graph model discussed in Section 5.3 is highly detailed and general for ESP systems. It includes an arbitrary number of pipe segments for the pipelines and the pump's shaft and an arbitrary number of stages for the ESP. Although it allows for an accurate assessment of the system dynamics, the computational tractability of this model is compromised. Additionally, obtaining the required system parameters for this model's level of detail in real conditions can be challenging. Therefore, to assess the model's validity when compared to experimental measurements of the assembly discussed in Section 4.1, certain simplifications are necessary for the model presented in Section 5.3. These simplifications are presented along with their justifications and potential limitations.

Assumption 5.4.1. *The upstream and downstream pipelines are modeled using a single pipeline bond graph segment.*

This assumption is grounded in the determination that a single pipe segment adequately captures the inertial dynamics of the system. Given that the primary focus of this work is on inertial dynamics rather than pressure wave propagation, the complexity of using multiple segments for detailed pressure wave dynamics representation involving up to 164 segments per 1 m, is not required within the scope of this study.

Assumption 5.4.2. *The shaft of the experimental assembly is considered a rigid body under both steady-state and dynamic loading conditions.*

While this assumption simplifies the analysis, it introduces certain limitations, particularly under dynamic loading conditions. This is notably relevant for ESP with large number of stages and long shafts, where torsional vibrations become increasingly significant due to the inverse relationship between shaft stiffness and length (Equation (5.7)). While these limitations are acknowledged but have yet to be explored further.

Assumption 5.4.3. *In the bond graph model of the impeller, leakage losses are excluded, and shock losses within the pump are aggregated into a single term.*

This simplification is necessitated by the challenges in obtaining accurate experimental data for the leakage coefficients. As discussed in Section 3.5.4, where the literature reports uncertainties of up to $\pm 30\%$. The pump shock losses were aggregated into a single term instead of separate terms for the inlet and discharge due to the experimental difficulties in isolating these variables. Despite these concessions, the methodology aligns with that of Biazussi [61], who also condensed the shock and leakage losses into one term, arguing that these phenomena effects are sufficiently interrelated and can be represented by a single term.

The bond graph model of the ESP system is presented in Figure 5.10. This model follows the experimental setup described in Section 4.1 and incorporates the aforementioned simplifications. The notations u and d as superscripts differentiate between the upstream and downstream segments of the pipeline. The term R_v is introduced as a modulated R-type element to encapsulate the valve resistance. The set of ODE arising from the bond graph model, obtained using the procedure described in Section 4.2, is expressed as:

$$\frac{dQ_p}{dt} = \frac{(P_1 - P_2 + k_3 \mu Q_p) A_p}{\rho L_p} + \frac{A_p (k_{1p} \omega Q_p + k_{2p} \omega^2 + k_{4p} Q_p^2)}{L_p}, \quad (5.8a)$$

$$\frac{d\omega}{dt} = \frac{\tau(t) - k_{1s} \rho Q_p^2 - k_{2s} \rho \omega Q_p - k_{3s} \mu \omega - k_{4s} \omega - k_{5s} \omega^2}{I_s}, \quad (5.8b)$$

$$\frac{dQ_1}{dt} = \frac{(k_{bd} \omega_t - Q_1) k_{bl} \mu + P_{in} - P_1 - f_f(Q_1, \mu, L_u, d_u) Q_1^2 A_u}{\rho L_u} - \frac{k_u Q_1^2}{2 L_u A_u}, \quad (5.8c)$$

$$\frac{dQ_2}{dt} = \frac{(P_2 - P_{out} - f_f(Q_2, \mu, L_d, d_d) Q_2^2) A_d}{\rho L_d} - \frac{k_d Q_2^2}{2 L_d A_d} - \frac{Q_2^2 A_d}{L_d C_v(a)^2 \rho^*}, \quad (5.8d)$$

$$\frac{dP_1}{dt} = \frac{(Q_1 - Q_p) B}{A_u L_u}, \quad (5.8e)$$

$$\frac{dP_2}{dt} = \frac{(Q_p - Q_2) B}{A_d L_d}. \quad (5.8f)$$

The input to the ESP system is denoted by $\tau(t)$, corresponds to the bond graph element Se: $\tau(t)$, representing the torque applied to the ESP shaft. Given that both the intake pressure, P_{in} , and the outlet pressure, P_{out} , are exposed to the same atmospheric separation tank, they are assumed to be constant at 0 Pa for simplification. They correspond to the bond graph elements Se: P_{in} and Se: P_{out} . Furthermore, the rotation of the twin-screw pump, ω_t , is encapsulated within the bond graph as Sf: ω_t . The friction factor model is represented by $f_f(\cdot)$, and its explicit form is dependent upon the flow characteristics, as elaborated in Section 3.3.

The Table 5.1 lists the state variables that define the ESP system, while the model parameters are outlined in Tables 5.2 and 5.3. The methodology for obtaining these parameter values is discussed in Section 4.1.6 and detailed in Appendix C. The Table 5.2 presents the parameters that are constant for the dynamic experimental investigations (Inv.), and Table 5.3 presents the parameters that change with the dynamic experimental investigation.

In the process of fitting parameters, presented in Tables 5.2 and 5.3, to experimental data, it encountered several challenges, particularly within the ESP system with P100L. The absence

of direct pressure measurements at the outlet of the twin-screw pump and including a bypass valve after the heat exchanger necessitated the fitting of upstream parameters for each dynamic experiment. This approach, while essential, occasionally resulted in the derivation of unrealistic parameters, as evidenced in Table 5.3. Moreover, the downstream pipeline of the ESP system with P100L lacked isolated measurements for valve pressure differences, leading to the aggregating of various terms into an equivalent valve model. Despite these constraints, the fitting process yielded a reasonable fit to the experimental data for upstream and downstream pipelines, suggesting acceptable model accuracy within the tested conditions. However, extrapolation of these results beyond the experimental scope requires caution.

In the ESP system with P47, similar challenges were encountered despite having direct measurements of pressure after the twin-screw pump and valve pressure losses. The twin-screw pump model exhibited limitations in accurately capturing the pressure gain, as indicated by the absolute error and R^2 values. Additionally, the fitting process for this system also resulted in unexpectedly high parameter values similar to those observed in the ESP system with P100L, highlighting the limitations of the twin-screw pump model and the parameters' applicability beyond the specific experimental setup and property range. Furthermore, the downstream pipeline's local loss fitting yielded a low R^2 value, although the magnitude of these errors is relatively minor compared to the pump's discharge pressure.

Lastly, the equivalent resistances k_u and k_d in the upstream and downstream systems, presented in Table 5.3, account for losses associated with manual tuning. This aspect and other details regarding the parameter fitting to experimental data are further elaborated in Section 5.5. For a comprehensive discussion, please refer to Appendix C.

Table 5.1: States of the ESP system bond graph model

#	Description	Symbol	Unit
1	Impeller volumetric flow-rate	Q_p	$\text{m}^3 \text{s}^{-1}$
2	Upstream pipeline volumetric flow-rate	Q_1	$\text{m}^3 \text{s}^{-1}$
3	Downstream pipeline volumetric flow-rate	Q_2	$\text{m}^3 \text{s}^{-1}$
4	Suction pressure	P_1	kPa
5	Discharge pressure	P_2	kPa
6	ESP angular velocity	ω	rad s^{-1}

It is important to mention that the set of ODE denoted by Equation (5.8a) is an expanded and simplified form of the initial ODE system derived from the bond graph model presented in Figure 5.10. This step is essential while assessing the identifiability of the model, which will be discussed in Chapter 6.

Table 5.2: Parameters for the ESP system bond graph model

#	Description	Symbol	P100L	P47	Unit
1	1 st impeller-fluid coupling and shock loss coefficient	k_{1p}	4.868	42.98	m^{-1}
2	2 nd impeller-fluid coupling and shock loss coefficient	k_{2p}	9.930E-3	14.39E-3	m^2
3	Pump viscous flow loss coefficient	k_{3p}	-63.06E6*	-290.5E6*	m^{-3}
4	Pump equivalent resistance	k_{4p}	-2.227E6*	-8.551E6*	m^{-4}
5	Shaft 1 st impeller-fluid coupling coefficient	k_{1s}	-61.26*	-111.7*	s m^{-2}
6	Shaft 2 nd impeller-fluid coupling coefficient	k_{2s}	7.813E-3	7.894E-3	m s
7	Fluid-impeller disk friction constant	k_{3s}	110.4E-3	242.3E-3	$\text{m}^2 \text{s}$
8	Shaft viscous damping coefficient	k_{4s}	67.32E-3	12.27E-3	kg m
9	Shaft second-order friction coefficient	k_{5s}	142.3E-6	232.4E-6	kg m s
10	Shaft moment of inertia	I_s	508.5E-6	508.5E-6	kg m^2
11	Fluid bulk modulus	B	1.310E9	1.310E9	Pa
12	Downstream pipeline diameter	d_d	76.20E-3	76.20E-3	m
13	Downstream pipeline cross-sectional area	A_d	4.560E-3	4.560E-3	m^2
14	Downstream pipeline length	L_d	28.00	28.00	m
15	Upstream pipeline diameter	d_u	76.20E-3	76.20E-3	m
16	Upstream pipeline cross-sectional area	A_u	4.560E-3	4.560E-3	m^2
17	Upstream pipeline length	L_u	31.50	31.50	m
18	Cross-sectional area of all impeller channels	A_p	4.897E-3	2.290E-3	m^2
19	Impeller channel length	L_p	47.50E-3	47.50E-3	m

* The negative sign indicates that the obtained parameter is opposite in sign to what is considered in the equations.

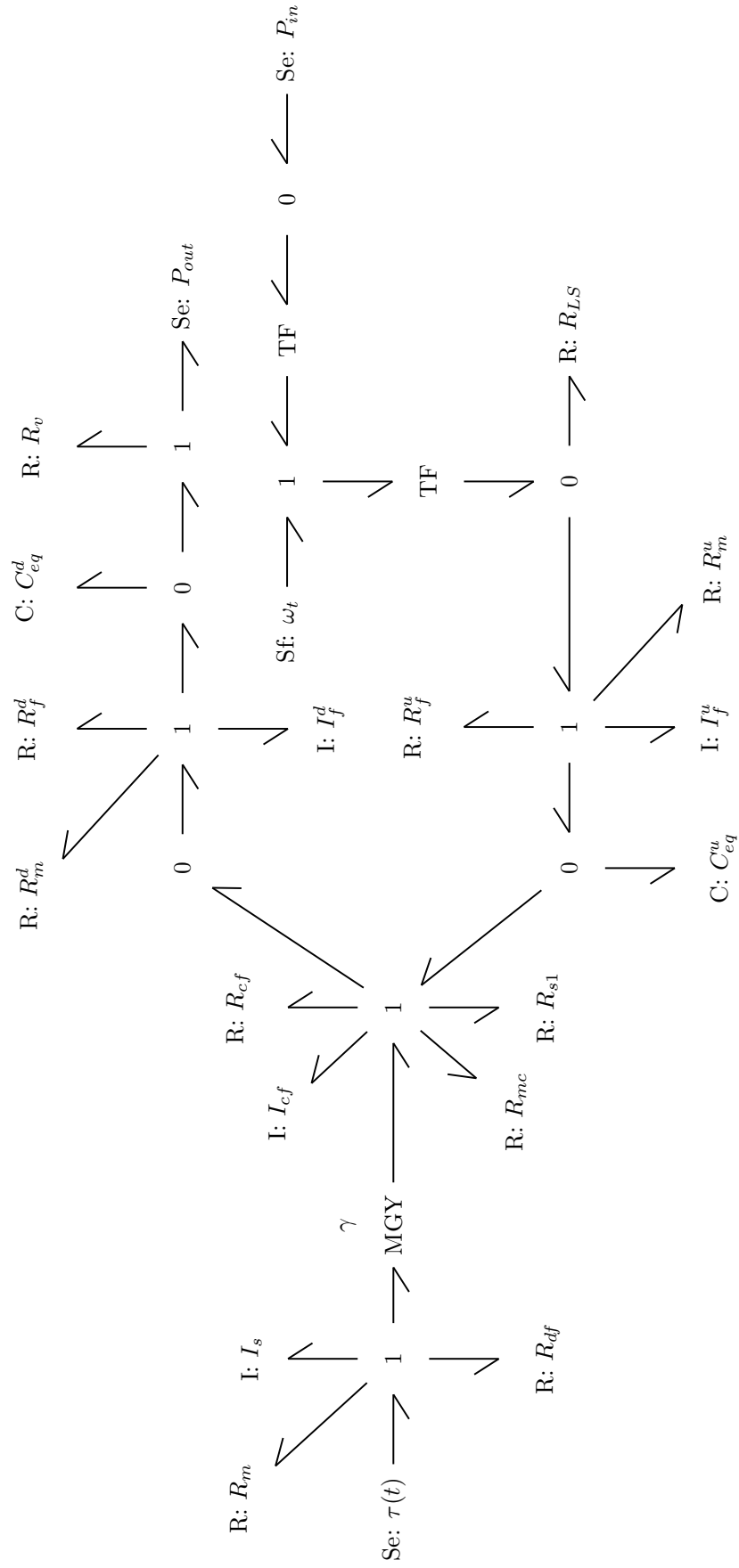


Figure 5.10: Simplified bond graph model for the ESP system.

Table 5.3: Parameters for the twin-screw pump and pipeline.

#	Description	Symbol	Inv. 1	Inv. 2	Inv. 3	Inv. 4	Inv. 5	Inv. 6	Unit
20	Fluid effective viscosity	μ	142.9E-3	228.1E-3	81.11E-3	62.59E-3	62.30E-3	96.34E-3	Pa m
21	Fluid density	ρ	882.2	872.6	878.4	875.6	880.0	889.1	kg m ⁻³
22	Upstream pipeline resistance coefficient	k_u	51.02	656.6	39.33	39.33	39.33	39.33	1
23	Downstream pipeline resistance coefficient	k_d	30.67	27.03	27.03	27.03	27.03	27.03	1
24	Twin-screw pump angular velocity	ω_t	1.280E3	1.160E3	200.0	400.0	400.0	200.0	RPM
25	Twin-screw pump flow-rate coefficient	k_{bd}	162.2E3	133.5E3	331.8E3	331.8E3	331.8E3	331.8E3	m
26	Twin-screw pump leaking coefficient	k_{bt}	11.44E9	23.72E9	9.565E9	23.72E9	23.72E9	23.72E9	m

5.5 Model validation

Utilizing the parameters acquired through the methodology delineated in Appendix C, the ordinary differential equations presented in Section 5.4 can be solved using the numerical solver as specified in Section 4.6. Prior to proceeding with the model validation, some assumptions required to solve the model need to be explicitly addressed.

The dynamic experimental investigations detailed in Section 4.1.7 exhibited laminar flow conditions, characterized by Reynolds numbers of 1657.78, 1028.10, 481.70, 1282.15, 1294.77 and 421.36 for the first through the sixth dynamic experiment, respectively. Thus, laminar flow is assumed in both the emulsion and oil flow lines, so it is necessary to specify the friction function for this study. Due to the laminar flow conditions, the friction function $f_f(Q, \mu, L, d)$ is derived using the correlation presented in Section 3.3.1 and is expressed as follows:

$$f_f(Q, \mu, L, d) = \frac{128 L \mu}{\pi Q d^4}. \quad (5.9)$$

Given the complexities of the emulsion flow discussed in Section 3.1, an appropriate model for emulsion viscosity is indispensable for accurate simulation. Although numerous models exist for this purpose (e.g., Einstein [142], Taylor [143], Pal and Rhodes [144]), this study employs the model proposed by Brinkman [69]. The choice is motivated by the model's widespread application in the oil industry. It is worth noting that Bulgarelli *et al.* [48] introduced a model specifically tailored for effective emulsion viscosity in ESP; however, this model lacks general applicability and does not extend to pipeline flows. Therefore, the Brinkman model was chosen, and it is expressed as follows:

$$\mu = \mu_c \left(\frac{1}{1 - \Omega} \right)^{2.5} \quad 0 < \Omega < 1, \quad (5.10)$$

where Ω represents the water cut and μ_c is the viscosity of the continuous phase.

Furthermore, the liquid bulk modulus for oil and emulsion were not experimentally measured. This represents a limitation in the accuracy of the proposed model. Instead, the liquid bulk modulus used in this study are from White [119]. This choice was a necessary compromise given the scope and constraints of the research, but future work should prioritize the direct measurement of this property to enhance the model's fidelity.

The subsequent sections present a comparison between the dynamic experimental investigation and the numerical solutions of Equation (5.8). These comparisons, which utilize the parameters and assumptions delineated thus far, can be found in Section 5.5.1. Additionally, a fine-tuning of the bulk modulus and its impact on the model is explored in Section 5.5.2.

5.5.1 Pump and pipeline tuning

Although the models detailed in Appendix C demonstrate reasonable accuracy under steady-state conditions, as evidenced by their R^2 values, additional fine-tuning is essential for improved alignment with experimental measurements. This tuning process follows the methodology outlined in Section 4.7.2.1. The Figures 5.11 to 5.16 provide a comparative analysis between experimental measurements and the numerical solutions of the model for the dynamic experiments delineated in Table 4.7, which includes ESP models P100L and P47. The correlation between the experimental and simulated data, quantified using the Pearson correlation coefficient, and the MAPE for each state, are detailed in Table 5.4. The MAPE was calculated as follows:

$$\text{MAPE}_{\text{val}} = \frac{1}{n_{\text{exp}}} \sum_{i=1}^{n_{\text{exp}}} \left| \frac{S_i - \hat{S}_i}{S_i} \right|, \quad (5.11)$$

where n_{exp} denotes the number of samples in the experiment interval, S_i and \hat{S}_i represent the measured and model-estimated state S at time instant i , respectively. The unmeasured states in the experimental setup were excluded from this evaluation. In each sub-figure, the blue line indicates the numerical solution, and the red dots are the measurements for a given state.

Table 5.4: Comparison of the MAPE and Pearson correlation coefficient between numerical solutions and experimental data. The units are percentages, and the parenthetical values correspond to the Pearson correlation coefficient, which is dimensionless.

#	P_1	P_2	Q_1	ω
1	16.97 (0.9740)	0.7795 (0.6413)	0.2088 (0.9145)	1.135 (0.9999)
2	6.583 (0.9825)	0.7728 (0.7113)	0.098 29 (0.9383)	0.7397 (0.9985)
3	9.583 (0.8431)	2.689 (0.7803)	1.504 (0.8066)	0.9579 (0.9950)
4	21.99 (0.8780)	2.629 (0.7039)	1.367 (0.8702)	0.5616 (0.9949)
5	74.61 (0.8509)	2.421 (0.5860)	0.5008 (0.8522)	2.925 (0.9961)
6	44.94 (0.7945)	4.079 (0.7424)	1.130 (0.7207)	5.612 (0.9967)

As illustrated in Figures 5.11 to 5.16, the tuned dynamic model effectively captures the main dynamics of the system across various states and ESP models. Notably, the model excels in replicating the ESP shaft angular velocity for both pumps (Figures 5.11d, 5.12d, 5.13d, 5.14d, 5.15d and 5.16d) and the upstream flow rate for the ESP model P100L (Figures 5.11c and 5.12c). However, for the ESP model P47, a consistent offset in upstream flow rates is observed (Figures 5.13c, 5.14c, 5.15c and 5.16c), likely due to limitations in the twin-screw pump model fit, as discussed in Appendix C. While the model aligns closely with experimental data under steady-state conditions, minor discrepancies are noted. For instance, a slight offset in ESP angular velocity is observed in dynamic experiments 1, 2, 3 and 4 (Figures 5.11d, 5.12d, 5.13d and 5.14d), particularly within the initial 5 s. In contrast, a consistent offset throughout the simulation is noted in experiments 5 and 6 (Figures 5.13d and 5.14d).

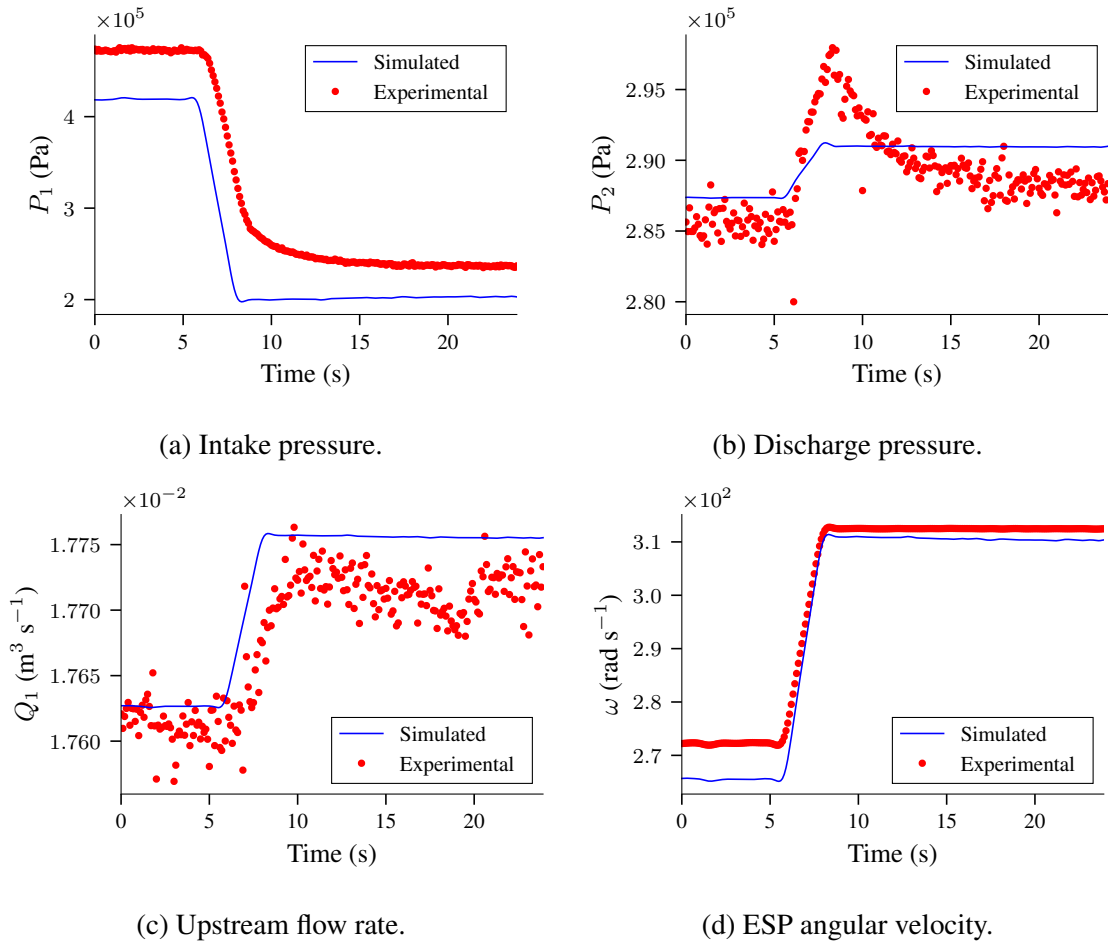


Figure 5.11: Comparison of the numerical solution and the measured states for the ESP P100L in the first dynamic experimental investigation (Table 4.7, row 1).

Conversely, in the case of Figures 5.11, 5.15 and 5.16, the intake pressure exhibits a more pronounced offset despite the tuning procedures outlined in Section 4.7.2.1. Specifically, in the ESP model P47 dynamic experiment 6 (Figure 5.16), the offset is also observed in the discharge pressure. Given that these cases have a higher water cut, this phenomenon might be attributed to the limitations of the Brinkman model for effective viscosity.

Upon analyzing the data presented in Table 5.4, it becomes evident that the MAPE values for most of the measured variables remain below 2.4%, ascertaining the reasonable accuracy of the model. This is further evidenced by the Pearson correlation coefficients, which exceed 0.8 in most experiments and states. The notable exception is the discharge pressure (P_2), which will be discussed further in this section. Regarding the MAPE values, the intake pressure (P_1) warrants particular attention; it exhibits the highest MAPE values, reaching up to 74.61% for the ESP model P47 and 16.97% for the ESP model P100L. Although the P_1 MAPE values are lower in other experiments, they are comparatively higher than for other states. The elevated MAPE values for P_1 and the relatively high Pearson correlation coefficients suggest that the primary contributor to this discrepancy is the offset error observed in the dynamic experiments. Despite this, the general response of the model aligns well with the experimental data, as indicated by

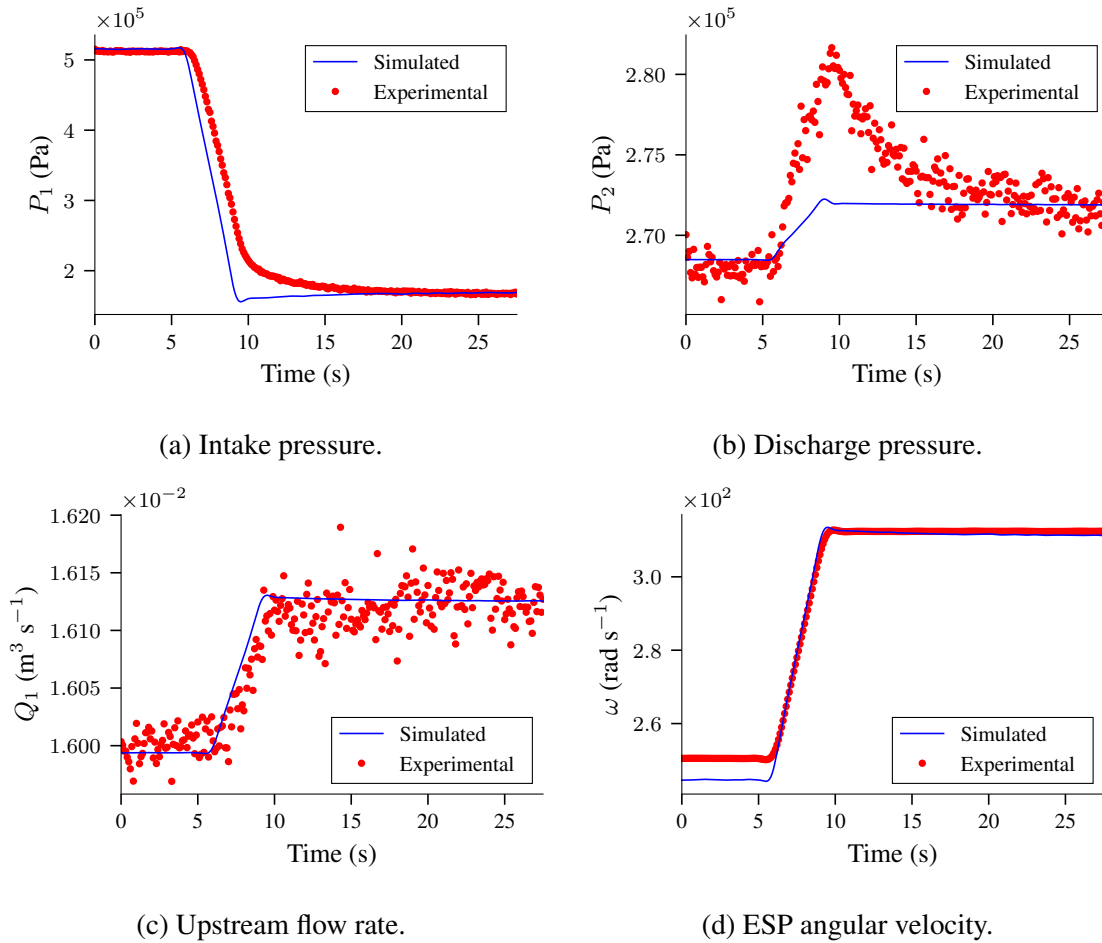


Figure 5.12: Comparison of the numerical solution and the measured states for the ESP P100L in the second dynamic experimental investigation (Table 4.7, row 2).

the high Pearson correlation values, which do not account for offset errors.

Across all experiments (Figures 5.11 to 5.16), the model reaches the steady state more rapidly than the experimental observations for intake and discharge pressures. This faster stabilization is particularly noticeable for the ESP model P47, where it is also observed in the upstream volumetric flow rate. The experimental data for both ESP models, in contrast, show a more pronounced overshoot in discharge pressures than the numerical solution. This disparity in pressure overshoot representation might be contributing to the lower Pearson correlation coefficients for discharge pressure (P_2) observed in Table 5.4, while the MAPE values remain relatively low.

Furthermore, a closer look at the ESP model P47 reveals a slower increase in volumetric flow rate (Figures 5.13c, 5.14c, 5.15c and 5.16c). This overall faster response of the model, compared to experimental data for ESP pumps, suggests that the current model parameters might not fully capture certain dynamic aspects. The initial suspicion fell on the inertia term assumptions for the impeller; however, adjustments to the inertia parameter of the model failed to improve the model's fidelity.

Upon a thorough re-evaluation of the bond graph elements and the associated system equa-

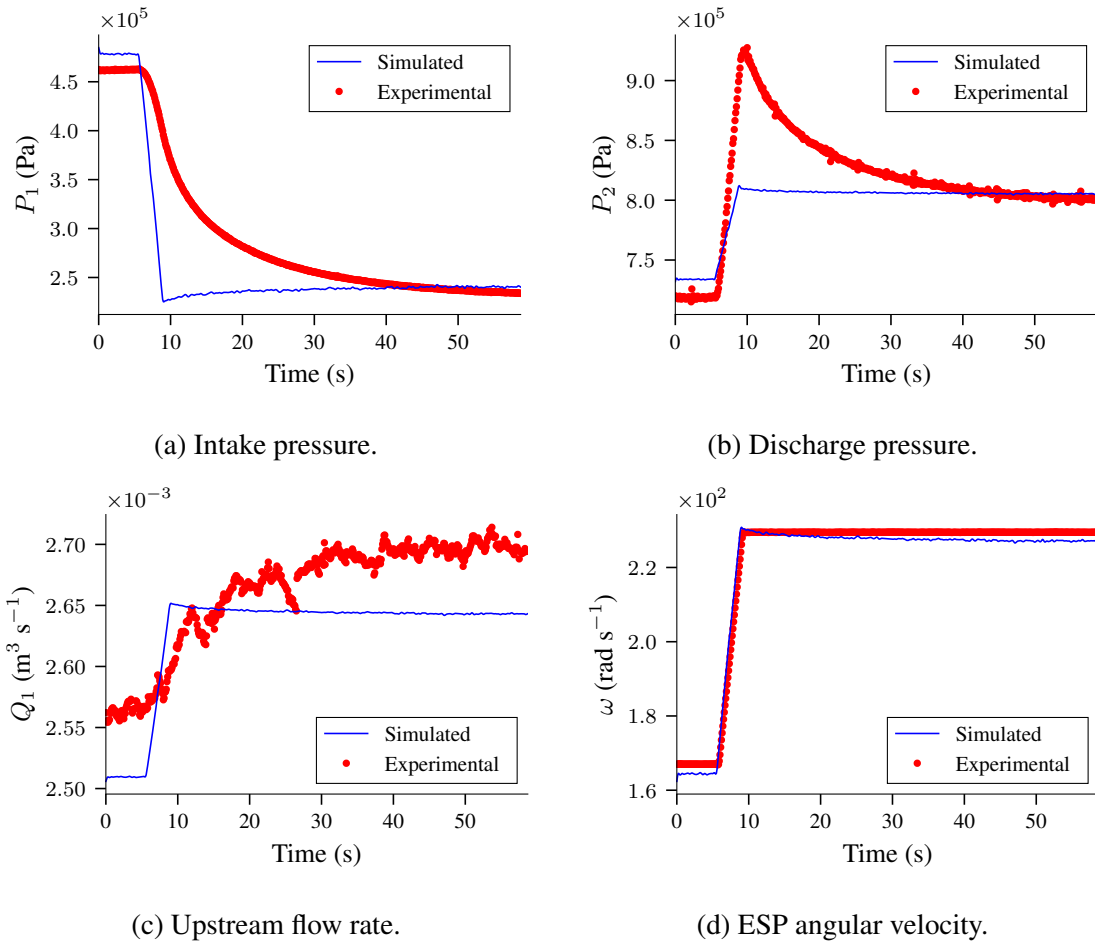


Figure 5.13: Comparison of the numerical solution and the measured states for the ESP P47 in the third dynamic experimental investigation (Table 4.7, row 3).

tions (Equation (5.8)), it became apparent that the liquid bulk modulus term (B) in Equation (5.8) is multifaceted, encompassing not only the liquid’s compressibility but also the elasticity of the fluid-pipe wall interaction, as detailed in Section 3.2.1 with the bond graph element C_{eq} . As observed in Equation (5.8), this term is responsible for determining the system’s pressure response to variations in flow rate between the inlet and outlet of a subsystem. The hypothesis for the observed discrepancies in the discharge pressure (pressure overshoot) is that the fluid within the ESP accelerates more rapidly than the fluid in the upstream and downstream pipelines. This results in an increased flow rate exiting the pump while the fluid in the pipeline is yet to accelerate, leading to fluid compressibility and pipe wall deformation at the pump discharge. Consequently, a pressure spike is observed at the pump discharge. As the mass of fluid in the pipeline begins to accelerate, the flow rates at the pump and downstream start to equalize, dissipating the pressure spike. Simultaneously, the “stored” fluid mass within the deformed pipe wall also dissipates. This hypothesis also applies to the intake pressure, where a gradual decrease in pressure is observed until the mass of fluid accelerates. Consequently, capturing these complex interactions between the fluid and the pump intake and discharge with the respective pipelines necessitated a separate tuning of the system’s compliance elements, further discussed

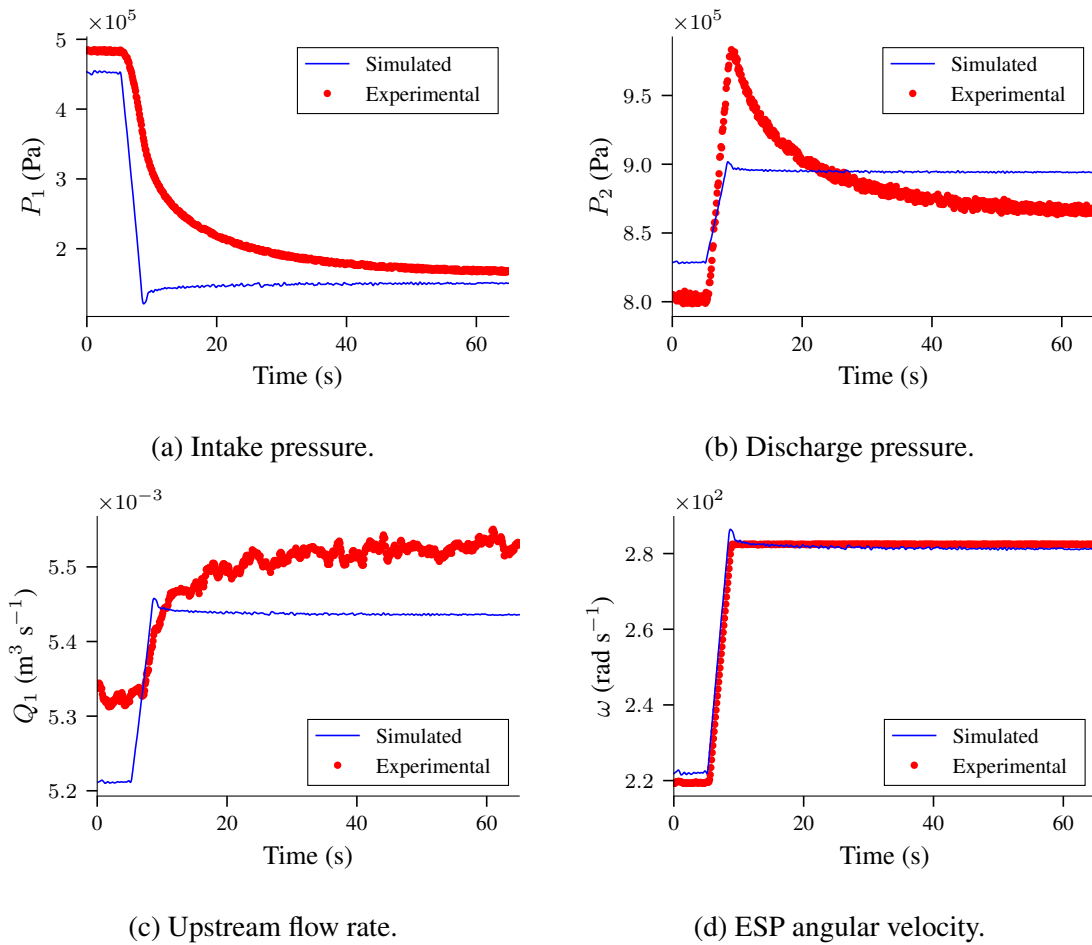


Figure 5.14: Comparison of the numerical solution and the measured states for the ESP P47 in the fourth dynamic experimental investigation (Table 4.7, row 4).

in Section 5.5.2.

Further analyzing the experimental data from the ESP P100L, specifically the dynamic experimental investigations 1 and 2 as shown in Figures 5.11 and 5.12, it was observed that prior to the increase in the ESP shaft's angular velocity, the intake pressure is higher than the discharge pressure. This trend reverses after the ESP shaft angular velocity increases, where the discharge pressure exceeds the intake pressure. This behavior can be attributed to the relative rotational velocity of the twin-screw pump, which was specifically set to facilitate dynamic experiments within the context of the ESP model P100L.

It is crucial to note that in this experimental setup, the ESP model P100L is operating as an energy source and a sink during dynamic experiments. However, the developed model, as detailed in Section 3.4, is based on the conservation of angular momentum. This principle does not restrict the impeller's role to be an energy source. Therefore, the model would be capable of simulating conditions similar to those observed in Figures 5.11 and 5.12. This is further substantiated by the comparison between the experimental data and the numerical solution discussed above, which exhibits a reasonable agreement.

Furthermore, the same model and methodology were applied to the dynamic experiments

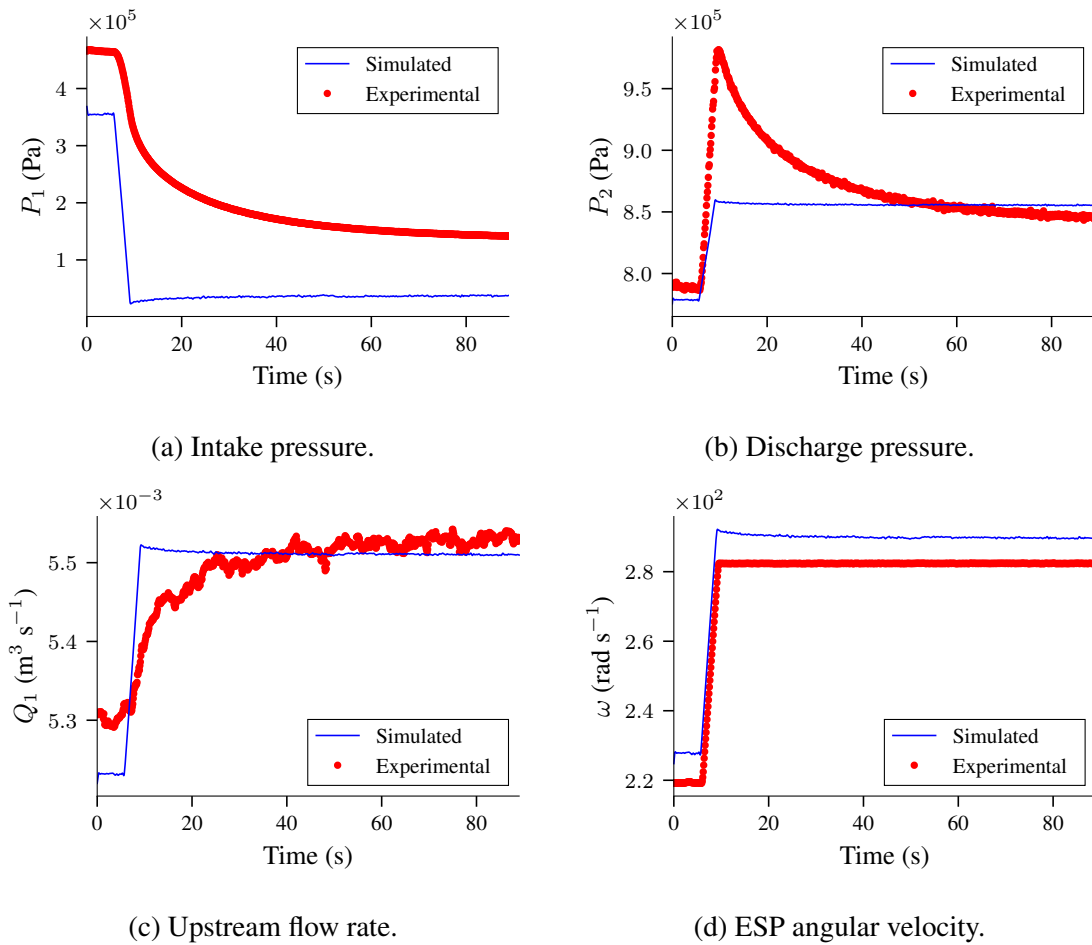


Figure 5.15: Comparison of the numerical solution and the measured states for the ESP P47 in the fifth dynamic experimental investigation (Table 4.7, row 5).

of the ESP model P47 which encompasses the dynamic experiments 3, 4, 5 and 6, presented in Figures 5.13 to 5.16. The results and the discussion above about the model satisfactorily representing the system dynamics in a condition where the ESP is operating as an energy source reinforce the model's validity and applicability across different conditions.

5.5.2 Compliance element tuning

In Section 5.5.1, it was demonstrated that the model's faster response in reaching the steady-state conditions and the observed spike in the discharge pressure could be primarily influenced by the compliance element, or C-elements in the bond graph model. Consequently, these elements were explicitly fine-tuned using the methodology elaborated in Section 4.7.2.2. This refinement was executed subsequent to the parameter adjustments described in Section 5.5.1. The results of this fine-tuning process, applied to both dynamic experimental investigations, are presented in Figures 5.17 and 5.18. The correlation between the experimental and simulated data, quantified using the Pearson correlation coefficient, and the MAPE calculated for each state, similarly to the Section 5.5.1, are presented in Table 5.5.

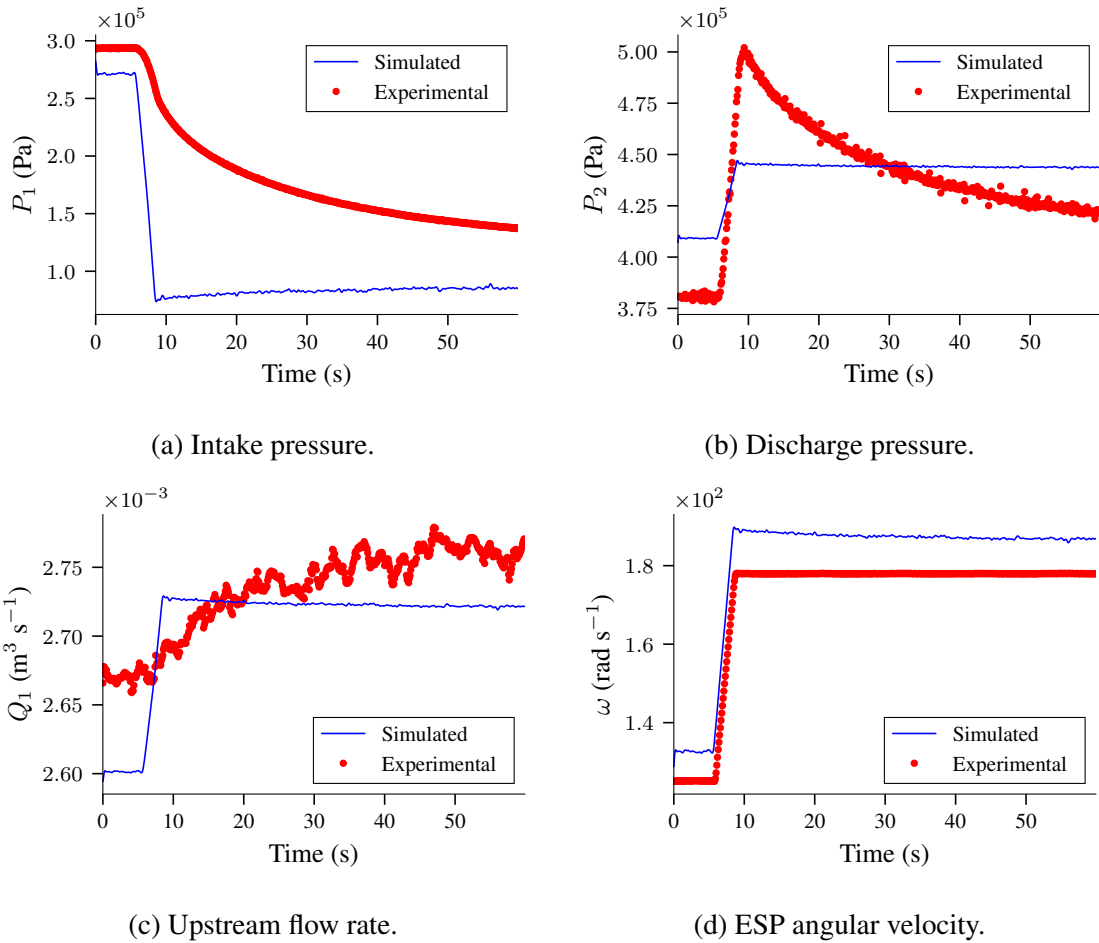


Figure 5.16: Comparison of the numerical solution and the measured states for the ESP P47 in the sixth dynamic experimental investigation (Table 4.7, row 6).

Table 5.5: Comparison of the MAPE and Pearson correlation coefficient between numerical solutions with tuned compliance element and experimental data. The units are percentages, and the parenthetical values correspond to the Pearson correlation coefficient, which is dimensionless.

#	P_1	P_2	Q_1	ω
1	15.12 (0.9968)	0.8673 (0.9392)	0.1893 (0.9353)	1.143 (1.000)
2	1.729 (0.9996)	0.5406 (0.9383)	0.085 23 (0.9521)	0.7159 (0.9988)
3	2.416 (0.9985)	1.050 (0.9956)	1.942 (0.9840)	0.9537 (0.9977)
4	11.97 (0.9976)	3.029 (0.9779)	1.697 (0.9898)	0.5480 (0.9975)
5	67.42 (0.9852)	1.034 (0.9589)	0.3597 (0.9829)	2.838 (0.9982)
6	33.10 (0.9886)	4.657 (0.9837)	1.462 (0.9500)	5.394 (0.9988)

As shown in Figures 5.17 to 5.22, the fine-tuning of the C-elements effectively induced the observed spikes in pressure, as evidenced by Figures 5.17b, 5.18b, 5.19b, 5.20b, 5.21b and 5.22b. After tuning, both the numerical solution and the experimental data exhibited comparable settling times for intake and discharge pressures. Notably, the settling behavior for the upstream flow rate in the ESP model P47 (Figures 5.19c, 5.20c, 5.21c and 5.22c) showed alignment with the

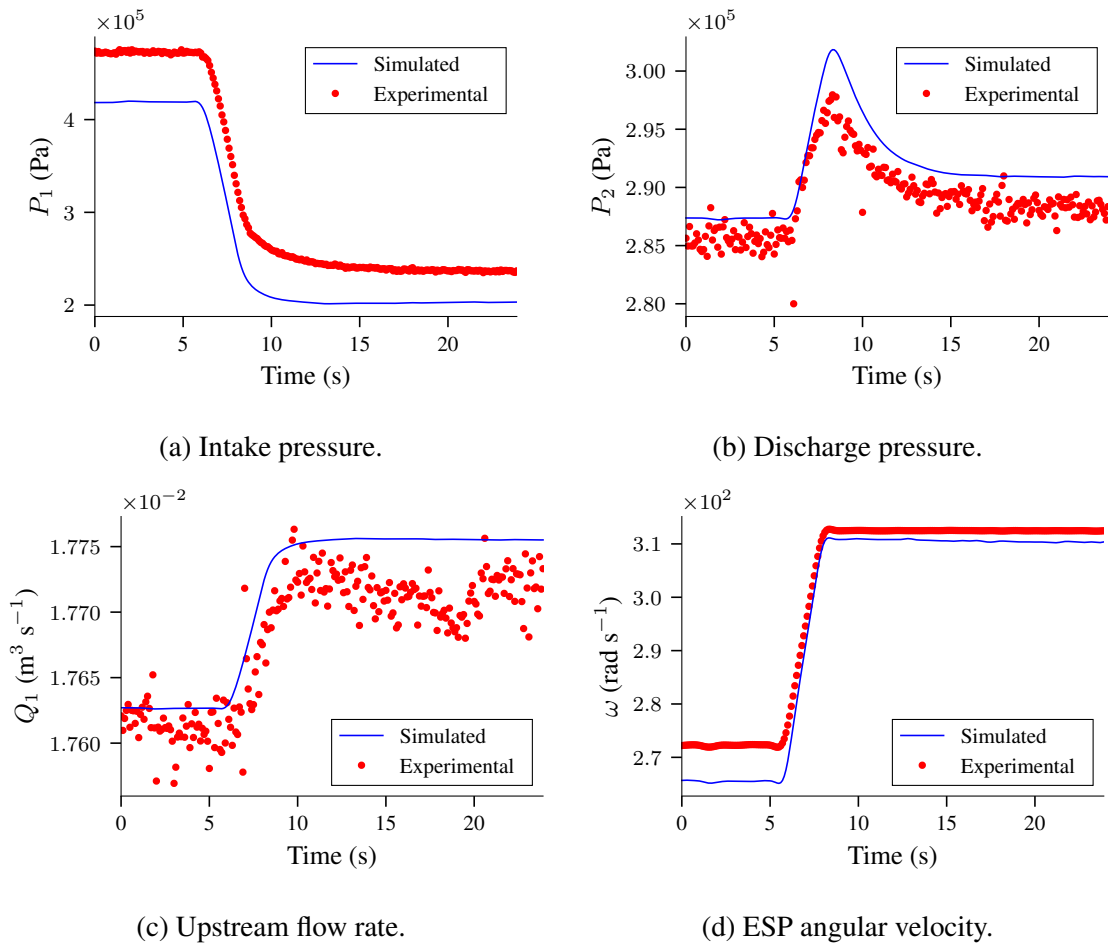


Figure 5.17: Comparison of the numerical solution and the measured states for the ESP P100L in the first dynamic experimental investigation (Table 4.7, row 1), after to the fine-tuning of compliance elements in the bond graph model.

experimental data, a contrast to the results without the tuning presented in Section 5.5.1.

A comparison of Tables 5.4 and 5.5 reveals a notable increase in the Pearson correlation coefficient for all states and experiments after tuning. For example, while Table 5.4 reported a Pearson correlation coefficient for P_2 as low as 0.5860, in the tuned cases, the lowest value for P_2 improved to 0.9589. However, examining the MAPE values in Tables 5.4 and 5.5 indicates that the overall improvement was not significant for all states and experiments. Despite the tuning process successfully inducing the pressure spike, it did not rectify the offset issue discussed in Section 5.5.1. This offset remains the primary cause of higher MAPE values, particularly in the intake and discharge pressures.

Despite certain inaccuracies in the twin-screw pump model, its overall impact on the system dynamics was not significant. The dynamics of pressure and volumetric flow rate, as illustrated in Figures 5.17 to 5.22, were modeled with reasonable accuracy, evidenced by the Pearson correlation coefficients values presented in Table 5.5. However, offsets in intake and discharge pressures, as well as in the volumetric flow rate, are still present. As discussed in Section 5.5.1, these offsets are likely attributable to errors in the twin-screw pump model. In real-world

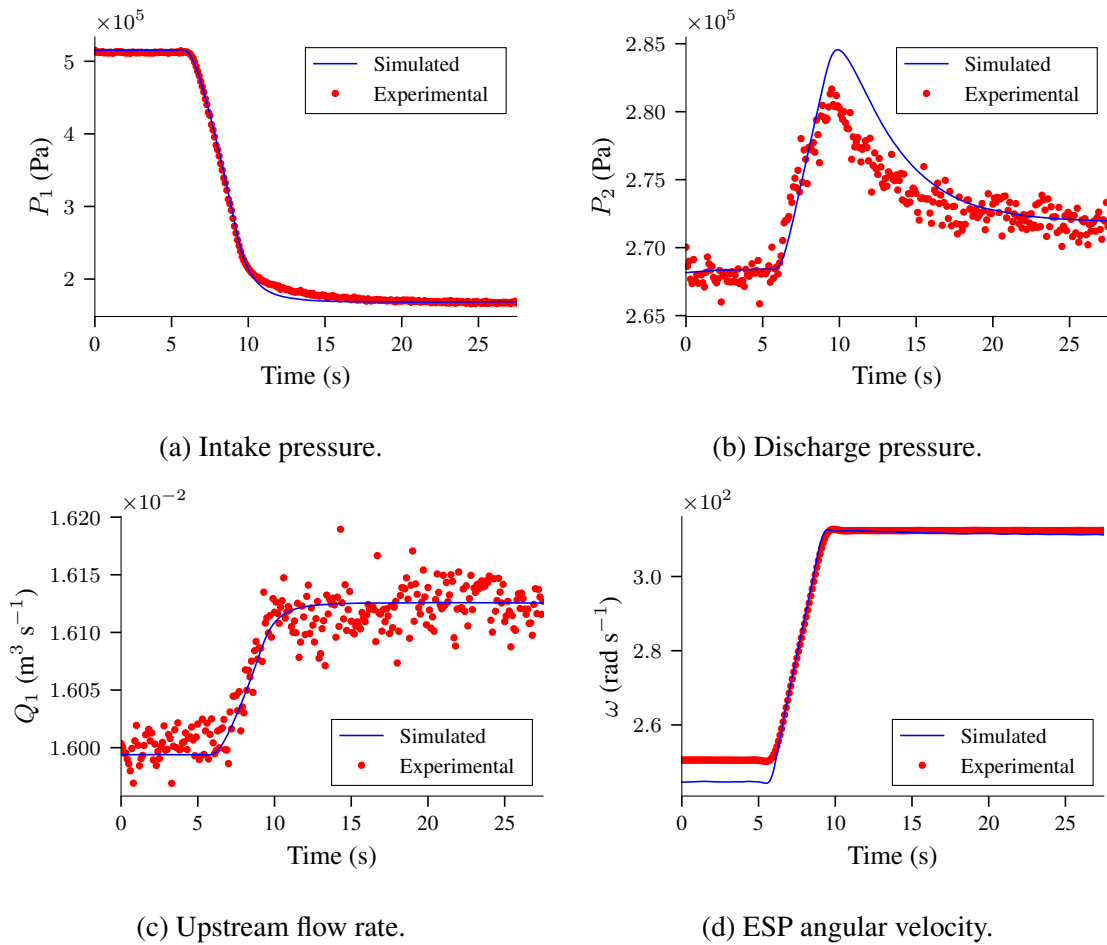


Figure 5.18: Comparison of the numerical solution and the measured states for the ESP P100L in the second dynamic experimental investigation (Table 4.7, row 2), after to the fine-tuning of compliance elements in the bond graph model.

applications, employing more sophisticated well models could prove beneficial. These advanced models might better account for the complexities of the actual system and enhancing the overall accuracy and reliability of the simulations.

Overall, the model proposed, despite all the assumptions and simplifications, could capture reasonably well the ESP system dynamics for almost single-phase and low water cut emulsion conditions and two ESP models (P100L and P47). The fine-tuning process in the C-elements was demonstrated to be crucial to obtaining a complete representation of the system dynamics. However, additional experimental investigations are required to model or obtain an expression for the C-element properly. In general, the results obtained are satisfactory, indicating the model's potential utility in applications related to monitoring, control, and parameter estimation within the field.

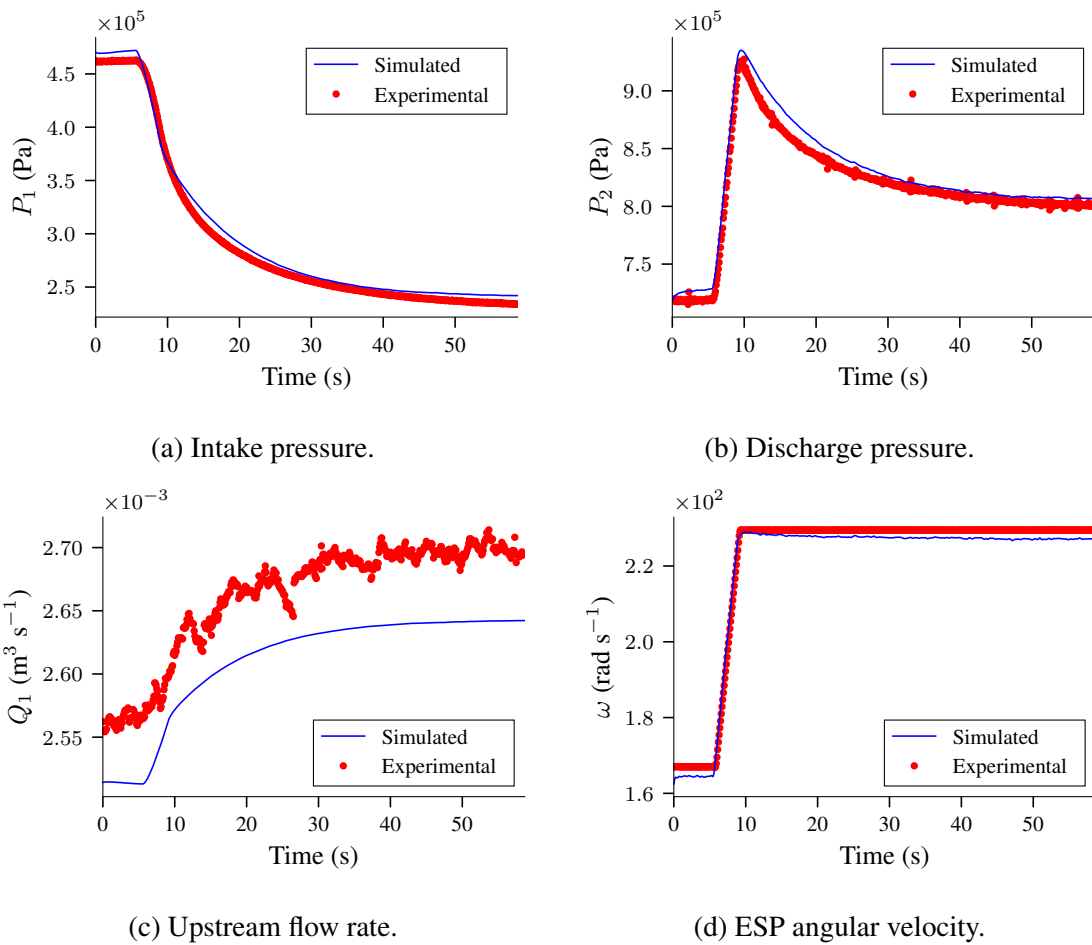


Figure 5.19: Comparison of the numerical solution and the measured states for the ESP P47 in the third dynamic experimental investigation (Table 4.7, row 3), after to the fine-tuning of compliance elements in the bond graph model.

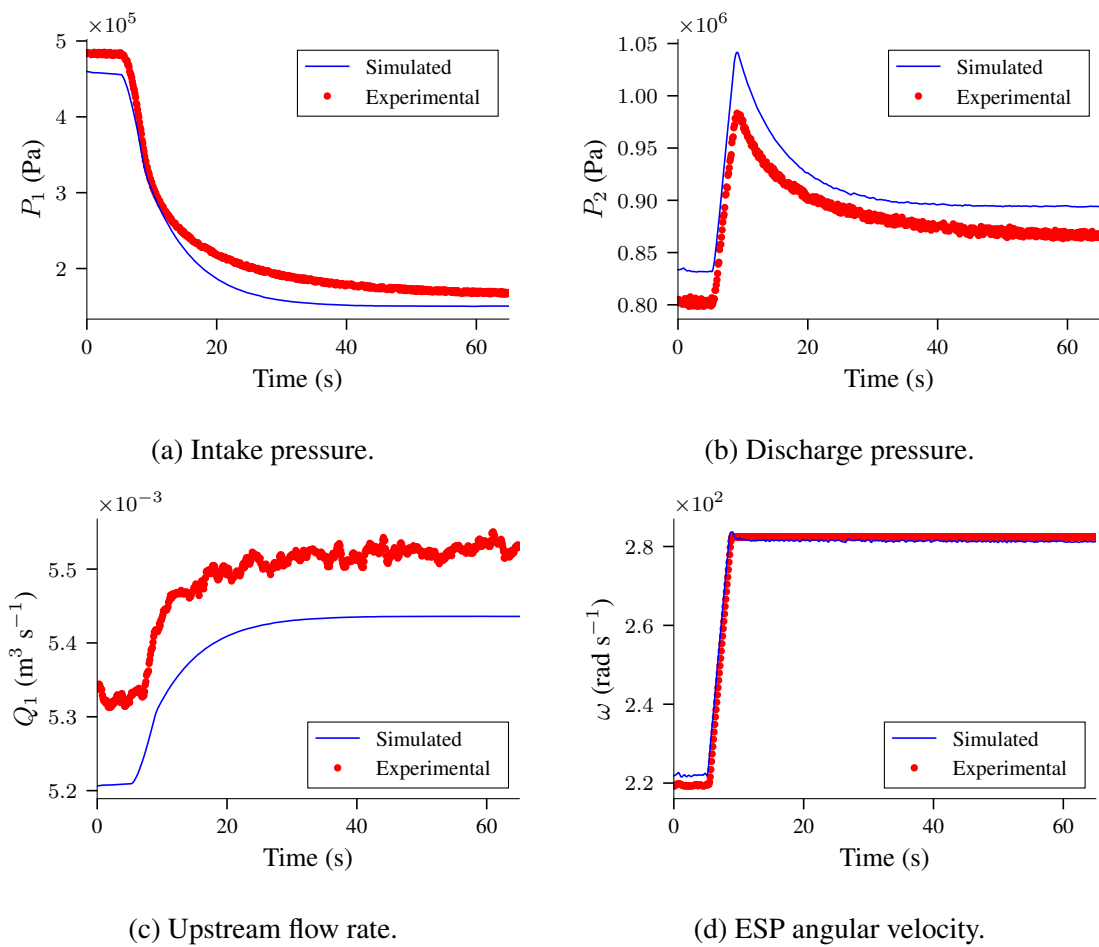


Figure 5.20: Comparison of the numerical solution and the measured states for the ESP P47 in the fourth dynamic experimental investigation (Table 4.7, row 4), after to the fine-tuning of compliance elements in the bond graph model.

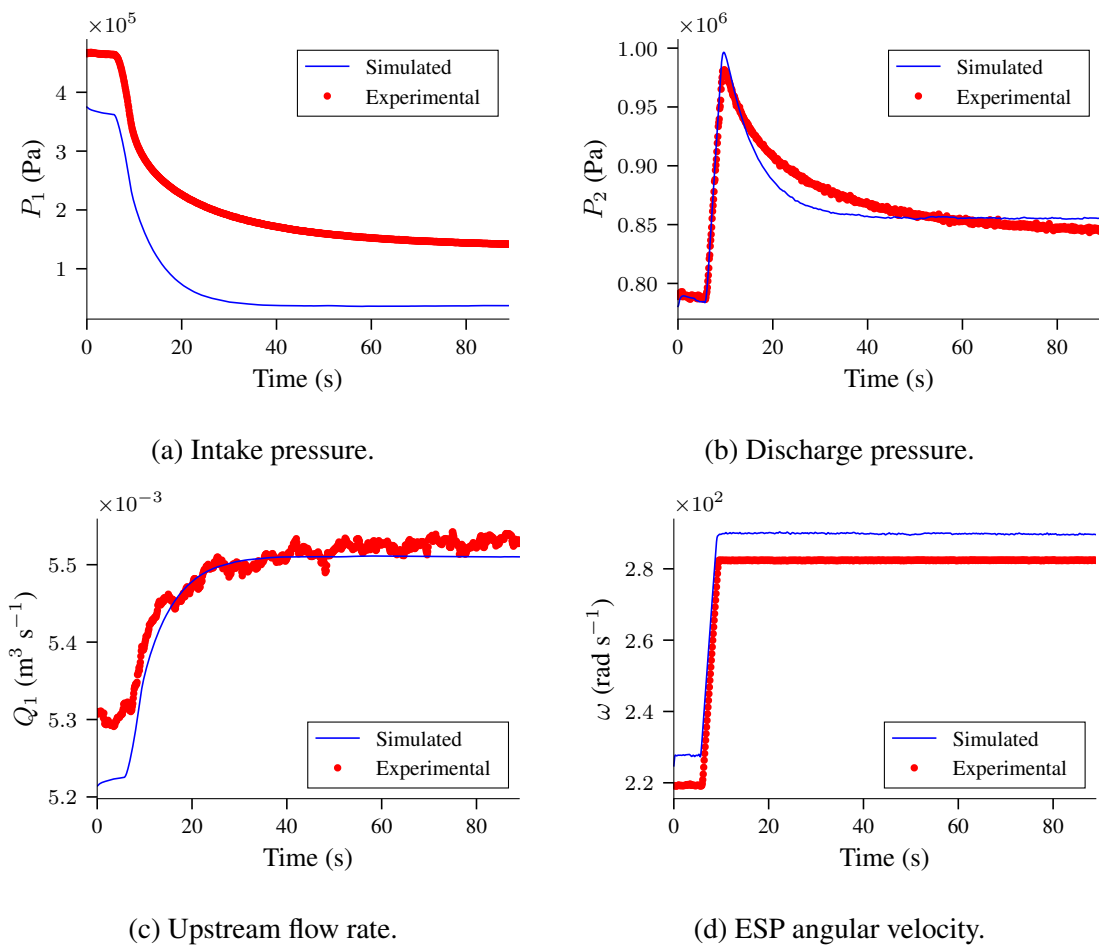


Figure 5.21: Comparison of the numerical solution and the measured states for the ESP P47 in the fifth dynamic experimental investigation (Table 4.7, row 5), after to the fine-tuning of compliance elements in the bond graph model.

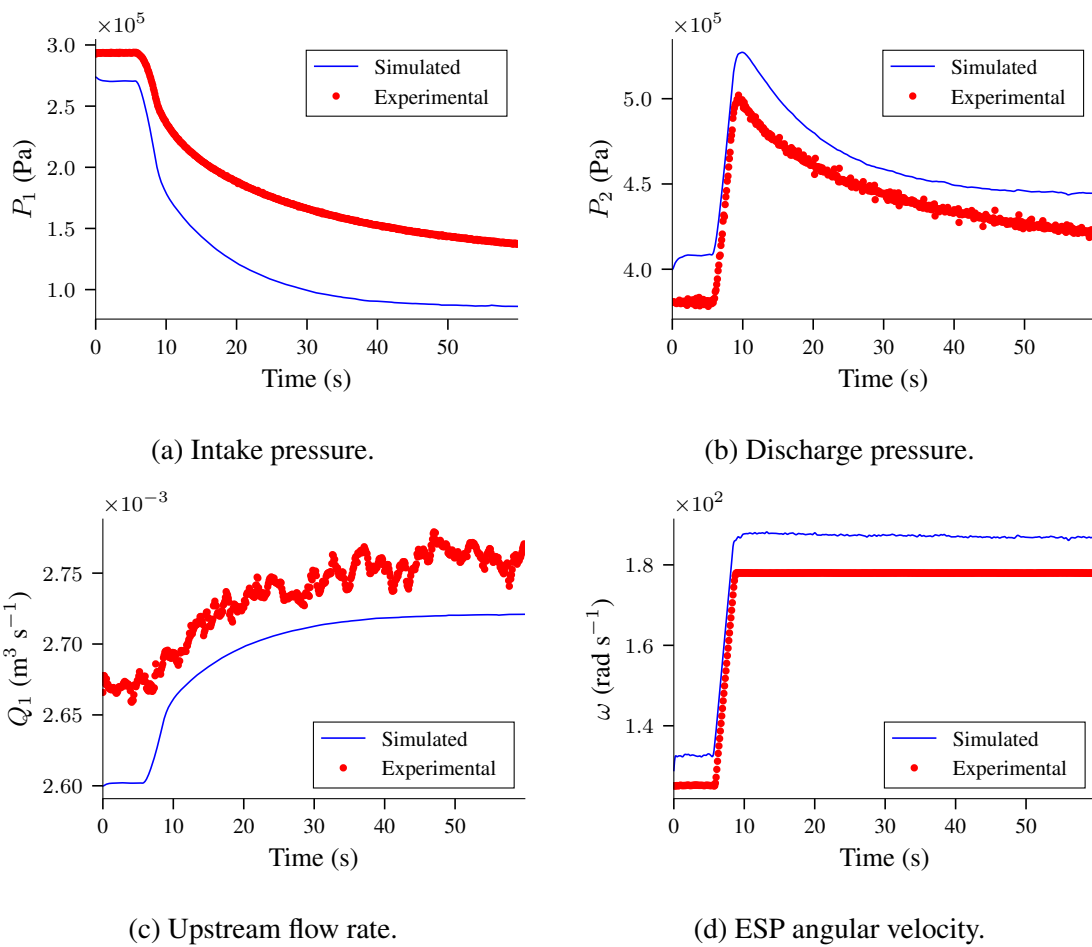


Figure 5.22: Comparison of the numerical solution and the measured states for the ESP P47 in the sixth dynamic experimental investigation (Table 4.7, row 6), after the fine-tuning of compliance elements in the bond graph model.

6 Identifiability analysis results

6.1 Structural local identifiability

To evaluate the structural identifiability of the ESP system model it was utilized the method of differential elimination for dynamical models via projections proposed by Dong *et al.* [96]. It is important to note that this analysis focused specifically on assessing local identifiability due to out-of-memory issues when attempting to test for structural global identifiability. Additionally, this investigation considered the suction and discharge pressure (P_1 and P_2) as available measurements, as they are typically measured in ESP deployments within oil fields.

From Tables 5.2 and 5.3, we observe that the ESP system model initially contains a total of 26 parameters. However, it is worth noting that 8 of these parameters are geometrical parameters, such as pipe diameter, cross-sectional area, and pipeline length. They can be readily obtained, and they were assumed as known for both the upstream and downstream pipelines. Furthermore, 3 parameters refer to the twin-screw pump, which serves as a pressure booster for the flow line. In actual oil field extraction, the pressure is a characteristic of the well. Thus, it was reduced the number of unknown parameters to 15. Subsequently, it was assessed the local identifiability of the ESP system model based on these 15 parameters. The corresponding results are displayed in the first row of Table 6.1.

Table 6.1: Local structural identifiability results of the ESP system model, considering that the intake pressure (P_1) and discharge pressure (P_2) are known.

k_{1p}	k_{2p}	k_{3p}	k_{4p}	k_{1s}	k_{2s}	k_{3s}	k_{4s}	k_{5s}	I_s	ρ	μ	B	k_u	k_d
×	×	✓	✓	×	×	×	×	×	×	✓	✓	✓	✓	✓
✓	✓	✓	✓	✓	✓	×	×	✓	—	✓	✓	✓	✓	✓
✓	✓	✓	✓	✓	✓	—	—	✓	—	✓	✓	✓	✓	✓

The ESP system model with 15 unknown parameters is found to be structurally locally unidentifiable, and it is impossible to estimate all the parameters simultaneously. As discussed by Daneker *et al.* [132], there are several approaches to address the identifiability issue, such as fixing specific parameters or introducing additional measured variables. For simplicity, when it is referred to fixing a parameter, it is considered that the parameter is known. In this study, it was opted to work with the available measurements from the actual field and consider only the suction and discharge pressures (P_1 and P_2). Therefore, it was decided to fix the shaft inertia (I_s). Despite this adjustment, the model remains structurally locally unidentifiable, with only k_{3s} and k_{4s} being locally unidentifiable. The corresponding results are shown in the second row of Table 6.1.

Finally, it was solved the issue of the model being locally unidentifiable by fixing both k_{3s} and k_{4s} . The results are shown in the third row of Table 6.1. It was found that fixing only one of them did not solve the problem. In summary, the ESP system model can only be structurally locally identifiable with the suction and discharge pressure measurements if the shaft inertia (I_s), viscous damping coefficient (k_{4s}), and disk friction coefficient (k_{3s}) are known.

6.2 Practical identifiability

In section Section 6.1, it was discussed the circumstances under which the ESP system is structurally locally identifiable. However, it is worth noting that this analysis was conducted assuming that the measured variables have no noise and that the model is error-free. Hence, we must also assess if we can estimate parameters accurately based on the available data's quantity and quality. This analysis is known as practical or posterior identifiability analysis, and it is possible that a structurally identifiable system may not be practically identifiable.

Following the procedure described in Section 4.4, the absolute of the correlation matrix of the parameters structurally locally identifiable of the ESP system is shown in Figure 6.1. For the practical identifiability analysis, it was considered the simulated case for the first experimental dynamic investigation of the test matrix Table 4.7.

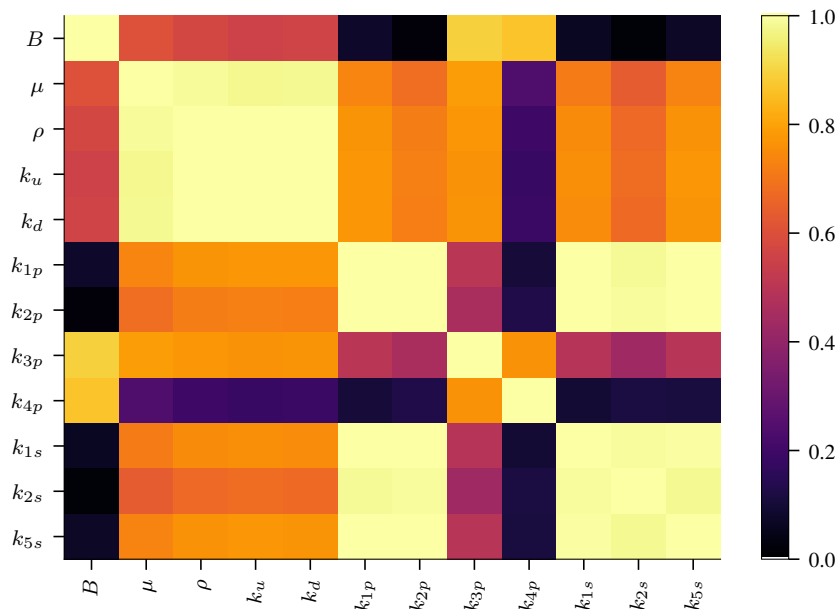


Figure 6.1: Correlation matrix of the ESP system model parameters.

The correlation analysis shown in Figure 6.1 clearly demonstrates a significant correlation among multiple parameters. Notably, the fluid density (ρ) and the pipeline resistances (k_u and k_d) exhibit a strong correlation. Consequently, although the initial analysis indicated structural local identifiability of these parameters, they are not practically identifiable within the context of the conducted investigation.

As many parameters are strongly correlated, we need to fix some parameters to make the system practically identifiable. Thus, it was defined that the main variables of interest are the fluid parameters and the pipeline resistances since the fluid parameters (B , μ , and ρ) change within the water cut, which changes with the well's life, and the pipeline resistance (k_u and k_d) changes with the actuation of valves and wax deposition for instance. Thus, the pump and shaft parameters were preferably fixed. The parameters fixing started with k_{1p} , then the k_{3s} , k_{2p} and k_{3p} successively. The resultant parameter correlation matrix is presented in Figure 6.2.

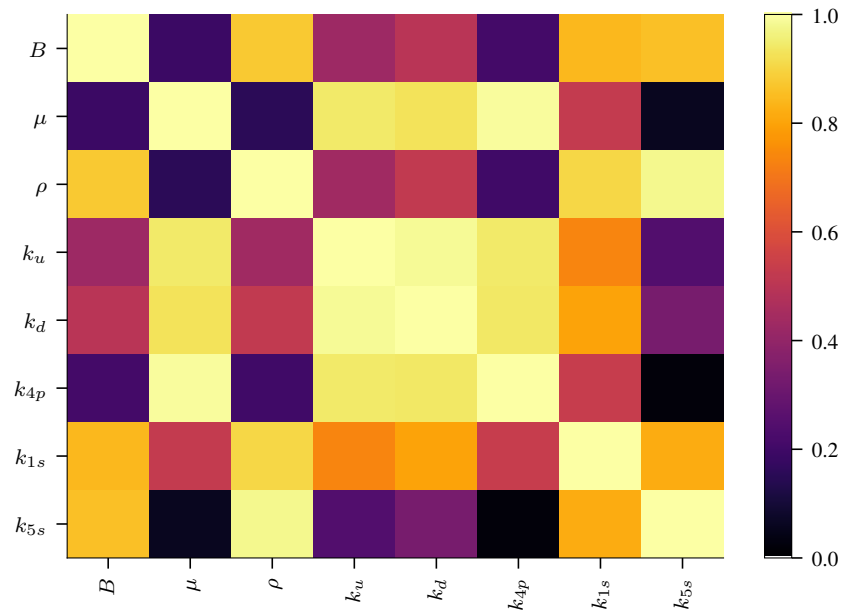


Figure 6.2: Correlation matrix of the ESP system model parameters after the practical identifiability analysis.

It is noticeable from Figure 6.2 that after fixing some parameters, they are less correlated. However, some parameters are still correlated, such as the viscosity (μ) and the pump equivalent resistance (k_{4p}). However, this correlation is not as strong as the correlation between density (ρ) and pipeline resistance (k_u) observed in Figure 6.1. In Figure 6.2, the correlation coefficient between μ and k_{4p} is 0.9880, while in Figure 6.1, the correlation coefficient between ρ and k_u is 0.9994.

7 Inverse problem results

From the structural identifiability analysis presented in Chapter 6, it was defined three cases to evaluate the PINN for parameter and state estimation in the ESP system. Consistent with Chapter 6, it was considered only the suction and discharge pressures as the measured variables. The three cases are as follows:

- Case 1 Flow parameters: In this case, it was assumed as known all parameters of the ESP system model except for the flow properties, namely, density (ρ), viscosity (μ), and the bulk modulus (B).
- Case 2 Flow, pipeline, and impeller parameters: Based on the local identifiability analysis results presented in the first row of Table 6.1, it was assumed as known the parameters marked as locally unidentifiable and estimate the remaining identifiable ones. The unknown parameters considered are the flow properties (B , μ , ρ), the upstream pipeline equivalent resistances (k_u and k_d) and the pump parameters k_{3p} and k_{4p} .
- Case 3 Flow, pipeline, impeller, and shaft parameters: Considering the findings from the practical identifiability analysis outlined in Section 6.2, the parameters depicted in Figure 6.2 were estimated while assuming as known the remaining parameters. The unknown parameters are fluid properties (B , μ , ρ), the upstream pipeline equivalent resistances (k_u and k_d), the pump parameter k_{4p} , and the shaft parameters k_{1s} and k_{5s} .

For each case, it will be evaluated the performance and effectiveness of PINN in estimating the unknown parameters and non-measured system states in three distinct data scenarios:

1. Simulated data: This scenario represents an ideal condition without any disturbances or modeling errors, allowing us to assess the baseline performance of the proposed method.
2. Simulated data with Gaussian noise: In this scenario, gaussian noise was introduced to the simulated data to evaluate the sensitivity of the proposed method to noisy data.
3. Experimental data: This scenario is closer to actual oil field conditions, incorporating noisy measurements, modeling errors, and missing information about certain parameters.

Furthermore, for each study, it was trained the PINN 30 times to evaluate the impact of the neural network weights initialization. The results are presented and discussed in each case for the first two experimental conditions defined in Table 4.7.

The Figure 7.1 presents a schematic representation of the cases and scenarios evaluated, where the two dynamic experimental investigations performed, considering different water cuts

and initial angular velocities, are highlighted in blue. Each experimental investigation is analyzed under three different data sources (scenarios): simulation data, simulation data with added Gaussian noise, and experimental data collected from the instruments (highlighted in green). For each scenario, three sets of unknown parameters, denoted as cases, are evaluated (highlighted in red). Thus, we have 9 different results for each experimental investigation.

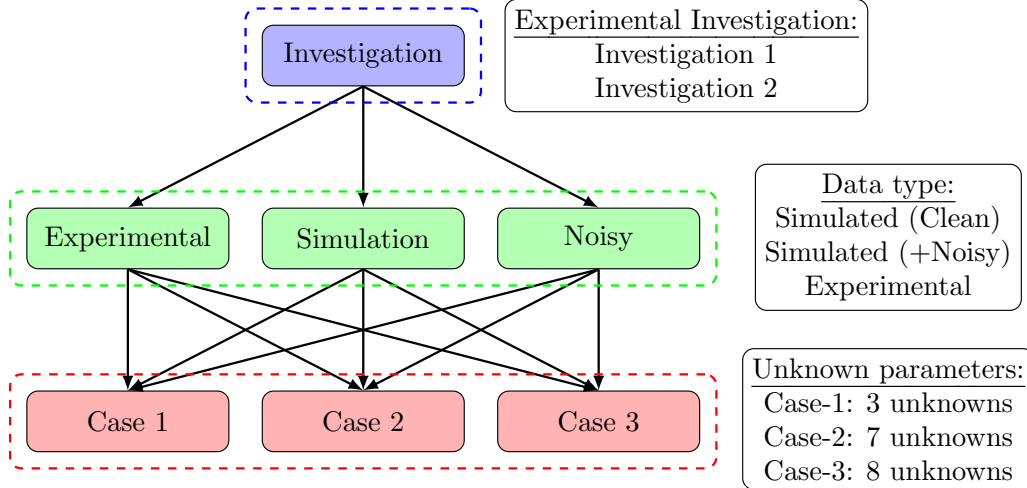


Figure 7.1: Cases and scenarios evaluated.

During the training of the PINN, it was observed that the significant difference in magnitude between the states, with pressure in the order of 10^5 and flow rates in the order of 10^{-2} , affected the training and tuning process despite the scaling in the physics loss and the usage of self-adaptive weights on the loss function. Therefore, the states units were converted from SI units to $\text{m}^3 \text{h}^{-1}$ for the volumetric flow rates and to MWC (meters of water column) for the pressure. After obtaining the results, they were converted back into SI units.

Furthermore, the transformation of the unknown parameters contributes to the convergence and accuracy of the PINN by restricting the search space to the local neighborhood of the parameter. It was first tried to keep the linear scaling for all parameters and cases during the development. However, in Case 3, it was not possible to achieve satisfactory results without restricting the parameter search space using bounded transformations such as \tanh . Also, it was taken advantage of that in our experiments. It is not possible to have a density higher than the water. Then, it was set an upper bound for it. It helped to improve the results in all cases. The transformation scheme for each parameter is shown in Table 7.1, and the scaling values are presented in Table 7.2.

The Table 7.1 presents a variety of functions used in the unknown parameter transformations. They are the softplus function $S_p(\cdot)$ and the $S_m(\cdot)$, defined as $S_m(x) = x - S_p(x) + 1$, are utilized along with a scaling constant Λ . The $L(\cdot)$ is a linear transformation given by $L(x) = x\Lambda$, which considers only a scaling constant Λ . For Case 3, the transformation for an unknown parameter is expressed as $\Lambda_{\text{sc}}(x) = \Lambda_{\text{true}} (\tanh(x)\alpha + 1)$, where x represents the PINN-estimated value of the unknown parameter, Λ_{true} is the parameter true value, and α denotes the span percentage

Table 7.1: Transformations of the unknown parameters for each case evaluated.

Case	B	μ	ρ	k_u	k_d	k_{3p}	k_{4p}	k_{1s}	k_{5s}
Case 1	$(S_p(x) + 0.9)\Lambda$	$L(x)$	$S_m(x)\Lambda$						
Case 2	$(S_p(x) + 0.9)\Lambda$	$L(x)$	$S_m(x)\Lambda$	$L(x)$	$L(x)$	$L(x)$	$L(x)$		
Case 3	$\Lambda_{sc}(x)$	$\Lambda_{sc}(x)$	$S_m(x)\Lambda$	$\Lambda_{sc}(x)$	$\Lambda_{sc}(x)$		$\Lambda_{sc}(x)$	$\Lambda_{sc}(x)$	$\Lambda_{sc}(x)$

Table 7.2: Scaling constants for the unknown parameters.

Case	B	μ	ρ	k_u	k_d	k_{3p}	k_{4p}
Case 1	1×10^9	1	1000				
Case 2	1×10^9	1	1000	3×10^2	1×10^1	-1.0×10^7	-1.0×10^2
Case 3			1000				

around the true value. For most parameters, it was set the span to $\pm 50\%$ ($\alpha = 0.5$), except for the B parameter, which spans $\pm 15\%$ ($\alpha = 0.15$). Furthermore, in Table 7.2 table presents the scaling constants used in linear parameter transformations and the scaling parameter for the liquid bulk modulus (B) and density (ρ) transformations.

7.1 State estimation results

In this section it is assessed the state estimation capabilities of the PINN when applied to the ESP system model. The PINN will estimate the remaining unknown system states using the suction and discharge pressure signals as known variables (P_1 and P_2). In the simulated cases, the unknown states include the pipeline and ESP volumetric flow rates (Q_1 , Q_2 , Q_p) and the ESP angular velocity (ω). However, in the experimental case, measurements of the downstream pipeline and ESP volumetric flow rates (Q_2 and Q_p) are unavailable, and therefore, they were excluded from the accuracy analysis. It is important to note that these results are from inverse problems with unknown parameters discussed above, not forward problems. First, it is presented the state estimation results for all the cases considered. Then, it is discussed the prediction of the unknown parameters for all the cases in Section 7.2.

It is worth mentioning that in PINN, it is common practice to use second-order optimization algorithms, such as L-BFGS, after training with the first-order algorithm. This additional step usually aims to fine-tune the PINN's performance. However, it was observed that using L-BFGS after Adam adversely affected the parameter estimation in the noisy and experimental case. Therefore, it was decided to rely solely on the first-order optimization algorithm, as our focus is on unknown parameter estimation in more realistic scenarios. It is important to note that the simulated cases serve as a baseline performance for assessing the PINN's performance, and it is expected that performance will be comparatively reduced under the more challenging conditions posed by experimental data and noise.

7.1.1 State estimation results for simulated data

As a baseline performance assessment, it is considered the simulated scenario. The predicted states from the neural network are shown in Figure 7.2, while the Mean Absolute Percentage Error (MAPE) corresponding to the prediction of different states is shown in Table 7.3. The MAPE is defined as

$$\text{MAPE} = \frac{1}{N^{\text{mape}}} \sum_{i=1}^{N^{\text{mape}}} \left| \frac{y_s(t_i) - \bar{y}_s(t_i; \boldsymbol{\theta})}{y_s(t_i)} \right|, \quad (7.1)$$

where N^{mape} is the total number of temporal data points. It was considered the same sample rate as the experimental data described in Section 4.1.3, 10 Hz ($\Delta t = 0.1$ sec). The variable $y_s(t_i)$ represents the true value of the state s at time t_i , and $\bar{y}_s(t_i; \boldsymbol{\theta})$ denotes the mean of the predicted value of the state s from the PINN across 30 different realizations of the results. These results are evaluated with different initialization of the parameters of the network and unknown parameters. For the sake of brevity, the discussion is restricted to the state prediction results and the MAPE table for the first experimental investigation in this section. Further results from the second investigation are presented in Appendix D. Additionally, the mean value of the predicted parameters and standard deviation for all the cases are presented in Tables D.4 and D.5.

The Table 7.3 presents the results for the simulation data considering three different cases of unknown parameters. The MAPE values represent the error of the simulation results for the states: P_1 , P_2 , Q_1 , Q_2 , Q_p , and ω . As the number of unknown parameters increased, from Case 1 to Case 3, the MAPE values also increased, indicating a slight performance loss. However, the MAPE values remain relatively small, and visual inspection of Figure 7.2 reveals a reasonable agreement with the actual values.

Table 7.3: MAPE for the simulated scenario.

	P_1	P_2	Q_1	Q_2	Q_p	ω
Case 1	0.142 %	0.008 %	0.004 %	0.006 %	0.007 %	0.025 %
Case 2	0.147 %	0.009 %	0.039 %	0.038 %	0.039 %	0.872 %
Case 3	0.932 %	0.010 %	0.041 %	0.040 %	0.041 %	0.618 %

In Figure 7.2, the blue line indicates the true values, while the \times markers denote the data points used for training the PINN. The red, black, and green lines represent the mean values of the predicted states calculated at each time instant across the 30 trained PINN for Cases 1 to 3, as defined earlier in this section (Chapter 7). Across all cases, the training dataset consists of 30 data points for the data loss in P_1 and P_2 and 100 collocation points for the physics loss.

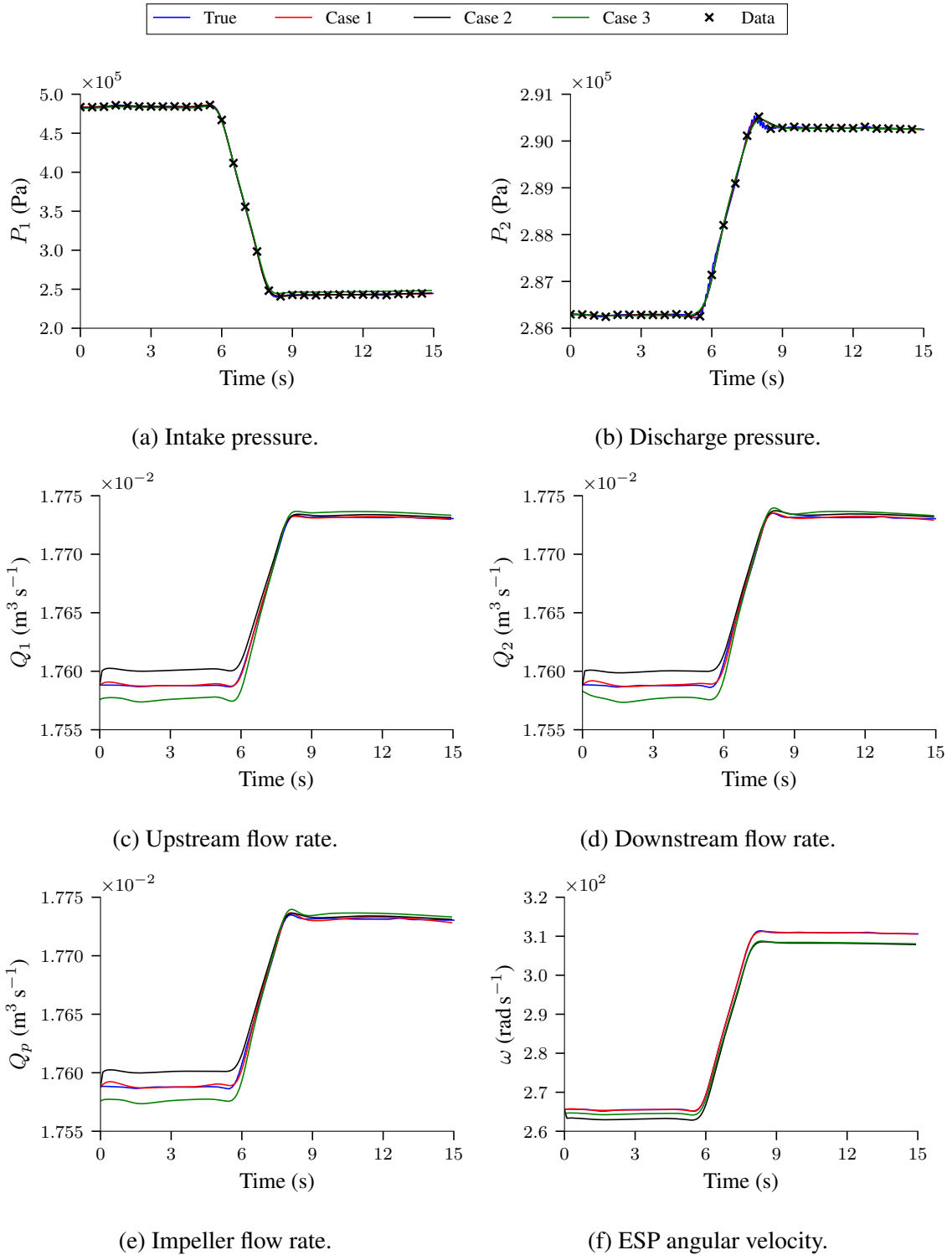


Figure 7.2: Comparison of predicted and true states for simulated scenario of the first experimental investigation with unknown parameters.

The comparison between the predicted dynamics of the states by the PINN model and the actual values, as shown in Figure 7.2, demonstrates a good overall agreement across all states and cases. Notably, a small error is observed for the P_1 and P_2 states in all cases. However, a slightly larger error is observed for the volumetric flow rate states (Q_1 , Q_2 , and Q_p) and the

ESP angular velocity state (ω). Among the different cases, Case 1 (red line) exhibits the best agreement across the entire simulation range in both investigations. This is also observed in Table 7.3, where the Case 1 presented the lower MAPE in all states except P_1 .

In the first investigation, the flow rates in Case 2 (black line) and Case 3 (green line) show a reasonable agreement with the simulation approximately from the 6th second. However, a slight offset from the actual value is observed from the beginning to the 6th second. As for the second investigation (Figure D.1), a slightly higher offset is observed in the flow rate states and in the ESP angular velocity across the entire simulation time for Case 3, while for Case 2, we no longer observe the offset.

7.1.2 State estimation results for simulated data with noise

To further evaluate the robustness of the PINN model, the analysis is extended to include a simulated scenario with Gaussian noise. This section aims to assess the performance of the PINN model when subjected to noise alone without considering missing physics or errors in the model parameter estimation. For each PINN realization, a different noise realization is also considered. Similarly to the previous section, this section will focus on presenting the result corresponding to the first experimental investigation, while the result for the second experimental investigation can be found in Appendix D for reference. The MAPE for the different predicted states are shown in Table 7.4, and the output of the predicted states from the neural network, along with the addition of noise on the pressure signals, are shown in Figure 7.3.

The Table 7.4 presents the MAPE for the states prediction in the simulated case with added noise data, considering three cases of unknown parameters. Similarly to Table 7.3, increasing the number of unknown parameters (Case 1 to Case 3) leads to higher MAPE values for all states, indicating a performance loss. Nevertheless, the MAPE values remain relatively small, and visual inspection of Figure 7.3 shows a reasonable agreement with the actual values, except for Case 2.

Table 7.4: MAPE for the simulated scenario with added noise.

	P_1	P_2	Q_1	Q_2	Q_p	ω
Case 1	0.180 %	0.073 %	0.017 %	0.017 %	0.017 %	0.027 %
Case 2	0.165 %	0.021 %	0.455 %	0.456 %	0.455 %	2.815 %
Case 3	0.182 %	0.034 %	0.048 %	0.045 %	0.048 %	0.159 %

In Figure 7.3a and Figure 7.3b, the blue line indicates the signal with added Gaussian noise. In other figures, the same blue line represents the noise-free simulated state. This differentiation aids in evaluating the PINN's accuracy by comparing its predictions with the actual state values and also presents the signal used for PINN training. Each PINN training used a different random seed. Therefore, the Gaussian noise in the signal varied for every PINN training and case.

Specifically, the noisy signals for P_1 and P_2 in Figure 7.3a and Figure 7.3b correspond to the first training for Case 1, and they were used as a reference. The added Gaussian noise considered the uncertainty from the pressure transducers as specified in Table 4.2. For all cases, the training dataset consisted of 37 data points for data loss in P_1 and P_2 and 100 collocation points for physics loss. The plots show the mean value of results for 30 realizations of PINN. The noisy data shown in the plots are one of the noisy data shown as a representative sample. The comparison between the predicted dynamics of the states by the PINN and the actual values, as depicted in Figure 7.3, demonstrates a good overall agreement in all states and investigations for almost all cases. However, in Case 2 (black line), the PINN was unable to accurately estimate the flow rate states (Q_1 , Q_2 and Q_p). They exhibit relatively higher errors. However, the model was able to predict the general shape of the time series. Remarkably, these higher errors were observed exclusively in the first experimental investigation (Figure 7.4) (higher water cut), whereas in the second investigation (Figure D.3) (with low water cut), Case 2 demonstrated performance similar to that of Case 1 (red line).

Notably, minor errors are observed in the P_1 and P_2 states for all cases and investigations. Specifically, in the discharge pressure state (Figure 7.3b), it is noticeable that the neural network did not overfit and successfully captured the signal trend and magnitude. Similarly to the simulated data without noise (Section 7.1.1), Case 1 (red line) exhibits the best agreement across the entire simulation range in both investigations. Additionally, as shown on Table 7.4, Case 1 had a lower MAPE than the other cases for the unknown states and a higher MAPE for the known state P_2 .

Despite the addition of noise, the state estimation for Cases 1 and 3 provides good accuracy without significant errors. These results were similar to those obtained in noise-free conditions, with a slight increase in MAPE values. In Case 3, there is a noticeable offset in the volumetric flow rates (Q_1 , Q_2 and Q_p) approximately after the 8th second, which is different from the observations made in Section 7.1.1, where the offset occurred only in the beginning. Additionally, the angular velocity, in this case, remains closely aligned with the actual values throughout the simulation, exhibiting no offset. It is observed that results for Case 2 deviate from the true values, particularly for flow rates (Q_1 , Q_2 , Q_p). It may be possible that, though Case 2 is structurally identifiable, it is not practically identifiable. However, it is observed that the angular velocity of the ESP (ω) was not significantly affected as that of the flow rates.

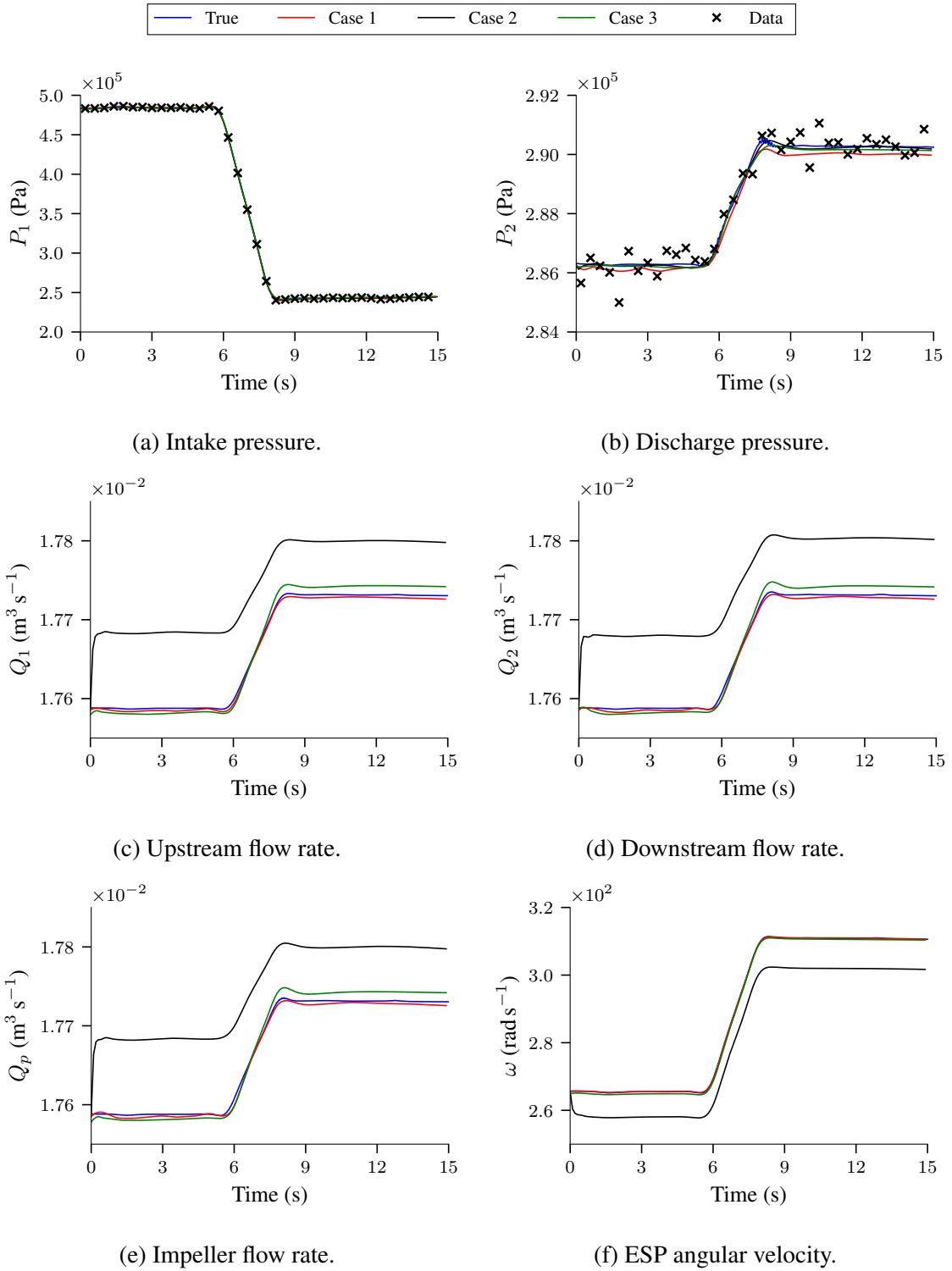


Figure 7.3: Comparison of predicted and true states for the simulated case with noise of the first experimental investigation and unknown parameters.

7.1.3 State estimation results for experimental data

This section assessed the performance of the PINN when subjected to experimental data, which is a more representative scenario of real-world oil field conditions. In this case, noise

in data and model uncertainties exist, posing a more challenging scenario for the PINN model. Similarly to the previous sections, the results from the first experimental investigation are provided in this section, while results from the second investigation can be found in Appendix D. The MAPE values for these predictions are presented in Table 7.5. Meanwhile, the predicted outputs of the neural network are shown in Figure 7.4.

The Table 7.5 presents the MAPE values for state predictions using experimental data across the three cases with varying unknown parameters. Among the cases evaluated, Case 1 shows the best agreement regarding the upstream volumetric flow rate (Q_1) and the ESP angular velocity ω . However, similarly to the noisy data scenario, Case 2 presented errors for ω and Q_1 that are considerably higher than the other states, as evident in Figures 7.4c and 7.4d. Nonetheless, the MAPE values remain relatively small for the other cases and states, and visual inspection of Figure 7.3 shows a reasonable agreement with the actual values.

Table 7.5: MAPE for the experimental data scenario.

	P_1	P_2	Q_1	ω
Case 1	4.517 %	0.245 %	0.137 %	1.065 %
Case 2	3.828 %	0.243 %	1.560 %	8.290 %
Case 3	2.963 %	0.252 %	0.218 %	1.300 %

In Figure 7.4, due to constraints in our experimental setup, it was only possible to directly measure the states Q_1 , P_1 , P_2 , and ω . Therefore, the PINN results analysis will primarily concentrate on these four states, denoted by the graphs' blue lines. Moreover, for all cases, the training dataset consists of 48 data points for data loss with 100 collocation points for physics loss. The plots show the mean value of results for 30 realizations of PINN.

By comparing the PINN-predicted dynamics with the actual values (Figure 7.4), a good overall agreement is evident across all states and cases, even in the presence of noise and model errors. However, similarly to the noisy data scenario, in Case 2 (black line), the PINN was unable to accurately estimate the flow rate (Q_1) and angular velocity (ω) states. While the predicted states follow the signal's shape, they exhibit relatively high errors. Remarkably, these higher errors were observed exclusively in the first experimental investigation (Figure 7.4) (high water cut), whereas in the second investigation (Figure D.3) (low water cut), Case 2 demonstrated performance similar to that of Case 3 (green line). These high errors are observed in Table 7.5, where the Case 2 values for Q_1 and ω had the highest MAPE values.

Notably, for the P_1 state (Figure 7.4a), a minor deviation in the PINN prediction's shape is noticeable when compared to the experimental data. This difference could be attributed to the influence of the C-elements, which, as discussed in Section 5.5.2, affects the system's settling time. In the parameter estimation section, it will be discussed the challenges encountered in estimating the bulk modulus for the experimental data, as it was not experimentally measured. Furthermore, in the discharge pressure state (Figure 7.4b), it is clear that the neural network

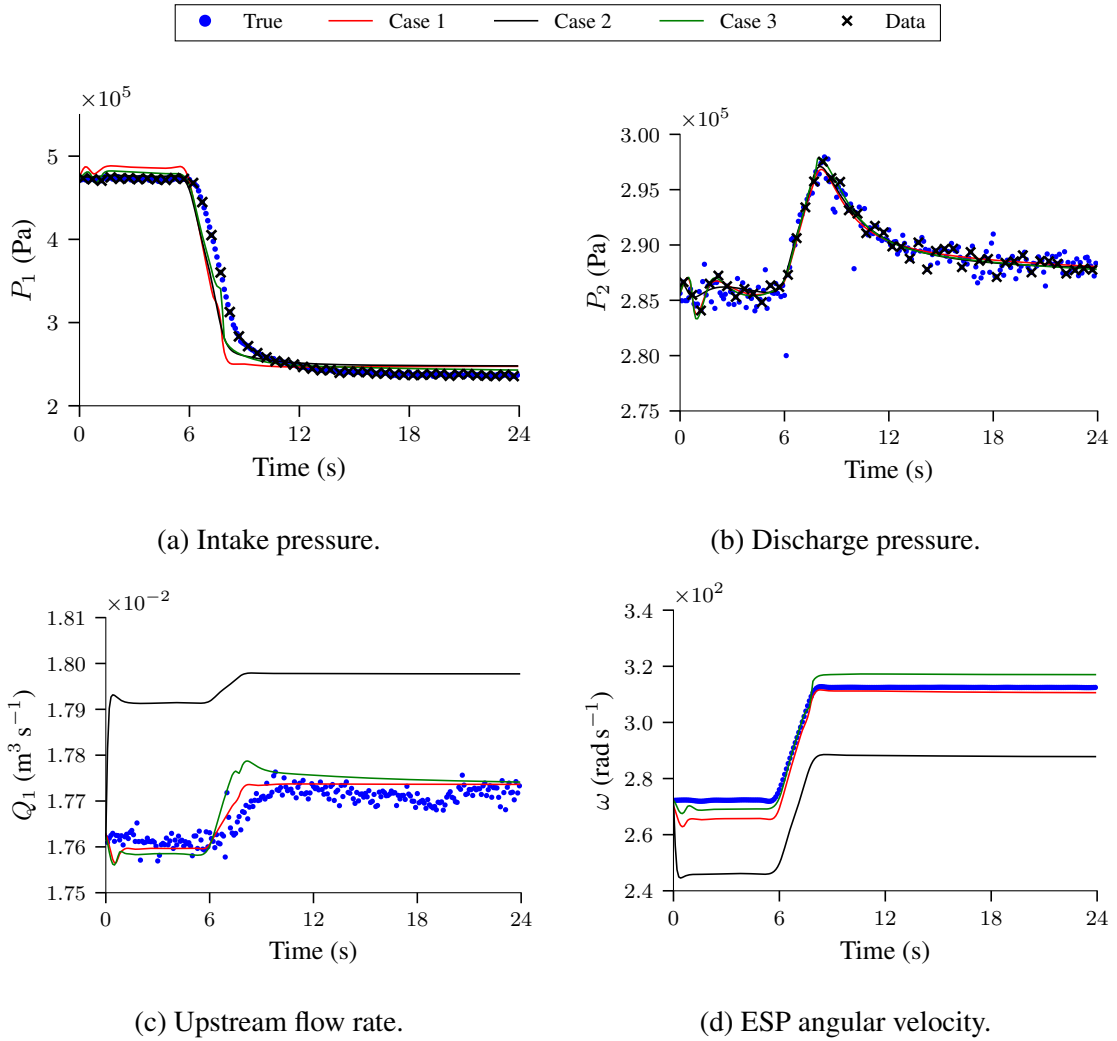


Figure 7.4: Comparison of predicted and true states for the experimental case of the first experimental investigation with unknown parameters.

did not overfit and successfully captured the signal trend and magnitude, including the signal overshoot between 6 s to 12 s, which was considerably smaller in the simulations.

Additionally, a systematic error is noticeable at the beginning of the ω state (Figure 7.4d) for Cases 1 and 3. Despite these deviations, the predicted ω signal aligns well with the experimental data regarding shape and magnitude. When comparing the simulated and measured angular velocity (ω), a systematic error is noticeable, indicating a difference between the actual and the obtained model parameters. However, despite this difference, the PINN could reasonably estimate the angular velocity state. It is possible that the observed discrepancies between the experimental data and model predictions could be attributed to multiple factors. These factors include model uncertainty arising from approximations, simplifications, and assumptions in the model, as discussed in Section 5.5, as well as the influence of noise in the experimental data.

7.2 Parameter estimation results

The results for parameter estimation in the experimental investigations 1 and 2 across three cases are presented in the following sections. It should be noted that the emulsion bulk modulus was not measured during the experiments. As a result, it is not possible to assess the accuracy of the values determined by the PINN in the experimental data scenario. The viscosity values obtained were compared to the Brinkman [69] model, described in Section 5.5. For density estimation, it was considered the measurements from the Coriolis meter. This section discusses absolute percentage error, but additional tables presenting actual values can be found in Appendix D.2.

In this section, the mean of the absolute percentage error (MAPE) for the parameter estimation results is defined as

$$\text{MAPE}_\Lambda = \frac{1}{N^{init}} \sum_{i=1}^{N^{init}} \left| \frac{\Lambda - \hat{\Lambda}_i}{\Lambda} \right|, \quad (7.2)$$

where N^{init} is the number of PINN random initializations, considered 30 in this study. The variable Λ represents the true value of the unknown parameter, and $\hat{\Lambda}_i$ is the estimated unknown parameter for the i -th PINN initialization. For simplicity, the error in this section is referred to as the absolute percentage error.

7.2.1 Case 1: Three unknown parameters B , μ and ρ for different types of data

In this section, it was focused on Case 1, where it was considered the bulk modulus (B), viscosity (μ), and density (ρ) as unknown while considering the remaining parameters as known. In Table 7.6, it is presented the MAPE for the two experimental investigations and all data scenarios.

Table 7.6: Mean of the absolute percentage error for Case 1.

	Data type	B	μ	ρ
Investigation 1	Simulation	0.31 %	0.03 %	0.02 %
	Noisy	0.58 %	0.12 %	0.09 %
	Experimental	N/A	1.80 %	0.80 %
Investigation 2	Simulation	0.61 %	0.32 %	0.29 %
	Noisy	0.48 %	0.21 %	0.21 %
	Experimental	N/A	4.30 %	2.40 %

As can be seen in Table 7.6, the PINN could successfully estimate the flow parameters for all cases. In the experimental data scenario, the MAPE was slightly higher, for investigation 1, the

errors were below 2 %, while investigation 2 had errors below 4.5 %. It is important to mention that for the experimental cases, the error refers to the difference between the obtained viscosity and the Brinkman [69] model, which may not be entirely accurate. Also, it is considered the single effective viscosity assumption, as described in Section 5.5. Thus, this higher percentage difference can also be related to these assumptions and limitations.

In addition to the mean analysis, it is important to assess the parameter absolute percentage error dispersion. The error dispersion for investigation 1 and 2 is visualized in Figure 7.5a and Figure 7.5b, respectively.

In Figure 7.5, each subfigure shows a specific experimental investigation and contains subplots for each unknown parameter under analysis. Within these subplots, three distinct box plots are presented: blue for the experimental data, red for the simulated data, and gray for the simulated data with added noise. These box plots include whiskers, outliers, and the mean value, represented by a triangle symbol. Outliers are identified as data points that lie more than 1.5 times the interquartile range (IQR) above the third quartile or below the first quartile. The horizontal axis represents the absolute percentage error calculated with respect to the reference value. This graphical structure is consistently employed in subsequent figures related to inverse problems.

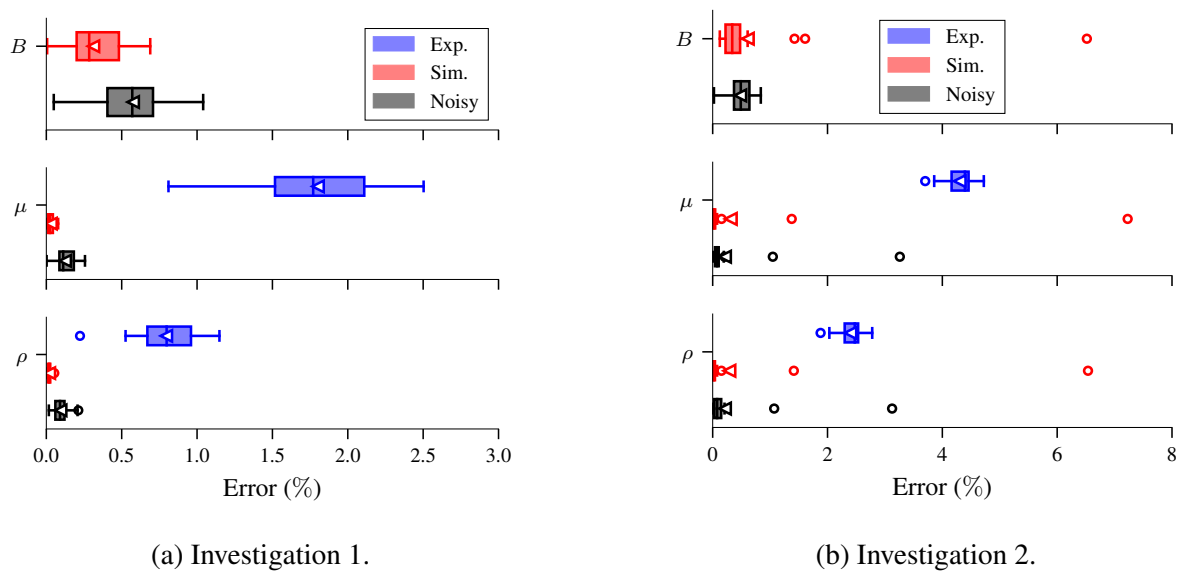


Figure 7.5: Box plot of the absolute percentage errors for Case 1.

In Figure 7.5a and Figure 7.5b, the fluid density (ρ) and viscosity (μ) parameters demonstrate consistent behavior across multiple initializations and data sources with relatively low dispersion. On the other hand, Investigation 2 presented outliers in all parameters for the simulated case and for ρ and μ in the simulated with noise scenario.

When comparing Investigations 1 and 2 in Table 7.6 simulated and simulated with noise, it is observable that the performance in Investigation 1 is superior to that in Investigation 2. However, the box plots for both investigations suggest a similar data spread. This discrepancy can be

attributed to the influence of outliers on the mean value calculation. As shown in Figure 7.5b, the mean value, denoted by a triangle symbol, lies outside the interquartile range, which suggests the impact of outliers. Furthermore, when we compare the median of the errors, they presented similar values, which further indicated the influence of these outliers on the mean.

Notably, the addition of noise negatively affected the results, as for most of the parameters, their distributions presented a slightly wider dispersion than the simulated. Further, analyzing the experimental data results, it is evident that they exhibit a wider distribution when compared to the simulated and simulated-with-noise data. This is expected as experimental data is more challenging due to noise and potential model inaccuracies.

7.2.2 Case 2: Seven unknown parameters B , μ , ρ , k_u , k_d , k_{3p} and k_{4p} for different types of data

In this section, it is examined the Case 2. The fluid's bulk modulus B , viscosity μ , and density ρ , along with the pump's viscous flow loss coefficient k_{3p} , the pump equivalent resistance k_{4p} , and the equivalent resistances of the upstream and downstream pipeline k_u and k_d respectively, are treated as unknowns. The remaining parameters were considered known. The MAPE from the two experimental investigations across all data scenarios is provided in Table 7.7.

Table 7.7: Mean of the absolute percentage error for Case 2.

		B	μ	ρ	k_u	k_d	k_{3p}	k_{4p}
Inv. 1	Sim.	2.52 %	13.10 %	1.31 %	24.22 %	6.15 %	4.28 %	3.80 %
	Noisy	1.34 %	36.43 %	5.68 %	40.58 %	19.07 %	9.79 %	10.51 %
	Exp.	N/A	120.19 %	9.72 %	77.35 %	56.31 %	27.68 %	29.26 %
Inv. 2	Sim.	0.98 %	1.38 %	0.18 %	0.28 %	1.20 %	3.98 %	2.27 %
	Noisy	1.29 %	13.01 %	3.10 %	3.62 %	12.62 %	6.45 %	6.57 %
	Exp.	N/A	14.50 %	7.99 %	4.82 %	15.39 %	9.73 %	5.73 %

The results presented in Table 7.7 demonstrate the PINN's successful estimation of flow parameters across most cases, except for the first investigation's simulated-with-noise and experimental data scenarios. In these cases, the mean of errors was significantly higher compared to the simulated, simulated, and Investigation 2 simulated-with-noise and experimental data scenario. Notably, for the experimental data scenario, the viscosity (μ) exhibited a difference of 120.19 %, and most other parameters had errors higher than 27 %. However, for the second investigation, the mean of errors in Table 7.7 were all below 15.5 %, indicating better performance in the experimental data scenario. As discussed earlier, the higher error in the experimental case may be caused due to model uncertainty, simplifications in the model, and experimental noise.

However, the results for Investigation 1 in the simulated data scenario require some attention. As shown in Figure 7.6a, all unknown parameters presented outliers. Furthermore, their computed means were observed to lie outside the IQR. It was also previously noted in Case 1 (Section 7.2.1),

which implies an influence of these outliers on the mean value. When examining the median values illustrated in Figure 7.6, the error metrics for simulated scenarios in both investigations were predominantly found to be below 1 %.

In Figure 7.6, the box plot illustrates the distribution of absolute percentage errors for each parameter in Case 2. Each subplot represents an unknown parameter for the data scenarios evaluated. The horizontal axis has been changed to logarithmic for better visibility. This graphical structure is consistently employed in subsequent figures related to inverse problems.

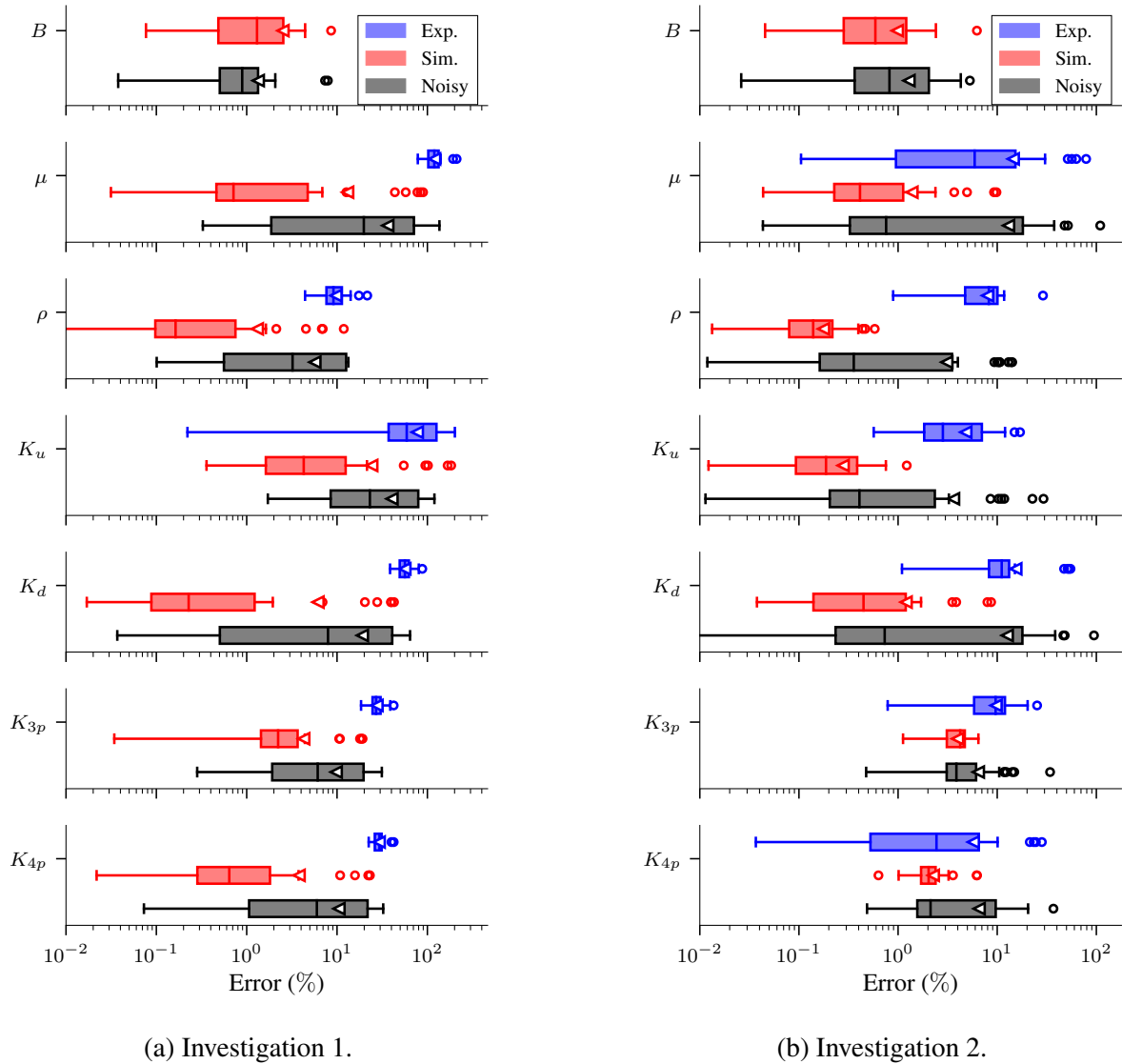


Figure 7.6: Box plot of the absolute percentage errors for Case 2.

The addition of noise considerably affected the results in both experimental investigations, leading to higher mean errors as shown in Table 7.7, whereas in investigation, the mean of the errors was smaller than in experimental Investigation 1. Analyzing the box plots in Figure 7.6, it is observable that the simulated noisy scenario resulted in greater dispersion for most parameters. This observation indicates that the introduction of noise adversely affected the accuracy of the estimated parameters. Moreover, it is noticeable that similar to the discussed in Section 7.2.1,

the experimental data scenario presented the highest mean errors across the initializations for both experimental investigations, except for the k_{4p} in the second experimental investigation.

Despite the high errors in Investigation 1's experimental data scenario, most estimated parameters exhibited relatively small dispersion across the weight initializations, as evident in Figure 7.6a. It is worth noting that the parameter selection for this case did not consider the practical identifiability analysis, which assessed, in this study, the parameter sensitivity to noise. Therefore, this higher mean error with relatively low dispersion suggests that the system might not be practically identifiable within the flow condition of experimental investigation 1. It is possibly converging to a parameter set other than the true one. It is important to note that as the water cuts increase up to the emulsion phase inversion, the fluid behavior becomes more complex, posing a more challenging scenario than lower water cuts. Further, our practical identifiability analysis considered only the sensitivity analysis rather than the Monte Carlo approach, where the optimization algorithm, in this case, the PINN, would also be included.

Therefore, to draw more definitive conclusions about how the parameter estimation is sensitive to the water cut, additional investigations need to be conducted with a larger experimental test matrix that covers a wider range of water cuts. Additionally, a Monte Carlo approach with the PINN on the practical identifiability analysis could potentially better evaluate the effects of the model uncertainties with the experimental data scenario, as the approach described in Section 6.2 considered only the simulated data. Further, as the local structural identifiability analysis assesses the identifiability of the neighborhood of the parameter set, it is possible that restricting the search range and imposing stricter bounds on the parameter search could lead to better results. This approach is suggested in [132].

7.2.3 Case 3: Eight unknown parameters B , μ , ρ , k_u , k_d , k_{4p} , k_{1s} and k_{5s} for different types of data

This section presents the results of the inverse problem for Case 3, specifically evaluating the performance of the parameter estimation. The evaluation is based on the MAPE, as shown in Table 7.8. The considered parameters, in this case, include the bulk modulus (B), viscosity (μ), and density (ρ) of the fluid, as well as the pump equivalent resistance (k_{4p}), the first impeller-fluid coupling coefficient (k_{1s}), the shaft second-order friction coefficient (k_{5s}), and the equivalent resistance of the pipeline upstream and downstream (k_u and k_d).

The results in Table 7.8 and Figure 7.7 indicate that the PINN successfully estimated the density and viscosity for all scenarios in Case 3, but it encountered challenges in estimating the bulk modulus. The 15% value represents the upper and lower bounds imposed on the output scaling transformation for the bulk modulus. Additionally, when analyzing the dispersion in Figure 7.7, it is evident that the distributions of the simulated with added noise case are similar to those of the simulated case, with similar IQR.

In Table 7.8, the distinction between data sources with smaller errors, as observed in Cases 1

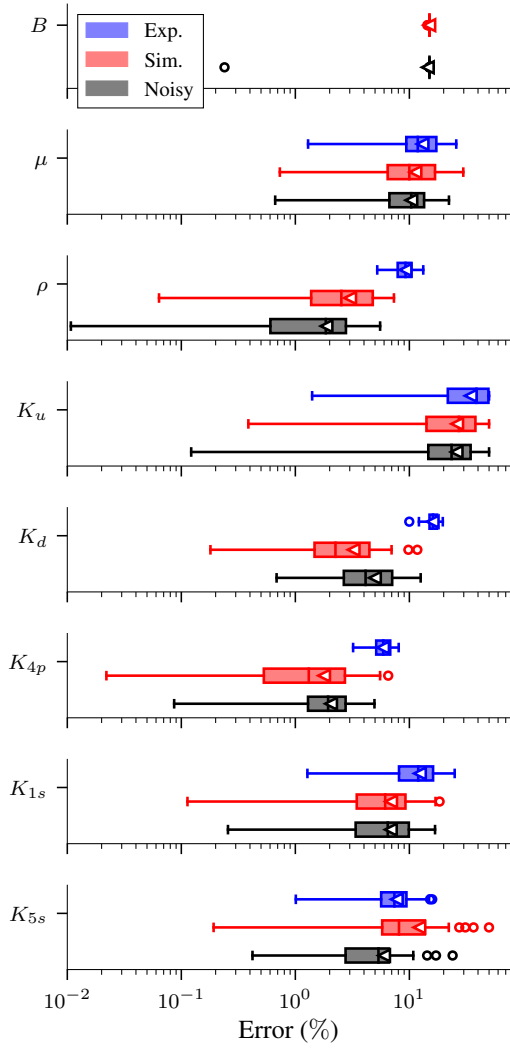
Table 7.8: Mean absolute percentage error for Case 3.

		B	μ	ρ	k_u	k_d	k_{4p}	k_{1s}	k_{5s}
Inv. 1	Sim.	14.95 %	11.31 %	3.02 %	26.27 %	3.25 %	1.79 %	6.92 %	12.24 %
	Noisy	14.51 %	10.41 %	1.88 %	25.97 %	4.99 %	2.06 %	6.88 %	6.00 %
	Exp.	N/A	13.05 %	9.26 %	34.51 %	16.01 %	5.87 %	12.37 %	7.76 %
Inv. 2	Sim.	15.00 %	14.34 %	4.12 %	6.90 %	6.66 %	3.43 %	12.71 %	6.96 %
	Noisy	15.00 %	13.66 %	3.77 %	4.92 %	13.63 %	7.04 %	11.86 %	12.22 %
	Exp.	N/A	1.60 %	10.16 %	1.96 %	12.05 %	5.28 %	7.01 %	9.25 %

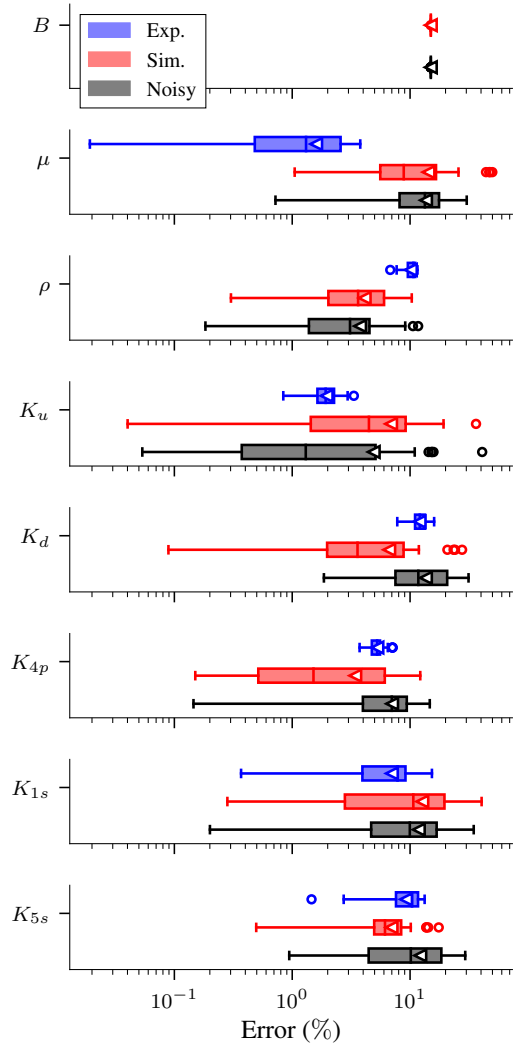
and 2 (Section 7.2.1 and Section 7.2.2), is not evident. The Investigation 1 and 2 demonstrated errors mostly below 13 %. Notably, in Investigation 1, the upstream pipeline equivalent resistance (k_u) exhibited the highest errors across all data sources, reaching up to 34.51 %. However, in Figure 6.2, it is noticeable that the k_u presented a relatively high correlation with other parameters, such as the k_d . On the other hand, in Investigation 2, we do not observe errors as high as in Investigation 1. This discrepancy can likely be attributed to the distinct flow characteristics of each investigation. As previously discussed in Section 7.2.2, further tests under diverse flow conditions are essential to understand the performance difference between Investigation 1 and 2 comprehensively.

It is noteworthy that, for Case 3, besides the fluid bulk modulus and density, the other parameters also have bounded output scaling transformations, which could have contributed to lower errors. Thus, although Case 3 poses an additional challenge compared to Case 2, once it involves estimating eight unknown parameters instead of seven, Case 3 and Case 2 are not directly comparable.

In Figure 7.7, the box plot illustrates the distribution of absolute percentage errors of each parameter in Case 3. The individual subplots correspond to the unknown parameters across the evaluated data scenarios. To enhance visibility, the horizontal axis has been changed to a logarithmic scale.



(a) Investigation 1.



(b) Investigation 2.

Figure 7.7: Box plot of the absolute percentage errors for Case 3.

8 Conclusions

This research aimed to model the electrical submersible pump system by leveraging the bond graph framework, which was then utilized for identifiability analysis and parameter estimation. The model was primarily designed to consider multiphase flow scenarios, typical in industrial contexts, with a particular emphasis on water-oil mixtures. A key criterion for the model was to strike a balance between simplicity and computational efficiency, thereby rendering it suitable for real-time applications such as monitoring, fault diagnosis, and control in industrial environments. The research was guided by the following objectives:

1. Derivation of elemental bond graph elements using fundamental equations of the subsystems in Sections 3.2, 3.3, 3.4.5 and 3.5 to 3.7.
2. The formulation and validation of a bond graph-based model for pipeline transients in Section 5.1.
3. The formulation of a bond graph-based model, accounting for both mechanical and hydraulic subsystems inherent to the ESP systems in Sections 5.2 to 5.4.
4. Validate the obtained model through comparison with experimental data, on different emulsion flow conditions in Section 5.5.
5. Identifiability analysis to assess the model's structural and practical identifiability, as well as parameter sensitivity in Chapter 6.
6. Utilization of Physics-Informed Neural Networks (PINN) for solving inverse problems, aimed at estimating unknown parameters and unmeasured states in Chapter 7.

The objectives were addressed across the chapters, each fulfilling specific objectives in the investigation of the dynamics of electrical submersible pump systems. Methodologically, the research employed a multifaceted approach combining analytical, numerical, and machine-learning techniques, including bond graph theory for modeling, identifiability analysis for parameter assessment, and PINN for state and parameter estimation.

The Section 5.2 elaborated on the development of a minimal system required to represent the centrifugal pump system, including the shaft and the pump subsystems. Then, in Section 5.3, a general bond graph model composed of these subsystems is proposed to represent a generic ESP system composed of n -impellers with an arbitrary number of pipe and shaft segments. However, despite the system's comprehensive description, the resultant system's complexity is significant. Thus, in Section 5.4, a simplification with a single pump stage is considered. The objective was to reduce the number of parameters and increase the tractability of the problem while maintaining

reasonable accuracy for the model. Then, besides the single impeller, two pipe elements were considered to represent the upstream and downstream pipelines, respectively. The bond graph model resulted in a set of ODEs composed of 6 equations, whose parameters can be obtained from the steady state conditions.

Then, for validating the model with experimental data, it was assumed that the flow was laminar in both emulsion and oil flow lines, as corroborated by the Reynolds number. Thus, the friction function was formulated to meet these conditions, with the friction factor expressions discussed in Section 3.3. Although real-world setups manifest complex variations in emulsion viscosity, the closed-loop system of the ESP studied allowed for the reasonable assumption of constant viscosity, and the Brinkman [69] model was chosen to represent emulsion viscosity due to its simplicity and widespread usage in the oil industry.

The parameters were then obtained using the steady state condition, and the model presented a reasonable accuracy as evidenced by the coefficient of determination and the error bounds shown in Appendix C. However, fine-tuning was required to align the model with the experimental data better. One limitation of the model was its reliance on literature-based values for the liquid bulk modulus, as it was not experimentally measured. This necessitated compromise identified an avenue for future research to improve model fidelity.

It followed the methodology described in Section 4.7.1 for pump and pipeline tuning. Then, a comparative analysis using metrics like Pearson correlation coefficient and Mean Absolute Percentage Error (MAPE) provided empirical evidence of the model's performance. Despite the model's strengths in capturing specific system dynamics, discrepancies like lower overshoot in discharge pressures and faster response in intake and discharge pressures offset were noted. The first assumption in fine-tuning the model was to adjust the inertance element. However, after attempts, it showed little to no effect on reproducing the pressure spikes observed in the experimental data.

After some observations and revisiting the assumptions taken regarding the pipeline subsystem capacitance and the development on the Section 3.2.1. The requirement for further fine-tuning was observed, particularly on the elasticity of fluid-pipe walls. Then, after fine-tuning the C-elements with the procedure described Section 4.7.2, the model's accuracy improved significantly. The model could capture the pressure spikes observed experimentally, and settling times for intake and discharge pressures were adjusted accordingly. Although the model proved effective in certain conditions, low and moderate water fraction emulsions flows, further experimental studies are needed to comprehensively understand the C-elements' characteristics.

A local structural identifiability analysis was conducted using the differential elimination method for dynamical models via projections, as proposed by Dong *et al.* [96]. The results revealed that the system is not locally structurally identifiable when both intake and discharge pressures are the only known parameters. For local structural identifiability, it was required to consider the parameters like shaft inertia (I_s), fluid-impeller disk friction (k_{3s}), and shaft viscous damping (k_{4s}) as known, resulting in 12 identifiable unknown parameters. Then, the parameter

correlation matrix was derived using the Fisher information matrix for the practical identifiability analysis. Practical identifiability provided a qualitative analysis of the unknown parameters in the presence of noise. To attain this identifiability, it became necessary to define more parameters as known. Thus, the most critical parameters in the context of the ESP's actual operation were selected as unknown, and other parameters as known. These unknown parameters included the fluid properties and pipeline equivalent resistance.

The proposed PINN model in this study successfully estimated the ESP's fluid properties (bulk modulus, density, and viscosity) and dynamics of the states with reasonable accuracy. The model provided reasonable accuracy when considering simulated data with low water cut when considering fluid properties, pipeline equivalent resistances, shaft, and pump parameters. However, a relatively higher error was observed for higher water cuts or when it was considered simulated with noise and experimental data with lower water cuts.

In this case, it was observed outliers in the predicted results. Further study may include a robust PINN method to eliminate the outliers and better performance. Furthermore, it was also observed that errors are higher in the case of higher water cuts. This error is higher in the case of noise and experimental data than in the simulated cases. These cases with more unknowns may require additional measurements of the state variables, which are generally not measured in the field. Future studies may also include further investigations with a broader range of water fractions to understand better the water cut influences. The study may also focus on updating the numerical model for higher water cuts if necessary, as assumptions made on the numerical model may not be valid for higher water cuts.

Obtaining the estimated parameters and states for the ESP system in oil production can be challenging, and the PINN offers a promising and cost-efficient alternative for estimating them. Although this approach has its benefits, it also has some limitations. One of the limitations is that the technique is computationally intensive. This means that for every desired estimation of properties, the PINN must undergo training. More efficient PINN algorithms need to be investigated for different operational conditions. Furthermore, the accuracy of the estimated properties using PINN is heavily reliant on the accuracy of the measured states and known parameters. In the event of a faulty reading or instrument failure, the PINN's ability to provide accurate estimations is compromised.

Additionally, a Monte Carlo approach with the PINN on the practical identifiability analysis could potentially better evaluate the effects of the model uncertainties with the experimental data scenario. As the experimental data contains noise, further study may include uncertainty quantification. Furthermore, an ESP system model that considers the multistage separately would be relevant for ESP in actual production, whose number of stages are considerably higher than the one considered in this study. Moreover, the current model does not consider the electrical domain and its inclusion would be more realistic. Another notable aspect is that the single viscosity assumption for the system remains a limitation.

Bibliography

- [1] D. G. Luenberger, *Introduction to Dynamic Systems: Theory, Models, and Applications*. New York: Wiley, 1979.
- [2] V. Marinca and N. Herisanu, *Nonlinear Dynamical Systems in Engineering: Some Approximate Approaches*. Berlin ; New York: Springer, 2011.
- [3] P. Mellodge, *A Practical Approach to Dynamical Systems for Engineers* (Woodhead Publishing in Mechanical Engineering). Cambridge: Woodhead Publ, 2016.
- [4] V. Damic and J. Montgomery, *Mechatronics by Bond Graphs*. Berlin, Heidelberg: Springer Berlin Heidelberg, 2015.
- [5] R. Merzouki, A. K. Samantaray, P. M. Pathak and B. Ould Bouamama, *Intelligent Mechatronic Systems*. London: Springer London, 2013.
- [6] H. M. Paynter, *Analysis and Design of Engineering Systems*. M.I.T. Press, 1961.
- [7] W. Borutzky, ‘Bond graph modelling’, *Simulation Modelling Practice and Theory*, Bond Graph Modelling, no. 1, pp. 1–2, 2009.
- [8] T. Bakka and H. R. Karimi, ‘Bond graph modeling and simulation of wind turbine systems’, *Journal of Mechanical Science and Technology*, no. 6, pp. 1843–1852, 2013.
- [9] C. W. Groetsch, *Inverse Problems: Activities for Undergraduates* (Classroom Resource Materials). Washington, DC: Mathematical Association of America, 1999.
- [10] C. W. Groetsch, *Inverse Problems in the Mathematical Sciences*. Wiesbaden: Vieweg+Teubner Verlag, 1993.
- [11] R. C. Aster, B. Borchers and C. H. Thurber, *Parameter Estimation and Inverse Problems*, 2nd ed. Waltham, MA: Academic Press, 2013.
- [12] A. Kirsch, *An Introduction to the Mathematical Theory of Inverse Problems* (Applied Mathematical Sciences). Cham: Springer International Publishing, 2021.
- [13] C. R. Vogel, *Computational Methods for Inverse Problems* (Frontiers in Applied Mathematics 23). Philadelphia: Society for Industrial and Applied Mathematics, 2002.
- [14] G. Falcone, ‘Chapter 1 Multiphase Flow Fundamentals’, in *Multiphase Flow Metering*, ser. Developments in Petroleum Science, G. Falcone, G. F. Hewitt and C. Alimonti, Eds., Elsevier, 2009, pp. 1–18.
- [15] O. Shoham, *Mechanistic Modeling of gas liquid two phase flow in pipes*. Richardson, Texas, EUA: The Society of Petroleum Engineers (SPE), 2006.
- [16] O. Shoham, *Mechanistic Modeling of Gas-Liquid Two-Phase Flow in Pipes*. Richardson, TX: Society of Petroleum Engineers, 2006.

- [17] J. Israelachvili, 'The science and applications of emulsions — an overview', *Colloids and Surfaces A: Physicochemical and Engineering Aspects*, A Selection of Papers Presented at the First World Congress on Emulsions, pp. 1–8, 1994.
- [18] F. Jahanzad, D. Josephides, A. Mansourian and S. Sajjadi, 'Dynamics of Transitional Phase Inversion Emulsification: Effect of Addition Time on the Type of Inversion and Drop Size', *Industrial & Engineering Chemistry Research*, no. 16, pp. 7631–7637, 2010.
- [19] A. Perazzo, V. Preziosi and S. Guido, 'Phase inversion emulsification: Current understanding and applications', *Advances in Colloid and Interface Science*, Reinhard Miller, Honorary Issue, pp. 581–599, 2015.
- [20] F. Goodarzi and S. Zendejboudi, 'A Comprehensive Review on Emulsions and Emulsion Stability in Chemical and Energy Industries', *The Canadian Journal of Chemical Engineering*, no. 1, pp. 281–309, 2019.
- [21] A. P. F. Machado, C. Z. Resende and D. C. Cavalieri, 'Estimation and prediction of motor load torque applied to electrical submersible pumps', *Control Engineering Practice*, pp. 284–296, 2019.
- [22] H. Zhu, J. Zhu, Z. Lin, Q. Zhao, R. Rutter and H.-Q. Zhang, 'Performance degradation and wearing of Electrical Submersible Pump (ESP) with gas-liquid-solid flow: Experiments and mechanistic modeling', *Journal of Petroleum Science and Engineering*, p. 108 399, 2021.
- [23] T. Nguyen, *Artificial Lift Methods: Design, Practices, and Applications* (Petroleum Engineering). Cham: Springer International Publishing, 2020.
- [24] M. A. Castillo, R. H. R. Gutiérrez, U. A. Monteiro, R. S. Minette and L. A. Vaz, 'Modal parameters estimation of an electrical submersible pump installed in a test well using numerical and experimental analysis', *Ocean Engineering*, pp. 1–7, 2019.
- [25] W. Monte Verde, 'Estudo Experimental de Bombas de BCS Operando com Escoamento Bifásico Gás-Líquido', Dissertação de Mestrado, Universidade Estadual de Campinas, 2011.
- [26] M. Pardo Varon, 'Estudo de uma bomba centrífuga submersa (BCS) como medidor de vazão', Dissertação de Mestrado, Universidade Estadual de Campinas, 2013.
- [27] L. F. R. Pineda, 'Controle do Ponto de Operação de Bombas Centrífugas Submersas em Escoamento Líquido-Gás Usando Redes Neurais', Dissertação de Mestrado, Universidade Estadual de Campinas, 2016.
- [28] I. Metwally and A. Gastli, 'Correlation between eddy currents and corrosion in electric submersible pump systems', *International Journal of Thermal Sciences*, no. 6, pp. 800–810, 2008.

- [29] P. Angeli and G. F. Hewitt, 'Pressure gradient in horizontal liquid–liquid flows', *International Journal of Multiphase Flow*, no. 7, pp. 1183–1203, 1999.
- [30] P. Angeli and G. F. Hewitt, 'Flow structure in horizontal oil–water flow', *International Journal of Multiphase Flow*, no. 7, pp. 1117–1140, 2000.
- [31] W. Honório, D. Lemos and R. de Lima, 'ESP Control and Monitoring System of Heavy Oil Peregrino Field', in *SPE Artificial Lift Conference — Latin America and Caribbean*, OnePetro, 2015.
- [32] J. G. Flores, X. T. Chen and J. P. Brill, 'Characterization of Oil-Water Flow Patterns in Vertical and Deviated Wells', in *SPE Annual Technical Conference and Exhibition*, San Antonio, Texas: Society of Petroleum Engineers, 1997.
- [33] W. Wang, W. Cheng, K. Li, C. Lou and J. Gong, *Flow Patterns Transition Law of Oil-Water Two-Phase Flow under a Wide Range of Oil Phase Viscosity Condition*, Research Article, 2013.
- [34] T. W. F. Russell, G. W. Hodgson and G. W. Govier, 'Horizontal pipeline flow of mixtures of oil and water', *The Canadian Journal of Chemical Engineering*, no. 1, pp. 9–17, 1959.
- [35] M. E. Charles, G. W. Govier and G. W. Hodgson, 'The horizontal pipeline flow of equal density oil-water mixtures', *The Canadian Journal of Chemical Engineering*, no. 1, pp. 27–36, 1961.
- [36] D. Hasson, V. Mann and A. Nir, 'Annular flow of two immiscible liquids I. Mechanisms', *The Canadian Journal of Chemical Engineering*, no. 5, pp. 514–520, 1970.
- [37] A. C. Bannwart, O. M. H. Rodriguez, C. H. M. de Carvalho, I. S. Wang and R. M. O. Vara, 'Flow Patterns in Heavy Crude Oil-Water Flow', *Journal of Energy Resources Technology*, no. 3, pp. 184–189, 2004.
- [38] S. A. Abood, M. A. Abdulwahid and M. A. Al-Mudhafar, 'Experimental Study of (Water–Oil) Flow Patterns and Pressure Drop in Vertical and Horizontal Pipes', *International Journal of Air-Conditioning and Refrigeration*, no. 04, p. 1 850 034, 2018.
- [39] K. Perera, C. Pradeep, S. Mylvaganam and R. W. Time, 'Imaging of oil-water flow patterns by Electrical Capacitance Tomography', *Flow Measurement and Instrumentation*, pp. 23–34, 2017.
- [40] A. K. Jana, G. Das and P. K. Das, 'Flow regime identification of two-phase liquid–liquid upflow through vertical pipe', *Chemical Engineering Science*, no. 5, pp. 1500–1515, 2006.
- [41] H. Hu, J. Jing, J. Tan and G. H. Yeoh, 'Flow patterns and pressure gradient correlation for oil–water core–annular flow in horizontal pipes', *Experimental and Computational Multiphase Flow*, no. 2, pp. 99–108, 2020.

- [42] C. A. M. Cavicchio, J. L. Biazussi, M. S. de Castro, A. C. Bannwart, O. M. H. Rodriguez and C. H. M. de Carvalho, 'Experimental study of viscosity effects on heavy crude oil-water core-annular flow pattern', *Experimental Thermal and Fluid Science*, pp. 270–285, 2018.
- [43] O. M. H. Rodriguez and A. C. Bannwart, 'Stability analysis of core-annular flow and neutral stability wave number', *AIChE Journal*, no. 1, pp. 20–31, 2008.
- [44] V. Preziosi, A. Perazzo, S. Caserta, G. Tomaiuolo and S. Guido, 'Phase inversion emulsification', *Chemical Engineering Transactions*, pp. 1585–1590, 2013.
- [45] F. Ravera, K. Dziza, E. Santini, L. Cristofolini and L. Liggieri, 'Emulsification and emulsion stability: The role of the interfacial properties', *Advances in Colloid and Interface Science*, p. 102 344, 2021.
- [46] S. Kokal, 'Crude-oil emulsions: A state-of-the-art review', *SPE Production & Facilities*, no. 01, pp. 5–13, 2005. eprint: <https://onepetro.org/PO/article-pdf/20/01/5/2568359/spe-77497-pa.pdf>.
- [47] N. A. V. Bulgarelli, J. L. Biazussi, W. Monte Verde, C. E. Perles, M. S. de Castro and A. C. Bannwart, 'A novel criterion based on slip ratio to assess the flow behavior of W/O emulsions within centrifugal pumps', *Chemical Engineering Science*, p. 117 050, 2022.
- [48] N. A. V. Bulgarelli, J. L. Biazussi, W. Monte Verde, C. E. Perles, M. S. de Castro and A. C. Bannwart, 'Relative viscosity model for oil/water stable emulsion flow within electrical submersible pumps', *Chemical Engineering Science*, p. 116 827, 2021.
- [49] R. Pal, 'Effect of droplet size on the rheology of emulsions', *AIChE Journal*, no. 11, pp. 3181–3190, 1996.
- [50] R. Pal, 'A novel method to correlate emulsion viscosity data', *Colloids and Surfaces A: Physicochemical and Engineering Aspects*, no. 1-3, pp. 275–286, 1998.
- [51] S. R. Derkach, 'Rheology of emulsions', *Advances in Colloid and Interface Science*, no. 1, pp. 1–23, 2009.
- [52] J. Plasencia, B. Pettersen and O. J. Nydal, 'Pipe flow of water-in-crude oil emulsions: Effective viscosity, inversion point and droplet size distribution', *Journal of Petroleum Science and Engineering*, pp. 35–43, 2013.
- [53] T. S. T. Ariffin, E. Yahya and H. Husin, 'The Rheology of Light Crude Oil and Water-In-Oil-Emulsion', *Procedia Engineering*, pp. 1149–1155, 2016.
- [54] C. Liu, M. Li, R. Han, J. Li and C. Liu, 'Rheology of Water-in-Oil Emulsions with Different Drop Sizes', *Journal of Dispersion Science and Technology*, no. 3, pp. 333–344, 2016.
- [55] F. D. Vita, M. E. Rosti, S. Caserta and L. Brandt, 'On the effect of coalescence on the rheology of emulsions', *Journal of Fluid Mechanics*, pp. 969–991, 2019.

- [56] L. Yi, F. Toschi and C. Sun, ‘Global and local statistics in turbulent emulsions’, *Journal of Fluid Mechanics*, A13, 2021.
- [57] L. Yi *et al.*, ‘Physical mechanisms for droplet size and effective viscosity asymmetries in turbulent emulsions’, *Journal of Fluid Mechanics*, A39, 2022.
- [58] G. Dutra Leite Do Amaral, ‘Modelagem do escoamento monofásico em bomba centrífuga submersa operando com fluidos viscosos:’ Mestre em Ciências e Engenharia de Petróleo, Universidade Estadual de Campinas, Campinas, SP, 2007.
- [59] T. S. Vieira, J. R. Siqueira, A. D. Bueno, R. E. M. Morales and V. Estevam, ‘Analytical study of pressure losses and fluid viscosity effects on pump performance during monophasic flow inside an ESP stage’, *Journal of Petroleum Science and Engineering*, pp. 245–258, 2015.
- [60] G. M. Paternost, A. C. Bannwart and V. Estevam, ‘Experimental Study of a Centrifugal Pump Handling Viscous Fluid and Two-Phase Flow’, *SPE Production & Operations*, no. 02, pp. 146–155, 2015.
- [61] J. L. Biazussi, ‘Modelo de deslizamento para escoamento gás/líquido em bomba centrífuga submersa operando com líquido de baixa viscosidade’, Doutor em Ciências e Engenharia de Petróleo, Universidade Estadual de Campinas, Campinas, SP, 2014.
- [62] E. M. Ofuchi, H. Stel, T. S. Vieira, F. J. Ponce, S. Chiva and R. E. M. Morales, ‘Study of the effect of viscosity on the head and flow rate degradation in different multistage electric submersible pumps using dimensional analysis’, *Journal of Petroleum Science and Engineering*, pp. 442–450, 2017.
- [63] A. J. Stepanoff, *Centrifugal and Axial Flow Pumps: Theory, Design, and Application*, Reprint ed. Malabar, Fla: Krieger Pub. Co, 1993.
- [64] G. Morrison, W. Yin, R. Agarwal and A. Patil, ‘Development of Modified Affinity Law for Centrifugal Pump to Predict the Effect of Viscosity’, *Journal of Energy Resources Technology*, no. 9, p. 092 005, 2018.
- [65] A. Patil and G. Morrison, ‘Affinity Law Modified to Predict the Pump Head Performance for Different Viscosities Using the Morrison Number’, *Journal of Fluids Engineering*, no. 2, 2018.
- [66] J. Zhu *et al.*, ‘A New Mechanistic Model To Predict Boosting Pressure of Electrical Submersible Pumps Under High-Viscosity Fluid Flow with Validations by Experimental Data’, *SPE Journal*, no. 02, pp. 744–758, 2020.
- [67] E. M. Ofuchi, J. M. C. Cubas, H. Stel, R. Dunaiski, T. S. Vieira and R. E. M. Morales, ‘A new model to predict the head degradation of centrifugal pumps handling highly viscous flows’, *Journal of Petroleum Science and Engineering*, p. 106 737, 2020.

- [68] J. Zhu *et al.*, ‘A New Mechanistic Model for Oil-Water Emulsion Rheology and Boosting Pressure Prediction in Electrical Submersible Pumps ESP’, in *Day 3 Wed, October 02, 2019*, Calgary, Alberta, Canada: SPE, 2019, D031S057R002.
- [69] H. C. Brinkman, ‘The Viscosity of Concentrated Suspensions and Solutions’, *The Journal of Chemical Physics*, no. 4, pp. 571–571, 2004. eprint: https://pubs.aip.org/aip/jcp/article-pdf/20/4/571/8113740/571_1_online.pdf.
- [70] A. Dazin, G. Caignaert and G. Bois, ‘Transient Behavior of Turbomachineries: Applications to Radial Flow Pump Startups’, *Journal of Fluids Engineering*, no. 11, pp. 1436–1444, 2007.
- [71] I. Chalghoum, S. Elaoud, M. Akrouit and E. H. Taieb, ‘Transient behavior of a centrifugal pump during starting period’, *Applied Acoustics*, pp. 82–89, 2016.
- [72] Y.-L. Zhang, Z.-C. Zhu, H.-S. Dou, B.-L. Cui, Y. Li and Z.-Z. Zhou, ‘Numerical Investigation of Transient Flow in a Prototype Centrifugal Pump during Startup Period’, *International Journal of Turbo & Jet-Engines*, no. 2, 2017.
- [73] J. Kullick and C. M. Hackl, ‘Dynamic Modeling and Simulation of Deep Geothermal Electric Submersible Pumping Systems’, *Energies*, no. 10, p. 1659, 2017.
- [74] T. Tanaka and N. Takatsu, ‘Transient characteristics of a centrifugal pump at rapid startup’, *IOP Conference Series: Earth and Environmental Science*, p. 052016, 2019.
- [75] Q. Li, X. Ma, P. Wu, S. Yang, B. Huang and D. Wu, ‘Study on the Transient Characteristics of the Centrifugal Pump during the Startup Period with Assisted Valve’, *Processes*, no. 10, p. 1241, 2020.
- [76] F. Omri, L. Hadj Taieb and S. Elaoud, ‘Numerical study on the transient behavior of a radial pump during starting time’, *Journal of Water Supply: Research and Technology-Aqua*, no. 3, pp. 257–273, 2021.
- [77] S. Das, *Mechatronic Modeling and Simulation Using Bond Graphs*. Boca Raton: CRC Press, 2009.
- [78] P. J. Gawthrop and E. J. Crampin, ‘Modular bond-graph modelling and analysis of biomolecular systems’, *IET Systems Biology*, no. 5, pp. 187–201, 2016.
- [79] L. Moin, V. Uddin, A. Y. Memon and S. H. Zaidi, ‘Bond graph model for the right atrium of heart’, in *2016 IEEE EMBS Conference on Biomedical Engineering and Sciences (IECBES)*, 2016, pp. 181–185.
- [80] V. Le Rolle, A. I. Hernandez, P. Y. Richard, J. Buisson and G. Carrault, ‘A Bond Graph Model of the Cardiovascular System’, *Acta Biotheoretica*, no. 4, pp. 295–312, 2005.
- [81] I. Abdallah, A.-L. Gehin and B. O. Bouamama, ‘Bond Graph for Online Robust Diagnosis Application: Hydraulic system’, *IFAC-PapersOnLine*, 20th IFAC World Congress, no. 1, pp. 13 538–13 543, 2017.

- [82] Y. Touati, R. Merzouki and B. Ould Bouamama, 'Robust diagnosis to measurement uncertainties using bond graph approach: Application to intelligent autonomous vehicle', *Mechatronics*, no. 8, pp. 1148–1160, 2012.
- [83] S. Benmoussa, R. Merzouki and B. O. Bouamama, 'Plant Fault Diagnosis using Bond Graph Approach: Application to Intelligent Autonomous Vehicle', *IFAC Proceedings Volumes*, 8th IFAC Symposium on Fault Detection, Supervision and Safety of Technical Processes, no. 20, pp. 952–957, 2012.
- [84] D. Karnopp, 'Bond Graph Models for Fluid Dynamic Systems', *Journal of Dynamic Systems, Measurement, and Control*, no. 3, pp. 222–229, 1972.
- [85] J. L. Baliño, A. E. Larreteguy and E. F. G. Raso, 'A general bond graph approach for computational fluid dynamics', *Simulation Modelling Practice and Theory*, no. 7, pp. 884–908, 2006.
- [86] Y. Li, Z. Zhu and G. Chen, 'Bond Graph Modeling and Validation of an Energy Regenerative System for Emulsion Pump Tests', *The Scientific World Journal*, pp. 1–12, 2014.
- [87] H. M. Paynter, 'The Dynamics and Control of Eulerian Turbomachines', *Journal of Dynamic Systems, Measurement, and Control*, no. 3, pp. 198–205, 1972.
- [88] K. Tanaka, W.-H. Rong, K. Suzuki, F. Shimizu, K. Hatakenaka and H. Tanaka, 'Detailed bond graph models of turbomachinery', in *2000 26th Annual Conference of the IEEE Industrial Electronics Society. IECON 2000. 2000 IEEE International Conference on Industrial Electronics, Control and Instrumentation. 21st Century Technologies*, 2000, 1550–1555 vol.3.
- [89] H. Higo, K. Yamamoto, K. Tanaka, Y. Sakurai and T. Nakada, 'Bondgraph analysis on pressure fluctuation in hydraulic pipes', in *2000 26th Annual Conference of the IEEE Industrial Electronics Society. IECON 2000. 2000 IEEE International Conference on Industrial Electronics, Control and Instrumentation. 21st Century Technologies and Industrial Opportunities (Cat. No.00CH37141)*, Nagoya, Japan: IEEE, 2000, pp. 1556–1561.
- [90] L. Ljung and T. Glad, 'On global identifiability for arbitrary model parametrizations', *Automatica*, no. 2, pp. 265–276, 1994.
- [91] R. Bellman and K. J. Åström, 'On structural identifiability', *Mathematical Biosciences*, no. 3, pp. 329–339, 1970.
- [92] N. Tuncer and T. T. Le, 'Structural and practical identifiability analysis of outbreak models', *Mathematical Biosciences*, pp. 1–18, 2018.
- [93] O.-T. Chis, J. R. Banga and E. Balsa-Canto, 'Structural Identifiability of Systems Biology Models: A Critical Comparison of Methods', *PLOS ONE*, no. 11, e27755, 2011.

- [94] A. Raue, J. Karlsson, M. P. Saccomani, M. Jirstrand and J. Timmer, ‘Comparison of approaches for parameter identifiability analysis of biological systems’, *Bioinformatics*, no. 10, pp. 1440–1448, 2014.
- [95] M. Castro and R. J. de Boer, ‘Testing structural identifiability by a simple scaling method’, *PLOS Computational Biology*, no. 11, e1008248, 2020.
- [96] R. Dong, C. Goodbrake, H. A. Harrington and G. Pogudin, *Differential elimination for dynamical models via projections with applications to structural identifiability*, 2022. arXiv: 2111.00991 [cs, eess, math, q-bio].
- [97] A. F. Villaverde and G. Massonis, ‘On testing structural identifiability by a simple scaling method: Relying on scaling symmetries can be misleading’, *PLOS Computational Biology*, no. 10, e1009032, 2021.
- [98] G. E. Karniadakis, I. G. Kevrekidis, L. Lu, P. Perdikaris, S. Wang and L. Yang, ‘Physics-informed machine learning’, *Nature Reviews Physics*, no. 6, pp. 422–440, 2021.
- [99] J. O. Ramsay, G. Hooker, D. Campbell and J. Cao, ‘Parameter Estimation for Differential Equations: A Generalized Smoothing Approach’, *Journal of the Royal Statistical Society Series B: Statistical Methodology*, no. 5, pp. 741–796, 2007.
- [100] X. Qi and H. Zhao, ‘Asymptotic efficiency and finite-sample properties of the generalized profiling estimation of parameters in ordinary differential equations’, *The Annals of Statistics*, no. 1, 2010.
- [101] W. Bradley and F. Boukouvala, ‘Two-Stage Approach to Parameter Estimation of Differential Equations Using Neural ODEs’, *Industrial & Engineering Chemistry Research*, no. 45, pp. 16 330–16 344, 2021.
- [102] F. Dondelinger, D. Husmeier, S. Rogers and M. Filippone, ‘ODE parameter inference using adaptive gradient matching with Gaussian processes’, in *Proceedings of the Sixteenth International Conference on Artificial Intelligence and Statistics*, PMLR, 2013, pp. 216–228.
- [103] H. Putter, S. H. Heisterkamp, J. M. A. Lange and F. de Wolf, ‘A Bayesian approach to parameter estimation in HIV dynamical models’, *Statistics in Medicine*, no. 15, pp. 2199–2214, 2002.
- [104] M. Raissi, P. Perdikaris and G. E. Karniadakis, ‘Physics-informed neural networks: A deep learning framework for solving forward and inverse problems involving nonlinear partial differential equations’, *Journal of Computational Physics*, pp. 686–707, 2019.
- [105] A. G. Baydin, B. A. Pearlmutter, A. A. Radul and J. M. Siskind, ‘Automatic differentiation in machine learning: A survey’, *Journal of Machine Learning Research*, pp. 1–43, 2018.

- [106] S. S. Haykin and S. S. Haykin, *Neural Networks and Learning Machines*, 3rd ed. New York: Prentice Hall, 2009.
- [107] I. Goodfellow, Y. Bengio and A. Courville, *Deep Learning* (Adaptive Computation and Machine Learning). Cambridge, Massachusetts: The MIT Press, 2016.
- [108] A. D. Jagtap, E. Kharazmi and G. E. Karniadakis, ‘Conservative physics-informed neural networks on discrete domains for conservation laws: Applications to forward and inverse problems’, *Computer Methods in Applied Mechanics and Engineering*, p. 113 028, 2020.
- [109] A. D. Jagtap, E. Kharazmi and G. E. Karniadakis, ‘Conservative physics-informed neural networks on discrete domains for conservation laws: Applications to forward and inverse problems’, *Computer Methods in Applied Mechanics and Engineering*, p. 113 028, 2020.
- [110] A. D. Jagtap and G. E. Karniadakis, ‘Extended physics-informed neural networks (XPINNs): A generalized space-time domain decomposition based deep learning framework for nonlinear partial differential equations’, *Communications in Computational Physics*, pp. 2002–2041, 2020.
- [111] E. Kharazmi, Z. Zhang and G. E. Karniadakis, ‘hp-VPINNs variational physics-informed neural networks with domain decomposition’, *Computer Methods in Applied Mechanics and Engineering*, p. 113 547, 2021.
- [112] X. Meng, Z. Li, D. Zhang and G. E. Karniadakis, ‘PPINN: Parareal physics-informed neural network for time-dependent PDEs’, *Computer Methods in Applied Mechanics and Engineering*, p. 113 250, 2020.
- [113] J. Cho, S. Nam, H. Yang, S.-B. Yun, Y. Hong and E. Park, *Separable PINN: Mitigating the curse of dimensionality in physics-informed neural networks*, 2022. arXiv: 2211.08761 [cs.LG].
- [114] L. McClenny and U. Braga-Neto, *Self-adaptive physics-informed neural networks using a soft attention mechanism*, 2022. arXiv: 2009.04544 [cs.LG].
- [115] I. Depina, S. Jain, S. Mar Valsson and H. Gotovac, ‘Application of physics-informed neural networks to inverse problems in unsaturated groundwater flow’, *Georisk: Assessment and Management of Risk for Engineered Systems and Geohazards*, no. 1, pp. 21–36, 2022.
- [116] K. Nath, X. Meng, D. J. Smith and G. E. Karniadakis, ‘Physics-informed neural networks for predicting gas flow dynamics and unknown parameters in diesel engines’, *arXiv preprint arXiv:2304.13799*, 2023.
- [117] A. D. Jagtap, Z. Mao, N. Adams and G. E. Karniadakis, ‘Physics-informed neural networks for inverse problems in supersonic flows’, *Journal of Computational Physics*, p. 111 402, 2022.

- [118] M. H. Chaudhry, *Applied Hydraulic Transients*. New York, NY: Springer New York, 2014.
- [119] F. M. White, *Fluid Mechanics*, Eighth edition. New York, NY: McGraw-Hill Education, 2016.
- [120] R. W. Fox, P. J. Pritchard and A. T. McDonald, *Fox and McDonald's Introduction to Fluid Mechanics*, 8th ed. Hoboken, NJ : Chichester: John Wiley & Sons, Inc. ; John Wiley [distributor], 2011.
- [121] C. C. Crane Co, Ed., *Flow of Fluids: Through Valves, Fittings and Pipe* (Technical Paper / Crane No. 410), Repr. Stamford, Conn: Crane, 2009.
- [122] R. W. Fox and J. W. Mitchell, *Fox and McDonald's Introduction to Fluid Mechanics*, 10th edition. Hoboken: Wiley, 2019.
- [123] C. Kallesøe, 'Fault detection and isolation in centrifugal pumps', Ph.D. dissertation, Department of Control Engineering, Aalborg University, 2005.
- [124] G. Takács, *Electrical Submersible Pumps Manual: Design, Operations, and Maintenance*, Second edition. Cambridge, MA: Gulf Professional Publishing, 2018.
- [125] J. F. Gülich, *Centrifugal Pumps*. Berlin, Heidelberg: Springer Berlin Heidelberg, 2010.
- [126] M. M. Khonsari and E. R. Booser, *Applied Tribology: Bearing Design and Lubrication*, Third edition. Hoboken, NJ: John Wiley & Sons Inc, 2017.
- [127] B. Jacobson, 'The Stribeck memorial lecture', *Tribology International*, no. 11, pp. 781–789, 2003.
- [128] ISA75.01.01, *Industrial-Process Control Valves. Part 2-1, Flow Capacity– Sizing Equations for Fluid Flow under Installed Conditions*. Research Triangle Park, N.C.: ISA, 2012.
- [129] I. J. Karassik, Ed., *Pump Handbook*, 4th ed. New York: McGraw-Hill, 2008.
- [130] A. J. Prang and P. Cooper, 'Enhanced multiphase flow predictions in twin-screw pumps', 2004.
- [131] G. Vetter, 'Multiphase Pumping With Twin-Screw Pumps - Understand And Model Hydrodynamics And Hydroabrasive Wear', 2000.
- [132] M. Daneker, Z. Zhang, G. E. Karniadakis and L. Lu, *Systems Biology: Identifiability analysis and parameter identification via systems-biology informed neural networks*, 2022. arXiv: 2202.01723 [cs, q-bio].
- [133] F. de Castro Teixeira Carvalho, M. de Melo Freire Figueiredo and A. L. Serpa, 'Flow pattern classification in liquid-gas flows using flow-induced vibration', *Experimental Thermal and Fluid Science*, p. 109 950, 2020.

- [134] Y. Ma, S. Gowda, R. Anantharaman, C. Laughman, V. Shah and C. Rackauckas, *Modelingtoolkit: A composable graph transformation system for equation-based modeling*, 2021. arXiv: 2103.05244 [cs.MS].
- [135] H. Miao, X. Xia, A. S. Perelson and H. Wu, ‘On Identifiability of Nonlinear ODE Models and Applications in Viral Dynamics’, *SIAM Review*, 2011.
- [136] X. Glorot and Y. Bengio, ‘Understanding the difficulty of training deep feedforward neural networks’, in *Proceedings of the Thirteenth International Conference on Artificial Intelligence and Statistics*, JMLR Workshop and Conference Proceedings, 2010, pp. 249–256.
- [137] D. P. Kingma and J. Ba, *Adam: A Method for Stochastic Optimization*, 2017. arXiv: 1412.6980 [cs].
- [138] J. Bradbury *et al.*, *JAX: Composable transformations of Python+NumPy programs*, version 0.3.13, 2018.
- [139] DeepMind *et al.*, *The DeepMind JAX Ecosystem*, 2020.
- [140] D. C. Karnopp, D. L. Margolis and R. C. Rosenberg, *System Dynamics: Modeling, Simulation, and Control of Mechatronic Systems*. Hoboken, NJ, USA: John Wiley & Sons, Inc., 2012.
- [141] J. P. Vítkovský, A. Bergant, A. R. Simpson and M. F. Lambert, ‘Systematic Evaluation of One-Dimensional Unsteady Friction Models in Simple Pipelines’, *Journal of Hydraulic Engineering*, no. 7, pp. 696–708, 2006.
- [142] A. Einstein, ‘Eine neue bestimmung der moleküldimensionen’, *Annalen der Physik*, no. 2, 289 – 306, 1906.
- [143] G. I. Taylor, ‘The viscosity of a fluid containing small drops of another fluid’, *Proceedings of the Royal Society of London. Series A, Containing Papers of a Mathematical and Physical Character*, no. 834, pp. 41–48, 1932.
- [144] R. Pal and E. Rhodes, ‘Viscosity/concentration relationships for emulsions’, *Journal of Rheology*, no. 7, pp. 1021–1045, 1989.
- [145] W. Borutzky, Ed., *Bond Graph Modelling of Engineering Systems: Theory, Applications and Software Support*. New York, NY: Springer New York, 2011.
- [146] B. Bhushan, *Introduction to Tribology* (Tribology Series), Second edition. Chichester, West Sussex, United Kingdom: Wiley, 2013.

Appendix A Bond graphs

The modeling of complex engineering systems often requires a structured, modular approach to capture the intricate interactions between various subsystems. Bond graph theory provides a unified framework, offering a versatile representation that spans multiple physical domains. This section aims to provide a brief yet comprehensive understanding of bond graph theory's foundational principles and notations.

The section commences with exploring multiports, the fundamental building blocks that serve as the nexus for subsystem interconnections (Section A.1). Following this, the section introduces the concept of causal stroke, a notation that is used to distinguish between dependent and independent power variables (Section A.3).

Subsequently, the section delves into the various bond graph elements that encapsulate the behavior of systems across different physical domains (Section A.4). These include energy storage elements like 1-port compliance (C-elements) and 1-port inertia (I-elements), dissipative elements (R-elements), and source elements (Se and Sf). Each element's constitutive relationships and potential modifications by external signals are discussed in detail. The section then introduces reversible transducer elements, which allows the connection of multiports across different physical domains or coordinate systems. Finally, the section culminates with a discussion on junction elements, which connect multiports within a consistent physical domain and coordinate system.

A.1 Multiports

In engineering, systems are often conceptualized as a collection of interconnected subsystems. Each of these subsystems interacts with each other, representing the entire system's behavior. Within the modeling framework, a given subsystem can describe different levels of detail of the larger system. Consider an electrical motor as an example. Its representation as a subsystem can span a broad spectrum: at one end, it might be portrayed in a rudimentary fashion, acting solely as a transducer converting electrical energy into mechanical motion. At a more detailed level, the model may integrate nuances such as winding resistance, inductance, parasitic capacitance, and the complex interplay of magnetic field dynamics and rotation.

The modeler must carefully determine the appropriate level of detail for a model based on its intended application. Valid assumptions must underpin such decisions. While a meticulously detailed model may offer unparalleled accuracy, it often comes at the expense of computational cost, presents challenges in analysis, and may rely on challenging parameters to obtain. Conversely, a more abstract model, although more computationally tractable, may potentially overlook certain

intricacies inherent to the real-world counterpart.

The points where the subsystems interconnect and allow power to flow between them are referred to as *ports*. The physical subsystems possessing one or more such connections are named multiports. These ports are characterized by two real, time-dependent variables: effort (e) and flow (f), whose product represents the instantaneous power (P) flowing through the port. These variables are commonly referred to as power variables or power conjugated. When interconnecting subsystem ports, it is pertinent to note that the variables e and f are not invariably a power conjugate. More generally, they can be described as *dynamically conjugated*. In this context, the power conjugate condition is realized when the product of the *dynamically conjugated* variables equates to power [140, 145].

The general notation of the power flowing through a port ($P_{wr}(t)$) is represented as:

$$P_{wr}(t) = e(t)f(t). \quad (\text{A.1})$$

Therefore, the energy $E(t)$ transmitted through the port is the integral of $P(t)$:

$$E(t) \equiv \int P_{wr}(t)dt = \int e(t)f(t)dt. \quad (\text{A.2})$$

From the power variables (e and f), it is possible to obtain other important quantities for dynamic systems, such as the momentum, $p(t)$, and the displacement, $q(t)$. The momentum is defined as the integral of the effort (e). Hence,

$$p(t) \equiv \int e(t)dt = p_0 + \int_{t_0}^t e(t)dt. \quad (\text{A.3})$$

In the definite integral representation, it is necessary to specify the initial momentum, p_0 , and the reference time, t_0 . Analogously, the displacement is expressed as the integral of the flow variable, $f(t)$. It is given by:

$$q(t) \equiv \int f(t)dt = q_0 + \int_{t_0}^t f(t)dt, \quad (\text{A.4})$$

where q_0 denotes the initial displacement at t_0 . Alternatively, the momentum and displacement expressions can be written in the differential form:

$$\frac{dp(t)}{dt} = e(t), \quad (\text{A.5})$$

$$\frac{dq(t)}{dt} = f(t). \quad (\text{A.6})$$

The relationship between the previously mentioned variables can be represented in a mnemonic device commonly called *tetrahedron of state*, shown in Figure A.1. In the tetrahedron, each of the four variables e , f , p , and q are placed in the vertices of the tetrahedron and the edges

indicate the relationship between them. The terms I , R , and C will be discussed in detail in further sections.

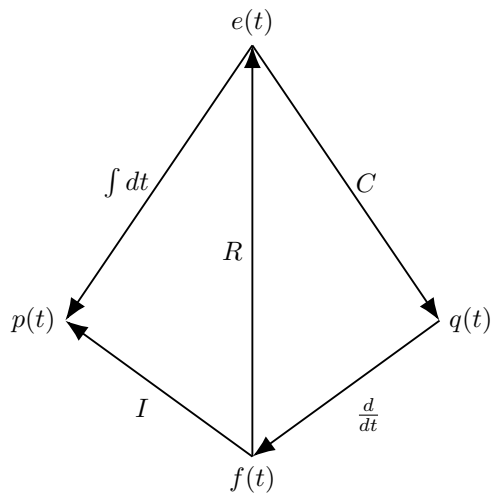


Figure A.1: The tetrahedron of state.

A.2 Ports and bonds

After connecting multiport subsystems through a port, the *dynamically conjugated* variables are simultaneously constrained to be equal for both subsystems. In this condition, the two multiports are said to have a common bond. In the case of power conjugates, the bond is termed as a *power bond*. Correspondingly, the port involved in this connection is denoted as a *power port*. In bond graphs, the power bond is represented by a *half-arrow* as illustrated in Figure A.2.

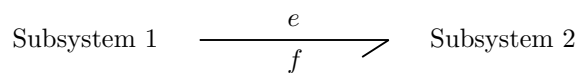


Figure A.2: Representation of a bond graph power bond from subsystem 1 to subsystems 2.

Importantly, the *half arrow* direction determines the assumed power flow direction. For instance, in Figure A.2, we assumed a positive power flow from subsystem 1 to subsystem 2. If the actual power flow or, for a certain period of the system, the power flows from subsystem 2 to subsystem 1; it will present a negative power flow [140, 145].

In addition to the *power bond*, a multiport can also have a *signal* attached to it, referred to as a *signal port*. Signal ports can be categorized into two types: inputs and outputs. A signal serves the purpose of linking an output to an input. The input and output signal can be from another multiport, an effort variable, a flow variable, or a generated signal. When a signal with an inward orientation connects to a multiport, the multiport is described as being modulated, commonly referred to as a *modulated multiport*.

Borutzky [145] states that a multiport fundamentally relates the efforts and flows across its ports. Each power port has a dependent and independent variable that can either be an effort or flow. The relationship between the power variables is called constitutive relations and can be affected by the input signals of the multiport, which act as its independent variable. Furthermore, the output signals of a multiport may come from any of its independent variables.

It is important to observe that the multiports can only connect with a power bond when the associated effort and flow variables belong to the same physical domain and coordinate system. In bond graphs, the connection across the physical domains and coordinate systems occurs through specific ports, a topic that will be elaborated on in subsequent sections. The Tables A.1 to A.4 enumerate various physical domains along with their corresponding power variables. Moreover, they also detail the generalized displacement and momentum variables pertinent to each domain.

Table A.1: Generalized variables for mechanical domain.

Generalized variables	Symbol and Quantity	Unit
Effort (e)	Force (F)	N
Flow (f)	Velocity (v)	m s^{-1}
Momentum (p)	Momentum (p)	N s
Displacement (q)	Displacement (x)	m
Power (P)	$F(t)v(t)$	W
Energy (E)	$\int F(t)v(t)dt$	J

Table A.2: Generalized variables for mechanical rotation domain.

Generalized variables	Symbol and Quantity	Unit
Effort (e)	Torque (τ)	N m
Flow (f)	Angular Velocity (ω)	rad s^{-1}
Momentum (p)	Momentum (p_τ)	N m s
Displacement (q)	Angle (θ)	rad
Power (P)	$\tau(t)\omega(t)$	W
Energy (E)	$\int \tau(t)\omega(t)dt$	J

Table A.3: Generalized variables for hydraulic domain.

Generalized variables	Symbol and Quantity	Unit
Effort (e)	Pressure (P)	Pa
Flow (f)	Volume Flow Rate (Q)	$\text{m}^3 \text{s}^{-1}$
Momentum (p)	Momentum (p_P)	Pa s
Displacement (q)	Volume (V)	m^3
Power (P)	$P(t)Q(t)$	W
Energy (E)	$\int P(t)Q(t)dt$	J

Table A.4: Generalized variables for electrical domain.

Generalized variables	Symbol and Quantity	Unit
Effort (e)	Voltage (V)	V
Flow (f)	Current (I)	A
Momentum (p)	Momentum (p_V)	V s
Displacement (q)	Charge (Q)	C
Power (P)	$V(t)I(t)$	W
Energy (E)	$\int V(t)I(t)dt$	J

A.3 Causal stroke

As previously mentioned in Section A.2, one of the power variables is independent, while the other depends on the constitutive relations and the independent variable. A crucial point to observe is that the power bond, represented by a half-arrow as outlined in Section A.2, does not explicitly differentiate between the dependent and independent variables. The distinction only occurs after a specific decision regarding the direction of either the effort or the flow variable. In bond graph methodology, this direction choice is represented by a small orthogonal line at the end of the half-arrow. The end marked by this orthogonal line denotes the effort direction. Consequently, the multiport nearest to this line receives the effort as an input, and serves the flow variable as an output, as depicted in Figure A.3.

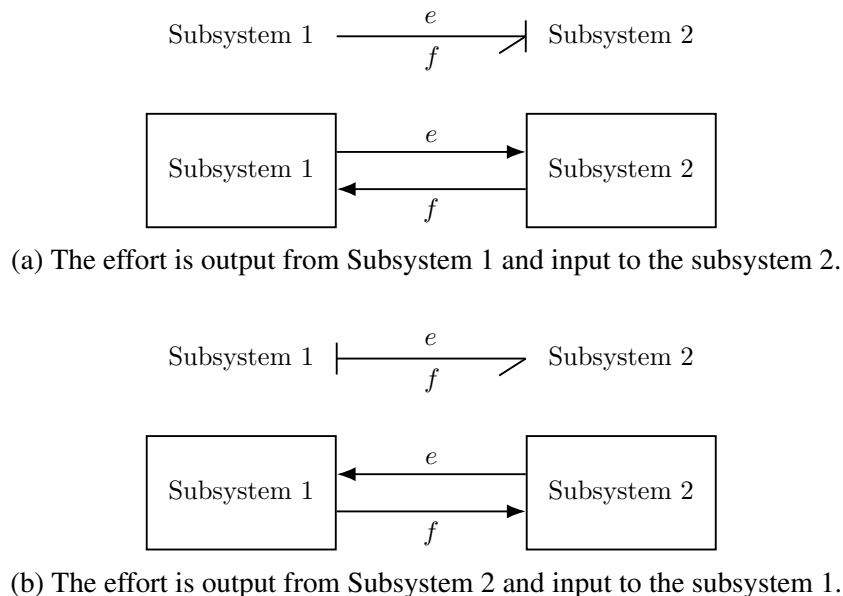


Figure A.3: Interpretation of the causal strokes in relation to the direction of power variables.

A crucial distinction to emphasize is that the half-arrow direction and the causal stroke, represented by the orthogonal line, serve different purposes. While the former defines the signal of the power variables, the latter clarifies which variable is dependent or independent.

A.4 Bond graph elements

In previous sections, the concept of multiport subsystems and the conditions when a power bond is established between two or more multiports was defined. Also, it was defined a visual representation for the power bonds and defined a visual representation to denote which power variable is dependent or independent through the causal stroke. However, it is still required to define a few basic multiport elements that represent the behavior of the systems across different physical domains. In the following sections, these elements are defined based on their behavior.

A.4.1 Energy storage elements

The relationship between power variables, e and f , and the physical quantities of momentum, p , and displacement, q , gives rise to the 1-port energy storage elements. The relationship is illustrated in Figure A.1. For these elements, one of the power variables must undergo either integration or differentiation with respect to time to contribute to the system's dynamics actively.

When the 1-port element associates the power variable with the generalized displacement q , it is termed as a *1-port compliance* or a *C-type port* or simply *C-element*. Conversely, when the power variable is linked with the generalized momentum p , the element is designated as a *1-port inertia* or an *I-type port* or simply *I-element*.

In both C-elements and I-elements, the constitutive relationship between power variables and energy variables (p and q) can be described by linear or non-linear relationships. In general form, for C-elements, we have that $e = \Phi_C(q)$, while for I-elements, we have $f = \Phi_I(p)$. Thus, the energy stored by these elements can be quantified as:

$$E(t) = \int_0^t e(t)f(t) dt + E_0, \quad (\text{A.7})$$

where E_0 represents the energy when $t = 0$. Considering the C-element, and referring to Section A.1, q is defined such that $dq(t) \equiv f(t) dt$. Hence, for C-elements:

$$E(t) = \int_0^t e(t) dq(t) + E_0 \therefore E(q) = \int_{q_0}^q e(q) dq + E_0, \quad (\text{A.8})$$

where q_0 denotes the initial displacement.

The C-element and I-element can be altered by an external signal. When subjected to such modifications, these elements are denoted as MC-element and MI-element for the C-element and I-element, respectively. In the context of the mechanical domain, the C-element characterizes the behavior of a spring. This behavior is represented by a constant for linear springs. Conversely, for non-linear springs, there exists a distinct functional relationship correlating the effort variable with the displacement. Additionally, within the mechanical domain, the I-element signifies the mass or inertia.

A.4.2 Dissipative element

The dissipative elements represent the conversion of power entering the port to thermal energy. It is termed as a *1-port resistor* or an *R-type port* or simply *R-element*. On the other hand, if a signal influences its behavior, this variant is denoted as a *modulated resistor* or an *MR-type port* or simply *MR-element*. While power ports ensure power conservation in interconnected multiport systems, the R-element specifically converts all input power to thermal energy without an explicit thermal port representation. This could be misconceived as energy loss. However, this perspective assumes that the temperature of the “implicit thermal port” remains mostly constant, or its deviations are slow compared to other significant variations [145].

The R-element establishes a relationship between the effort and flow variables, which can be either linear or non-linear. In its generalized form, for R-elements, the relationship is represented as $e = \Phi_R(f)$ or alternatively $f = \Phi_R^{-1}(e)$. In the context of the mechanical domain, the R-element could represent phenomena such as the friction experienced between two juxtaposed sliding surfaces. In scenarios where the relationship is linear, this can be comprehended as a constant, such as the viscous friction consideration. Conversely, it manifests as a more intricate functional relationship in non-linear instances, such as in the Stribeck curve [146].

A.4.3 Source elements

In bond graphs, source elements are characterized by their dependent variable being unaffected by their independent variable. These variables can either be constant (in the linear scenario) or a time-dependent function in modulated sources. As a result, multiport sources can be reduced to an individual 1-port source modulated or not [145, 140]. Effort-based and flow-based sources are denoted by Se and Sf , respectively. When modulated by a signal, they adopt the notations MSe and MSf .

Conceptually, these source elements represent power supplies. Considering the bond graph’s power sign convention, power is transferred from the source to the system when the product of effort, $e(t)$, and flow, $f(t)$, is positive. Though source elements can consistently maintain effort or flow, either as a constant or a time function, irrespective of the source’s power dynamics, real-world devices might not strictly adhere to these model idealizations. Accurate modeling of such devices might necessitate a combination of both source types along with other bond graph elements [145, 140].

A.4.4 Reversible transducer elements

In Section A.1, it was mentioned that the multiports could only be connected when the power variables belong to the same physical domain and same coordinate system, despite the connection through a power bond, whose product of the power variable has the same units. When connecting the different physical domains or coordinate systems, it is necessary to establish the constitutive

relationship between them while keeping the power across them constant [145]. This is achieved by considering a 2-*port* element (TP) with the following sign convention:

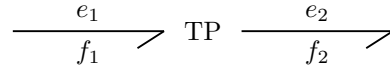


Figure A.4: 2-port element sign convention.

The 2-port element illustrated in Figure A.4 can be expressed mathematically as function of time by:

$$P_{wr,1}(t) = P_{wr,2}(t) \implies e_1(t)f_1(t) = e_2(t)f_2(t). \quad (\text{A.9})$$

It essentially states that the product of the power variables at 1 is consistently equal to the product of the power variables at 2 for any given time t . From this relationship, we can introduce a non-zero constant α_r . By multiplying both sides of Equation (A.9) by α_r , we obtain:

$$\alpha_r e_1(t)f_1(t) = \alpha_r e_2(t)f_2(t). \quad (\text{A.10})$$

Rearranging Equation (A.10), we can express it as:

$$e_1(t)\alpha_r f_1(t) = \alpha_r e_2(t)f_2(t). \quad (\text{A.11})$$

From which, we deduce:

$$e_1(t) = \alpha_r e_2(t), \quad (\text{A.12a})$$

$$\alpha_r f_1(t) = f_2(t). \quad (\text{A.12b})$$

The relationship given by Equations (A.12a) and (A.12b) is a multiport called transformer denoted by TF . When modulated by a signal, it adopts the notation MTF . Alternatively, by rearranging the terms differently, we infer:

$$e_1(t)\alpha_r f_1(t) = e_2(t)\alpha_r f_2(t). \quad (\text{A.13})$$

Leading to the following relationships:

$$e_1(t) = \alpha_r f_2(t), \quad (\text{A.14a})$$

$$\alpha_r f_1(t) = e_2(t). \quad (\text{A.14b})$$

The relationship given by Equations (A.14a) and (A.14b) is a multiport called gyrator denoted by GY . When modulated by a signal, it adopts the notation MGY .

A.4.5 Junction elements

Junction elements serve to interconnect multiports, integrating them into subsystem or system models within a consistent physical domain and coordinate system. As mentioned by Karnopp *et al.* [140], these elements represent one of the most fundamental principles of the bond graph formalism. Importantly, junction elements neither dissipate nor store power; rather, they strictly follow the power sign convention as denoted by the half-arrow symbol. Given this, for n -connected multiports, we can express the power relationship as:

$$\sum_{i=1}^n \epsilon_i P_{\text{wr},i}(t) = 0 \quad \forall \epsilon_i \in \{-1, +1\}, \quad (\text{A.15})$$

where ϵ_i denotes the sign of the power (P_i), determined by the orientation of the half-arrow. Expanding based on Equation (A.15), we can represent the relationship in terms of the individual power variables as:

$$\sum_{i=1}^n \epsilon_i e_i(t) f_i(t) = 0 \quad \forall \epsilon_i \in \{-1, +1\}. \quad (\text{A.16})$$

From Equation (A.16), we deduce:

$$\sum_{i=1}^n \epsilon_i f_i(t) = 0 \quad \forall \epsilon_i \in \{-1, +1\}, \quad (\text{A.17a})$$

$$e_i = e_j \quad \forall i \neq j. \quad (\text{A.17b})$$

This set of relationships is termed as *0-junction* or zero-junction, symbolized by 0 . Alternatively, reinterpreting Equation (A.16), we can express:

$$\sum_{i=1}^n \epsilon_i e_i(t) = 0 \quad \forall \epsilon_i \in \{-1, +1\}, \quad (\text{A.18a})$$

$$f_i = f_j \quad \forall i \neq j. \quad (\text{A.18b})$$

This alternative representation is known as *1-junction* or one-junction, denoted by 1 .

Appendix B Experimental setup

B.1 Fluid characterization

The viscosity of the oils used in the ESP P100L and P47 were measured using a HAAKE MARS III rotational rheometer. These measurements were taken across a temperature range of 10 °C to 60 °C, with incremental steps of approximately 0.5 °C for both oils. For each temperature point, the oils' viscosities were determined three times. The results are graphically represented in Figure B.1, where the viscosity is plotted against temperature.

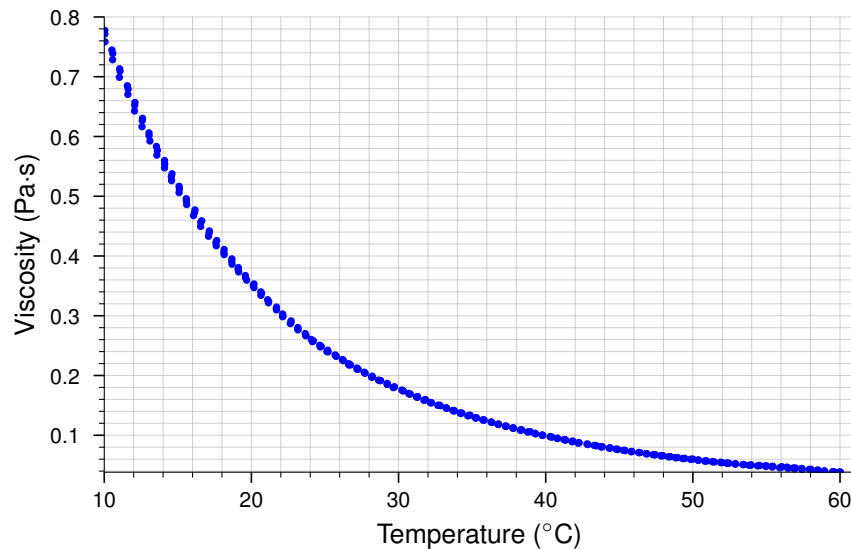


Figure B.1: Oil viscosity plotted against temperature, ranging from 10 °C to 60 °C for the system with the ESP P100L.

A fourth-order polynomial was fitted to the dataset using the least squares method to characterize the relationship between viscosity and temperature. This relationship is described by Equation (B.1) for the ESP system with P100L and Equation (B.2) for the ESP system with the P47.

$$\mu(T) = \frac{0.000\,264\,4T^4 - 0.048\,64T^3 + 3.436T^2 - 114.3T + 1610}{1000} \quad (\text{B.1})$$

$$\mu(T) = \frac{0.000\,109\,6T^4 - 0.020\,16T^3 + 1.422T^2 - 47.24T + 669.2}{1000} \quad (\text{B.2})$$

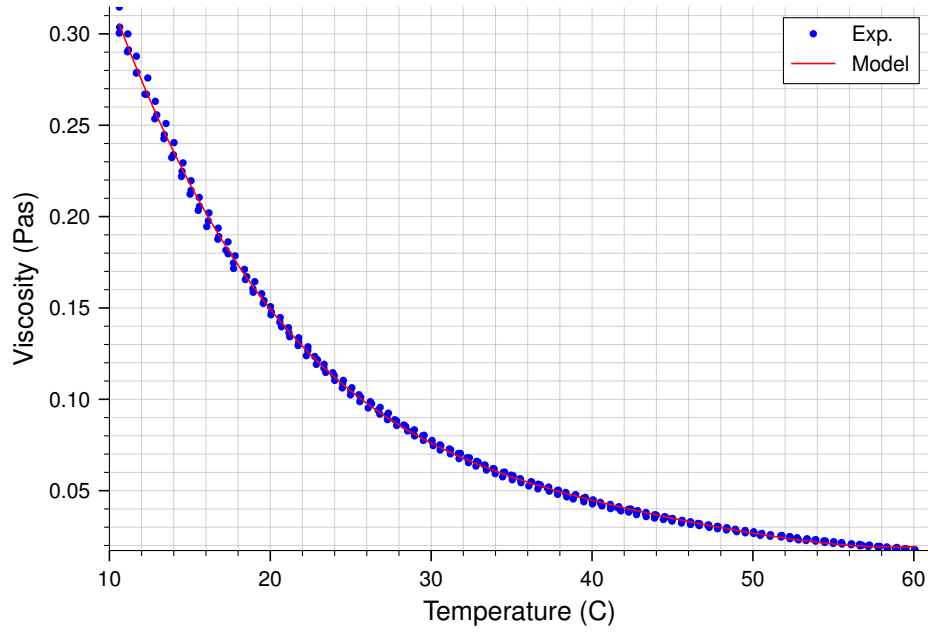


Figure B.2: Oil viscosity plotted against temperature, ranging from 10 °C to 60 °C for the system with the ESP P47.

Appendix C ESP system parameter estimation

For estimating the system parameters for both pumps, it was followed the procedure described in Section 4.7.1 on the Equations (5.8a) to (5.8d), the performance of the parameters obtained for each of these equations are shown in Appendices C.1 to C.4. The steady-state experimental data employed was obtained from the test matrix described in Section 4.1.6. The geometrical attributes, such as the pipeline diameter, length, and cross-sectional area, were directly obtained from the experimental setup.

It is important to mention that, in cases where parameters were adjusted in the context of two-phase flows, the viscosity was estimated using the effective viscosity model proposed by Brinkman [69]. The rationale and assumptions for employing this model are elaborated in Section 5.5.

C.1 ESP pump parameters

To obtain the parameters for the ESP pumps P100L and P47, the intake pressure (PT-102) and discharge pressure (PT-103) were measured. The viscosity was estimated based on the average temperature between the pump intake (TT-101) and discharge (TT-102). In the steady-state condition, the ESP volumetric flow rate (Q_p) is equivalent to the upstream volumetric flow rate measured by FT-101 (Q_1). The ESP shaft angular velocity ω is also directly measured by TE-101.

The model fitting procedure was described in Section 4.7.1. The values of these parameters are provided in rows 1, 2, 3 and 4 of Table 5.1. The regression plots in Figures C.1 and C.2 compare the measured and estimated values of pressure gain (ΔP) for pumps P100L and P47, respectively. An identity line ($y = x$) serves as the reference for ideal model predictions. Two additional lines, representing error bounds ($y = x \pm \epsilon$), are included, with $\epsilon = 4 \times 10^4$ Pa. Upon analysis, 95 % of the measured data points exhibited an absolute error below 2.25×10^4 Pa for P100L and 3.53×10^4 Pa for P47. Furthermore, the coefficients of determination (R^2) for the P100L and P47 pumps are 0.9981 and 0.9987, respectively, indicating a high degree of accuracy in the model predictions.

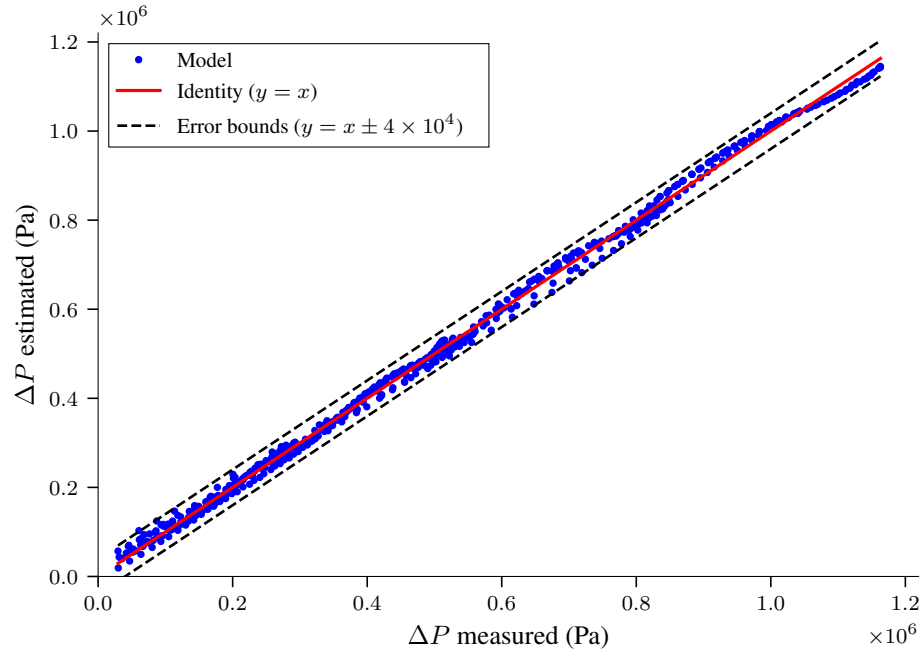


Figure C.1: Regression plot comparing measured and estimated values of pressure gain, ΔP , for the ESP system with the P100L.

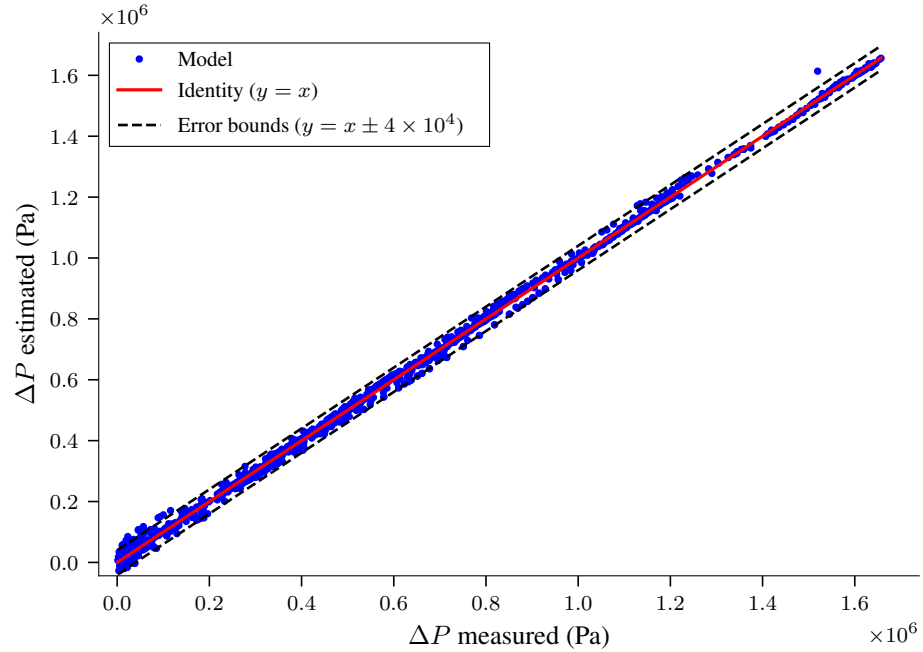


Figure C.2: Regression plot comparing measured and estimated values of pressure gain, ΔP , for the ESP system with the P47.

C.2 ESP shaft parameters

To obtain the shaft torque parameters for the ESP pumps P100L and P47, the shaft torque ($\tau(t)$) was directly measured with TTQ-101. Additionally, the ESP shaft angular velocity ω is

directly measured by TE-101 as part of the experimental assembly. The viscosity was determined by calculating the average temperature from the pump intake (TT-101) to the discharge (TT-102). When in a steady state, the ESP volumetric flow rate (Q_p) is equivalent to the upstream volumetric flow rate measured by FT-101 (Q_1).

The procedure for fitting the model was described in Section 4.7.1. The values of these torque-related parameters are presented in rows 5, 6, 7, 8 and 9 of Table 5.1. The Figures C.3 and C.4 display regression plots comparing the measured and estimated values of shaft torque (τ) for the P100L and P47 pumps, respectively. An identity line ($y = x$) is included to serve as the reference for ideal model predictions. Two additional lines are included. They represent the error bounds ($y = x \pm \epsilon$) of $\epsilon = 3.5 \text{ N m}$. Upon analysis, 95% of the measured data points exhibited an absolute error below 1.858 N m for P100L and 1.5 N m . The coefficient of determination (R^2) for the P100L and P47 pumps are 0.9957 and 0.9965, respectively, attesting to the model's reasonable accuracy.

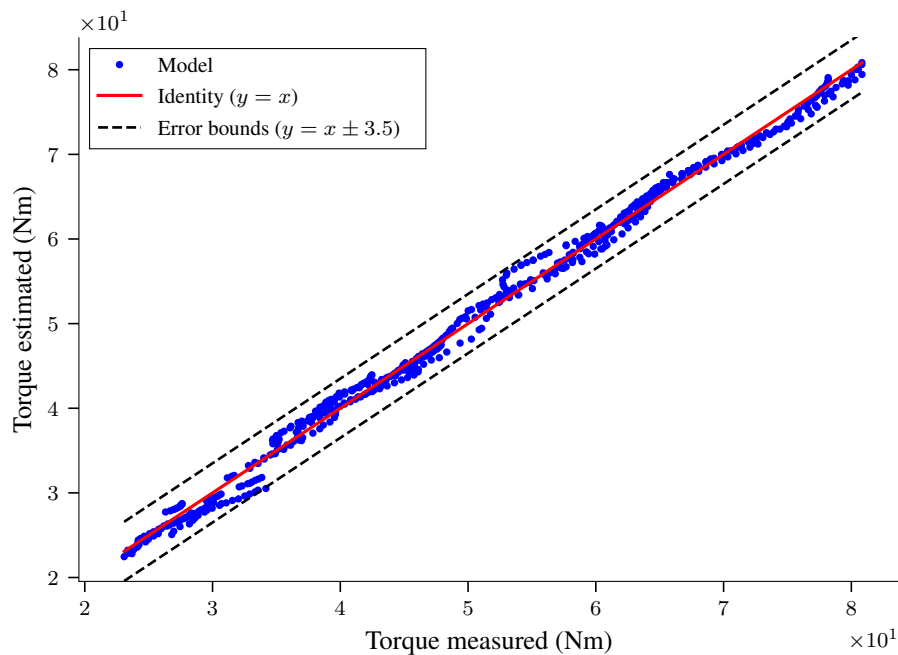


Figure C.3: Regression plot comparing measured and estimated values of shaft torque for the ESP system with the P100L.

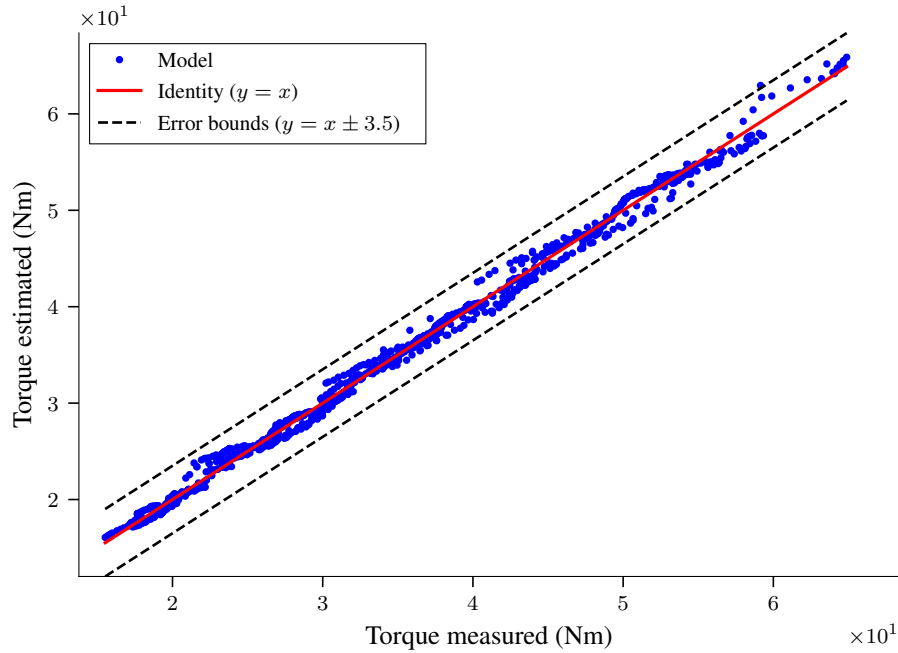


Figure C.4: Regression plot comparing measured and estimated values of shaft torque for the ESP system with the P47.

C.3 Upstream pipeline parameters

As outlined in Section 4.1.1, the experimental setup was modified following the replacement of the ESP pump from model P100L to P47. A notable alteration was the integration of a pressure measurement device at the entrance of the heat exchanger. This difference resulted in a distinct approach adopted for the P100L and P47 pump models. The approaches are detailed in Appendices C.3.1 and C.3.2, respectively.

C.3.1 ESP system with P100L

The experimental setup for the P100L permits only the pressure measurement at the ESP intake (P_1) via sensor PT-102. Consequently, individual pressure gain due to the twin-screw pump remains undetermined. To approximate both the upstream pipeline pressure drop from the tank to the ESP intake and the twin-screw pump's pressure gain, a methodology similar to Appendix C.4 is employed. The pipeline upstream local losses are encapsulated into a single constant that includes valve and pipeline fittings, while the static pressure due to gravity is initially considered as $h_u = 0.5$ m.

Given $P_{in} = 0$ Pa due to the tank being open to the atmosphere and measured pressure P_1 from PT-102, constants k_{bd} , k_{bl} , and k_u can be estimated through rearrangement of Equation (5.8c), under the assumption of a steady-state condition. By incorporating the static pressure

term, the resulting equation is formulated as:

$$P_1 + f_f(Q_1, \mu, L_u, d_u) = (k_{bd}\omega_t - Q_1)k_{bl}\mu - \frac{k_u\rho Q_1^2}{2A_u^2} + \rho gh_u. \quad (\text{C.1})$$

The term $f_f(Q_1, \mu, L_u, d_u)$ is readily estimated using models described in Section 3.3, leaving the right-hand side terms of Equation (C.1) dependent on constants to be estimated.

Due to constraints in temperature control within the experimental setup, a heat exchanger bypass valve is employed for fine temperature regulation (Figure 4.1). It necessitated individually distinguishing the equivalent resistance of the upstream pipeline and twin-screw pump parameters. Such differentiation was feasible due to additional steady-state tests within the dynamic test matrix (Table 4.7).

The model fitting procedures follow the methodology delineated in Section 4.7.1. Regression plots comparing the estimated and measured values of P_1 are displayed in Figures C.5 and C.6. An identity line (red line) and error bounds (dashed black lines) are also presented for reference. Upon analysis, 95 % of the considered data points exhibited an absolute error 1.320×10^4 Pa and 1.000×10^4 Pa for the first and second experimental dynamic investigation, respectively. The coefficient of determination (R^2) were 0.9912 and 0.9975 for the first and second experimental dynamic investigation, respectively. These metrics indicate a satisfactory model performance.

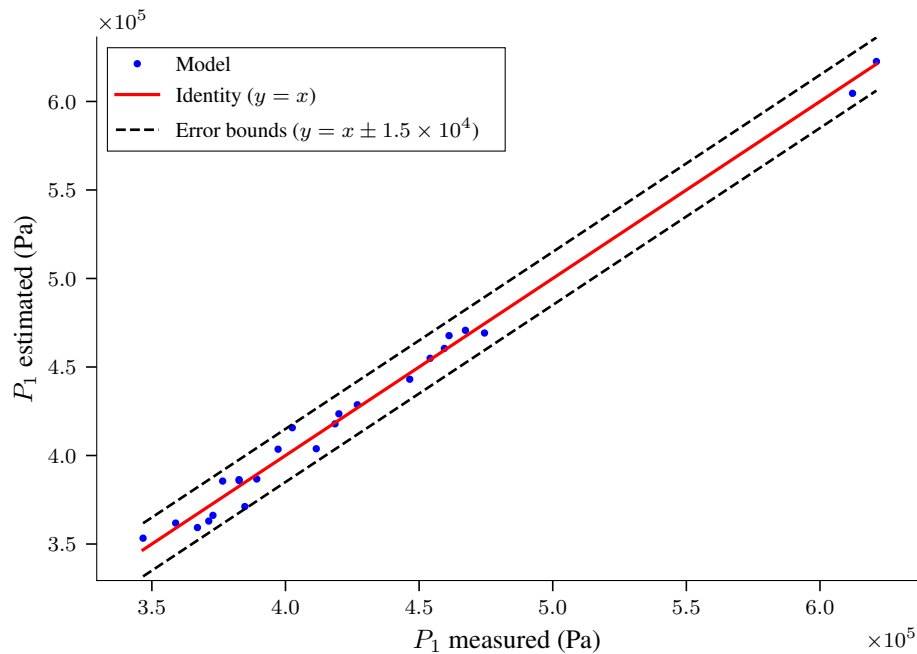


Figure C.5: Regression plot comparing estimated and measured values of P_1 for the first experimental dynamic investigation.

In the second dynamic experimental investigation, challenges emerged in parameter estimation. A negative value for equivalent resistance (k_u) was initially obtained, which would mean that a resistance element is instead a source element. This behavior is physically implausible.

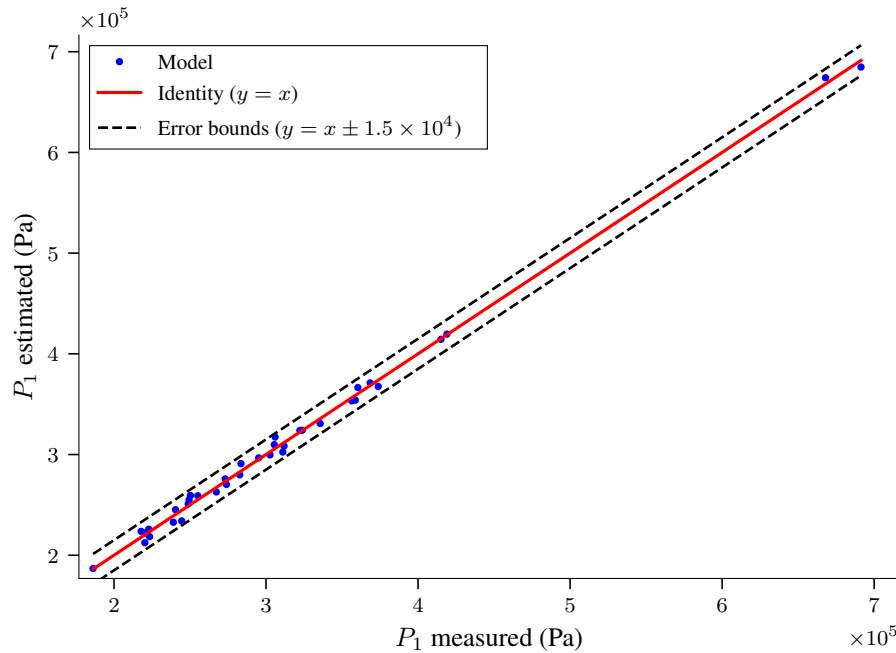


Figure C.6: Regression plot comparing estimated and measured values of P_1 for the second experimental dynamic investigation.

Attempts to bound the k_u value through constrained least squares fitting led to diminished model performance in absolute error and R^2 values. Also, it resulted in values of approximately zero for k_u . Consequently, a fit that included the static pressure yielded reasonable performance, as shown in Figure C.6, but yielded surprisingly high h_u and k_u values, 4.392×10^2 m and 6.566×10^2 respectively. While the model fit remains reasonable within the property range used and is suitable for evaluating the system dynamics, extrapolation should be approached cautiously. The high h_u and k_u values indicate potential model overfit, rendering estimations beyond the property range unreliable.

Lastly, the upstream equivalent resistance k_u in Table 5.3 also accounts for losses associated with manual tuning, elaborated further in Section 5.5.

C.3.2 ESP system with P47

Incorporating the pressure sensor PT-101 at the heat exchanger's entrance refines the experimental setup for the P47 pump. This setup enables the estimation of pressure gain attributable to the twin-screw pump and the pressure losses extending from the heat exchanger to the ESP's entrance (P_1) separately. Therefore, the addition of PT-101 allows for a different approach when estimating the parameter. Additionally, during the experimental procedure for the P47 the heat exchanger bypass valve were remained closed to prevent the issues observed in Appendix C.3.1.

For the parameter fitting, the upstream pipeline was divided into two distinct segments: the first extending from the tank to the heat exchanger's entrance and the second spanning from the heat exchanger to the entrance of the ESP's pump. For the first segment, assumptions similar to

those for the tank were applied, as outlined in Appendix C.3.1. Consequently, Equation (C.1) was slightly modified to:

$$P_0 + f_f(Q_1, \mu, L_u, d_u) = \underbrace{(k_{bd}\omega_t - Q_1)k_{bl}\mu}_{\text{Twin-screw pump}} - \frac{k_u\rho Q_1^2}{2A_u^2} + \rho gh_u, \quad (\text{C.2})$$

where P_0 represents the pressure readings from sensor PT-101. For the segment from the heat exchanger entrance to the ESP's pump entrance, Equation (C.2) was adapted to:

$$P_0 - P_1 - f_f(Q_1, \mu, L_u, d_u) = \frac{k_u\rho Q_1^2}{2A_u^2} - \rho gh_u. \quad (\text{C.3})$$

The model fitting procedures were conducted following the methodology outlined in Section 4.7.1. Regression plots, which compare the estimated and measured values of P_0 and P_1 , are presented in Figure C.7 and Figure C.8. These plots include an identity line (in red) and error bounds (as dashed black lines) for visual reference.

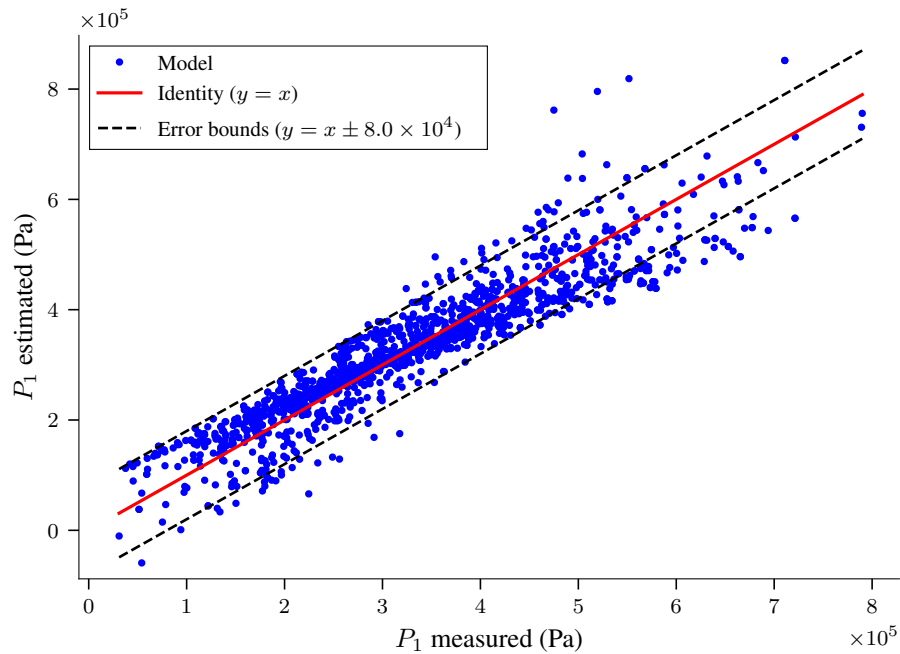


Figure C.7: Regression plot comparing estimated and measured values of P_0 for the twin-screw pump segment.

Analysis revealed that 95% of the data points had an absolute error within 1.03×10^5 Pa for the twin-screw pump segment and 7.302×10^3 Pa for the segment from the heat exchanger to the ESP pump entrance. The coefficient of determination (R^2) values were 0.8369 for the twin-screw pump segment and 0.9960 for the segment from the heat exchanger to the ESP pump entrance, respectively. These metrics indicate a satisfactory model performance, particularly for the heat exchanger to ESP pump entrance segment. However, for the twin-screw pump need some discussion.

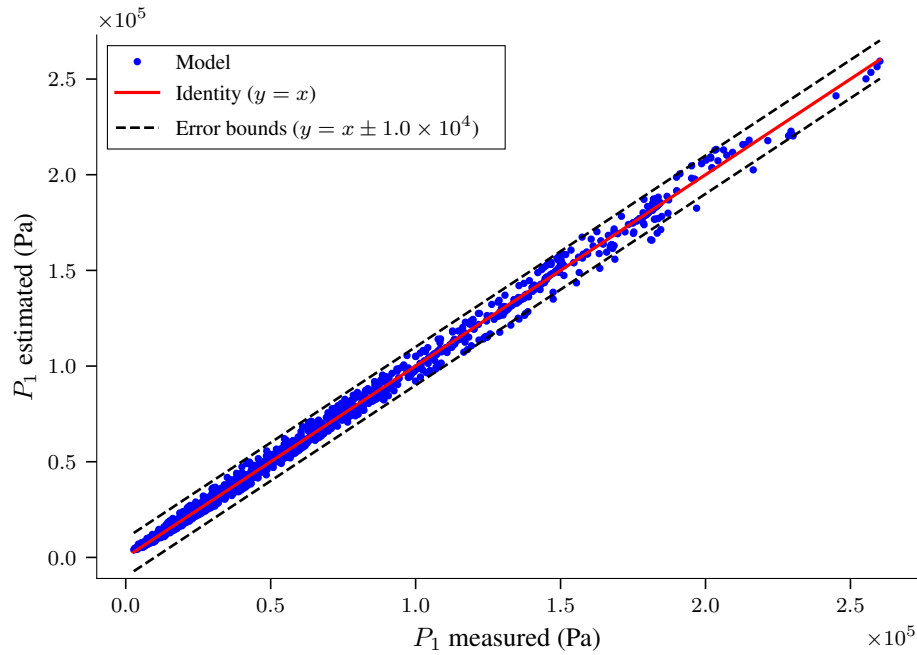


Figure C.8: Regression plot comparing estimated and measured values of P_1 for the heat exchanger to ESP pump entrance segment.

Challenges in parameter estimation were encountered in the twin-screw pump segment. As illustrated in Figure C.7, there is notable dispersion in the measurements of P_0 (PT-101), as indicated by the low R^2 value and substantial percentage errors, depicted in Figure C.9. This figure presents a histogram of the absolute percentage error in the P_0 estimations, revealing that approximately 85% of the data points exhibit errors up to 25%. The errors and dispersion suggests limitations in the twin-screw model's ability to fully capture the phenomena associated with the twin-screw pump. This is further evidenced by the estimated values of h_u and k_u , 1.773×10^1 m and 4.663×10^1 respectively, which are notably high and unrealistic. Nonetheless, this model is still useful in depicting the general behavior of the twin-screw pump. While these inaccuracies in the twin-screw pump model may lead to overestimation of the ESP's intake and discharge pressures, they are unlikely to significantly impact the system's overall dynamics. In practical applications, the twin-screw pump model would be substituted with a more realistic well model.

Similarly to the Appendix C.3.1 the upstream equivalent resistance k_u in Table 5.3 also accounts for losses associated with manual tuning, elaborated further in Section 5.5.

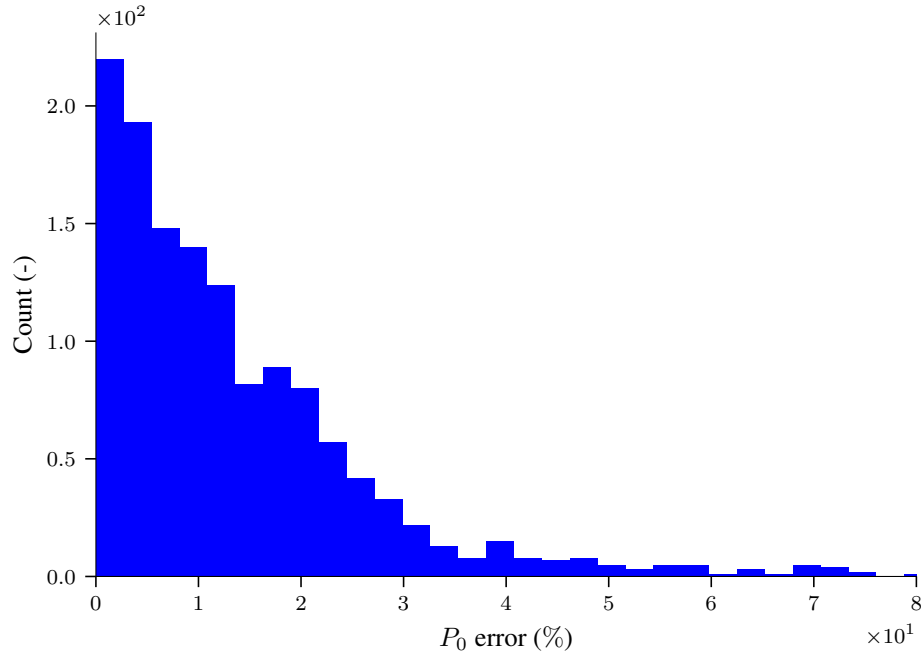


Figure C.9: Histogram of absolute percentage errors in P_0 for the twin-screw pump model.

C.4 Downstream pipeline parameters

As elaborated in Section 3.3, calculating pressure loss due to viscous friction is straightforward. However, taking into account the local losses associated with valves and fittings requires some attention. Although coefficients for these exist, they are predominantly derived for turbulent flows in Newtonian fluids, limiting their applicability for systems involving emulsions as detailed in ISA75.01.01 [128] and Sections 3.6 and 4.3.

Given these limitations and in line with the discussed in Section 3.3, where the literature recommendation is to utilize experimental data when possible, the valve flow coefficient C_v was obtained experimentally. Then, to estimate the downstream pressure loss, an equivalent C_v was calculated as a function of the valve aperture a by rearranging Equation (4.8). This yields:

$$C_v = \frac{Q}{\sqrt{\frac{\Delta P_v}{\rho^*}}}. \quad (\text{C.4})$$

The function $C_v(a)$ is defined on the closed interval $[0, 1]$, mapping to the real numbers as $C_v : [0, 1] \rightarrow \mathbb{R}$. This function characterizes the range of aperture values the valve can assume. Within this interval, the valve subsystem, discussed in Section 3.6, exhibits neither discontinuities nor abrupt changes, making it a continuous function. Additionally, $C_v(a)$ is bounded within this interval, reaching its minimum and maximum values at $a = 0$ and $a = 1$, respectively. Given its continuous and bounded nature, $C_v(a)$ can be accurately approximated by a polynomial function over the interval $[0, 1]$. To find the best-fitting polynomial, the Bayesian Information Criterion

(BIC) was utilized for model selection. The BIC is defined as:

$$\text{BIC} = n_v \ln \left(\frac{1}{n_v} \sum_{i=1}^{n_v} \left(C_v^i - \hat{C}_v^i \right)^2 \right) + \kappa_v \ln(n_v), \quad (\text{C.5})$$

where n_v is the number of samples, κ_v is the number of coefficients in the polynomial, C_v^i and \hat{C}_v^i are the i -th calculated and estimated values of C_v , respectively. The procedure for fitting the polynomials was described in Section 4.7.1.

As detailed in Section 4.1.1, the experimental setup underwent modifications subsequent to the replacement of the ESP pump, transitioning from model P100L to P47. A notable change involved the direct measurement of valve pressure drop. This adjustment directly quantified valve pressure loss in the P47 scenario and separately from the pipeline contributions. Consequently, this led to a slightly divergent approach in handling the ESP systems for the P100L and P47 pumps, as elaborated in Appendices C.4.1 and C.4.2.

In both instances, initial efforts to model the entire dataset with a polynomial approach were unsuccessful. Nonetheless, as discussed in Section 4.3, the relevance of experimentally obtained C_v values may be confined to specific viscosity and density conditions. Therefore, the valve's C_v curve was fitted specifically to its corresponding viscosity range for each scenario.

C.4.1 ESP system with P100L

In the setup involving the P100L model of the ESP, the experimental assembly was limited to measuring the discharge pressure at PT-103. This constraint prevented the measurement of the pressure drop across the valve individually. Consequently, the pressure drop across the valve and pipe fittings was aggregated into a single term. This term also encompasses the static pressure attributable to gravity. Therefore, in Equation (C.4), $\Delta P_v = P_2 - Q_2 R_f^d$ represents a combination of the pressure measured by PT-103 (P_2) and the viscous friction-related pressure loss, expressed using bond graph notation ($Q_2 R_f^d$).

The polynomial that minimized the BIC was of sixth degree, yielding:

$$C_v(a) = 86.36a^6 + -228.7a^5 + 200.3a^4 + -66.64a^3 + 12.07a^2 + 0.9966a + 0.1194 \quad (\text{C.6})$$

The fit is shown in Figure C.10. Additionally, Figure C.11 compares the calculated and estimated C_v values. An identity line and error bounds are included, where the error considered was of $\epsilon = 0.15$. Upon analysis, 95% of the data points presented an absolute error below 0.06530. The coefficient of determination R^2 was 0.9980, indicating a reasonable accuracy.

Furthermore, the polynomial fit, presented in Figures C.10 and C.11, for C_v was restricted to experimental points with a viscosity range of $0.1 \mu < 0.3 \text{ Pa}\cdot\text{s}$. It is pertinent to note that the dynamic experiments for the P100L, shown in Table 4.7, are in the range of viscosity considered.

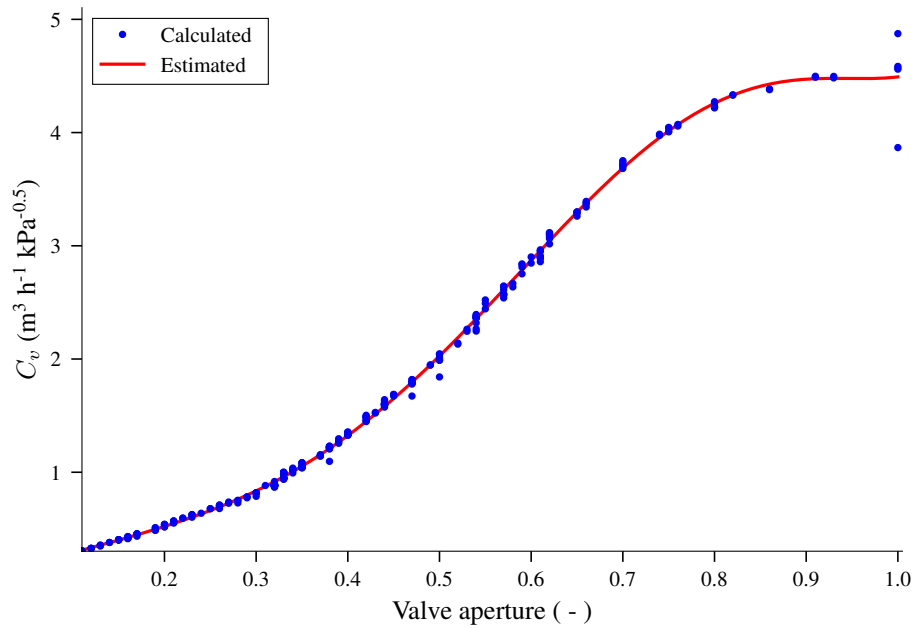


Figure C.10: Valve C_v as a function of the valve aperture a .

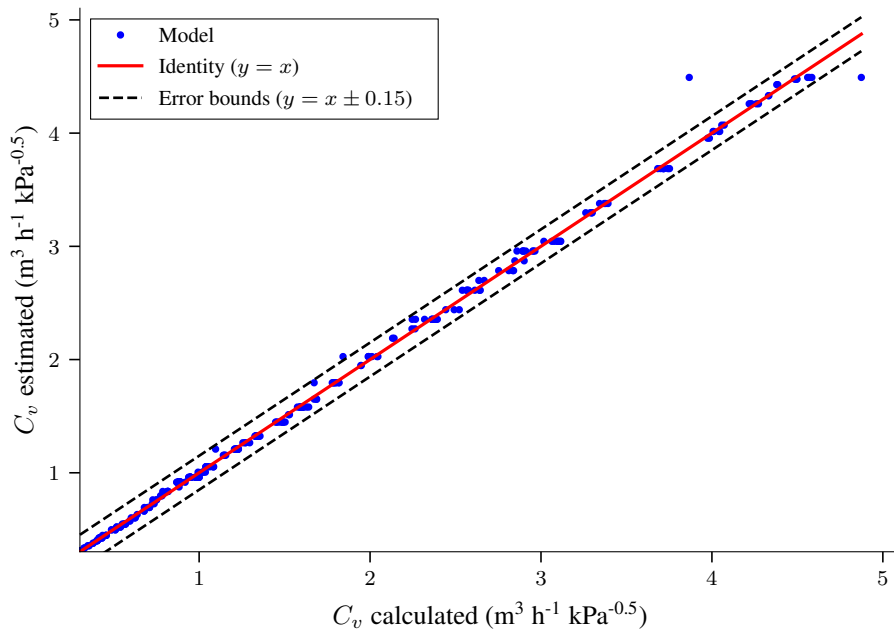


Figure C.11: Regression plot comparing calculated and estimated values of the valve C_v .

C.4.2 ESP System with P47

In the configuration featuring the P47 model of the ESP, the experimental setup was enhanced to enable the direct measurement of individual valve pressure loss. This capability facilitated the independent adjustment of valve pressure, followed by the adjustment of downstream pipeline parameters delineated in Equation (5.8d).

Considering $P_{out} = 0$ Pa, due to the tank's exposure to atmospheric pressure, and the mea-

sured pressure P_9 from PT-103, the constant k_{kd} can be deduced by rearranging Equation (5.8d), assuming steady-state conditions. By incorporating the static pressure term, the resulting equation is formulated as:

$$P_2 - \underbrace{\frac{\rho Q_2^2}{C_v(a)^2 \rho^*} - f_f(Q_2, \mu, L_d, d_d)}_{\text{Remaining losses } (P_r)} = \frac{k_d \rho Q_2^2}{2A_d^2} + \rho g h_d. \quad (\text{C.7})$$

The term $f_f(Q_1, \mu, L_u, d_u)$ is readily estimated using models described in Section 3.3, leaving the right-hand side terms of Equation (C.7) dependent on constants to be estimated.

Firstly, the valve's C_v value was fitted with a polynomial that minimized BIC. This optimization resulted in a fifth-degree polynomial, expressed as:

$$C_v(a) = -32.27a^5 + 31.29a^4 + 18.55a^3 + -12.66a^2 + 4.716a + -0.06075. \quad (\text{C.8})$$

The fit is demonstrated in Figure C.12. Furthermore, Figure C.13 compares the calculated and estimated C_v values, incorporating an identity line and error bounds with an error margin of $\epsilon = 0.15$. Analysis revealed that approximately 95% of the data points had an absolute error below 0.221. The coefficient of determination, R^2 , was calculated as 0.9978, indicating a reasonable accuracy.

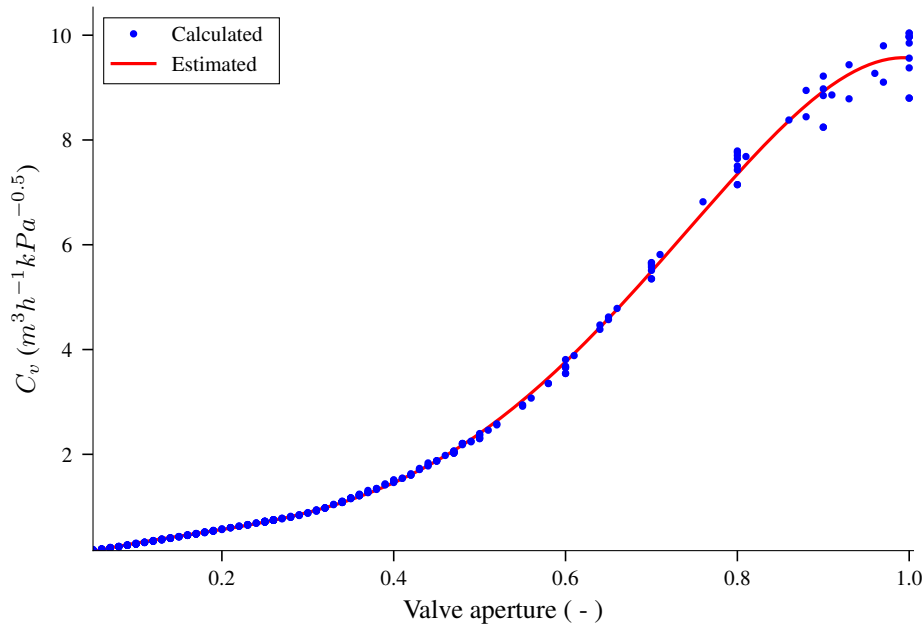


Figure C.12: Valve C_v as a function of valve aperture a .

Moreover, the polynomial fitting of C_v , as depicted in Figures C.10 and C.11, was confined to experimental data within a viscosity range of $0.04 \mu < 0.09 \text{ Pa}\cdot\text{s}$. This range encompasses the dynamic experiments for the P47 model, as detailed in Table 4.7.

Subsequently, the pipeline parameters delineated in Equation (C.7) were fitted using the

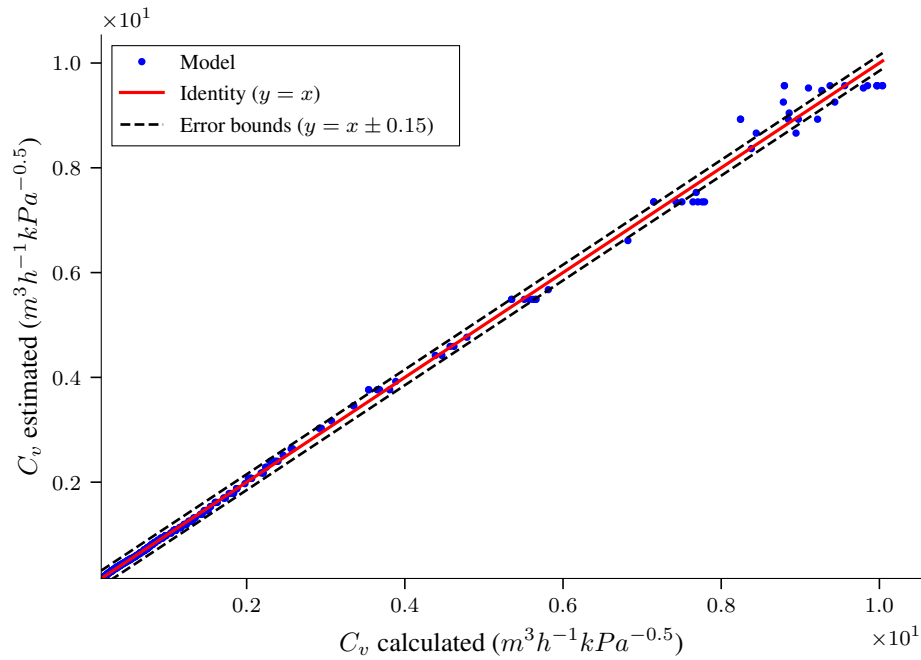


Figure C.13: Regression plot comparing calculated and estimated values of valve C_v .

methodology outlined in Section 4.7.1. The Figure C.14 presents the regression plot, comparing the estimated and measured values of the remaining pressure (P_r), as defined in Equation (C.7). The plot features an identity line (red line) and error bounds (dashed black lines) for reference. Analysis revealed that approximately 95% of the data points had an absolute error of 7949.838 400 509 748 Pa. The coefficient of determination (R^2) was calculated as -3.674 , suggesting that the model does not accurately represent the remaining pressure. However, it is important to note that the magnitude of these errors is relatively small compared to the pump's discharge pressure, with most points exhibiting an error below 1%. In the downstream pipeline, the valve predominantly contributes to the pressure drop, and the impact of this inaccurate model is limited due to the magnitude of the pressure.

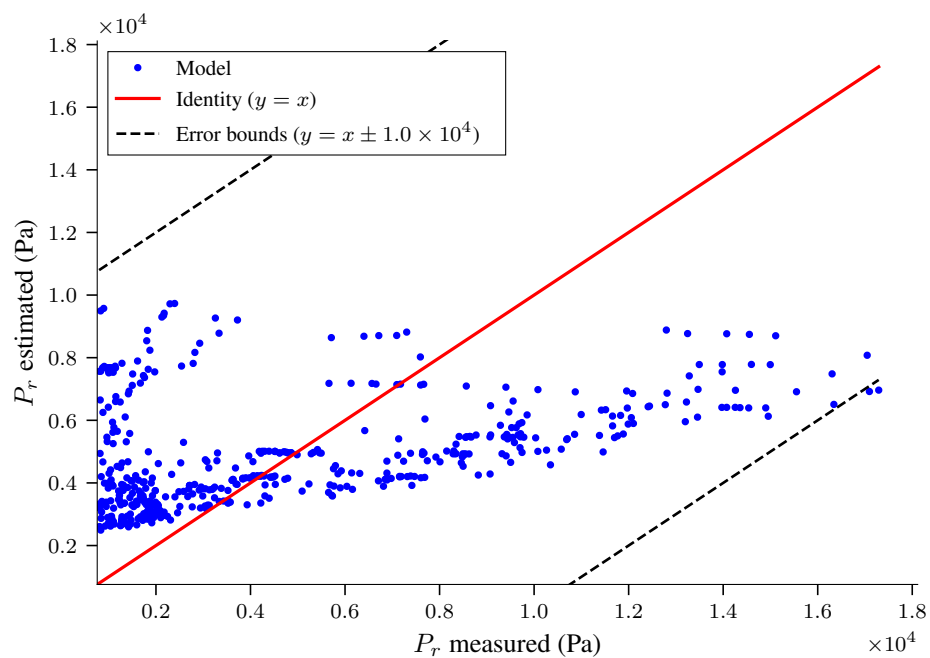


Figure C.14: Regression plot comparing estimated and measured values of P_r .

Appendix D Additional PINN results

Across all cases, the training dataset comprises 30 data points and by 100 collocation points.

D.1 State estimation results

Table D.1: Mean absolute percentage error for the simulation case.

	P_1	P_2	Q_1	Q_2	Q_p	ω
Case 1	0.136 %	0.007 %	0.002 %	0.004 %	0.004 %	0.017 %
Case 2	0.103 %	0.007 %	0.012 %	0.011 %	0.011 %	0.039 %
Case 3	0.303 %	0.007 %	0.070 %	0.093 %	0.090 %	2.083 %

Table D.2: Mean absolute percentage error for the simulation with added noise case.

	P_1	P_2	Q_1	Q_2	Q_p	ω
Case 1	0.256 %	0.123 %	0.013 %	0.014 %	0.015 %	0.024 %
Case 2	0.275 %	0.118 %	0.019 %	0.025 %	0.023 %	0.102 %
Case 3	0.344 %	0.120 %	0.019 %	0.018 %	0.020 %	0.959 %

Table D.3: Mean absolute percentage error for the experimental case.

	P_1	P_2	Q_1	ω
Case 1	7.120 %	0.263 %	0.091 %	0.669 %
Case 2	7.335 %	0.249 %	0.186 %	1.330 %
Case 3	5.651 %	0.251 %	0.124 %	2.182 %

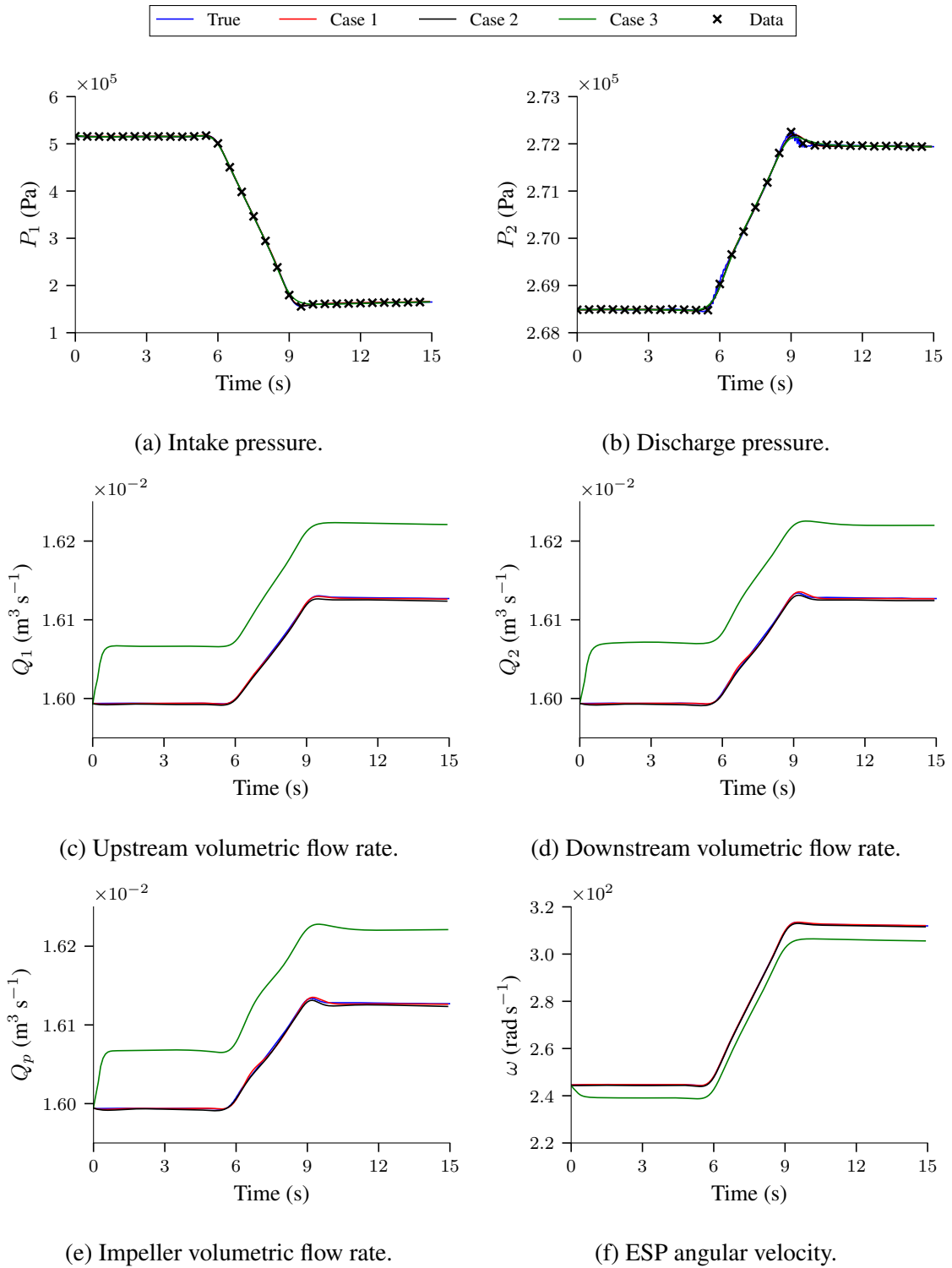


Figure D.1: Predicted states for the simulated and unknown flow parameters for the second experiment.

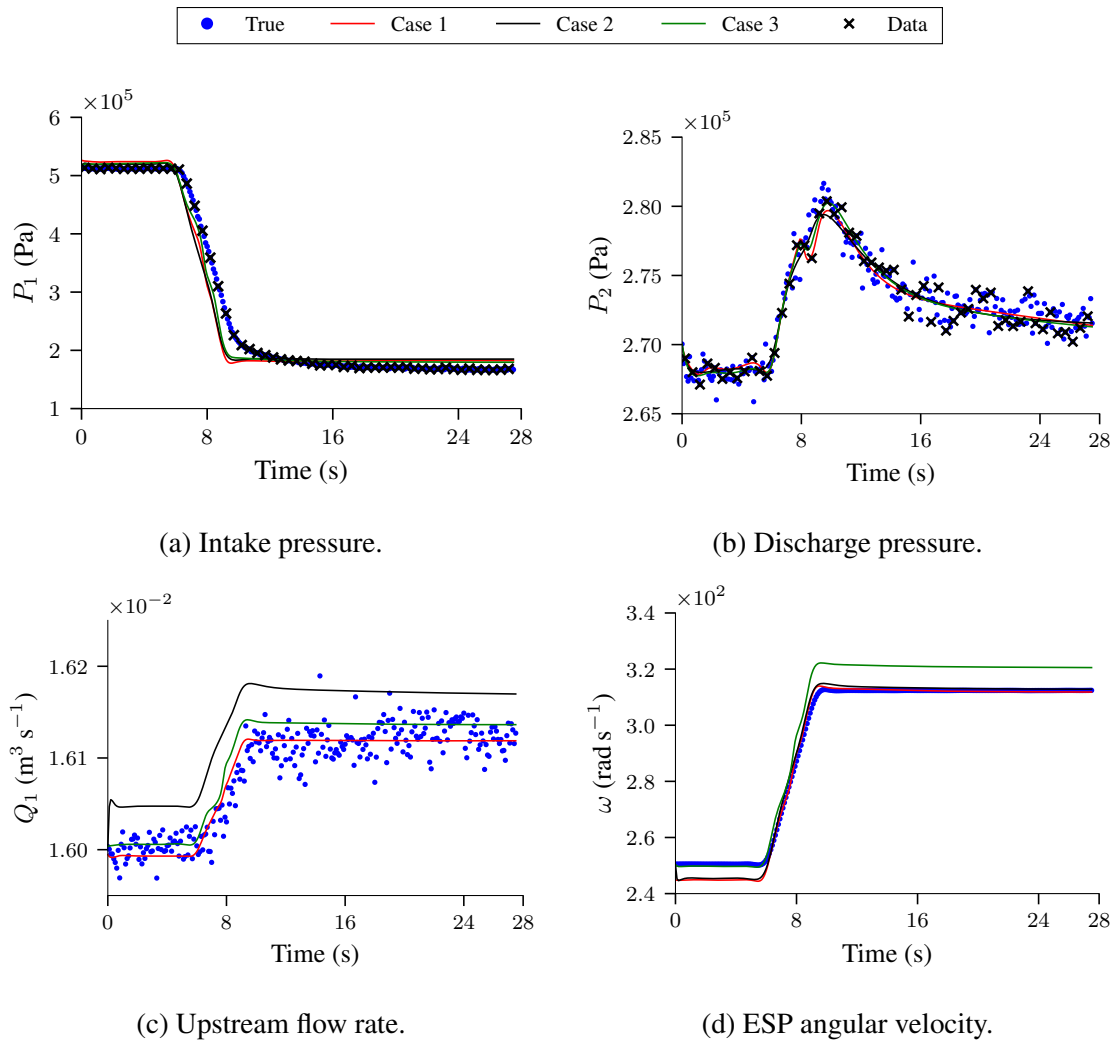


Figure D.3: Predicted states for the experimental data and unknown flow parameters for the second investigation.

D.2 Estimated unknown parameters mean and standard deviation

In this section, we present additional PINN results for parameter estimation in the ESP system model. These results are obtained by averaging parameter estimations over the PINN 30 training runs and computing the standard deviation. The tables Tables D.4 and D.5 contain the results of the first and second experimental investigations, respectively. It is important to note that these tables serve as complementary results of the discussed in Section 7.2 and are not the focus of detailed discussion in this work. They are included for the sake of completeness and may be of interest to future research works.

Appendix E Physics loss function for the PINN model for the ESP system detail

As presented in Section 4.5, the PINN physics loss function for the ESP system is defined as

$$\mathcal{L}^{ode}(\boldsymbol{\theta}, \boldsymbol{\Lambda}, \boldsymbol{\lambda}_r) = \sum_{s \in \Phi} m(\lambda_r^s) \mathcal{L}_s^{ode}, \quad \Phi = \{Q_p, \omega, Q_1, Q_2, P_1, P_2\}, \quad (\text{E.1})$$

where, $\boldsymbol{\theta}$ represents the neural network hyperparameters, $\boldsymbol{\Lambda}$ are the unknown parameters, and $\boldsymbol{\lambda}_r$ are the physics loss self-adaptive weights for each ESP system equation. The function $m(\cdot)$ acts as a mask and is considered to be a softplus function. Expanding Equation (E.1) for every state, we get:

$$\mathcal{L}_{Q_p} = m(\lambda_r^{Q_p}) \frac{1}{N} \sum_{i=1}^N r(Q_p)^2 = m(\lambda_r^{Q_p}) \frac{1}{N} \sum_{i=1}^N \left(\frac{dQ_p}{dt} - \frac{(P_1 - P_2 + k_3 \mu Q_p) A_p}{\rho L_p} + \frac{A_p (k_{1p} \omega Q_p + k_{2p} \omega^2 + k_{4p} Q_p^2)}{L_p} \right)_i^2, \quad (\text{E.2a})$$

$$\mathcal{L}_{\omega} = m(\lambda_r^{\omega}) \frac{1}{N} \sum_{i=1}^N r(\omega)^2 = m(\lambda_r^{\omega}) \frac{1}{N} \sum_{i=1}^N \left(\frac{d\omega}{dt} - \frac{\gamma(t) - k_{1s} \rho Q_p^2 - k_{2s} \rho \omega Q_p - \frac{k_{3s} \mu \omega - k_{4s} \omega - k_{5s} \omega^2}{I_s}}{I_s} \right)_i^2, \quad (\text{E.2b})$$

$$\mathcal{L}_{Q_1} = m(\lambda_r^{Q_1}) \frac{1}{N} \sum_{i=1}^N r(Q_1)^2 = m(\lambda_r^{Q_1}) \frac{1}{N} \sum_{i=1}^N \left(\frac{dQ_1}{dt} - \frac{(k_{bd} \omega t - Q_1) k_{bl} \mu + P_{in} - P_1}{\rho L_u} - \frac{f_f(Q_1, \mu, L_u, d_u) Q_1^2 A_u}{\rho L_u} - \frac{k_u Q_1^2}{2 L_u A_u} \right)_i^2, \quad (\text{E.2c})$$

$$\mathcal{L}_{Q_2} = m(\lambda_r^{Q_2}) \frac{1}{N} \sum_{i=1}^N r(Q_2)^2 = m(\lambda_r^{Q_2}) \frac{1}{N} \sum_{i=1}^N \left(\frac{dQ_2}{dt} - \frac{(P_2 - P_{out}) A_d}{\rho L_d} - \frac{(f_f(Q_2, \mu, L_d, d_d) Q_2^2) A_d}{\rho L_d} - \frac{k_d Q_2^2}{2 L_d A_d} - \frac{Q_2 A_d}{L_d C_v(a)^2 1000} \right)_i^2, \quad (\text{E.2d})$$

$$\mathcal{L}_{P_1} = m(\lambda_r^{P_1}) \frac{1}{N} \sum_{i=1}^N r(P_1)^2 = m(\lambda_r^{P_1}) \frac{1}{N} \sum_{i=1}^N \left(\frac{dP_1}{dt} - \frac{(Q_1 - Q_p) B}{A_u L_u} \right)_i^2, \quad (\text{E.2e})$$

$$\mathcal{L}_{P_2} = m(\lambda_r^{P_2}) \frac{1}{N} \sum_{i=1}^N r(P_2)^2 = m(\lambda_r^{P_2}) \frac{1}{N} \sum_{i=1}^N \left(\frac{dP_2}{dt} - \frac{(Q_p - Q_2) B}{A_d L_d} \right)_i^2, \quad (\text{E.2f})$$

where N denotes the collocation point, $r(\cdot)$ represents the residual, and the subscript i indicates that the state variables are evaluated at $t = t_i$.

Appendix F PINN training settings

The training algorithm settings employed for each analyzed case are detailed in Tables F.1 to F.3. The training procedure involved multiple steps characterized by specific Adam optimization settings. The tables present the number of epochs alongside the learning rates denoted as NN for the neural network weights, PS for the ESP model’s unknown parameters, and SA for the self-adaptive weights. The maximum number of epochs employing self-adaptive weights for each step is also indicated as Max. SA. It is important to note that the training process is continuous.

In the Case 1 settings, described in Table F.1, the same training procedure was applied to the simulated and simulated-with-noise (Sim. noisy) data scenarios. However, it was necessary to adapt it to suit the experimental data scenario. Importantly, the settings were maintained across the investigations.

Table F.1: Adam training settings for neural network training in Case 1 (three unknown parameters).

Scenario	Adam				
	Epoch (#)	NN	PS	SA	Max. SA
Simulated Sim. noisy	0 to 32k	1.0E−3	1.0E−3	8.0E−4	12k
	32k to 38k	2.0E−5	1.0E−4	1.0E−6	12k
	38k to 60k	1.0E−5	1.0E−6	1.0E−5	12k
Experimental	0 to 32k	1.0E−3	5.0E−3	5.0E−4	32k
	32k to 38k	2.0E−5	1.0E−4	1.0E−6	38k
	38k to 60k	1.0E−5	1.0E−6	1.0E−5	60k

In the Case 2 settings, described in Table F.2, it was employed a consistent training process for both the simulated data and the simulated with noise data (Sim. noisy). However, adjustments were necessary for the experimental data. In the initial step of each scenario, it was employed a linear learning rate schedule for both the neural network weights (NN) and the unknown ESP parameters (PS). For the learning rate of the neural network weights, denoted as χ_{NN} , it was initiated at 1.0×10^{-3} and linearly transitioned to 1.0×10^{-4} between epochs 4000 and 6000. Similarly, for the learning rate of the unknown ESP parameters, denoted as χ_{PS} , it was started at 1.0×10^{-3} and transitioned to 1.0×10^{-4} between epochs 4000 and 8000.

In the Case 3 settings, described in Table F.3, the same training approach was used for both the simulated and simulated-with-noise (Sim. noisy) data scenarios. However, it was required to adjust the training settings for the experimental data scenario. It is worth noting that the training settings were kept consistent throughout our experimental investigations.

Table F.2: Adam training settings for neural network training in Case 2 (seven unknown parameters).

Scenario	Adam				
	Epoch (#)	NN	PS	SA	Max. SA
Simulated Sim. noisy	0 to 52k	χ_{NN}	χ_{PS}	$5.0E-3$	24k
	52k to 63k	$2.0E-5$	$1.0E-4$	$1.0E-6$	24k
	63k to 83k	$1.0E-5$	$1.0E-6$	$1.0E-5$	24k
Experimental	0 to 48k	χ_{NN}	χ_{PS}	$5.0E-3$	8k
	48k to 59k	$2.0E-5$	$1.0E-4$	$1.0E-6$	8k
	59k to 79k	$1.0E-5$	$1.0E-6$	$1.0E-5$	8k

Table F.3: Adam training settings for neural network training in Case 3 (eight unknown parameters).

Scenario	Adam				
	Epoch (#)	NN	PS	SA	Max. SA
Simulated Sim. noisy	0 to 44k	$5.0E-4$	$1.0E-2$	$1.0E-3$	16k
	44k to 70k	$5.0E-4$	$5.0E-4$	$5.0E-4$	16k
	70k to 80k	$2.0E-5$	$1.0E-5$	$2.0E-5$	16k
	80k to 90k	$1.0E-5$	$1.0E-6$	$1.0E-5$	16k
Experimental	0 to 16k	$5.0E-4$	$2.0E-3$	$1.0E-3$	6k
	16k to 36.3k	$5.0E-4$	$5.0E-4$	$5.0E-4$	6k
	36300 to 41k	$5.0E-4$	$5.0E-4$	$5.0E-4$	6k
	41k to 51k	$2.0E-5$	$1.0E-5$	$2.0E-5$	6k
	51k to 61k	$1.0E-5$	$1.0E-6$	$1.0E-5$	6k

The initial self-adaptive weight values significantly impacted the experimental data scenario of Case 2 and all scenarios in Case 3. These cases were more challenging due to their higher number of unknown parameters, noisy data, and model uncertainties. Although the self-adaptive weights could adapt and achieve satisfactory state and parameter estimation results, they needed further adjustment of the initial weights to improve performance and accuracy in these scenarios. The initial weights are shown in Table F.4.

The Table F.4 presents the initial weights for data, physics, and initial conditions losses for the cases and scenarios evaluated in this work. The Q_p , ω , Q_1 , Q_2 , P_1 , and P_2 represent initial weights for the state corresponding ODE. The ‘‘Data’’ column is the initial weight for data loss, and the ‘‘I.C.’’ column is the initial condition weights. The ‘‘Sim.’’ case is for the simulated and simulated with noise scenarios, and ‘‘Exp.’’ is for the experimental data scenario.

Table F.4: Initial weights for the data, physics, and initial conditions (I.C.) losses.

Case	Data	Physics						I.C.
		Q_p	ω	Q_1	Q_2	P_1	P_2	
Case 1: Sim.	4.00E2	1.0E-6	1.0E-6	1.0E-6	1.0E-6	1.0E-6	1.0E-6	1.0
Case 1: Exp.	1.0E1	1.0E-6	1.0E-6	1.0E-6	1.0E-6	1.0E-6	1.0E-6	1.0
Case 2: Sim.	1.0E1	1.0E-6	1.0E-6	1.0E-6	1.0E-6	1.0E-6	1.0E-6	1.0
Case 2: Exp.	1.0E-4	1.0E-6	1.0E-6	1.0E-4	1.0E-4	1.0E-6	1.0E-6	1.0
Case 3: Sim.	1.0E1	1.0E-6	1.0E-6	1.0E-4	1.0E-4	1.0E-6	1.0E-6	1.0
Case 3: Exp.	1.0E1	1.0E-6	1.0E-6	1.0E-4	1.0E-4	1.0E-6	1.0E-6	1.0